Universidade de Aveiro

Departamento de Geociências

2016

Ricardo Lionel Gonçalves Correia

Morfologia detalhada da plataforma continental da Antártida Este, entre 128º e 134ºE

Detailed seafloor morphology of the East Antarctic continental shelf, between 128º and 134ºE

Universidade de Aveiro

Departamento de Geociências

2016

Ricardo Lionel Gonçalves Correia

Morfologia detalhada da plataforma continental da Antártida Este, entre 128º e 134ºE

Detailed seafloor morphology of the East Antarctic continental shelf, between 128º and 134ºE

Dissertação apresentada à Universidade de Aveiro para cumprimento dos requisitos necessários à obtenção do grau de Mestre em Engenharia Geológica, realizada sob a orientação científica da Dra. Caroline Lavoie, investigadora auxiliar do CESAM e do Departamento de Geociências da Universidade de Aveiro, e do Dr. Frank Oliver Nitsche, investigador do *Lamont-Doherty Earth Observatory*, Universidade Columbia.

Este trabalho teve o apoio financeiro primário da fundação National Science Foundation dos EUA (NSF), Centro de programas polares à universidade de Columbia (concessão ANT-1245879) e aos contratantes de apoio Antártico/Edison Chouest Offshore. Ricardo Correia recebeu o apoio financeiro do Programa Polar Português - PROPOLAR para participar do cruzeiro NBP1503**.**

This work had primary financial support from the US National Science Foundation (NSF), Office of Polar Programs to Columbia University (Award ANT-1245879) and to Antarctic Support Contractors/Edison Chouest Offshore. Ricardo Correia received the financial support of PROPOLAR (Programa Polar Português) to participate in the NBP1503 cruise.

o júri

Presidente	Prof. Doutor Jorge Manuel Pessoa Girão Medina Professor Auxiliar do Departamento de Geociências da Universidade de Aveiro
Arguente	Prof. Doutor Luis Filipe Fuentefria de Menezes Pinheiro Professor Associado do Departamento de Geociências da Universidade de Aveiro
Orientador	Doutora Caroline Lavoie Investigadora Auxiliar do CESAM e do Departamento de Geociências da Universidade de Aveiro

agradecimentos

Em primeiro lugar, quero expressar a minha sincera gratidão à minha supervisora Dra. Caroline Lavoie pelo seu apoio constante durante a minha formação académica. Pela paciência, motivação, entusiasmo e conhecimento transmitido em glaciologia e geomorfologia. A sua orientação por inúmeras horas, mesmo à distância, foi indispensável na realização desta tese. Quero agradecer, principalmente, por ter acreditado em mim e por me ter dado a oportunidade de viajar até à Antártida: uma experiencia única, que vai para além do conhecimento transmitido pela literatura.

Gostaria de agradecer ao Prof. Luis Menezes por me introduzir nos campos da Geologia e Geofísica marinha. Estou-lhe grato pela excelente oportunidade de trabalhar no laboratório de Geologia e Geofísica Marinha (LGGM/DGEO), que permitiu fortalecer a minha formação académica, progredir a nível profissional e também pessoal. Um agradecimento especial aos jovens cientistas que passaram pelo laboratório que foram e continuam a ser uma inspiração para mim: Dr. Clara Sena, Dr. Daniela Gonçalves e Catarina Lemos.

Quero estender o meu agradecimento ao Dr. Frank Nitsche, investigador principal da campanha NBP1503, pela oportunidade de participar nesta investigação e de navegar ao longo da costa Este da Antártida. Obrigado pelo excelente ambiente, as conversas durante a campanha e pela partilha de informação e de experiências.

Estou também agradecido ao Dr.Omar Bennazzouz pelo apoio e ajuda no uso do *software SPW*, estando sempre disponível para responder às minhas questões. Um agradecimento, também, ao Prof. Eduardo Silva pelo esclarecimento de dúvidas relativas à análise estatística.

Agradeço à equipa científica da campanha NBP1503, ao capitão e à corporação do R/V Nathaniel B. Palmer pela ativa contribuição e cooperação. Em particular, a Kathleen Gavahan (ASC crew) pelos ensinamentos e orientação na aquisição de dados de batimetria multifeixe. Um especial agradecimento à fantástica “Night Watch Team”, da qual fazia parte juntamente com o Dr. Raul Guerrero, Eva Cougnon, David Branson e George Aukon. Obrigado pelos bons momentos, pelas experiências inesquecíveis e pelo apoio.

agradecimentos

Muito obrigado a todos os amigos que estiveram ao meu lado durante esta etapa tão importante da minha vida. Estou imensamente agradecido à minha família: pais e irmão. Sempre estiveram ao meu lado, apoiando, dando os melhores conselhos e desejando que tudo corresse pelo melhor. Por fim, quero agradecer à Elisabete Vieira pela ajuda e todo o encorajamento. Ela esteve sempre presente, nos bons e maus momentos.

palavras-chave

batimetria multifeixe, sismica de alta resolução, geomorfologia glaciar, morfometria, análise estatistica, extensão glacial, dinâmica glaciar

resumo

Dados de batimetria multifeixe e de sísmica de alta resolução, adquiridos na plataforma continental da Antártida, região Este, permitiram o reconhecimento de aspetos geomorfológicos derivados da dinâmica glaciar associada a um manto de gelo mais extenso no passado. No âmbito do projeto científico Norte-americano, *Vulnerability of East Antarctic ice shelves* da NSF (*National Science Foundation*), e do projeto *EAIS-MARGINS* do Programa Polar português (PROPOLAR), foi realizada a interpretação e análise quantitativa dos diversos aspetos morfológicos através da morfometria e análise estatística, com o objetivo de melhor entender a dinâmica do manto de gelo no passado. A área de estudo inclui um segmento da plataforma continental compreendida entre os glaciares Frost e Dibble (128ºE e 134ºE). Os dados foram adquiridos na campanha de investigação NBP1503 em Abril de 2015, a bordo do navio RVIB Nathaniel B. Palmer dos Estados Unidos da América.

Os resultados revelam uma plataforma continental situada entre os 300 e 990 m de profundidade. A zona proximal e intermédia é caracterizada por um aspeto irregular, onde é possível constatar a presença de *meltwater channels* com mais de 230 m de profundidade e formas semelhantes a *drumlins,* identificadas entre os 800 e 900 m de profundidade. Sulcos deixados pela deriva de icebergs são esporadicamente observados na zona distal da plataforma continental entre os 380-410 m de profundidade. No limite da plataforma continental encontra-se presente um sistema de *gullies* que se desenvolvem ao longo do talude. Além disso a análise quantitativa dos aspetos morfológicos associados às formas de *drumlin* e *gullies* permitiu uma descrição morfológica mais detalhada, e encontrar padrões que permitiram obter mais informações sobre os fatores de controlo envolvidos durante a sua formação.

A distribuição observada das diferentes morfologias identificadas é coerente com estudos anteriormente realizados e constituem uma forte evidência de que o manto de gelo teve uma extensão até ao limite da plataforma continental e que a sua dinâmica foi mais ativa do que se tem constatado.

acknowledgments

First and foremost, I greatly thank and express my sincere gratitude to my supervisor Dr. Caroline Lavoie for her continuous support during my academic formation, for her patience, motivation, enthusiasm and knowledge in Glaciology and Geomorphology. Her guidance trough countless hours, even at distance, was indispensable for the realisation of this master thesis. I would like to thank her for believing in me and for the opportunity to travel to the East Antarctic: an amazing experience which goes way beyond the textbooks.

I am thankful to Prof. Luis Menezes, who first introduced me into marine geology and geophysics field. I thank him for the opportunity and great experience to be part of the marine geology geophysics lab (LGGM/DGEO), which given me a strong and solid academic formation, and a professional and moral growing. Also, special thanks to young and inspiring scientists: Dr. Clara Sena, Dr. Daniela Gonçalves and Catarina Lemos.

I would like to extend my sincerest gratitude to Dr. Frank Nitsche, scientific chief of the NBP1503 cruise, for the opportunity to conduct this research and to sail along the East Antarctic coast. Thank you for the great environment, the discussion during the campaign, and also for the provided insightful comments and expertise.

Also, I am indebted to Dr. Omar Bennazzouz for his support and help with the use of the SPW software, being many times available to answer questions, and to Prof. Eduardo Silva for the clarification of specific doubts on statistical analysis.

My thanks to the Shipboard Scientific Party of NBP1503, and the captain and crews of the R/V Nathaniel B. Palmer for their efforts. In particular, I thank Kathleen Gavahan (ASC crew) for teachings and guidance on swath bathymetry data acquisition. Also, thank you to the awesome 'Night watch' team, in which I was a member along with Dr. Raul Guerrero, Eva Cougnon, David Branson and George Aukon, for the great moments, memories and support.

acknowledgments

To those friends who walked beside me during this important moment of my life, a very special thanks. I am especially thankful to my family: my parents and brother. They always supported and encouraged me with their best wishes. Finally, I would like to thank Elisabete Vieira for her help and encouragement, she stood by me through the good times and harder ones.

keywords

swath bathymetric data, sub-bottom CHIRP data, glacial geomorphology, morphometry, statistical analisys, glacial extent, glacial dynamics.

abstract

Swath bathymetric and sub-bottom CHIRP data collected on the East Antarctica continental shelf and seaward allowed detailed mapping of the geomorphic features formed during past times of extended grounded ice from an expanded East Antarctic Ice Sheet (EAIS). Under the umbrella of the American National Science Project 'Vulnerability of East Antarctic ice shelves' and the Portuguese PROPOLAR project EAST-MARGINS, the seafloor morphology was interpreted and submitted to quantitative analyses, through morphometry and statistical analysis, to better understand the EAIS dynamic in the past. The study area included a segment of the continental shelf, slope and rise between the Frost and Dibble Glaciers (128ºE and 134ºE). The data were collected during the cruise NBP1503 in April 2015, on board the U.S. RVIB Nathaniel B. Palmer.

The results revealed a continental shelf with depths varying between 300 m and 990 m. The inner and mid shelf area is characterised by a crudely streamlined landscape where subglacial meltwater channels up to 230 m deep and drumlin-like bedforms at 800-900 m water depth have been identified. Sporadic iceberg scours occur in the outer continental shelf between 380-410 m of water depth. The shelf break is defined by a gully system which extends along the continental slope, followed by sediment mounds observed on the continental rise. Moreover, quantitative analyses on drumlin-like bedforms and gullies allowed a further morphological description to better delineate patterns, and provided more details related to the controlling factors involved during their formation.

The distribution of identified glacial features is coherent with other previous studies and constitutes a strong evidence that the grounded ice reached the continental shelf break in the past and was more dynamic than previously thought.

Table of contents

Agradecimentos

Resumo

Acknowledgments

Abstract

List of figures iii

List of Tables xiii

CHAPTER 1: Introduction 1

1.1 Nature and scope of the thesis 1

1.2 Objectives 1

1.3 NBP1503 expedition 2

1.4 Study area 5

1.5 Structure of the thesis 7

References 8

CHAPTER 2: Background 9

2.1 Antarctica 9

2.1.1. Geological context of Antarctica 10

2.1.2. Present and Past Glacial Setting 13

2.1.3. Weather and climate 22

2.1.4. Physical oceanographic setting 23

2.1.5. Antarctica's role in the global environment 25

2.2. East Antarctica 26

2.2.1. Glacial character of the EAIS 26

2.3. Glacial seafloor morphology and forming processes 29

2.3.1. Inner continental shelf 31

2.3.2. Middle continental shelf 41

2.3.3. Outer continental shelf 43

2.3.4. Ice-marginal depocentres and other landforms 44

2.4. Continental slope and rise bedforms and processes 50

References 53

CHAPTER 3: Methods 61
3.1 Swath bathymetry 61
3.1.1 System description and operations 61
3.1.2 Data processing and visualisation 62
3.2 Geomorphometry 65
3.2.1 Drumlin-like parameters 66
3.2.2 Gully parameters 68
3.3 Statistical Analysis 71
3.4 Sub-Bottom profiler 72
3.4.1 System description and operations 72
3.4.2 Data processing 74
3.5 Considerations and limitations 75
References 78

CHAPTER 4: Results and interpretation 79
4.1 Inner to outer continental shelf 80
4.1.1 Subglacial meltwater channels 80
4.1.2. Drumlin-like bedforms 81
4.1.3 Iceberg scours 89
4.2 Continental shelf edge and slope 91
4.2.1 Submarine gullies 91
4.3 Continental rise 101
References 104

CHAPTER 5: Discussion 107
5.1 Glacial bedforms context and control factors 107
5.2 Extent and dynamics of the EAIS since LGM 115
References 117

CHAPTER 6: Conclusions and recommendations 121
6.1. Conclusions 121
6.2. Recommendations for further study 122
References 122

Appendix I – Drumlin-like measurements..... 123
Appendix II – Correlation matrix of drumlin-like morphological parameters... 124
Appendix III – Gully measurements 125

List of figures

Figure 1.1. The icebreaker RVIB Nathaniel B. Palmer (**A**) and the navigation routes during the NBP1503 expedition (**B**). 3

Figure 1.2. Geophysical working area (**A**) and Probe (Rosette) operation for CTD measurements (**B**) during the NBP1503 expedition. **C**- Schematic view of a warm waters intrusion into the continental shelf by a cross-shelf trough (from: http://forum.arctic-sea-ice.net/index.php?topic=874.50). 4

Figure 1.3. Sea ice covers in March 13 2015 (**A**) and April 28 2015 (**B**). Images from NBP1503 cruise report. 4

Figure 1.4. The study area considered on this research project (yellow box), confined between Frost and Dibble Glaciers (between 128º E and 134º E). 5

Figure 1.5. Wilkes Land bathymetric map from Escutia et al. (2003) previously modified from Chase et al. (1987) and Eittreim et al. (1995) showing the general seafloor physiography. The study area considered in this work is represented by yellow boundary line. 6

Figure 1.6. Map from Escutia et al. (2003) showing the location of multichannel seismic data recorded by the 'Institut Français du Petrole (IFP)', the United States Geological Survey (USGS) and the Japan National Oil Corporation (JNOC) along the Wilkes Land continental margin. The study area considered in this work is approximately represented with yellow boundary line. ... 7

Figure 2.1. Geographic map of Antarctica (Source: http://www.polarhistory.net/antarctica-map geographic/). 9

Figure 2.2. The main geological provinces, a broad division, of the East Antarctic Shield (pink), West Antarctic domain (green) and the Trans-Antarctic domain (purple). The South Pole is indicated by the cross symbol in the East Antarctica Shield (from Harley, 2011). 11

Figure 2.3. Geological time-scale with details regarding the formation and evolution of the Antarctic continent. This figure is a compilation of information from: Anderson, 1999 (1); Walton, 2013 (2); Goodge, 2007 (3); Stampfli et al., 2013 (4); ten Brink et al., 1997 (5); Harley, 2011 (6); Meert et al., 1997 (7) Smellie, 1981 (8) and Pisarevsky et al.2003 (9). 12

Figure 2.4. Reconstruction of Gondwana 180 million years ago (Ma) and its subsequent fragmentation. The red dots show the location of possible mantle hot spots that may have contributed to the continental fragmentation. **A-** Gondwana 180 Ma; **B-** South Atlantic opening 130 Ma; **C-** Australia and New Zealand rifting 100 Ma; **D-** Isolation of Antarctica 35 Ma (Image adapted from Walton, 2013. Credit: Bryan Storey). 13

Figure 2.5. Overall morphological aspects of the Antarctic continent. **A-** Surface topography, **B-** Ice Sheet thickness, **C-** Bed topography (from Fretwell et al., 2013). **D-** W-E Cross-sectional profile of the Antarctic continent (from National Research Council, 2011). 14

Figure 2.6. The WAIS and its respective subdivision: Amundsen Sea sector; Weddell Sea sector and Ross Sea sector (from Bindschadler, 2006). 15

Figure 2.7. Antarctic Peninsula map (Source: 16

Figure 2.8. High resolution mosaic of the ice motion in Antarctica from multiple satellite interferometric synthetic-aperture radar data (from Rignot et al., 2011), and surface topography (from Walton, 2013; Credit: Gaël Durand, using the data synthesis of Anne Le Brocq). 17

Figure 2.9. Glacial environment of outer regions and dynamics of Antarctica. The transition line where grounded ice reaches the floatation point is designed Grounding line (Image from:..... 18

Figure 2.10. Components of the mass balance of a glacier, note that arrows are not totally indicative of physical pathways of mass transfer (from Cogley et al., 2011)..... 19

Figure 2.11. Surrounding Sea ice concentration during Antarctic Maximum (Left) and Minimum (Right), from September 2008 to February 2009 (Source: http://earthobservatory.nasa.gov/Features/SeaIce/ page4.php 19

Figure 2.12. Cenozoic variation of ice sheet from proxies showing ice cover variation trough time: (a) global eustatic sea-level from sequence stratigraphy; (b) oxygen isotope ratios in Atlantic benthic foraminifera; (c) Topography of the Antarctic continent without ice cover and (d) hypotetical ice cover (adapted from Barker et al., 1999 and Pollard and DeConto, 2009). . 21

Figure 2.13. Total ice cover volume variation in Antarctica from last 1.5 million years (a) and snapshots at particular times (b) resulted from a long term simulation. On the graphic (a) is shown the total volume of ice on the Antarctic continent (red line) in long term simulation mainly from deep-sea-core $\delta^{18}O$ record. (adapted from Pollard and DeConto, 2009). 21

Figure 2.14. Surface temperatures and precipitation gradients over the Antarctic continent (adapted from Walton, 2013). 22

Figure 2.15. Prevailing wind direction over Antarctica, on the left (from King and Turner, 2007) and a diagram showing the downfall winds (katabatic winds), source: http://climatestate.com /2013/07/26 /antarctic-methane-emissions/. 23

Figure 2.16. On left, atmospheric pressure distribution at sea level displaying the major high and low pressure systems, which determine the winds over the Southern Ocean (From Walton, 2013,

Credit: Eberhard Fahrbach, AWI). On the right, schematic map showing the major currents and fronts of the Southern Ocean (F-Front, C-Current, G-Gyre). The figure ilustrates the Polar Front and Sub-Antarctic Front, which are the major fronts of the Antarctic Circumpolar Current, and regional currents of the Weddell and Ross Sea (Weddell Gyre and Ross Gyre, repectivelly) Image adpted from Convey et al. (2009). 24

Figure 2.17. Depth-latitude diagram showing the major circulation and water masses of the Southern Ocean, representing also Deep Water upwelling, in this case from Atlantic sideways (Source: https://en.wikipedia.org/wiki/North_ Atlantic_Deep_Water). 25

Figure 2.18. Mass balance estimates of EAIS and other polar regions over the period 2003 to 2008, based from four independent techniques, Input output method (Red), Radar altimetry (Blue), Laser altimetry (Green) and Gravimetry (Cian) (from Shepherd et al., 2012). 27

Figure 2.19. Antarctic ice-shelf ice-thickness change rate (ΔT/Δt, 2003–2008) and relative ice losses for ice sheet drainage basins (grey circles) between 1992 and 2006. The white labels indicate the ice shelves. Image from Pritchard et al. (2012). 28

Figure 2.20. Basal melt rates of Antarctic ice shelves (perimeters in 2007–2008) coded from < –5 m/year (freezing) to > +5 m/year (melting). Each circle graph is proportional in area to the mass loss from each shelf, in gigatons (1 Gt = 1012 kg) per year, partitioned between iceberg calving (hatch fill) and basal melting (black fill). Image from Rignot et al. (2013). 28

Figure 2.21. Spatial and temporal variations in EAIS glacier terminus position from all measurements in 1974, 1990, 2000 and 2010. The rate of terminus position change for each glacier and period is shown by the single-colour circles. Pie charts represent the percentage of glaciers advancing and retreating in each major region. Image from Miles et al. (2013). 29

Figure 2.22. Representative bathymetric profiles from the West (A-B) and East (C-F) Antarctic continental shelves illustrating the great depth, irregular relief, and landward-sloping profile of the shelf. Image adapted from Anderson (1999). 30

Figure 2.23. Palaeo-ice stream land system model of the continental shelf (A) (Source: http: //www.geog.cam. ac.uk/research/projects/submarineglacialatlas/) and generalized distribution of the glacial geomorphic features (B) (from Benn and Evans, 2010 reproduced from Wellner et al., 2006). 31

Figure 2.24. Drumlinoid glacial landforms and internal composition. (Source: http://www.landforms.eu/ lothian/Drumlinoid% 20glacial%20landforms.htm) 32

Figure 2.25. Different formation processes of drumlins. Formation through **A**- deforming sediments (Benn and Evans, 2010), **B**- the meltwater hypothesis (John Shaw, 2002, reproduced by Benn and Evans, 2010); **C** – a vortex generated in front of an obstacle (Shaw et al., 2008). 33

Figure 2.26. Details of the seafloor continental shelf from multibeam images (**A** and **B**) (from Graham et al. (2009) and Wellner et al. (2006)) and exemplified photos where it is possible to

identify drumlinised bedforms (**C** and **D**) (from Shaw et al. (2008); http://www.geol.umd.edu/~jmerck/geol100 /lectures /36a.html). 34

Figure 2.27. Formational process of a crag and tail (**A**), and examples on the seafloor (**B**, from Graham et al. (2009)) and. near the University of Stirling, UK (**C**, from https://en. wikipedia.org/wiki/Crag_and_tail. 35

Figure 2.28. Formation process of a roche moutonnée (**A**) and examples from the seafloor (from Wellner et al., 2006) (**B**) (from http://people.uwec.edu/jolhm/Superior2007/TeamC/rouche.html) and visible on land (C) (from http://brian-mountainman.blogspot.pt/2013/11/another-roche-moutonnee.html. 36

Figure 2.29. Model for the development of whalebacks and roches moutonnées based on erosional bedform distribution (from Benn and Evans, 2010) (**A**), and examples of whaleback forms on the seafloor (**B**) (from Graham et al., 2009) and on land in SW Sweden (**C**) (Source: http://www.land forms.eu/cairngorms/whaleback.htm). 37

Figure 2.30. Examples of grooves on the seafloor (**A**) (image from Graham et al., 2009) and on land (**B**) source: https://en.wikipedia.org/wiki/Kelleys_Island,_Ohio). 37

Figure 2.31. Examples of P-Forms on the seafloor (**A**) (image from Lowe and Anderson, 2003) and on land (**B**) (source: http://www.geocaching.com/geocache/GC460Q5_stone-chutes). ... 38

Figure 2.32. Ice sheet hydrologic systems for land-terminating and marine-terminating glacier outlets (**A**) (Source: http://www.venachu.com/research.html) and examples of meltwater channels on the seafloor (**B**) (Graham et al., 2009) and on land (**C**) (https://notendur.hi.is/oi/glacial_geology_photos.htm). 39

Figure 2.33. Examples of tunnel valleys on the seafloor, plan view (**A,** from Wellner et al., 2006) and oblique view (**B**, from Bradwell et al., 2008). 40

Figure 2.34. Example of basins on the seafloor (**A**, from Nitsche et al., 2013) and on land (**B**, photo from Bennett and Glasser, 2009). 40

Figure 2.35. Formation process of glacial trough in a region during the glacial maxima (**A**) the and subsequent morphology (**B**), with an example of direct observation, photo of the Gleen Tilt tourgh (**C**) and trough multibeam imagery (**D**). Sources: http://brian-mountainman.blogspot.pt/2014/07/glen-tilt-classic-glacial-trough.html; http://jupiter.plymouth.edu/~sci_ed/Turski/Courses/Earth_Science/Images/ 10.3glacial.JPG; http://mareano.no/en/news/nyheter_2010/mapping_seabe d_soroya. 41

Figure 2.36. Mega scale glacial lineations on the seafloor (**A**, from Graham et al., 2009) and on land (**B**, Source: https://www.sheffield.ac.uk/drumlins/msgl). 42

Figure 2.37. Example of Iceberg furrows (gouge) on the seafloor (**A**, from Wellner et al., 2006) and their formation (**B**, from: https://en.wikipedia.org /wiki/Seabed_gouging_ by_ice). 43

Figure 2.38. Gullies on the seafloor (**A**, from Dowdeswell et al., 2006) and diagram of marine-terminating glacier showing gullies formation (**B**, adapted from: https://notendur.hi.is/oi/glacial_geology_ photos.htm)..... 44

Figure 2.39. Schematic diagram with the position of the grounding zone at the margin of an ice sheet/glacier with a floating ice shelf (**A**) and at a tidewater ice-sheet margin (**B**). Typical ice-stream landforms assemblage produced by fast (**C**) and slow (**D**) ice-stream flow on a continental shelf. Image from Batchelor and Dowdeswell (2015)..... 45

Figure 2.40. Grounding zone wedges (GZWs) from Larsen A Ice Shelf, AP (**A**) and GZWs from Vestfjorden, north Norway (**B**). The white arrows show the direction of the former ice flow. (Adapted from Dowdeswell et al., 2008). **C** - Depositional model explaining the formation of the grounding-line wedges (from Benn and Evans, 2010). 46

Figure 2.41. Schematic diagram showing a case of a transverse moraine formation (a). Image adapted from: https://www.geocaching .com/geocache/GC5MWT9_mor-y03-005-utterinvuori-hauho. 47

Figure 2.42. Case of large terminal and recessional moraine ridges founded trough multibeam images (A and B respectively) and through direct observations (C and D). Sources: Batchelor and Dowdeswell, 2015; Dowdeswell et al., 2014 and http://www.mleziva.info/unit5/U05L01.htm. 47

Figure 2.43. Hummocky moraines observed on the seafloor (**A**) (from Batchelor and Dowdeswell, 2015) and on land (**B**) (Photo: Ó. Ingólfsson, 2004. in https://notendur.hi.is/oi/bruarjokull_project.htm). 48

Figure 2.44. Small retreat moraines (or De Geer moraines) on the seafloor (**A**) and on land, Baffin Island (Canada) (**B**). Sources: Batchelor and Dowdeswell, 2015; http://brian-mountainman.blogspot.pt/ 2015_04_01_archive.html. 48

Figure 2.45. Different landsystem models with examples of swath-bathymetric data, showing different recession rates (from Dowdeswell et al., 2008)..... 49

Figure 2.46. Processes of sediment transport and deposition that constitute a marine grounding-line fan (from Benn and Evans, 2010). 50

Figure 2.47. Sequence model of deposition on shelf and slope through a glacial cycle (from Barker et al., 1999). 50

Figure 2.48. Multibeam image showing evidences of small-scale mass wasting, where it is possible to recognize several characteristics such steep headwalls, and absence of well-defined gullies (from Gales, 2013). 51

Figure 2.49. Schematic diagram with main processes which control morphology in Antartic submarine slopes. Image taken from Gales, 2013. 52

Figure 2.50. Channels observed in a multibeam image (from Gales, 2013). 52

Figure 2.51. A sediment mound/drift observed trough multibeam image (from Gales, 2013) and schematic diagram showing the formation of the sediment drifts (from Barker et al., 1999)... 53

Figure 3.1. NBP primary reference frame established during MBES array installation in 2002. The origin was at the center of the RX array face using axis orientations and sign conventions in agreement with Kongsberg conventions. Image from Johnson and Jerram (2015). 62

Figure 3.2. Overview of workflow states. Adapted from Caris Training Module (for HIPS and SIPS 9.0). 63

Figure 3.3. ASCII file (**A**) used to generate a DEM with 40 m resolution (**B**). From the DEM was generated a relief-shaded map (**C**) with idealised light source was defined with 45° azimuth (red arrow) and 45° elevation..... 64

Figure 3.3.4. Relief-shaded maps with three azimuth illumination (red arrows) and an elevation of 30° to support the drumlin-like mapping (**A**, **B** and **C**), presented with a vertical exaggeration of 3. **D** Slope component map from the DEM: dark colours for steep regions and lighter colours for flat regions. 64

Figure 3.5. Gullies visualization using relief-shaded maps with different azimuth illumination (red arrows) and an elevation of 30° to support gullies mapping (**A** and **B**, vertical exaggeration of 3). **C** Slope map from the DEM: dark colours for steep regions and lighter colours for flat regions. 65

Figure 3.6. Quantitative parameters derived from the DEM (general morphometry): slope, curvature and ruggedness..... 66

Figure 3.7. Morphological parameters of a classical drumlin (smooth hill) (Adapted from: https://www.geocaching.com/geocache/GC3WT7R_ulsters-only-fjord?guid=54c443fa-0a70-4bfb-956c-f80d71ec0298). 66

Figure 3.8. Definition of drumlin-like relief for (A) flat and (B) hillslope contexts. This figure show clearly the difference between altitudinal range and the real relief when drumlins are found on hillslopes. From a drumlin-like profile is possible to determine the vertical offset (a), which is then converted to drumlin relief based on the equation: h= a x cos(θ), where θ is the slope angle of the apparent drumlin-like base. Image from Spagnolo et al., 2012. 67

Figure 3.9. An example of drumlin profile extracted from ArcGIS for length (L) and relief (h) calculation. Once defined the drumlin base equation, is possible to determine the slope angle (θ) and that value to find the real length and relief values of a drumlin. The vertical offset (a) correspond to the difference between the reference point on the profile and its projection on the drumlin base equation**.** 68

Figure 3.10. Morphometric parameters of a gully: **A**- width, length and incision depth, **B**-sinuosity. From Gales (2013). 69

Figure 3.11. Schematic of cross-sectional shape (U/V) and associated 'b' values derived from the General Power Law programme (from Gales, 2013). 69

Figure 3.12. A representation of curve fitting with GPL (dotted line) of a cross-profile (**A**) and the respective RMS error calculation in function of b value (**B**). For this case the optimal b value is 0.92 and the origin has the following coordinates: xo=2081 m, yo=1642 m (from Pattyn and Van Huele, 1998). 70

Figure 3.13. Diagnostic diagram to identify Antarctic gullies based on the quantitative parameters measured at 50 m below the shelf edge including: gully branching order, depth, cross-sectional shape, sinuosity and length (from Gales et al., 2013). 71

Figure 3.14. Knudsen sub-bottom control interface..... 73

Figure 3.15. Main processing work flow applied on Chirp data with respective results from each step. Example from line 0030_095_1333_130038 CHP3.5_FLT_000. 75

Figure 3.16. Comparison between DEMs with different resolution, 25 m (**A**) and 40 m (**B**)..... 76

Figure 3.17. Example of artefacts found on the swath bathymetric data (DEM with 40 m resolution). A - Artefacts caused by changes in vessel speed. B - False depth soundings. C – Lines-drop out..... 77

Figure 4.1. General swath bathymetric image of the study area. The black rectangles show the location of the main glacial geomorphic features presented in this chapter. (**A**) Regions map identifying the inner continental shelf (**I**), slope (**II**) and continental rise (**III**). 79

Figure 4.2. Swath-bathymetric record showing irregular crudely streamlined bedforms and elongated meltwater channels on inner continental shelf. 80

Figure 4.3. Sub-bottom profile showing an acoustically impenetrable substrate, without any distinct sub-bottom information. This record suggests the presence of a hard subtract such bedrock. For location see figure 4.2..... 81

Figure 4.4. Swath bathymetric imagery of the mid continental shelf showing drumlin-like bedforms field (**A**) and close-up to the features (**B**, **C** and **D**). The inset image D corresponds to a shaded relief image with an illumination from west and 30^{o} elevation were the former ice flow direction is represented by withe arrows. 82

Figure 4.5. Graphical summary and descriptive statistics of drumlin-like parameters: length, width, elongation ration and relief. The class number was defined though empirical rule of: $2^{K} >$ N, where k is the number of classes and N the number of samples. Superimposed on the histograms is represented the best fit Gaussian curve (in red). 83

Figure 4.6. Dendrogram showing relationships between the four measured morphological parameters: relief, width, elongation ratio and length. The diagram was generated based on

Ward's method and the similarity factor considered was the correlation coefficient Pearson r. 85

Figure 4.7. Scatterplot of the cluster relief-width, with the respective correlation (r) and 95 % confidence intervals (red dashed curves). The adjacent histograms show the defined classes according to the main grid of the scatter plot. 85

Figure 4.8. Scatterplot of the cluster elongation ratio-length, with the respective correlation (r) and 95 % confidence intervals (red dashed curves). The adjacent histograms show the defined classes according to the main grid of the scatter plot. 86

Figure 4.9. Scatter plot showing the correlation (r) between morphometric variables length and relief, and the 95 % confidence intervals (red dashed curves). The adjacent histograms show the classes defined according to the main grid of the scatter plot. 87

Figure 4.10. Superposition of standard curvature raster on top of the swath bathymetry imagery, with gradual transition. This figure demonstrates how convex forms (as drumlins-like bedforms) and concave forms (as channel-like depressions) can be highlighted. 87

Figure 4.11. A- Sub-bottom Chirp profile along the drumlin-like field (for location see Fig. 4.4). The profile show general low acoustic penetration, and (**B**) a thin potential sediment layer (black arrow) covering some drumlin-like bedforms. 88

Figure 4.12. Longitudinal profiles taken from five identified drumlin-like bedforms: **A**- Three dimensional view of the drumlin-like filed; **B**- Graphical representation of profiles taken. 88

Figure 4.13. Iceberg scours observed on the outer continental shelf: **A**- shaded-relief swath bathymetric image; **B** - curvature index showing convex (dark colour) and concave (bright colour) forms; **C** - close up showing a more detailed representation (with a vertical exaggeration of 3). 89

Figure 4.14. Sub-bottom chirp profile along the iceberg scours region. For location of the profile see Fig. 4.13A, where iceberg scours are identified by red segments. 90

Figure 4.15. Roughness index over the swath bathymetry grid. On this image are displayed two roughness surfaces with neighbourhood size of 11x11 cells for the general multibeam data, and 5x5 for detailed inset figures. 90

Figure 4.16. Swath bathymetry showing general morphology of the continental shelf margin (**A**).The general character of the slope is plotted on topographic profiles (**B**). 91

Figure 4.17. A- General swath bathymetry imagery along the continental slope showing **B**- analysed gullies for morphometric parameters, **C**- Close up on converging gullies and **D**- Shaded relief image showing the morphological aspect of the gullies. 92

Figure 4.18. Shaded-relief image showing elongated and amphitheatre-like depressions formed at the upper stream area of the gullies (gully heads). Illumination with 45^{o} azimuth and vertical exaggeration of 3. 92

Figure 4.19. 3D perspective view of the shelf break and the continental slope showing morphological aspects of four sampled gullies (a, b, c and d). For each example, three cross-sections taken along the slope exhibit variation between U and V shapes..... 93

Figure 4.20. Sub-bottom profile taken from the continental shelf edge to lower slope regions showing the presence of gullies. On the inset figure **B** the seafloor is marked with a red dashed line to make gully incision more evident. For location see Fig. 4.17. 94

Figure 4.21. Graphical summary and descriptive statistics of gully parameters at 50 m below shelf break: U/V index, length, sinuosity width, depth and W/D. The modal classes for each parameter are respectively: 1.5-2.1; 2068-1750 m; 1.02-1.04; 154-198 m; 14-20 m and 6.3-8.7. The class number was defined though empirical rule of: $2^K > N$, where k is the number of classes and N the number of samples. Superimposed on the histograms is represented the best fit Gaussian curve (in red)..... 96

Figure 4.22. Graphical summary and descriptive statistics of gully parameters at 100 m below shelf break: U/V index, Length, Sinuosity width, depth and W/D. The modal classes for each parameter are respectively: 1-2.6; 1572-2150 m; 1.04-1.05; 206-249 m; 11-18 m and 7.5-9.7. The class number was defined though empirical rule of: $2^K > N$, where k is the number of classes and N the number of samples. Superimposed on the histograms is represented the best fit Gaussian curve (in red)..... 96

Figure 4.23. Screen plot showing the six PCs and the proportion of variation (%) explained by the PCs. 97

Figure 4.24. Score plot from the combinations of PC1-PC2 (**A**) and PC1-PC3 (**B**) for Groups A (green cross) and B (blue circle). The most representative variables (parameters) for each PC are also indicated on the plots. 99

Figure 4.25. Graphical summary and descriptive statistics of gully parameters of joined Groups A and B: U/V index, length, sinuosity width, depth and W/D. The modal classes for each parameter are respectively: 1.4-1.9; 1676-2117 m; 1.02-1.03; 150-200 m; 18-24 m and 7.5-9.7. The class number was defined though empirical rule of: $2^K > N$, where k is the number of classes and N the number of samples. Superimposed on the histograms is represented the best fit Gaussian curve (in red)..... 99

Figure 4.26. Slope grid surface represented by a colour scale between green (low steepness values) and red (high steepness values). 100

Figure 4.27. Roughness index over the swath bathymetry grid. On this image are displayed two roughness surfaces with neighbourhood size of 11x11 cells for the general multibeam data, and 5x5 for detailed inset figure. 100

Figure 4.28. Swath bathymetry image showing three sediment mounds with their crest, sub-perpendicular to the continental shelf edge, and the pervasive dendritic v-shaped eroded ravines 101

Figure 4.29. Sub-bottom profile which intercepts the tree sediment mounds. For location see Fig. 4.28. 102

Figure 4.30. Swath bathymetry image showing the wide channelised bedform which extends more than 30 km long (A). Several profiles where taken to demonstrate the general character of the channel (B). 103

Figure 5.1. A- Modelled basal temperatures based on geothermal flux values (inferred trough crustal age and identified geological units). The yellow areas correspond to melted ice at the base of Antarctic ice sheet; B- Ice melting rate estimate for the Antarctic ice sheet from the geothermal flux influence. Image adapted from Llubes et al. (2006). 108

Figure 5.2. Slope gradient map (A) and spatial interpolation of drumlin parameters (relief, length, width and elongation ratio) based on 29 validated samples through the regression method IDW (Inverse Distance Weighting) (B). 110

Figure 5.3. Drumlin formation considering sediment deformation/sediment flux rate fluctuation between the different interfaces. Image adapted from Menzies et al. (2016). 111

Figure 5.4. Scatterplot showing the correlation between the morphometric variables length and width trough tendency lines. 112

Figure 5.5. Slope gradient map (A) and spatial interpolation of gully parameters (U/V index, W/D, Sinuosity and Length) based on 64 validated samples trough the regression method IDW (Inverse Distance Weighting) (B)..... 114

Figure 5.6. A - Schematic diagram showing the influence of sediment bedload on cross-sectional shape of a gully (adapted from Vietz et al., 2016). B – Potential influence sedimentary structure on gully cross sectional shape (adapted from: http://www.fao.org/docrep/006/ad082e /AD082e01.htm). 114

Figure 5.7. Distribution of geomorphic features identified in the study area and used to reconstruct the glacial history since LGM**.** 116

List of Tables

Table 3-I. Description of measured drumlin parameters. 67

Table 3-II. Description of measured gully parameters based on Gales, 2013. 69

Table 3-III. Most frequent settings/acquisition parameters used during the sub-bottom imaging on board the RVIB Nathaniel B. Palmer (NBP15-03)..... 73

Table 4-I. Coefficient variation (Coef. Var.) determined for all drumlin-like parameters, based on their respective mean and standard deviation (Std. Dev.). 84

Table 4-II. Geomorphical Gully types found in Group A (gully set with cross section profiles taken 50 m bellow continental shelf edge)..... 94

Table 4-III. Geomorphical Gully types found in Group B (gully set with cross section profiles taken 100 m bellow continental shelf edge)..... 94

Table 4-IV. Eigenvalues for the first three principal components of the PCA. The larger considered correlations are in boldface..... 98

Table 5-I. Summarized morphology of the bedforms observed in the continental shelf, slope and rise, and their comparison (West Antarctica and AP)..... 108

CHAPTER 1:
Introduction

1.1 Nature and scope of the thesis

This research work is presented in fulfilment of the requirements for a master degree in Geological Engineering, branch of Geological Resources, at the Geosciences Department of the University of Aveiro (UA), Portugal. Under the umbrella of the United States of America (USA) National Science Foundation (NSF) project 'Vulnerability of East Antarctic ice shelves' and the Portuguese PROPOLAR project EAIS-MARGINS, this master project aimed to enlarge our previous knowledge about the maximum ice extent and past ice sheet dynamics of the East Antarctic Ice Sheet (EAIS). The research activities were based on the interpretation of the seafloor morphology between 128º E and 134º E, East Antarctica, a practically unexplored region until now. For the first time, the detail of the seafloor morphology has been analysed between Frost and Dibble Glaciers, and the interaction with past EAIS has been assessed.

I had the opportunity to participate on the NBP1503 expedition that surveyed the study area, as a member of the shipboard scientific party, helping with swath bathymetry and sub-bottom acquisition and processing tasks. The post-cruise processing and interpretation of the data were carried out at the Marine Geology and Geophysics Laboratory (LGGM) of the Geosciences Department at UA.

This work was performed under the supervision of Dr. Caroline Lavoie, from UA, with the support of Dr. Frank Nitsche (Lamont-Doherty Earth Observatory, Columbia University, USA).

1.2 Objectives

The main objective of this project was the integration of the geophysical data acquired during the NBP1503 scientific survey, in order to study the seafloor morphology and reconstruct past ice flows to better understand the retreat history of the EAIS. The specific objectives were to:

- analyse in detail the swath bathymetry seafloor imagery to identify morphological features that allowed the reconstruction of the past ice flow behaviour and extent;
- interpret the nature of the identified features based on their morphological description and sub-bottom seismic data;
- obtain quantitative parameter measurements and comparable variables through individual bedforms digitalisation and mapping;
- identify potential patterns and relationships between extracted morphological parameters from different mapped features.

1.3 NBP1503 expedition

The 41-days NBP1503 cruise was carried out in East Antarctica, between 115°E and 135°E, from March 26th to May 3rd in 2015, on board the United States Antarctic Program (USAP) RVIB Nathaniel B. Palmer icebreaker (Fig. 1.1). The main objective of the scientific expedition was to seek potential causes for recently discovered EAIS instability (e.g. Rignot, 2006; Rignot et al., 2013), testing the hypothesis of the possible intrusion of warm water into the continental shelf, as observed for the West Antarctic Ice Sheet (WAIS) (e.g. Shepherd et al., 2004).

Using swath bathymetry and a CHIRP acoustic-remotely sonar and water column CTD (Conductivity, Temperature and Depth) measurements (Fig. 1.2A and B), the goal of the expedition was to detect possible seafloor topography pathways, such as cross-shelf troughs, and measure the presence (or not) of warm water intrusions that can lead to the EAIS instability (Fig. 1.2C): relative warm waters mostly associated to the circumpolar deep water currents (CDW).

The access of the targeted regions (Frost Glacier, Totten Glacier and Scott-Denman Glaciers) were strongly conditioned by the sea ice cover, particularly on the continental shelf in front of ice streams. When the continental shelf break was reached in April 4th, the region already presented significant sea ice cover, which made the access to the continental shelf regions more difficult (Fig.1.3A). Progressively the sea ice cover continued to increase, and by the end of the expedition most of the continental shelf and slope was completely covered (Fig. 1.3B).

Throughout the expedition, the original plan was always revised to target the more open areas. The research vessel successfully reached the continental shelf close to the

Dibble Glacier and the shelf break north of the Totten Glacier and Moscow University Ice Shelf (see Fig. 1.1B).

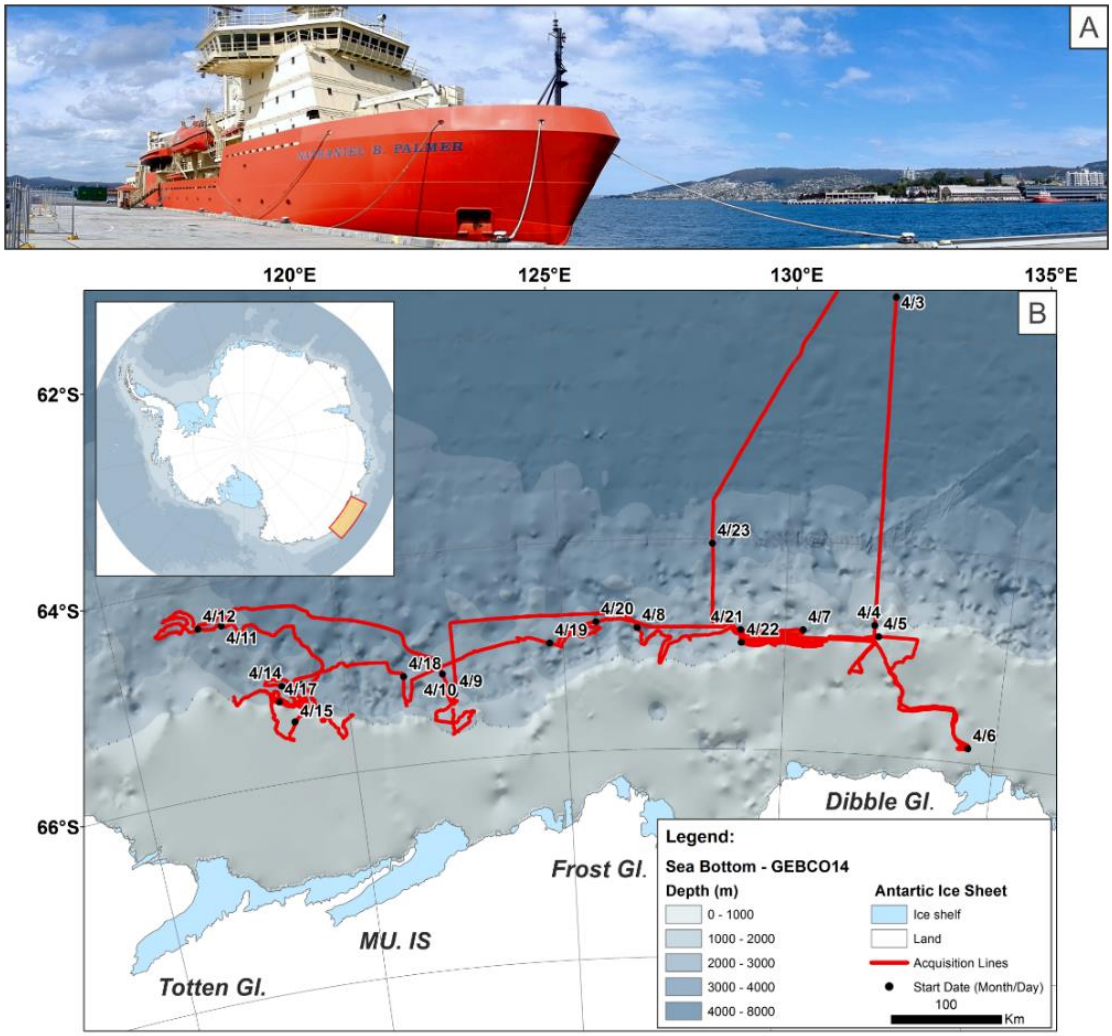

Figure 1.1. The icebreaker RVIB Nathaniel B. Palmer (**A**) and the navigation routes during the NBP1503 expedition (**B**).

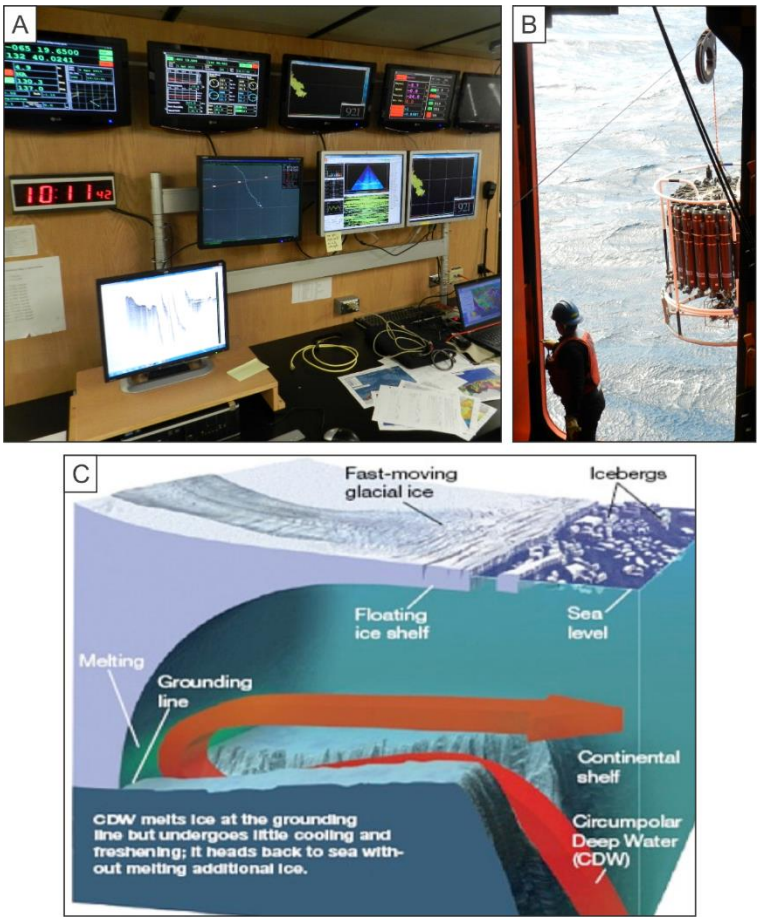

Figure 1.2. Geophysical working area (**A**) and Probe (Rosette) operation for CTD measurements (**B**) during the NBP1503 expedition. **C**- Schematic view of a warm waters intrusion into the continental shelf by a cross-shelf trough (from: http://forum.arctic-sea-ice.net/index.php?topic=874.50).

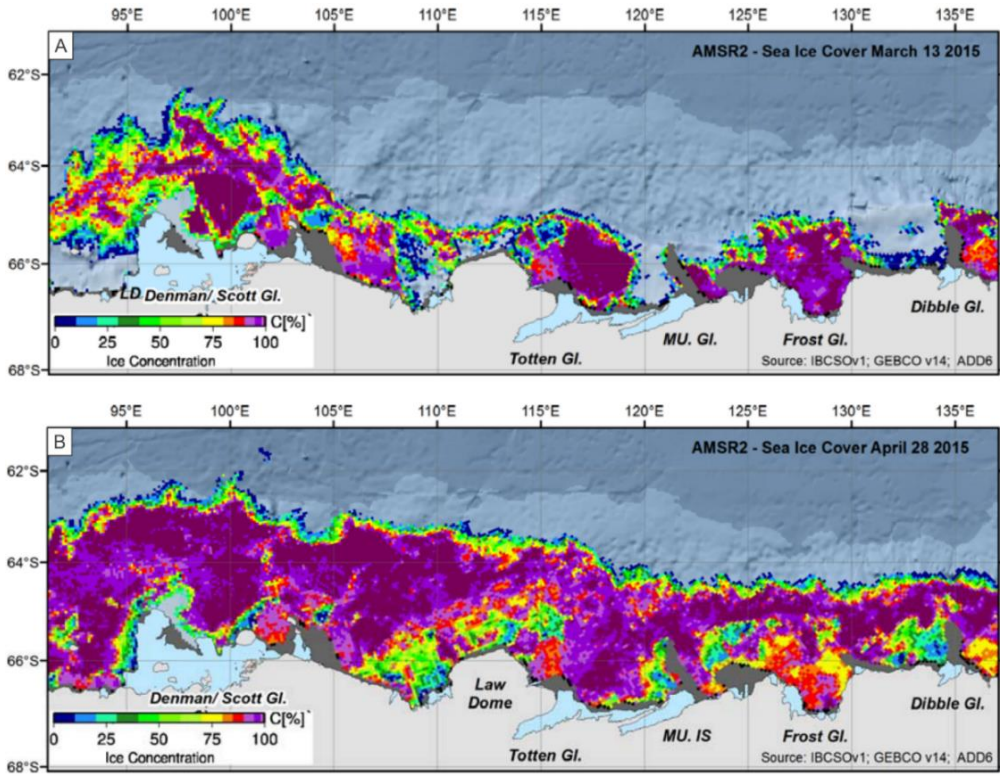

Figure 1.3. Sea ice covers in March 13 2015 (**A**) and April 28 2015 (**B**). Images from NBP1503 cruise report.

1.4 Study area

This research project focused on the data set segment between Frost and Dibble Glaciers (between 128º E and 134º E) (Fig. 1.4, yellow box). Those glaciers present fast-flowing ice outlets that were recently considered to be in negative state of mass balance (Rignot, 2006; Rignot et al., 2013). According to Rignot et al. (2013), Dibble Glacier presents melt rates of 4-11 m/year and a mass deficit of -2.3 (±0.7) Gt/year: values that are higher than normally expected from an EAIS glacier. The increase of ice calving at the edge of the glacier contribute to this negative mass balance. Hence, parts of the EAIS might be more vulnerable to future ice retreat than previously thought, and for this reason the continental shelf in front of Dibble Glacier was considered for this project.

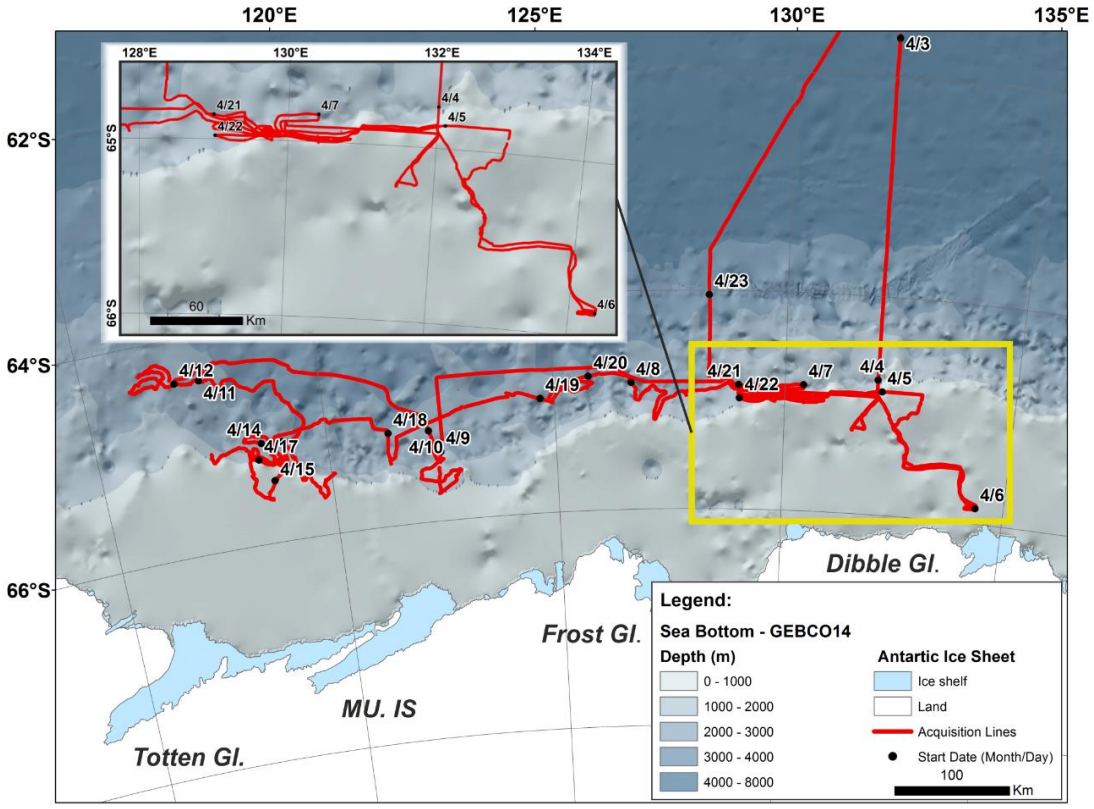

Figure 1.4. The study area considered on this research project (yellow box), confined between Frost and Dibble Glaciers (between 128º E and 134º E).

Frost and Dibble Glaciers belong to Wilkes Land, a mid-Jurassic/Cretaceous formation formed by a tectonic extensional episode that separated Australia and Antarctica (Escutia et al., 2003). Through time, the dynamic process of ice sheets and glaciers on the Antarctic continent left behind several morphological aspects on land and on the continental shelf. Until now, the morphological information of the continental shelf in front of Dibble Glacier was mainly based on broad bathymetric information (Fig. 1.5)

and sporadic seismic reflection profiles (Fig. 1.6) that provided an estimated and coarse overview of the seafloor morphology. Previous research expeditions realized by the 'Institut Francais du Pétrole (IFP)' and the United States Geological Survey (USGS) were precursors of first morphological and seismic stratigraphy studies on Wilkes Land shelf (Eittreim et al., 1995), with the aim to understand the role of the flow ice from the continent and potential climate changes during the past. Added with more recent studies, the broad bathymetric information suggest the presence of a cross-shelf trough in front of Dibble Glacier by constraining the geographic limits of submarine banks (e.g. Eittreim et al., 1995; Escutia et al., 2003; Crosta et al., 2007).

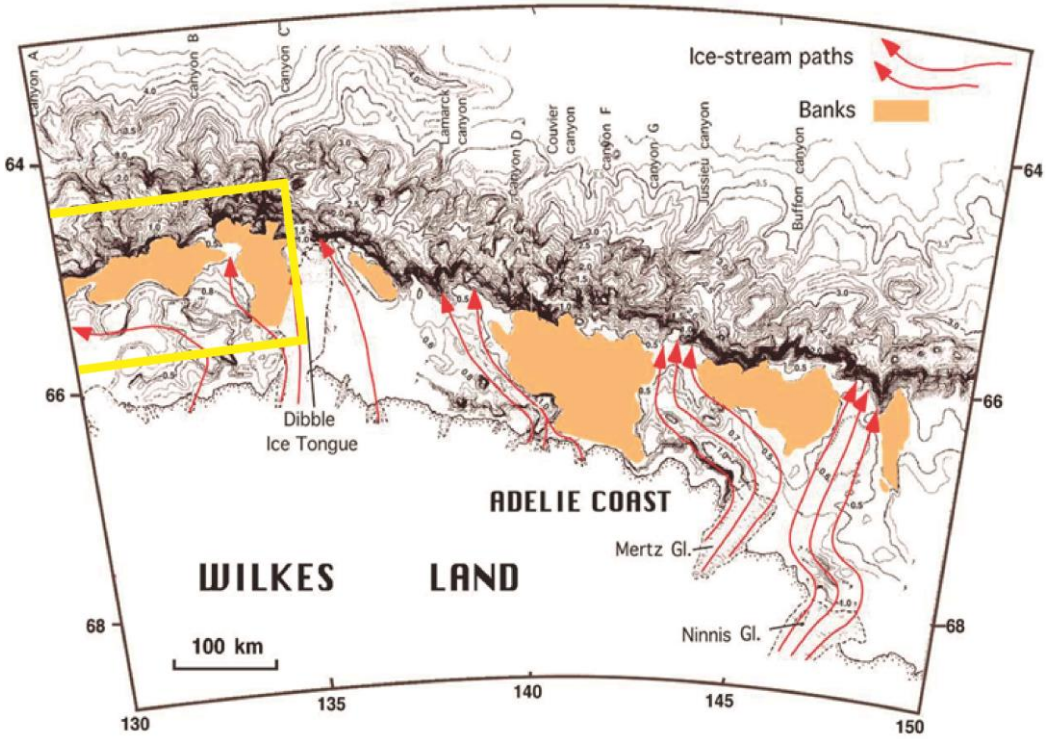

Figure 1.5. Wilkes Land bathymetric map from Escutia et al. (2003) previously modified from Chase et al. (1987) and Eittreim et al. (1995) showing the general seafloor physiography. The study area considered in this work is represented by yellow boundary line.

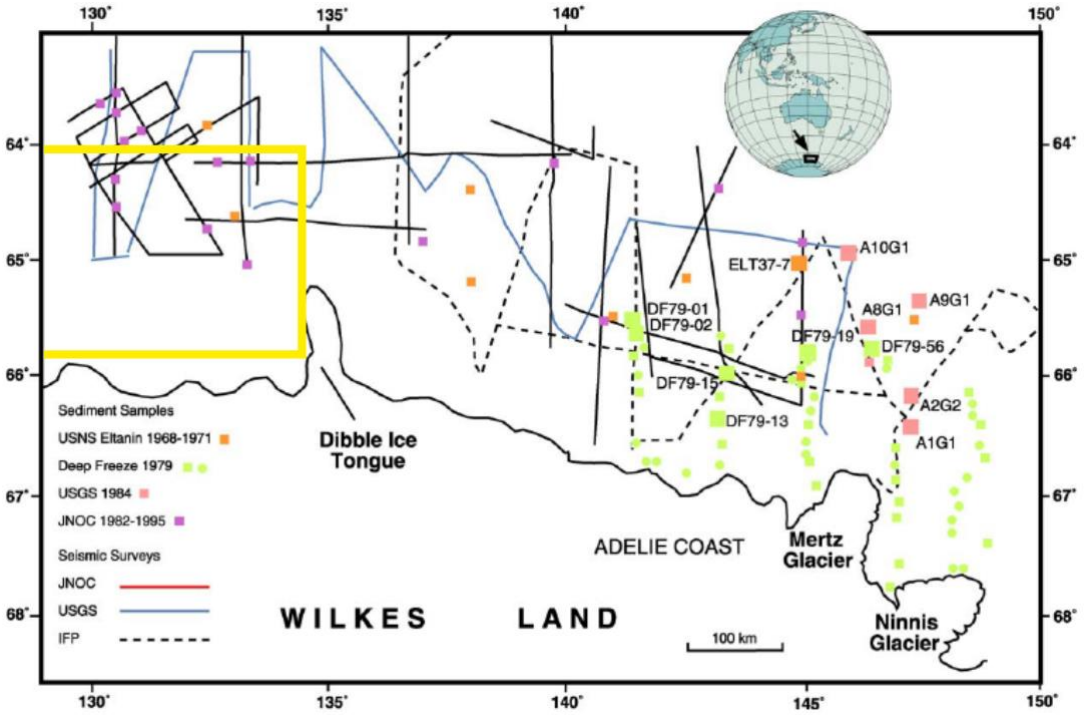

Figure 1.6. Map from Escutia et al. (2003) showing the location of multichannel seismic data recorded by the 'Institut Français du Petrole (IFP)', the United States Geological Survey (USGS) and the Japan National Oil Corporation (JNOC) along the Wilkes Land continental margin. The study area considered in this work is approximately represented with yellow boundary line.

1.5 Structure of the thesis

The present document is divided into six chapters. After this brief introduction on the research project, the second chapter - *Background* - seeks to provide basic knowledge about the various components of Antarctica. This part of the thesis is intended to provide geomorphological aspects, such as geological, glacial, atmospheric and oceanographic, for a better comprehension of that environment.

The third chapter - *Methods* - contains a succinct description of applied methods in this research work. It contains the description of procedures and acquisition parameters used during the NBP1503 survey, and data processing steps. In this section, the geomorphometric and statistical analyses are also documented, ending with considerations and limitations of the data set.

The fourth chapter - *Results and Interpretation* - draws the results and interpretation of the geophysical data and geomorphometric and statistical analyses.

The fifth chapter - *Discussion* - discusses the results obtained in the previous chapter to reconstruct, in part, the paleo-ice sheet history of the studied region. Also, a comparative study with other Antarctic continental margins is presented.

Lastly, the chapter - *Conclusions and Recommendations* - presents final conclusions of the research work and some recommendations for future work/research activities.

References

Chase T. E., Seekins, B.A., Young, J.D., Eittreim, S.L., **1987**. Marine topography of offshore Antarctica. In: Eittreim, S.L., Hampton, M.A. (Eds.), The Antarctic Continental Margin: Geology and Geophysics of Offshore Wilkes Land: Circum-Pacific Council for Energy and Mineral Resources. Earth Sciences Series, 5A, Houston, pp. 147–150.

Crosta, X., Debret, M., Denis, D., Courty, M. A., and Ther, O., **2007**. Holocene long-and short-term climate changes off Adelie Land, East Antarctica. *Geochemistry, Geophysics, Geosystems*, 8(11), 1-15.

Eittreim, S. L., Cooper, A. K., and Wannesson, J., **1995**. Seismic stratigraphic evidence of ice-sheet advances on the Wilkes Land margin of Antarctica. *Sedimentary Geology*, 96(1), 131-156.

Escutia, C., Warnke, D., Acton, G. D., Barcena, A., Burckle, L., Canals, M., and Frazee, C. S. **2003**. Sediment distribution and sedimentary processes across the Antarctic Wilkes Land margin during the Quaternary. *Deep Sea Research Part II: Topical Studies in Oceanography*, 50(8), 1481-1508.

Livingstone, S. J., Cofaigh, C. Ó., Stokes, C. R., Hillenbrand, C. D., Vieli, A., and Jamieson, S. S. **2012**. Antarctic palaeo-ice streams. *Earth-Science Reviews*, 111(1), 90-128.

Rignot, E. **2006**. Changes in ice dynamics and mass balance of the Antarctic ice sheet. *Philosophical Transactions of the Royal Society of London A: Mathematical, Physical and Engineering Sciences*, 364(1844), 1637-1655.

Rignot, E., Jacobs, S., Mouginot, J., and Scheuchl, B. **2013**. Ice-shelf melting around Antarctica. *Science*, 341(6143), 266-270.

Shepherd, A., Wingham, D., and Rignot, E., **2004**. Warm ocean is eroding West Antarctic ice sheet. *Geophysical Research Letters*, 31(23), 1-4.

CHAPTER 2:
Background

2.1 Antarctica

Antarctica is the southernmost continent on Earth, containing the geographic and magnetic South Poles, being surrounded by the Southern Ocean, an extension of the southernmost parts of the Atlantic, Pacific and Indian Oceans (Fig. 2.1). It is mostly unpopulated and protected by the Antarctic Treaty since 1959 forbidding military activity, as well as mining, nuclear testing and dumping nuclear waste. Currently, almost 40 bases are used mainly for research and scientific activity, and in some cases sightseeing.

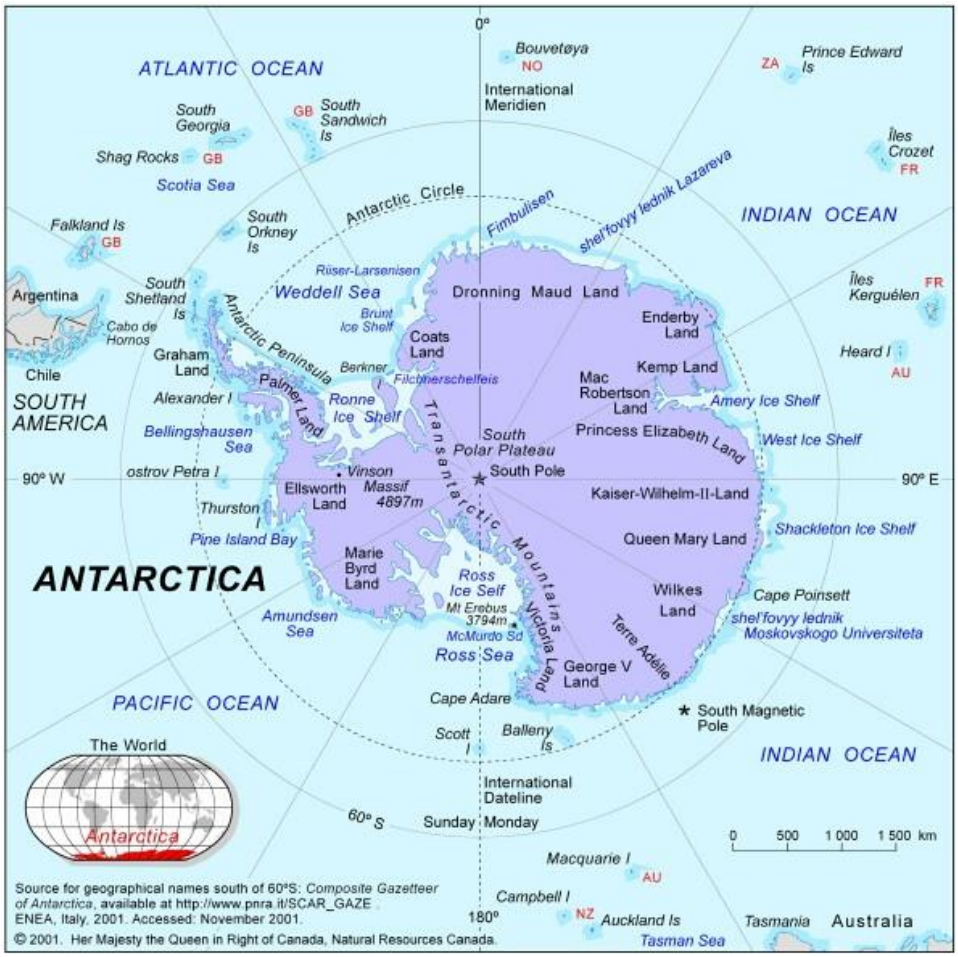

Figure 2.1. Geographic map of Antarctica (Source: http://www.polarhistory.net/antarctica-map geographic/).

As a vast and icy continent almost entirely south of the Antarctic Circle, Antarctica is a land of extreme conditions. It is the coldest, driest, and windiest continent (e.g. Turner et al., 2009; Convey et al., 2009; National Research Council, 2011; Walton, 2013). With 14 million km^2, it is the fifth-largest continent in terms of total area covering approximately 20 percent of the Southern Hemisphere (Australian Antarctic Division, 2004; National Geographic, 2015). Over 99% of Antarctica is covered by the Antarctic ice sheet (AIS) divided in three main parts: the West Antarctic Ice Sheet (WAIS) and East Antarctic Ice Sheet (EAIS) separated by the Transantarctic Mountains (TAM) and the Antarctic Peninsula Ice Sheet (APIS). The AIS contains 90 percent of the world's ice and around 70 percent of Earth's freshwater (Convey et al., 2009; British Antarctic Survey, 2015). Ice shelves, ice rises and sea ice occur around its periphery.

The Antarctic continent is also surrounded by a number of Antarctic and sub-Antarctic islands, which range in size from small clusters of rocks to larger islands such as South Shetland islands north of the Antarctic Peninsula (AP), or Alexander Island, the largest island of Antarctica, which lies west side of the Palmer Land (AP) (Fig. 2.1). Some of the islands are almost completely covered by ice, while others, are ice-free and have no permanent cover of snow (Australian Antarctic Division, 2004; British Antarctic Survey, 2015).

Due to the inhospitable environment of the Antarctic continent, terrestrial life is mainly confined along the coasts of the AP and on the sub-Antarctic islands: slightly more temperate regions (Turner et al., 2009).

2.1.1. Geological context of Antarctica

The geological history of Antarctica is barely known in comparison with other continents, since less than 1% of the land is ice-free (Anderson, 1999; Convey et al., 2009). However, through geological records from scarce exposed rocks and drilling projects together with geophysical and remote sensing techniques, it has been possible to understand the key components of the geological and geotectonic evolution of the continent (Anderson, 1999; Torsvik et al., 2008). These studies still contribute to solve many questions related with the formation and the evolution of Antarctica (e.g. Anderson, 1999; Satish-Kumar et al., 2008; Fretwell et al., 2013).

The TAM separates morphologically and geologically the East and West Antarctica (Dalziel, 1992; Anderson, 1999; Torsvik et al., 2008). It is one of the longest mountain

chains on Earth which extends across the continent and reaches more than 4,500 m in length. The mountain range is located on a tectonic boundary between Archean-Proterozoic lithosphere in East Antarctica and Paleozoic-Mesozoic accreted terranes in West Antarctica (Anderson, 1999; Lawrence et al., 2007), with a tectonic evolution that appears to have begun during the late Cretaceous (Fig. 2.2). TAM is characterized by the absence of compressional deformation within sediments, folding and thrust faulting (Lawrence et al., 2007). The way that TAM were formed are still debated. Existing explanations can be divided into thermally driven uplift, mechanically driven uplift, or a combination of the two (Lawrence et al., 2007). This natural sub-division of the Antarctic continent gives valuable means for the discussion on the geology and plate tectonic reconstruction (Anderson, 1999).

The East Antarctica, covered by the main polar ice cap, corresponds to a large stable continental craton composed mainly of Precambrian metamorphic basement rocks with granitic intrusions that are unconformably overlain by generally flat-lying sedimentary rocks. Its formation began during the Archean and ceased, for the most part, during the Cambrian (Anderson, 1999). In contrast, the younger West Antarctica is an archipelago of several microplates with mountainous metamorphic and volcanic terranes, with most of its developmental history confined to the Mesozoic and Cenozoic (Anderson, 1999; Harley, 2011).

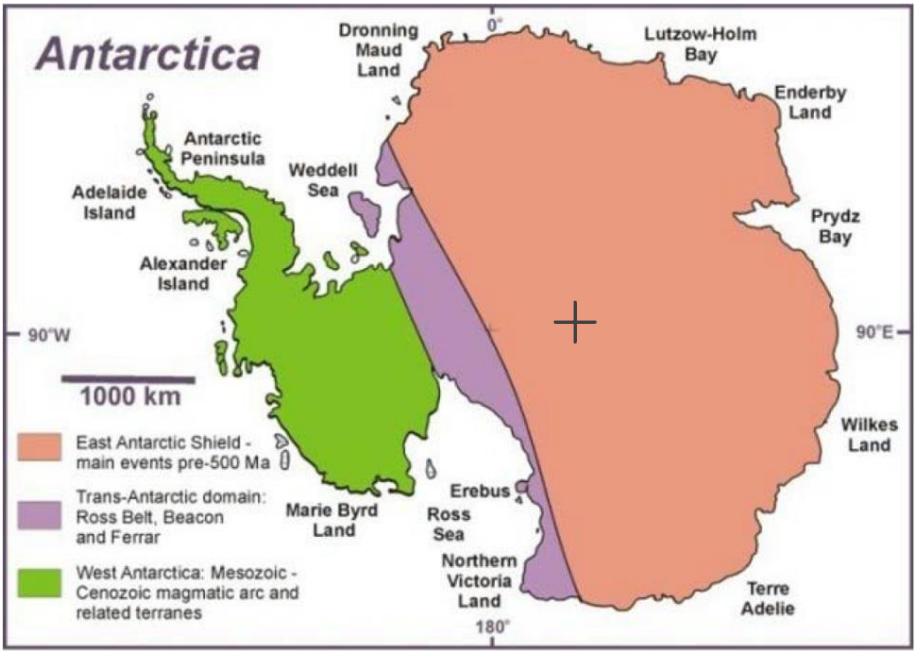

Figure 2.2. The main geological provinces, a broad division, of the East Antarctic Shield (pink), West Antarctic domain (green) and the Trans-Antarctic domain (purple). The South Pole is indicated by the cross symbol in the East Antarctica Shield (from Harley, 2011).

In contrast to the present isolated position of Antarctica, the continent has amalgamated and combined with other continental fragments, being part of larger supercontinents (Fig. 2.3). The earliest entitled Rodinia, is the least well known, but its successors Gondwana and Pangaea are well constrained by geophysical and geological data (Walton, 2013). For much of the Phanerozoic (from 540 to 180 million years ago (Ma)) Antarctica was the keystone of the Gondwana supercontinent, being in contact with South America, India, Africa, Australia and New Zealand mass lands (Fig. 2.4A) (Walton, 2013). Around 180 Ma, this supercontinent began to break apart and Antarctica commenced moving into its present polar position (Fig. 2.4C) (National Research Council, 2011; Walton, 2013). In the final fragmentation stage of Gondwana, the Antarctic circumpolar current began circulating and likely reduced the amount of heat that the ocean previously brought from the mid-latitudes to the edges of Antarctica (Fig. 2.4D). At approximately 32 Ma, the isolation and cooling of the southern continent began (National Research Council, 2011; Walton, 2013).

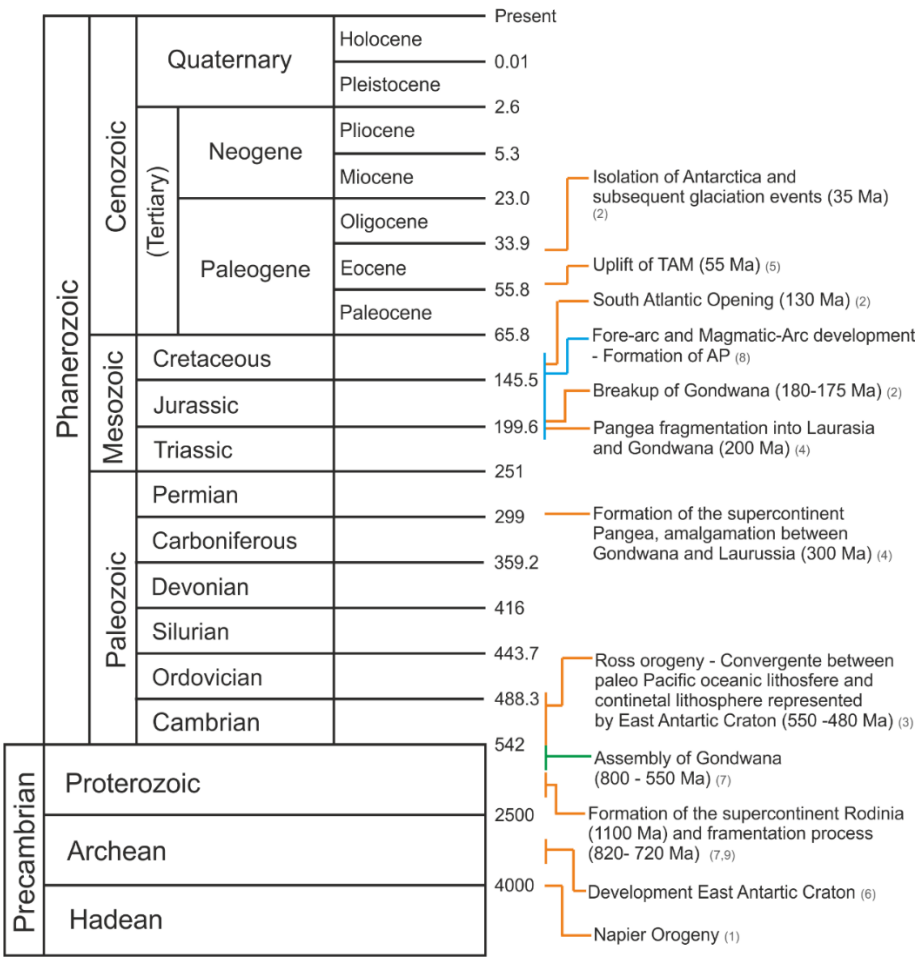

Figure 2.3. Geological time-scale with details regarding the formation and evolution of the Antarctic continent. This figure is a compilation of information from: Anderson, 1999 (1); Walton, 2013 (2); Goodge, 2007 (3); Stampfli et al., 2013 (4); ten Brink et al., 1997 (5); Harley, 2011 (6); Meert et al., 1997 (7) Smellie, 1981 (8) and Pisarevsky et al.2003 (9).

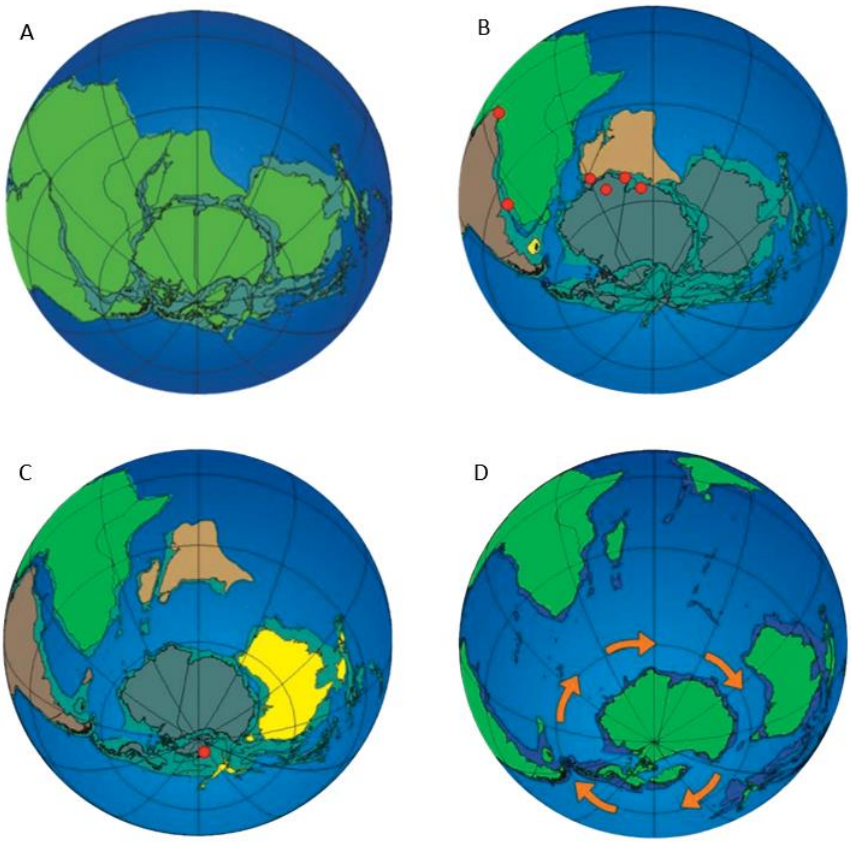

Figure 2.4. Reconstruction of Gondwana 180 million years ago (Ma) and its subsequent fragmentation. The red dots show the location of possible mantle hot spots that may have contributed to the continental fragmentation. **A-** Gondwana 180 Ma; **B-** South Atlantic opening 130 Ma; **C-** Australia and New Zealand rifting 100 Ma; **D-** Isolation of Antarctica 35 Ma (Image adapted from Walton, 2013. Credit: Bryan Storey).

2.1.2. Present and Past Glacial Setting

The continent of Antarctica is dominated by the AIS, a contiguous mass of glacial ice that rests on the continent, nourished at their surface by deposition of snow and frost that accumulates year-on-year. Surrounded by the Southern Sea, AIS contains around 30 x 10^6 km^3 of ice or 70% of the Earth's freshwater that covers about 99.6% of the continent (Fox and Cooper, 1994; Turner et al., 2009). It is the largest glacial system on Earth (Fig. 2.5).

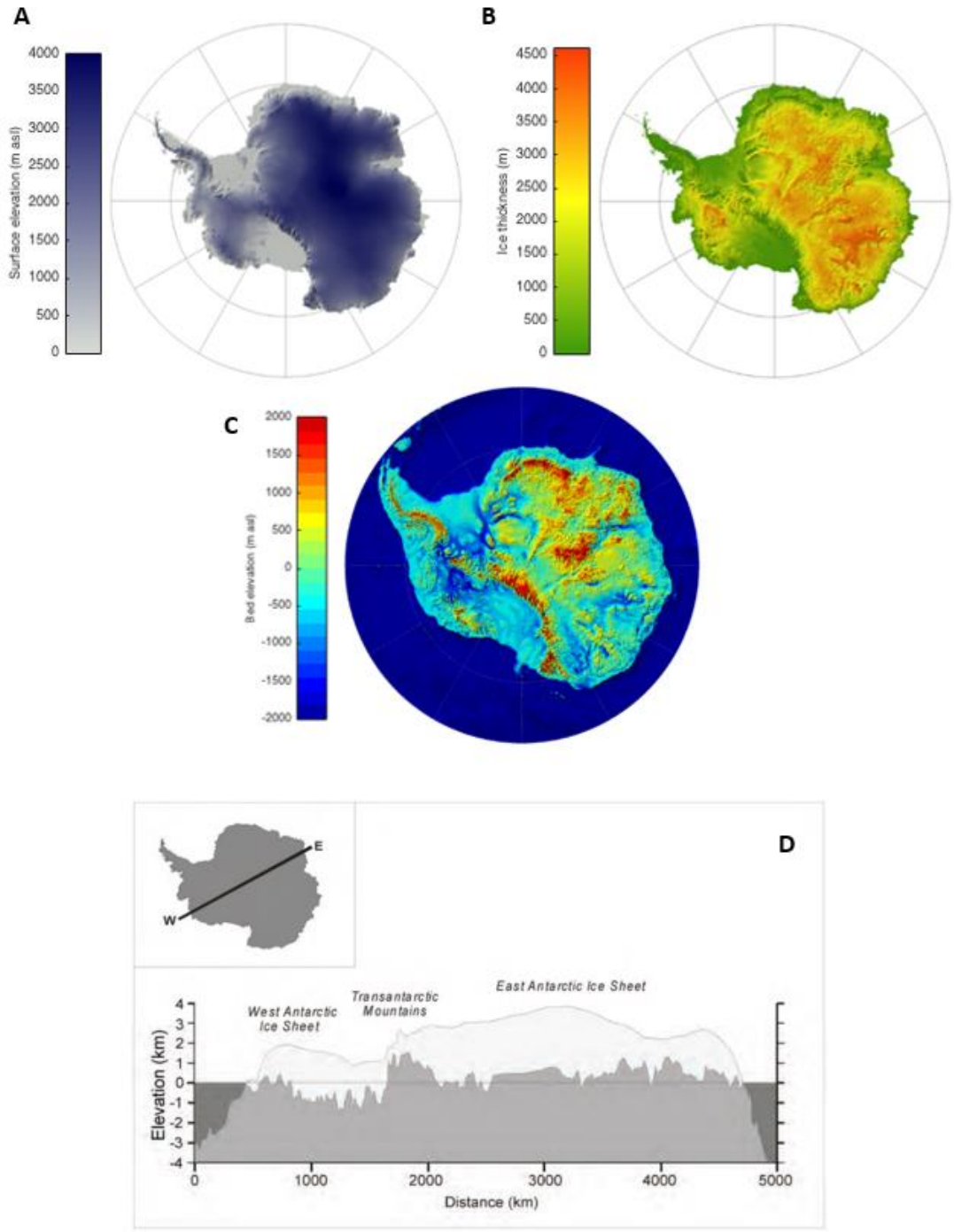

Figure 2.5. Overall morphological aspects of the Antarctic continent. **A-** Surface topography, **B-** Ice Sheet thickness, **C-** Bed topography (from Fretwell et al., 2013). **D-** W-E Cross-sectional profile of the Antarctic continent (from National Research Council, 2011).

AIS is made up of three distinct glaciological zones, consisting of the EAIS (covering an area of 10.35×10^6 km^2), the WAIS (1.97×10^6 km^2) and the APIS (0.52×10^6 km^2) (Convey et al., 2009). The EAIS represents the larger portion of the AIS regarding area and ice thickness, with 80.6% of total area (considering the values referred by Convey

et al., 2009) and over 2 km thick in average (Anderson, 1999; Fretwell et al., 2013; NASA-LIMA, 2014). EAIS rests predominantly above sea level (terrestrial ice sheet) with subglacial basins depressed below sea level, essentially caused by the great amount of ice (Anderson, 1999; Turner et al., 2009; Fretwell et al., 2013). As a consequence of the great ice thickness and heat flow from the Earth beneath, many places in EAIS are close to the melting point giving rise to a significant number of subglacial lakes (about 145 lakes, see Siegert et al., 2005). The largest lake known is the Lake Vostok with a water volume estimated ca. around 2,000 km^3 (Turner et al., 2009). The EAIS largely consists of a relatively flat dome (a broad upstanding area with slow moving ice), called South Polar Plateau (Benn and Evans, 2010), which comprises minor domes such as Argus, Circe, Fuji and Taylor Domes. The South Polar Plateau rises to a maximum elevation of over 4,000 m in Dome Argus (Yang et al., 2010). In contrast, the WAIS is a warm marine ice sheet where most of the ice is grounded below sea level (Anderson, 1999; Turner et al., 2009; Katz and Worster, 2010). WAIS is considered inherently unstable (Hughes, 1973; Bamber et al., 2009; Turner et al., 2009). In general, it is characterized by an average thickness of over 1 km (NASA-LIMA, 2015) and occupies 15.3% of the AIS. This iced region as relatively more complex topography when compared to the EAIS, it is divided into three sectors based on the major converged topographic divides, which determine the ice flow (ice divides). The main ice sectors are: Amundsen Sea sector; Weddell Sea sector and Ross Sea sector (Fig. 2.6) (Bindschadler, 2006; Benn and Evans, 2010).

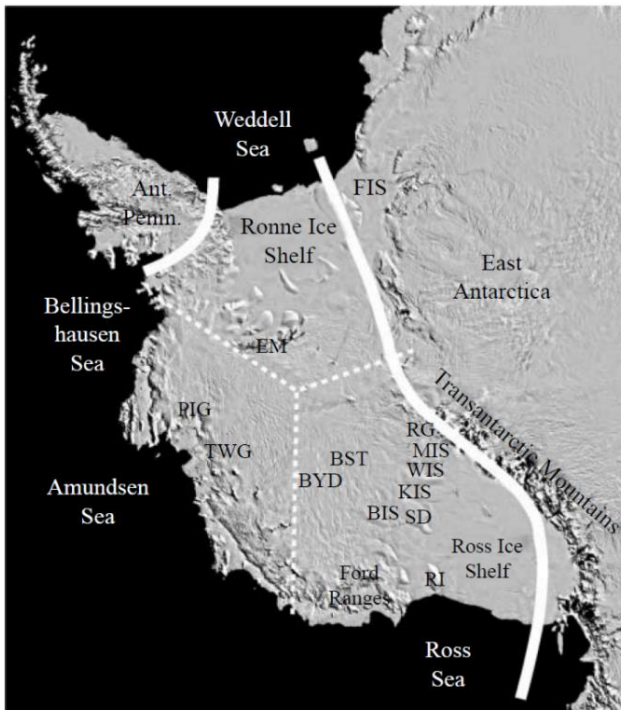

Figure 2.6. The WAIS and its respective subdivision: Amundsen Sea sector; Weddell Sea sector and Ross Sea sector (from Bindschadler, 2006).

The APIS that extends northwards from WAIS and covers the AP, represents the smallest portion of AIS, with 4.1% of total area (Bindschadler, 2006). APIS covers 80% of the peninsula and have distinguishing glacial character from the remaining AIS (Fig. 2.7). It consists in a set of much smaller and much thinner ice caps (ice masses with continuous coverage area lower than 50,000 km^2), that remain in the central mountain chain and in some of the larger outlying islands (Turner et al., 2009). The APIS ice caps are nourished locally and independently from the WAIS, for this reason this ice cover portion is not considered to be part of WAIS (Benn and Evans, 2010).

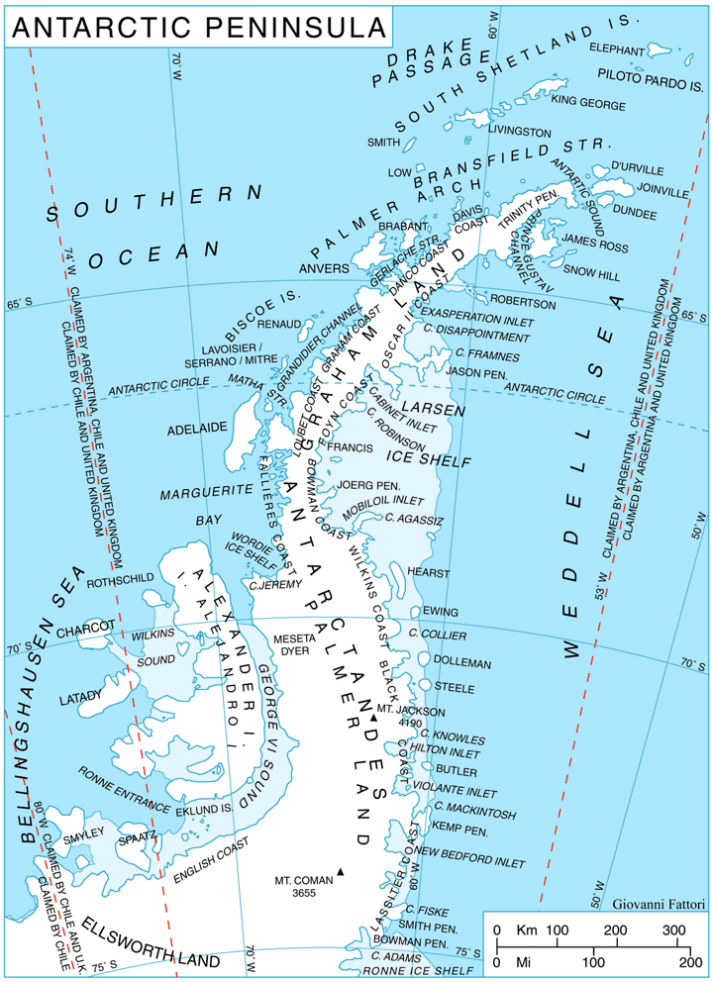

Figure 2.7. Antarctic Peninsula map (Source: https://en.wikipedia.org/wiki/Southwest_Anvers_Island_and_Palmer _Basin).

In general, AIS transports ice radially (by internal ice deformation and/or by sliding on the rock base) from dome systems to the coast, acting as dispersal centers, at a rate of around 2000 billion tons per year (Turner et al., 2009; Benn and Evans, 2010). Peripherally most of the ice is discharged rapidly (stream flow) through ice streams or outlet glaciers (channeled ice flows of greater magnitude flanked by slowly moving ice or confined in troughs or valleys, respectively), and some cases to sea or into ice shelves,

where ice sheet float in the ocean (Figs. 2.8 and 2.9) (Benn and Evans, 2010; IPCC, 2013). The most significant ice drainage region in EAIS is the Lambert Glacier Basin representing 16% of the ice sheet total drainage (Manson et al., 2000), with three representative and exceptional confluent ice streams: Lambert, Mellor and Fisher Glaciers (Benn and Evans, 2010). On the other hand, the WAIS outflow is predominantly channelized in more critical ice streams (Fig. 2.8) confined into (1) Amundsen Sea sector, where main drainage is confined to Pine Island Glacier, Thwaites Glacier and other channeled ice flows giving place to ice shelves such Getz and Abbot ice shelves; (2) Weddell Sea sector with a drainage system from the Ellesworth Mountains to the vast Ronne Ice Shelf through major ice streams such Institute, Rutford and Evans Ice streams; and (3) Ross Sea sector draining into Ross Ice Shelf, via the Ross or Siple Coast ice streams (Benn and Evans, 2010). The ice caps from APIS drain into the sea through relatively narrow alpine-type glaciers. The ice flow in APIS gives place to main ice shelves like George IV and Wilkins ice shelves on the west side and Larsen Ice shelf system on the east side (Fig. 2.7), which have been suffering strong recession during the last two decades (e.g. Cook et al., 2005; Turner et al., 2005).

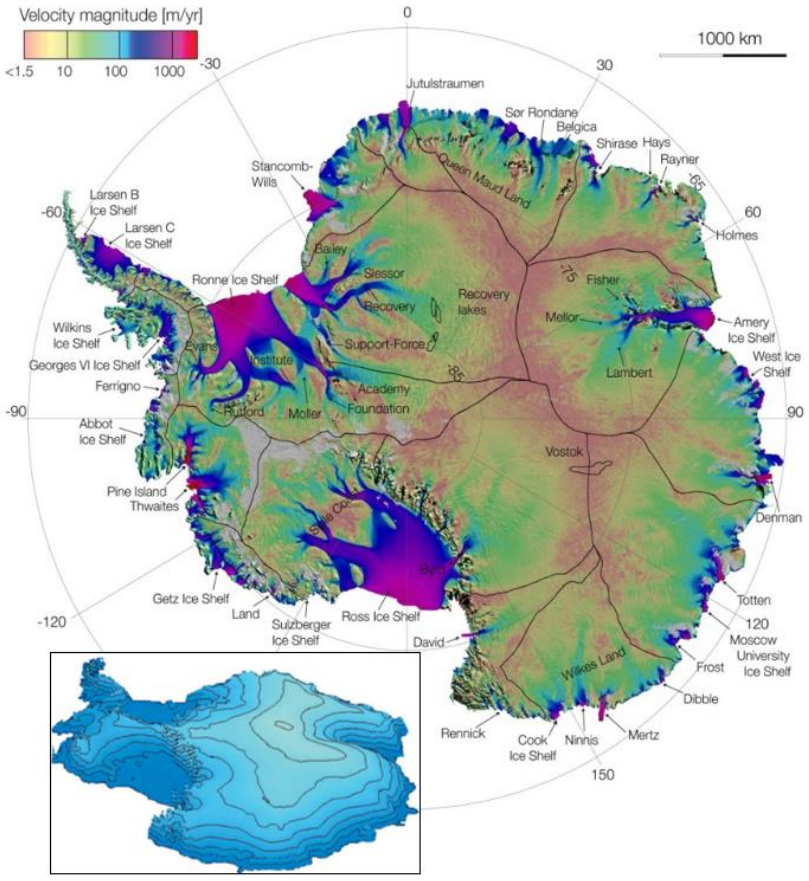

Figure 2.8. High resolution mosaic of the ice motion in Antarctica from multiple satellite interferometric synthetic-aperture radar data (from Rignot et al., 2011), and surface topography (from Walton, 2013; Credit: Gaël Durand, using the data synthesis of Anne Le Brocq).

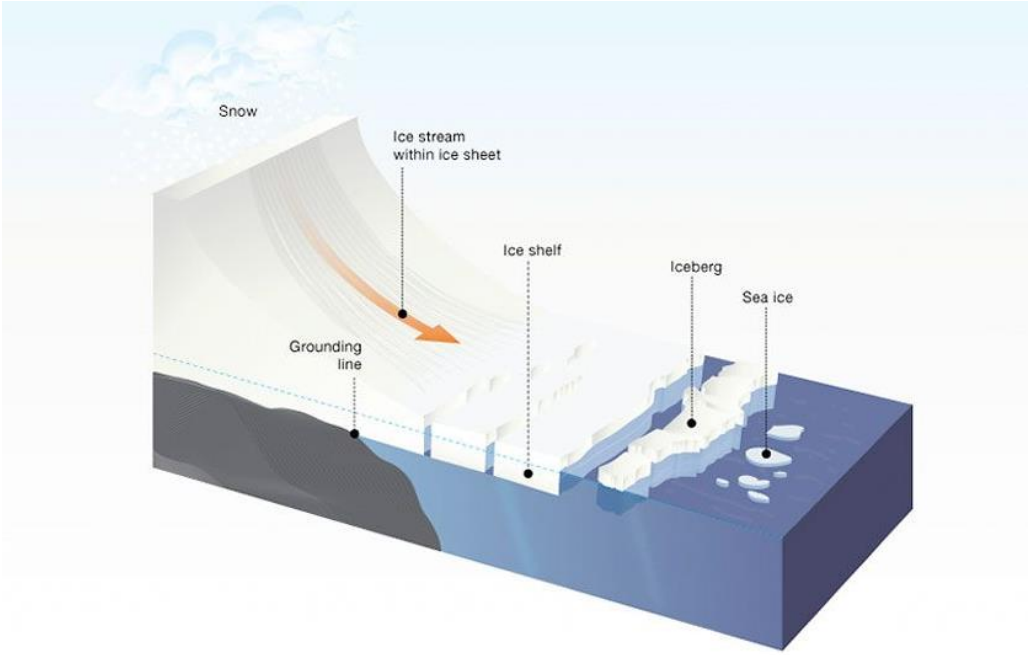

Figure 2.9. Glacial environment of outer regions and dynamics of Antarctica. The transition line where grounded ice reaches the floatation point is designed Grounding line (Image from: http://www.nasa.gov/centers/goddard/news/topstory/2004/0913larsen.html).

The Antarctic ice shelves cover about 1.561×10^6 km^2, representing 75% of Antarctica's coast line (Rignot et al., 2013) and 11% of the total Antarctic area (Convey et al., 2009). The main ice shelves are the Ronne- Filchner Ice Shelf in the Weddell Sea and the Ross Ice Shelf in the Ross Sea (Figs. 2.5 and 2.8). Generally, these ice bodies have an inferior thickness when compared to the ice sheets, the thicknesses vary from nearly 2,000 m, close to grounding line, to about 100 m, at the seaward edge (Doake, 2001). Ice shelves are the floating extension of the glaciers/ice streams, which turn them more susceptible to mass exchanges with the involving environment. The ice starts to float when the ice streams get thinner than the water depth, after ice mass loss occur by calving icebergs, basal melting and sublimation (Fig. 2.10) (Cuffey and Paterson, 2010; Cogley et al., 2011; Rignot et al., 2013). Ice shelves represent an important role on the AIS mass balance and stability (Rignot et al., 2013). The mass balance is the net result after a time interval, of mass gain (trough precipitation/accumulation) and mass loss (ablation) which are strongly dependent of climate factors (Bennett and Glasser, 2009; Hanna et al., 2013). EAIS and WAIS lose mass primarily through iceberg calving and melt from the base of ice shelves. On the other hand, the APIS experiences much higher temperatures, due to its geographical position, making runoff from surface melt a significant component in the mass balance (Turner et al., 2009).

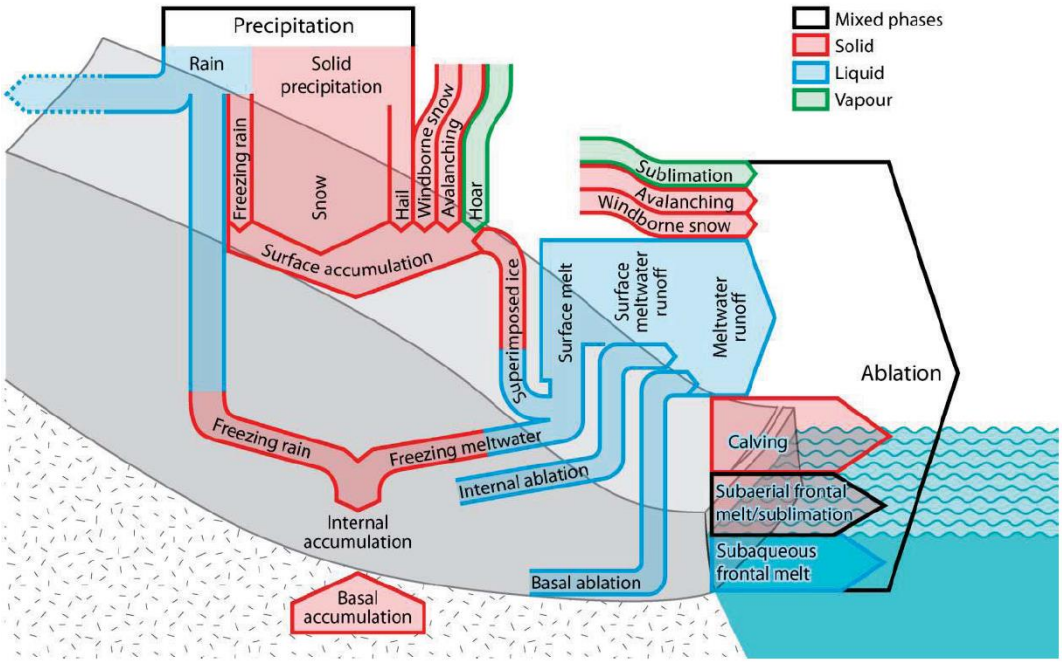

Figure 2.10. Components of the mass balance of a glacier, note that arrows are not totally indicative of physical pathways of mass transfer (from Cogley et al., 2011).

Beyond the ice shelves is common to observe the presence of sea ice (Fig. 2.9), formed when the sea freezes (IPCC, 2013; British Antarctic Survey, 2015). The area covered by sea ice varies with the seasons, from a minimum of about 3×10^6 km^2 in summer to a maximum of about 18×10^6 km^2 in winter (Comiso et al., 2011), doubling almost the size of Antarctica (Fig. 2.11) (British Antarctic Survey, 2015).

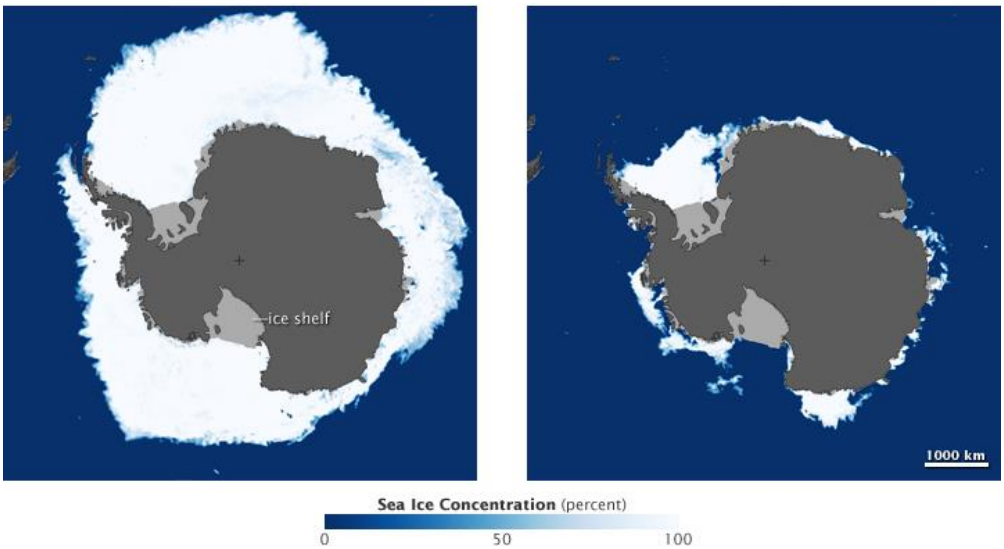

Figure 2.11. Surrounding Sea ice concentration during Antarctic Maximum (Left) and Minimum (Right), from September 2008 to February 2009 (Source: http://earthobservatory.nasa.gov/Features/SeaIce/page4.php

The AIS coverage had different configurations through time (e.g. Anderson et al., 2002; Ingólfsson, 2004). His history is poorly known, and the associated events are mainly inferred from marine geophysical and geological studies (e.g. Anderson et al., 2002) and from proxies in ice cores or marine and lake sediment cores (e.g. Zachos et al., 1992; Pettit et al., 1999; Bentley and Hodgson, 2009). The glaciation events in Antarctica started at the Paleogene (mid-Tertiary), probably related to the Gondwana fragmentation and the subsequent isolation of the Antarctic continent, prevailing for about 35-40 Ma and reaching continental proportions by the latest Eocene-Early Oligocene (Ingólfsson, 2004) (Fig. 2.12). During the Miocene the formed ice sheets were covering on both West and East Antarctica (Anderson, 1999). After a broad and significant ice build-up events, the AIS experienced a considerable ice volume fluctuations during Pliocene. Mainly based on East Antarctic records, the ice sheet went through extensive collapse to an extensive build. The collected data show a tendency for a Pliocene period with interglacial conditions warmer than the present day (Ingólfsson, 2004). In late Pliocene and perhaps early Pleistocene ice sheets extended to the edge of the continental shelf around Antarctica. Later this glaciation episode would be interrupted by new important interglacial events where, during Pleistocene, the WAIS suffered at least one significant collapse (Fig. 2.13) (Ingólfsson, 2004). Around 20,000 – 18,000 years ago Antarctica enters in the last glacial/interglacial cycle, the glacial episode is known as Last Glacial Maximum (LGM) (Ingólfsson et al., 1998). With an extension more significant for the WAIS than the EAIS during LGM (Anderson et al., 2002), the AIS entered in the last interglacial phase with evolutionary paths that created the configuration and ice distribution that we know today.

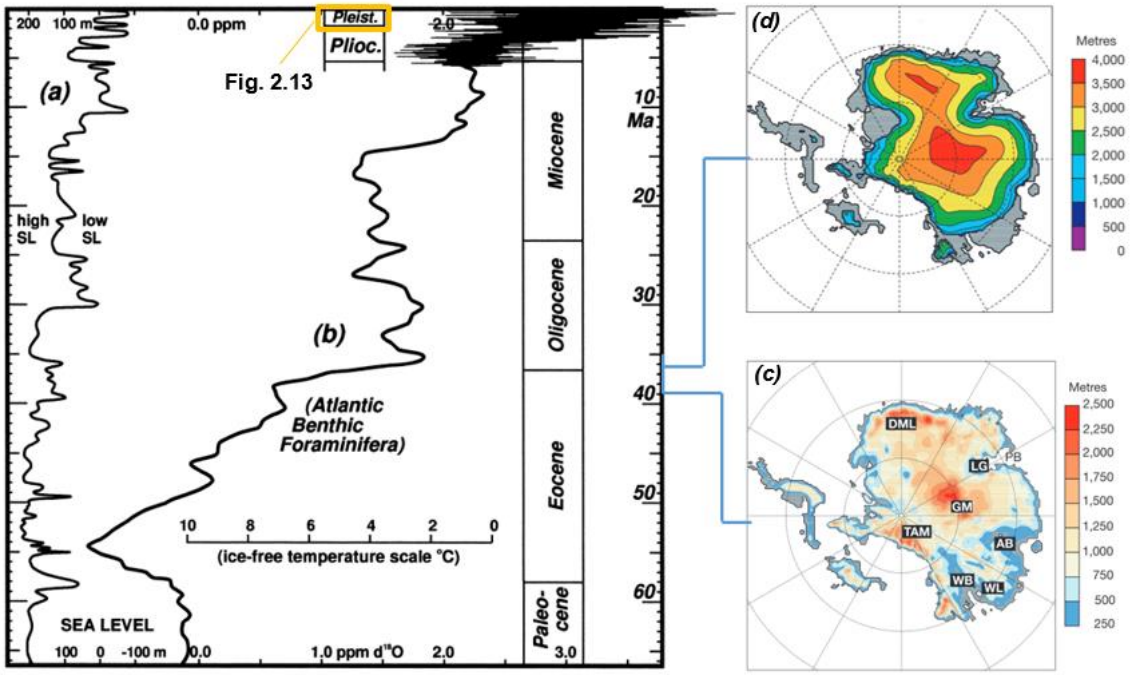

Figure 2.12. Cenozoic variation of ice sheet from proxies showing ice cover variation trough time: (a) global eustatic sea-level from sequence stratigraphy; (b) oxygen isotope ratios in Atlantic benthic foraminifera; (c) Topography of the Antarctic continent without ice cover and (d) hypotetical ice cover (adapted from Barker et al., 1999 and Pollard and DeConto, 2009).

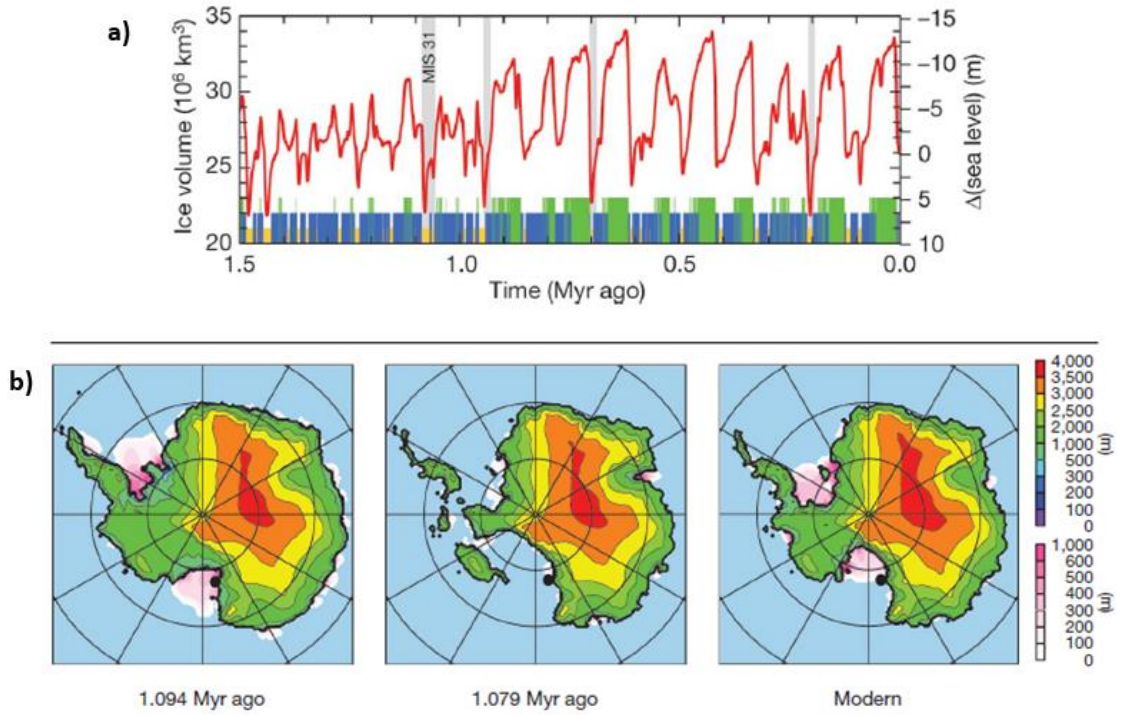

Figure 2.13. Total ice cover volume variation in Antarctica from last 1.5 million years (a) and snapshots at particular times (b) resulted from a long term simulation. On the graphic (a) is shown the total volume of ice on the Antarctic continent (red line) in long term simulation mainly from deep-sea-core $\delta^{18}O$ record. (adapted from Pollard and DeConto, 2009).

2.1.3. Weather and climate

Antarctica is the coldest, windiest and driest continent on Earth. The climate highlights extreme conditions in the interior of the continent going at more moderate behavior along the coastal regions (Anderson, 1999). The continent retains the lowest recorded temperature on Earth, -89.2°C (at Russia's Vostok Station), low precipitation levels and wind speeds that can reach hurricane strength (Walton, 2013) (Figs. 2.14 and 2.15). This extreme climate conditions are derived from the geographical polar position, where a net radiation deficit and an important relief (elevation) of the continent make it even colder than North Pole regions.

Antarctica temperatures during summer range from 0°C near the coast to -30°C in the interior, during winter the temperatures are about -15°C near coast and drop to -65°C in the interior (Walton, 2013). The strong winds, typical from this continent have origin from the input of dense air adjacent to the ice sheet (cold advection) due to the horizontal temperature contrasts and flow out from the interior of the continent. These winds are known as katabatic winds (Walton, 2013), which have lower speeds on flat areas of the continent increasing intensity on coastal escarpment, where are registered annual values between 5-10 ms^{-1} (King and Turner, 2007; Benn and Evans, 2010). Due to cold advection the Antarctic region is broadly associated to sinking motion area, which causes clouds dissipation and consequently suppresses the development of precipitation. In that way, Antarctica receives an annual precipitation of ca 130 mm in average, being considered as a desert as more than 99% of the continent is covered by ice (Walton, 2013).

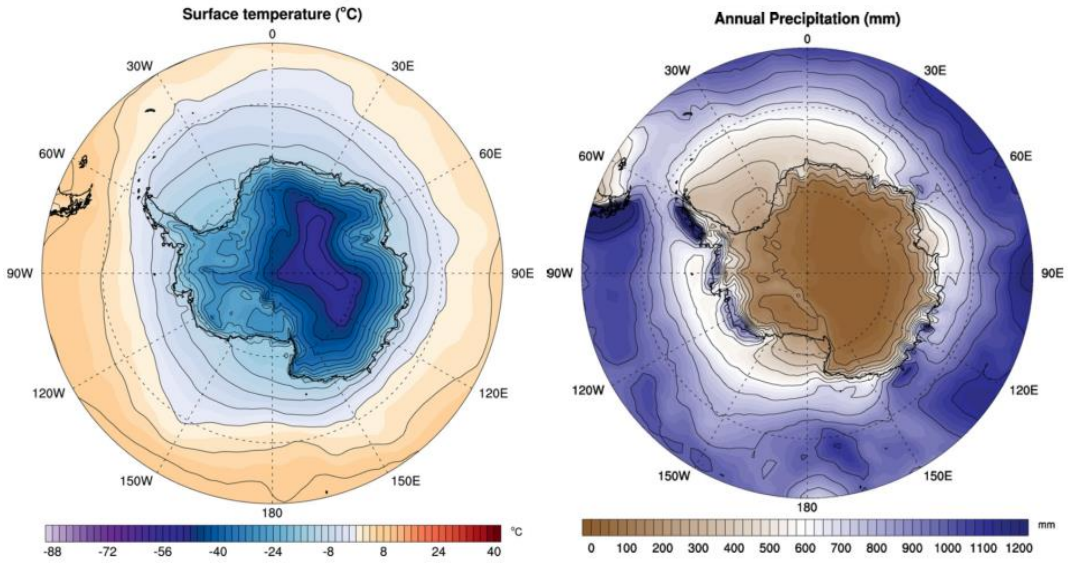

Figure 2.14. Surface temperatures and precipitation gradients over the Antarctic continent (adapted from Walton, 2013).

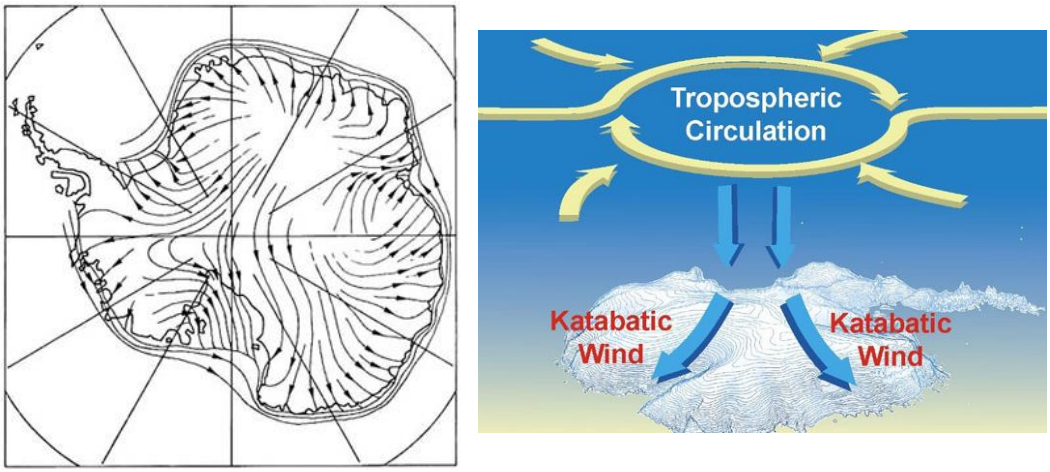

Figure 2.15. Prevailing wind direction over Antarctica, on the left (from King and Turner, 2007) and a diagram showing the downfall winds (katabatic winds), source: http://climatestate.com /2013/07/26 /antarctic-methane-emissions/.

2.1.4. Physical oceanographic setting

Antarctica is surrounded by the Southern Ocean, formed about 120 million years ago during the Gondwana breakup. The ocean covers 70 million km^2, that is 20% of the world´s oceans (Walton, 2013). The fully connected Southern Ocean was formed after the opening of the Drake Passage, which initiated 49 Ma ago, and after the opening of the Tasmania-Antarctic pathway (from 35.5 to 33. 5 Ma) (Scher and Martin, 2006). This ocean connects the Atlantic, Pacific and Indian Oceans and is defined by very few shallow areas (National Research Council, 2011).

The dominant circulation of the Southern Ocean is mainly promoted by a wind system in bands known as West Wind Drift (WWD). The WWD is created by the difference of pressure between the subtropical high pressures and the low pressure belt (centered at about 60°S, Fig. 2.16), combined with the action of Earth rotation. Thus, it drives the eastward flowing ocean current, and with no mass land connecting with the Antarctic continent the resulting current, being designed has Antarctic Circumpolar Current (ACC), runs clockwise from west to east around the southern hemisphere (Walton, 2013) (Fig. 2.16). This current extends also trough the seabed in most of places (Barker and Thomas, 2006). One of the major fronts of the ACC is the Antarctic Convergence or Antarctic Polar Front (APF), which marks the location where cold northward-flowing Antarctic waters meet the relative warmer waters of the Sub-Antarctic

Zone creating a zone of upwelling nutrients (Pickard and Emery, 1982; Moore et al., 1999).

The cold and fresh surface waters is led by the westerly wind combined with the Coriolis force and diverted northward. At some places of upwelling, the surface waters are replaced by the Circumpolar Deep Water (CDW) (Figs. 2.16 and 2.17), a key component of the ACC derived from a mixture of the deep waters from all world's oceans (Convey et al., 2009; Dinniman et al., 2012). CDW is a relatively salty and warm current which flows onto the continental shelf at depths of 300 m (e.g. Jacobs et al., 2011).

Adjacent to the ACC system are the regional clockwise gyres, mainly represented by Wedell Gyre and Ross Gyre, and getting closer to the Antarctic continent the Eastwind Drift (Fig. 2.16).

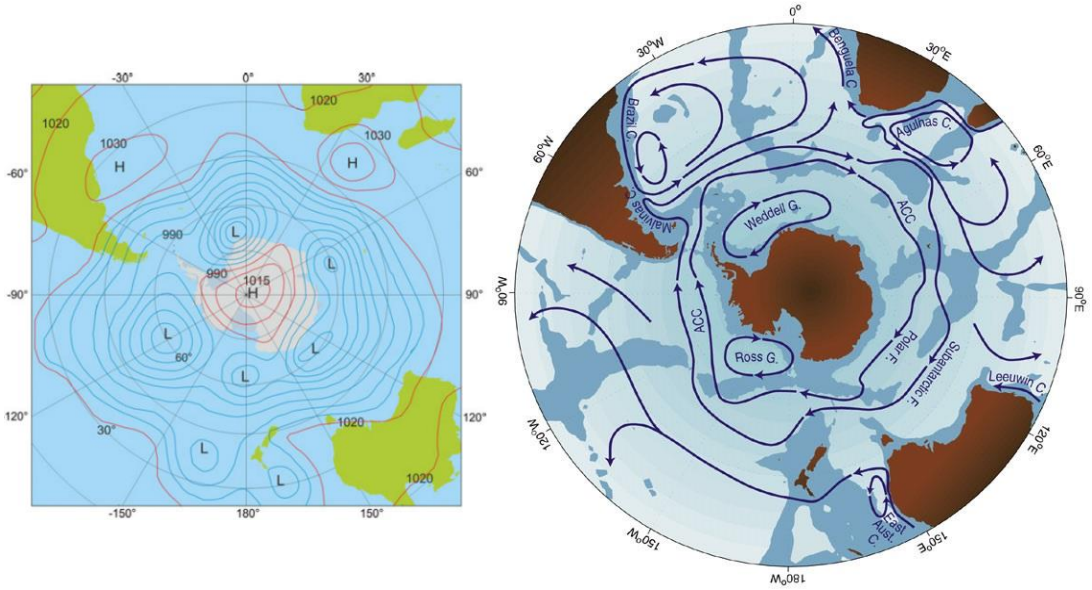

Figure 2.16. On left, atmospheric pressure distribution at sea level displaying the major high and low pressure systems, which determine the winds over the Southern Ocean (From Walton, 2013, Credit: Eberhard Fahrbach, AWI). On the right, schematic map showing the major currents and fronts of the Southern Ocean (F-Front, C-Current, G-Gyre). The figure ilustrates the Polar Front and Sub-Antarctic Front, which are the major fronts of the Antarctic Circumpolar Current, and regional currents of the Weddell and Ross Sea (Weddell Gyre and Ross Gyre, repectivelly). Image adapted from Convey et al. (2009).

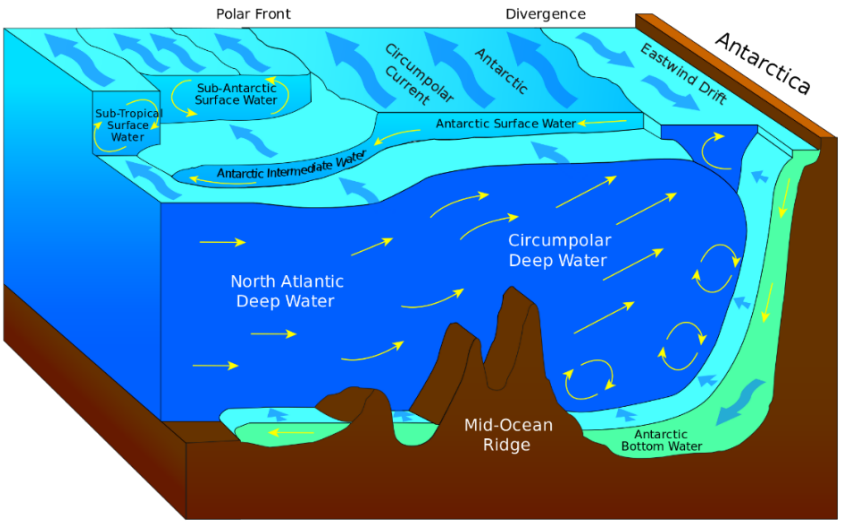

Figure 2.17. Depth-latitude diagram showing the major circulation and water masses of the Southern Ocean, representing also Deep Water upwelling, in this case from Atlantic sideways (Source: https://en.wikipedia.org/wiki/North_ Atlantic_Deep_Water).

2.1.5. Antarctica's role in the global environment

Although Antarctica being physically distant from other continents, it has strong connection and influence with the entire global Earth's system. This connectivity is made essentially trough an atmosphere-ocean interaction (Anderson, 1999; National Research Council, 2011).

Antarctica serves as an atmospheric heat sink causing a large temperature gradient that drives the atmospheric circulation in the Southern Hemisphere (Anderson, 1999; National Research Council, 2011). As several regions in the world, the atmosphere that resides over the Antarctic continent was not immune from anthropogenic chemicals release or green-house effect gases: atmospheric changes that lead to remarkable consequences or benchmarks of climate change, as for instance ice shelf collapses (e.g. Turner and Overland, 2009; Cook et al, 2005).

The interaction of Antarctica with surrounding mass waters, constitute an important interface with global ocean circulation that equally has an important role in global climate system. The associated CDW allow the existence of overturning circulations contributing for the global water moisture and heat balance (Rintoul et al., 2001; National Research Council, 2011).

The Antarctic ice cover contributes with valuable information on climate variations; the associated records constitute a natural and representative indicators of past climate variations (Barker et al., 1999; Walton, 2013). The AIS has a strong relation with the air and seawater, producing direct impacts on ice evolution, temperature/circulation and sea level. It is important to underline that the AIS represents 90 percent of the world's ice and around 70 percent of Earth's freshwater (Convey et al., 2009; British Antarctic Survey, 2015), if melted, it would contribute for a raise of the sea levels by nearly 60 meters (Bennett and Glasser, 2009).

Thus, Antarctica is considered as an important piece of global interacting systems that allow scientists to better understand the global climate system and predict possible variations in the future. Most human beings feel like living far away from Antarctica, but changes in this extremely inhospitable place are affecting our quotidian life particularly for those living along the coasts.

2.2. East Antarctica

2.2.1. Glacial character of the EAIS

EAIS is the largest portion of AIS with distinctive geography and dynamics. Most of the ice sheet remains above sea level, with subglacial basins depressed below sea level, essentially caused by the great amount of ice (Fig. 2.5-B and C) (Anderson, 1999; Turner et al., 2009; Fretwell et al., 2013). In that way, EAIS is usually considered to be a stable ice sheet. The considerable mass of EAIS has an estimated value of around 22 million km^3 of grounded ice, equivalent to 53 m of global sea level (Lythe et al., 2001; Fretwell et al., 2013).

The EAIS largely consists of a relatively flat dome (a broad upstanding area with slow moving ice), designed as South Polar Plateau (Benn and Evans, 2010), with very dynamic margins mainly represented by important ice streams. The lowest temperature and precipitation values are founded in EAIS at highest elevations of ice sheet surface, from where they have tendency to ascend toward margins (Fig. 2.8). However, according to some studies on the interior of the ice sheet precipitation levels are increasing (Rignot, 2006). Those variations are possibly reflecting changes in snow fall, which are leading

to the ice thickening in the interior part of the EAIS (Davis et al., 2005), and enhance ice sheet dynamics.

The East of Antarctica is relatively closer to a state of mass balance (Fig 2.18), although marine sectors (outlet glaciers) are the exceptions (Fig. 2.19) (Rignot, 2006; Rignot et al., 2008). Ice sheets lose mass through melting (surface or basal) and dynamic changes (for example, the acceleration and retreat of outlet glaciers) (Miles, 2013). Many glaciers of EAIS, especially those in contact with the sea are actually melting, consequently thinning and losing mass faster than considered, for example Cook Ice Shelf, Ninnis/Mertz Glacier, Frost, Moscow University Ice Shelf and Totten Glacier, (Figs. 2.19 and 2.20) (Rignot, 2006; Rignot et al., 2013).

A study from Miles et al. (2013) along 5,400 km of the EAIS coastal region, stretching from Queen Mary Land (longitude 90º E) to Victoria Land (170º E), encompasses significant regions of mass loss (Fig. 2.21). The study reveals the magnitude of advance or retreat by different glaciers between 1974 and 2010, revealing an increased number of glaciers undergoing retreat from 2000. Those observations suggest that East Antarctica is not totally immune to changes and cannot be so stable that has been considered until now.

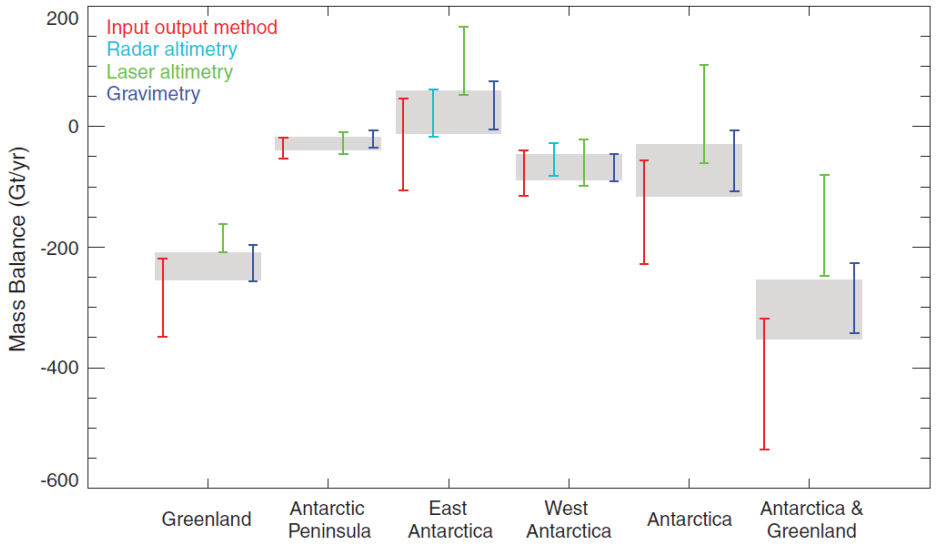

Figure 2.18. Mass balance estimates of EAIS and other polar regions over the period 2003 to 2008, based from four independent techniques, Input output method (Red), Radar altimetry (Blue), Laser altimetry (Green) and Gravimetry (Cian) (from Shepherd et al., 2012).

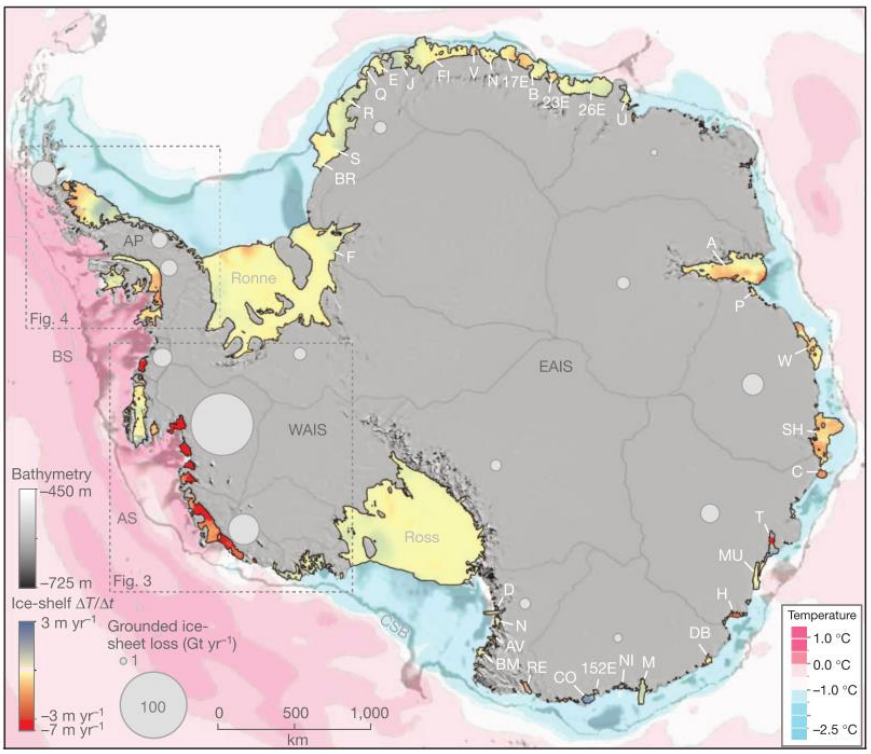

Figure 2.19. Antarctic ice-shelf ice-thickness change rate (ΔT/Δt, 2003–2008) and relative ice losses for ice sheet drainage basins (grey circles) between 1992 and 2006. The white labels indicate the ice shelves. Image from Pritchard et al. (2012).

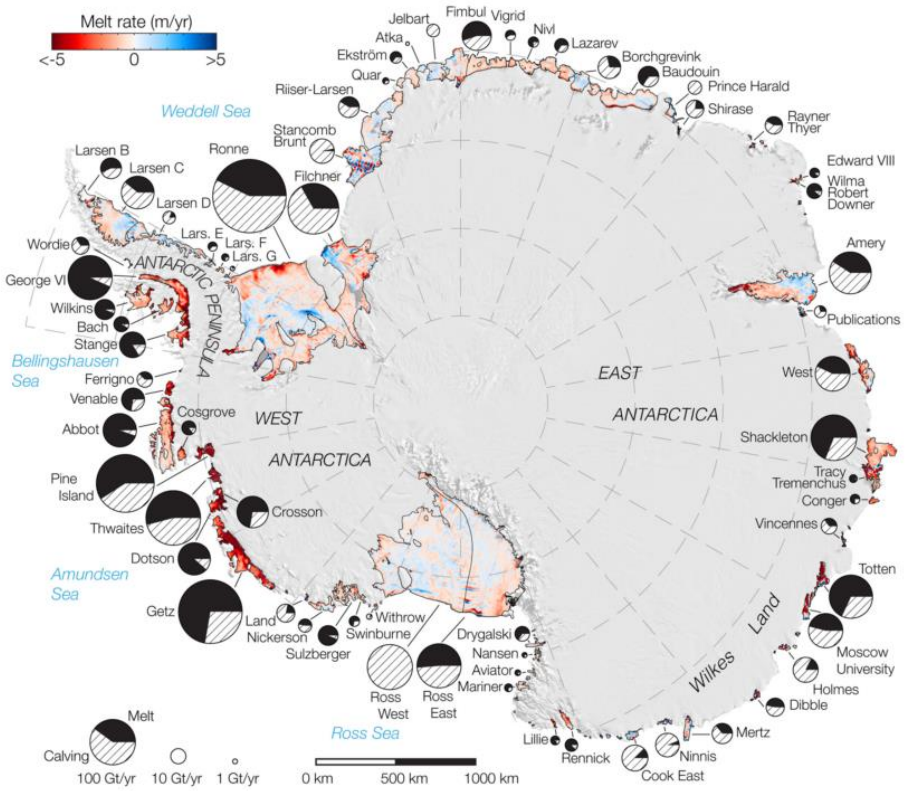

Figure 2.20. Basal melt rates of Antarctic ice shelves (perimeters in 2007–2008) coded from < –5 m/year (freezing) to > +5 m/year (melting). Each circle graph is proportional in area to the mass loss from each shelf, in gigatons (1 Gt = 1012 kg) per year, partitioned between iceberg calving (hatch fill) and basal melting (black fill). Image from Rignot et al. (2013).

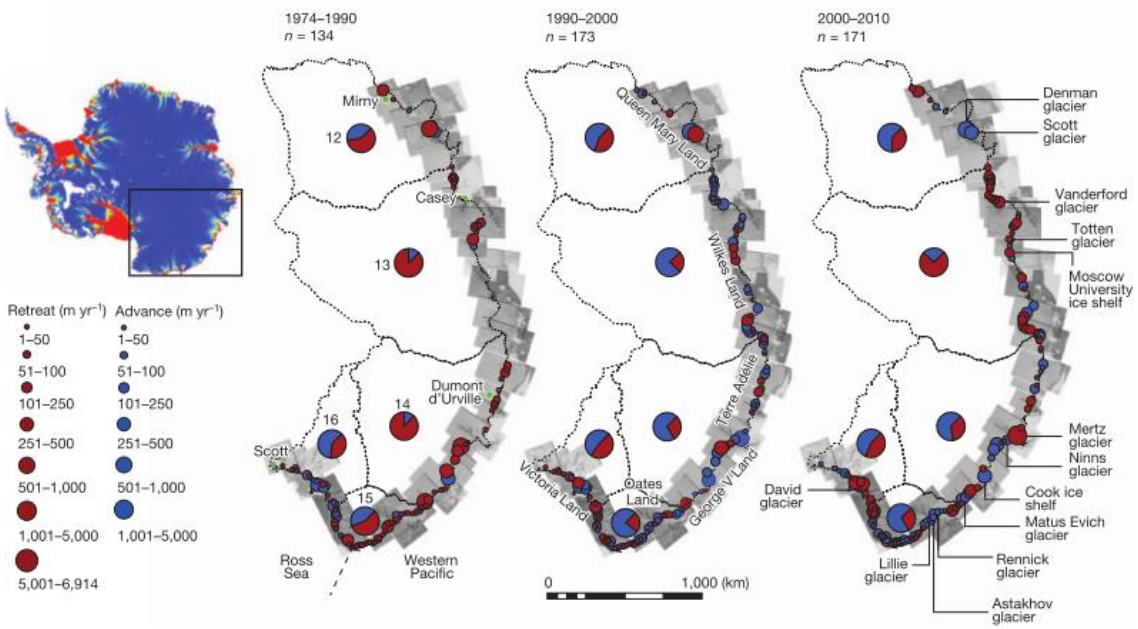

Figure 2.21. Spatial and temporal variations in EAIS glacier terminus position from all measurements in 1974, 1990, 2000 and 2010. The rate of terminus position change for each glacier and period is shown by the single-colour circles. Pie charts represent the percentage of glaciers advancing and retreating in each major region. Image from Miles et al. (2013).

2.3. Glacial seafloor morphology and forming processes

The dynamic evolution of ice sheets and glaciers leave behind distinct geomorphic features through erosion and accumulation on the subsequent bedrock surface (e.g. Anderson, 1999; Bennett and Glasser, 2009). The AIS advanced and retreated through several of glacial-interglacial cycles over past few million years, where the glacial processes molded the Antarctic continental shelf (e.g. Anderson et al., 2002).

The Antarctic continental shelf presents peculiar characteristics showing high depths, very rugged topography and a land-sloping profile derived from glacial erosion and, in part, glacio-isostatic rebounds (Fig. 2.22). The general profile of the Antarctic continental shelf displays regional morphological characters that allow to subdivide it into three main sectors: the inner, middle and outer shelf (Wellner et al., 2006). In general, the inner shelf is characterized by crystalline bedrock and rugged relief that progressively, toward open sea, give place to smother surface shaped by glacial sedimentary sequences on outer shelf (Fig. 2.23).

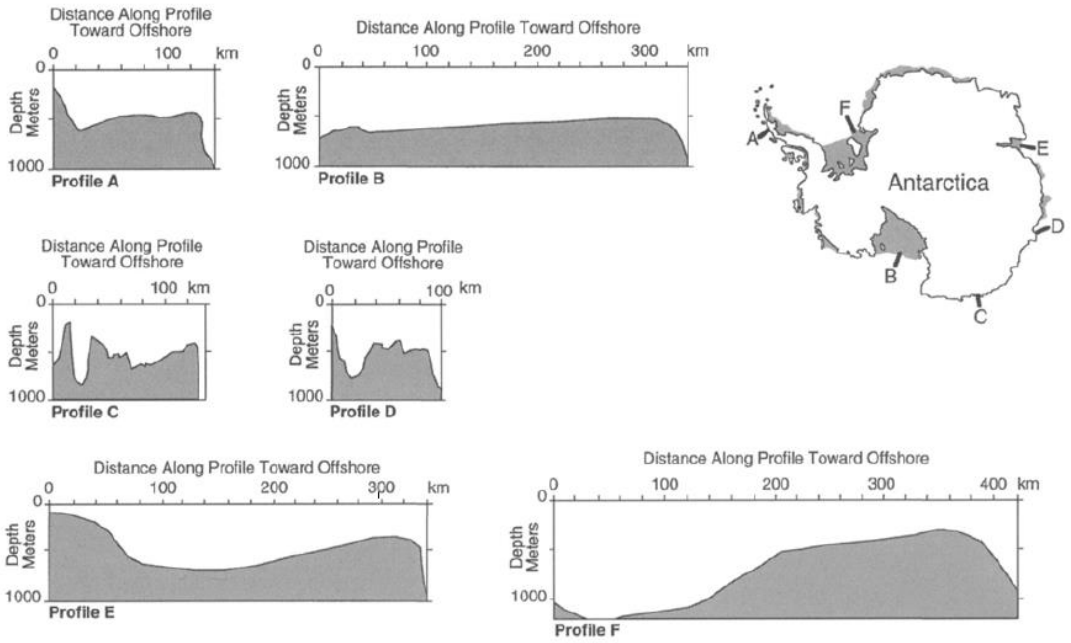

Figure 2.22. Representative bathymetric profiles from the West (A-B) and East (C-F) Antarctic continental shelves illustrating the great depth, irregular relief, and landward-sloping profile of the shelf. Image adapted from Anderson (1999).

On large scale, the morphology of the Antarctic continental shelf is dominated by glacial cross-shelf troughs, adjacent ridges and banks (Anderson, 1999). From inner to outer shelf, the increase of more unconsolidated material (sediments) is associated to more elongated glacial features, where material was less competent and more erodible during the past ice flow (Gales, 2013). The preserved glacial bedforms and sediments on continental shelf regions offer information that allow the reconstruction of past ice sheets in terms of their extent, flow dynamics and nature of their retreat on the past (Ó Cofaigh, 2012; Dowdeswell et al., 2008). The glacial bedforms can be broadly divided in two main series, bedforms parallel to ice flow and those transverse to ice flow. The parallel ones are indicative of paleo-ice flow direction and are dependent of the substrate changes. On the other hand, the transverse glacial features, such as grounding-zone accumulations, are indicative of ice fronts locations from the past ice sheet extensions.

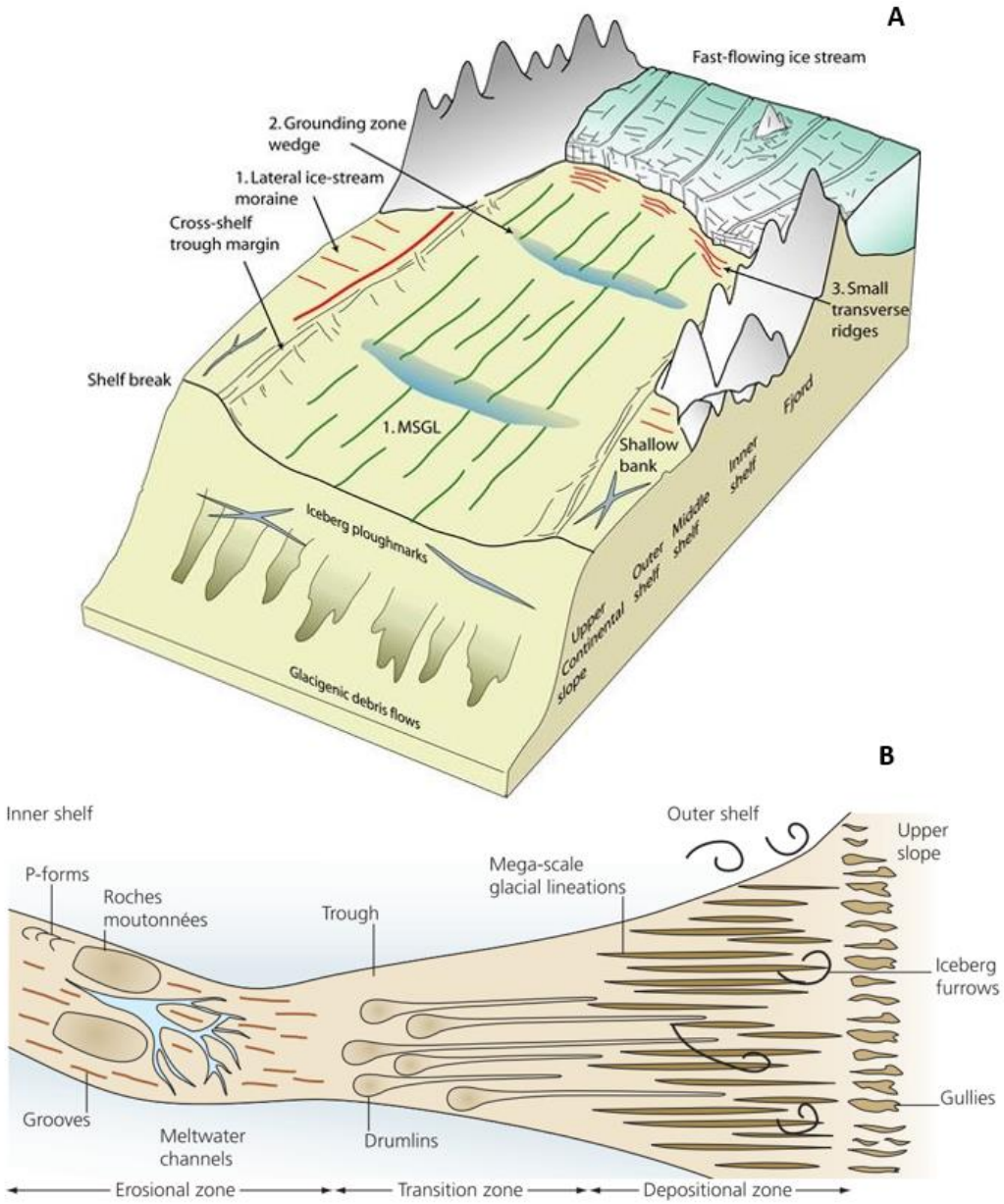

Figure 2.23. Palaeo-ice stream land system model of the continental shelf (A) (Source: http: //www.geog.cam. ac.uk/research/projects/submarineglacialatlas/) and generalized distribution of the glacial geomorphic features (B) (from Benn and Evans, 2010 reproduced from Wellner et al., 2006).

2.3.1. Inner continental shelf

The inner shelf is generally characterized by rock substrate (outcrops or subcrops of igneous and sedimentary rock) with frequent and irregular erosional forms that create a typical high relief (Shaw et al., 2008; Wellner et al., 2006). This region, can exhibit great variability of bedforms such as (i) drumlins, (ii) crag and tails, (iii) roches moutonnées,

(iv) whale backs, (v) Grooves, (vi) P-forms, (vii) meltwater channels and tunnel valleys, and (viii) basins and troughs.

i) Drumlins

The drumlins are elongated hills of a tear drop shape, parallel to ice flow with the stoss or front side defined by a more abrupt relief than the lee or rear side. They present similarities and relations with other features such as roches moutonnées, crag and tail, whale backs and other drumlinoid bedforms, they are streamlined bodies produced under flowing ice (Fig 2.24). The drumlins are composed of a variety of materials, including: (i) bedrock; (ii) part bedrock/part till; (iii) till; (iv) part till/part sorted sediments and (v) sorted sediments (Stokes et al., 2011). On the Antarctic shelf, drumlins are usually confined to the inner shelf, frequently formed in bedrock and having crescentic scours at their proximal ends (Shaw et al., 2008) Also, drumlins can be found in the proximal parts of the middle shelf, but in attenuated form (Shaw et al., 2008; Wellner et al., 2006).

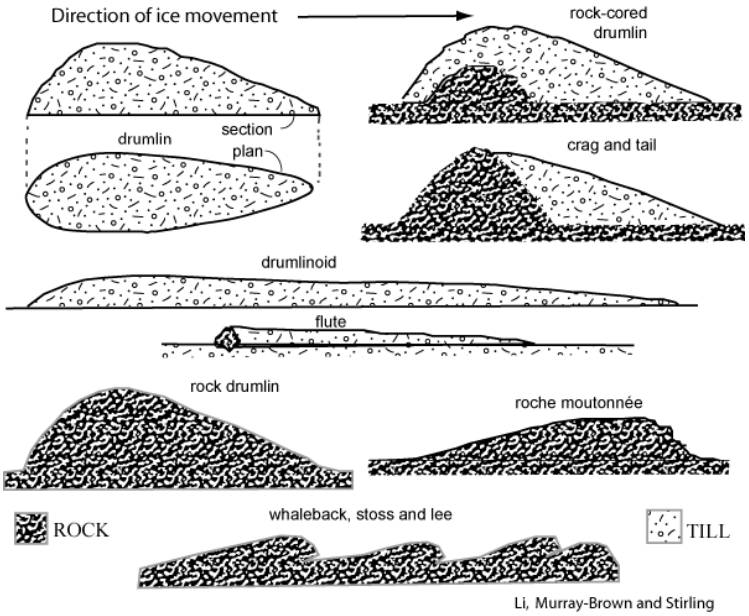

Figure 2.24. Drumlinoid glacial landforms and internal composition. (Source: http://www.landforms.eu/lothian/Drumlinoid% 20glacial%20landforms.htm)

Due to the great variability of the internal composition of the drumlins, some studies suggest that there is no single mechanism responsible for their formation. Numerous models and explanations were proposed for the formation of drumlins, which are largely represented by the subglacial deformation theory (e.g. Hart, 1997) and the subglacial

floods theory (e.g. Shaw and Sharp 1987; Shaw, 2002). The subglacial deformation hypothesis consider the movement of the ice above softer materials, such as sediments, which impose a stress that drag and shape them along the direction of flow (Hart, 1997). On the other hand, the subglacial floods hypothesis attributes drumlin formation to erosion and deposition by violent turbulent floods (meltwater) of enormous magnitude (Shaw, 2002). The common factor of these main theories is the requirement of the presence of an obstacle-obstruction (Fig. 2.25C) that can be a rock protuberance or an important accumulation of till (e.g. Hart, 1997; Shaw et al., 2008).

According to Stokes et al. (2011), the bedrock drumlins are formed from the glacial abrasion and meltwater erosion, which smooth and polish bedrock protrusions and, also, superimposes a variety of small scale erosional landforms.

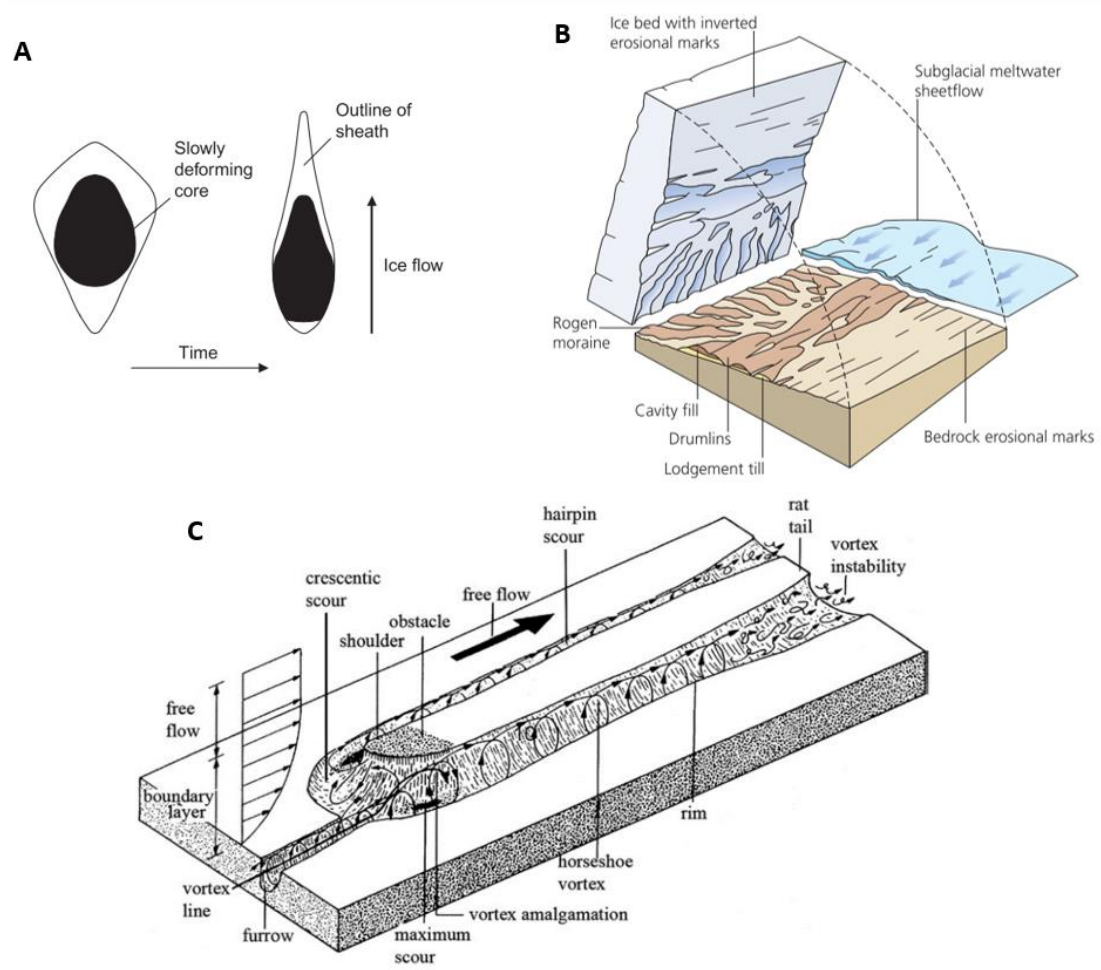

Figure 2.25. Different formation processes of drumlins. Formation through **A**- deforming sediments (Benn and Evans, 2010), **B**- the meltwater hypothesis (John Shaw, 2002, reproduced by Benn and Evans, 2010); **C** – a vortex generated in front of an obstacle (Shaw et al., 2008).

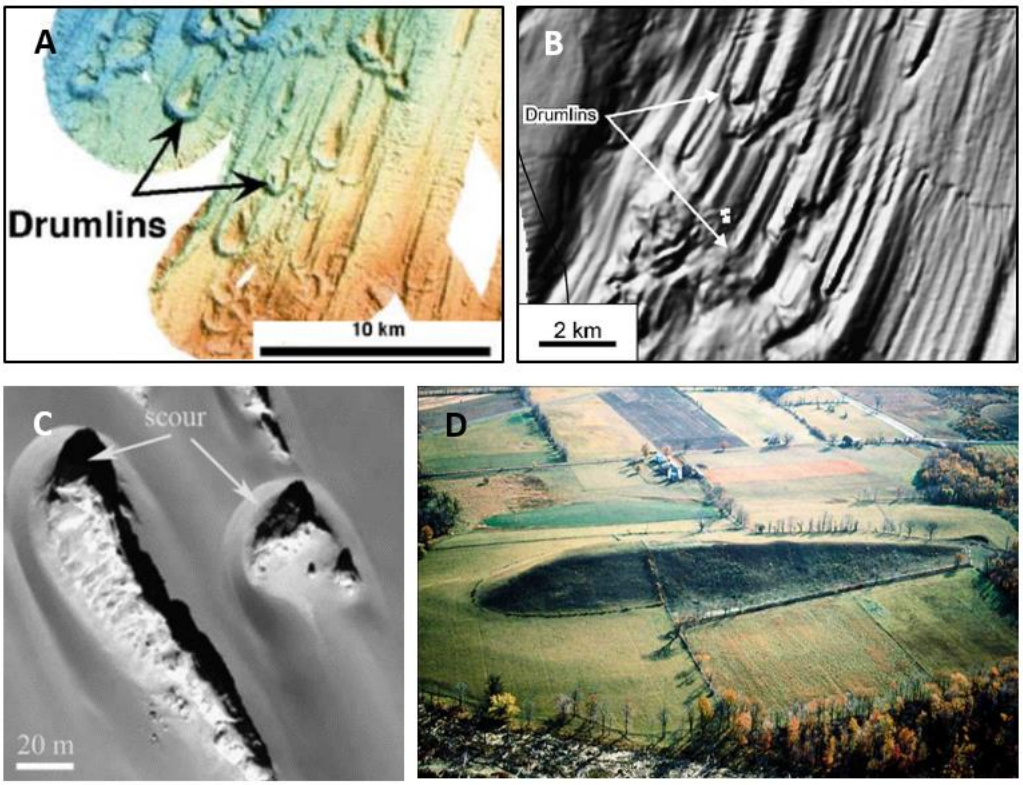

Figure 2.26. Details of the seafloor continental shelf from multibeam images (**A** and **B**) (from Graham et al. (2009) and Wellner et al. (2006)) and exemplified photos where it is possible to identify drumlinised bedforms (**C** and **D**) (from Shaw et al. (2008); http://www.geol.umd.edu/~jmerck/geol100 /lectures /36a.html).

Besides the theories of their formation, the scale and shape of the drumlins also do not have a strict definition. Their length can vary from tens of meters and reach kilometers. An important study from Clark et al. (2009) on size and shape characteristics of the drumlins show that their length vary commonly between 250 and 1,000 m with most frequent elongation ratios are between 2 and 2.3.

ii) Crags and tails

A crag and tail is a streamlined bedform and consists of a large bedrock head or protrusion (crag) and a tail downslope of the ice flow, similar to drumlins but with cruder form (Graham et al., 2009; Benn and Evans, 2010). The crags and tails are formed by streaming ice action over a resistant rock and surrounding softer material, where the rock protrusion constitutes an obstacle for the ice flow, leaving behind a tail relatively protected from erosional action (Fig. 2.27). Their scale can vary from meters to several kilometers (Benn and Evans, 2010).

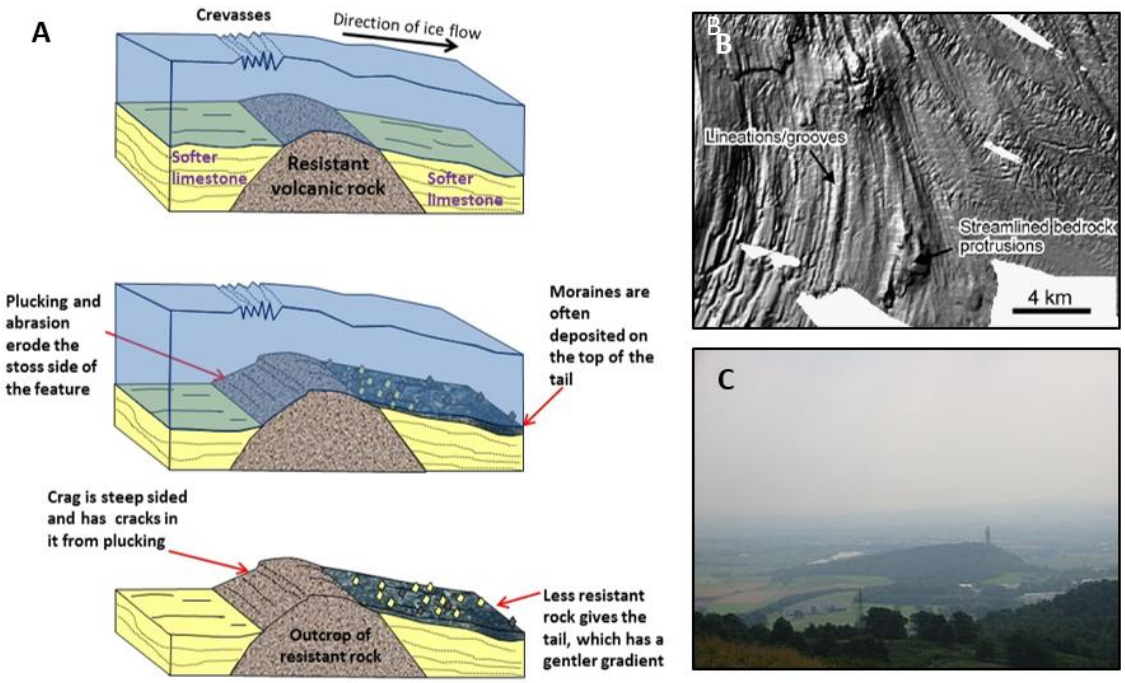

Figure 2.27. Formational process of a crag and tail (**A**), and examples on the seafloor (**B**, from Graham et al. (2009)) and. near the University of Stirling, UK (**C**, from https://en. wikipedia.org/wiki/Crag_and_tail.

iii) Roches moutonnées

The roches moutonnées are asymmetrical rock elevations formed by glacial abrasion (Fig. 2.28). Under the ice, high pressures occur on the stoss (up-ice) side of the bedform and lower pressure on the lee (down-ice) side. Consequently, the up-ice side experiences glacial abrasion while the down-ice side is glacially plucked (Bennett and Glasser, 2009; Benn and Evans, 2010). This bedforms range in size from less than 1 m to several hundreds of meters across (Benn and Evans, 2010).

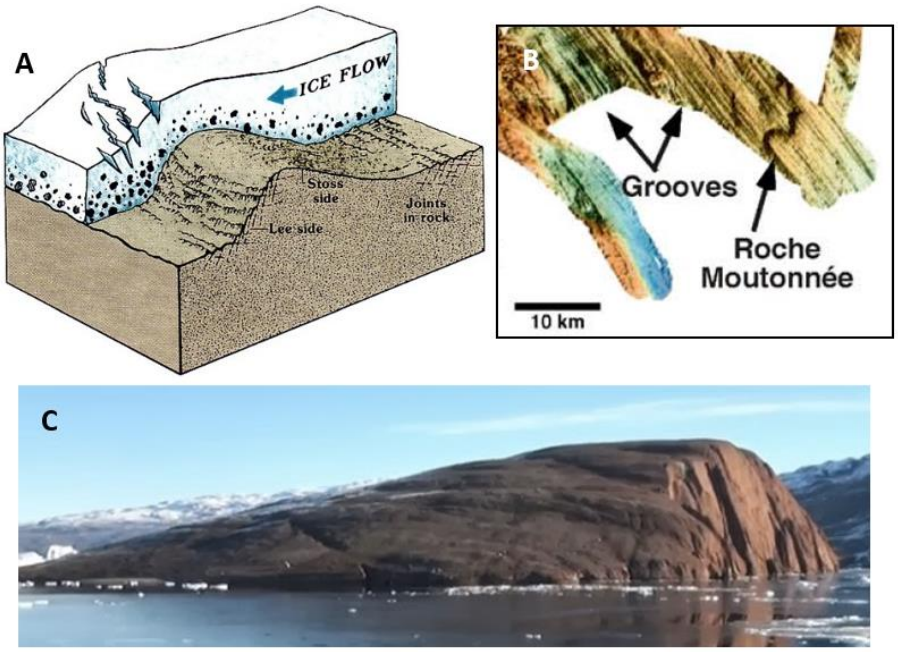

Figure 2.28. Formation process of a roche moutonnée (**A**) and examples from the seafloor (from Wellner et al., 2006) (**B**) (from http://people.uwec.edu/jolhm/Superior2007/TeamC/rouche.html) and visible on land (C) (from http://brian-mountainman.blogspot.pt/2013/11/another-roche-moutonnee.html.

iv) Whalebacks

The whalebacks are bedrock elevations that have been smoothed and rounded on all sides by a glacier (Fig. 2.29). They are approximately symmetrical, with peculiar forms that reminds the back of whales breaking the ocean surface (Bennett and Glasser, 2009; Benn and Evans, 2010).In some punctual cases whalebacks may be slightly elongated in the direction of the ice flow, although the structural attributes of the bedrock (e.g., joints, bedding planes and foliations) constitute an important factor that can affect the morphology of their overall shape. Whalebacks tend to have low height to length ratios (Benn and Evans, 2010).

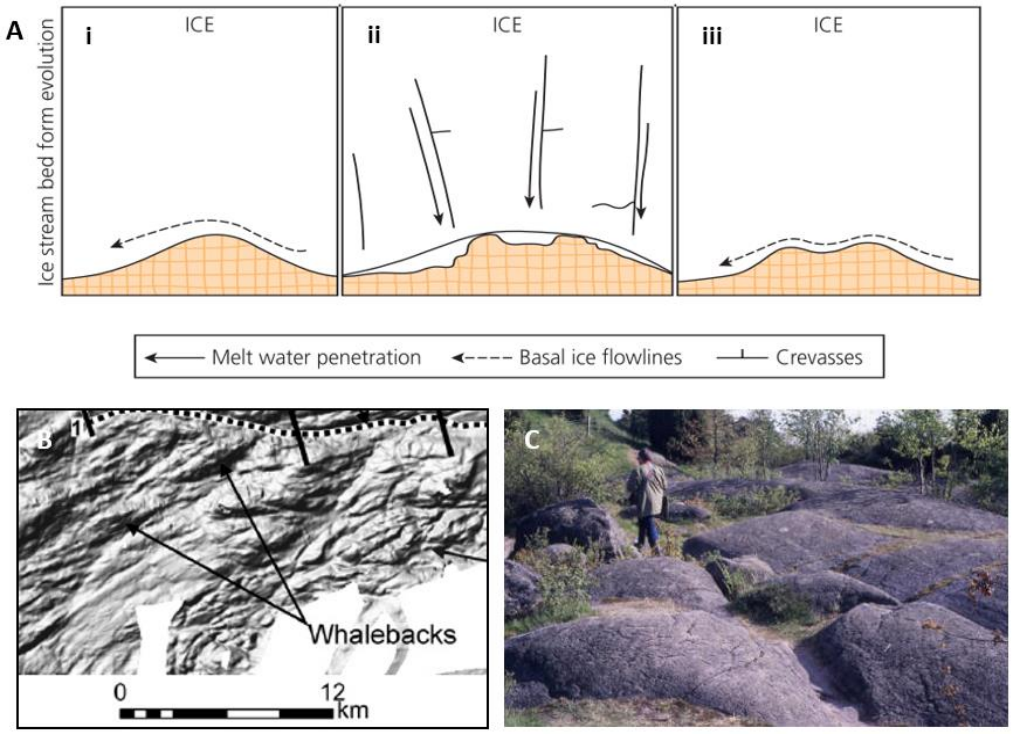

Figure 2.29. Model for the development of whalebacks and roches moutonnées based on erosional bedform distribution (from Benn and Evans, 2010) (**A**), and examples of whaleback forms on the seafloor (**B**) (from Graham et al., 2009) and on land in SW Sweden (**C**) (Source: http://www.landforms.eu/cairngorms/whaleback.htm).

v) Grooves

The grooves are morphological features generally found on bedrock and similar to striations: the grooves have greater size and depths, and are parallel to the ice flow direction (Fig. 2.30) (Bennett and Glasser, 2009; Benn and Evans, 2010). They are probably associated to the glacial abrasion, although the presence of meltwater can be also important. The location and orientation of individual grooves are influenced by structural weaknesses within the bedrock (Bennett and Glasser, 2009).

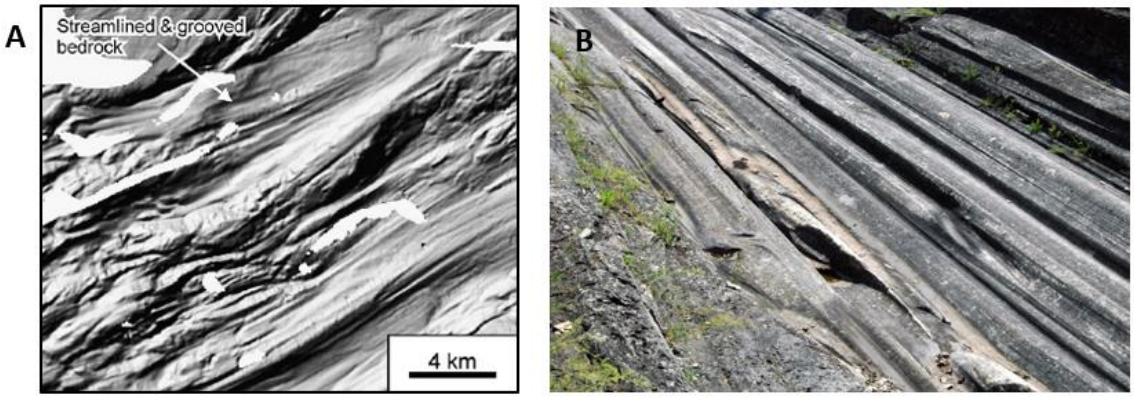

Figure 2.30. Examples of grooves on the seafloor (**A**) (image from Graham et al., 2009) and on land (**B**) source: https://en.wikipedia.org/wiki/Kelleys_Island,_Ohio).

vi) P-Forms

The P-forms or plastically molded forms are assembly of smoothed forms sculpted in the bedrock. They are formed by sinuous depressions and large grooves, giving impression that they are formed by a plastic medium (Fig. 2.31) (Bennett and Glasser, 2009; Benn and Evans, 2010). The origin of the P-Forms still being discussed, but three main hypotheses are considered: (i) formation by glacial abrasion; (ii) formation due to abrasion by a till slurry; and (iii) formation by meltwater (Bennett and Glasser, 2009).

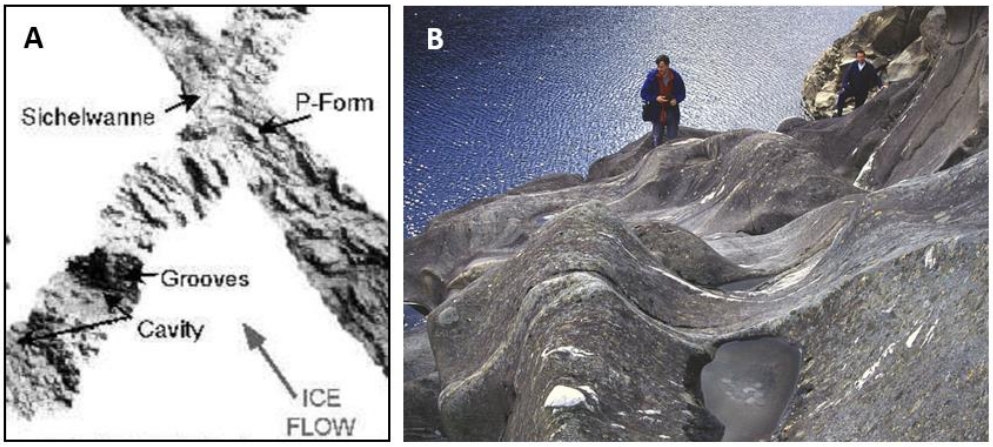

Figure 2.31. Examples of P-Forms on the seafloor (**A**) (image from Lowe and Anderson, 2003) and on land (**B**) (source: http://www.geocaching.com/geocache/GC460Q5_stone-chutes).

vii) Meltwater channels and Tunnel valleys

Meltwater has an important role in many glacial processes. It can act as an agent of erosion or/and transport, and even enhance ice movement acting as lubricator (Eyles, 2006). Meltwaters are derived from direct ice melting on the surface (function of solar radiation) or within/beneath a glacier (from geothermal heat; friction during ice flow) (Bennett and Glasser, 2009). The meltwater channels and tunnel valleys are the main features formed with prevailing action of meltwater.

The meltwater channels can be subglacial (beneath the ice), englacial (within the ice), supraglacial (ice surface), or in proglacial locations (in front of the ice) (Fig. 2.32) (Bennett and Glasser, 2009). The subglacial channels are found on the seafloor of the Antarctic inner continental shelf. Their orientation and size are defined by the hydraulic potential gradient beneath the ice, which is determined by glacier surface slope and by the subjacent topography (Bennett and Glasser, 2009).

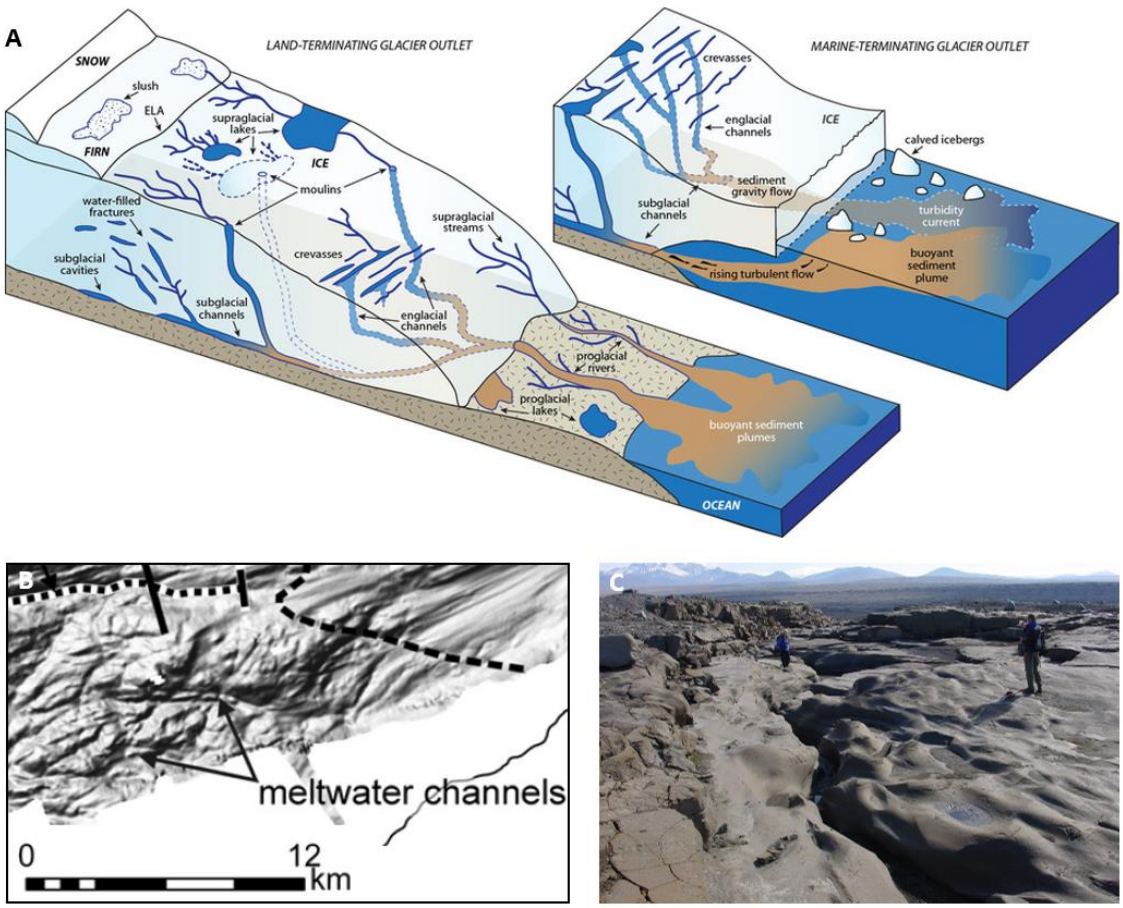

Figure 2.32. Ice sheet hydrologic systems for land-terminating and marine-terminating glacier outlets (**A**) (Source: http://www.venachu.com/research.html) and examples of meltwater channels on the seafloor (**B**) (Graham et al., 2009) and on land (**C**) (https://notendur.hi.is/oi/glacial_geology_photos.htm).

The tunnel valleys are elongate incisions into bedrock or unconsolidated sediment with overdeepened areas along their floors (Fig. 2.33) (Ó Cofaigh, 1996; Bennett and Glasser, 2009; Van Der Vegt, 2012). They are formed through erosional processes related to subglacial meltwater flow during multiple subglacial meltwater discharge events, or modified by constant and steady-state meltwater erosion over successive glacial phases (Ó Cofaigh, 1996; Graham et al., 2009). Tunnel valleys are frequently sinuous in plan view, normally with an intermediate u-to-v-shaped cross-profile and abrupt initiation and termination points (Graham et al., 2009). Also, they may occur in anastomosing networks (Ó Cofaigh, 1996; Bennett and Glasser, 2009).

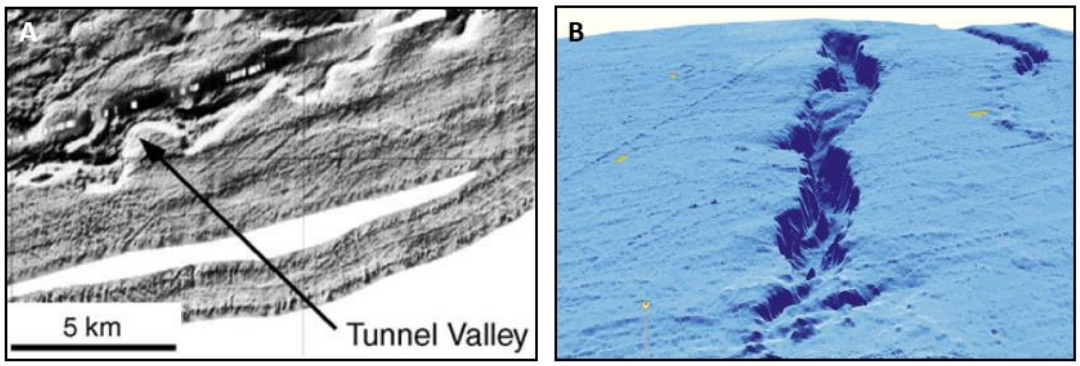

Figure 2.33. Examples of tunnel valleys on the seafloor, plan view (**A,** from Wellner et al., 2006) and oblique view (**B**, from Bradwell et al., 2008).

viii) Basins and troughs

The basins are individual depressions generally carved in bedrock (Fig. 2.34). Their development is controlled by the combination of glacial and meltwater erosional action in function of the structural distribution of the bedrock weaknesses, which can be exploited by glacial quarrying and, later, modified by meltwaters (Lowe and Anderson, 2003; Bennett and Glasser, 2009; Nitsche et al., 2013). Quarrying and abrasion processes are particularly effective when the glacier is predominantly wet-based, such as for temperate glaciers or in the base of fast-flowing ice streams. (Benn and Evans, 2010). Generally, the basins act as sediments traps where meters of sediment can be accumulated.

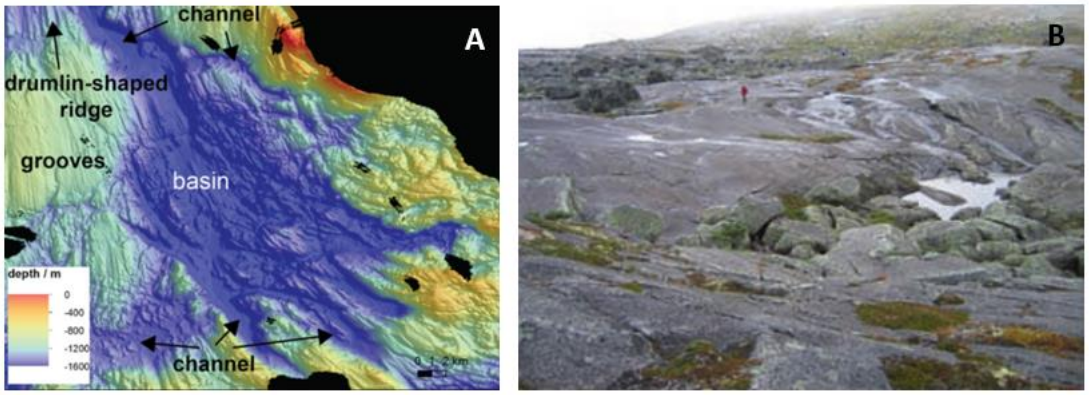

Figure 2.34. Example of basins on the seafloor (**A**, from Nitsche et al., 2013) and on land (**B**, photo from Bennett and Glasser, 2009).

Differently from basins the glacial troughs are deep linear features carved into bedrock resulted from high glacial erosion rates (abrasion and quarrying), where ice flow is confined by topography (Bennett and Glasser, 2009) (Fig. 2.35). The cross-sectional

profiles of glacial troughs show, in the most of the cases U-shaped profiles with steeped sides (Bennett and Glasser, 2009; Benn and Evans, 2010).

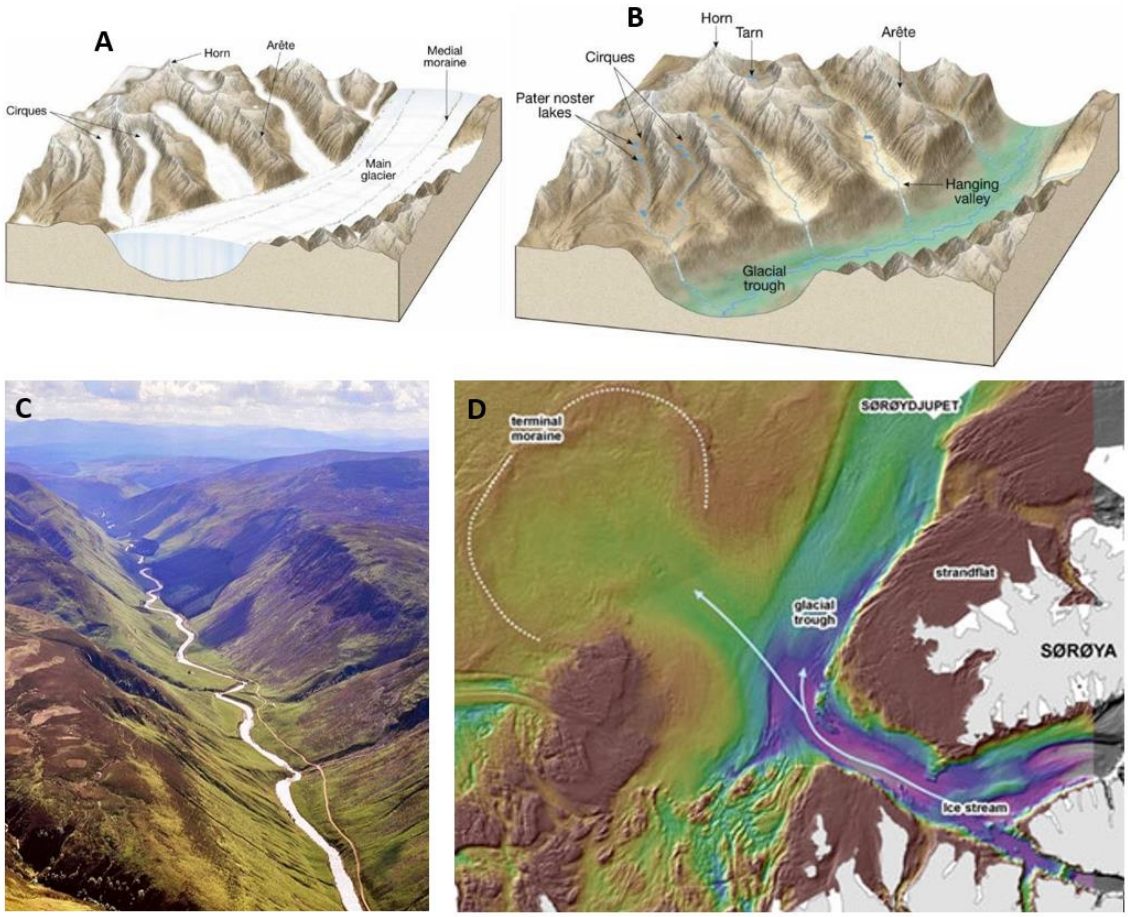

Figure 2.35. Formation process of glacial trough in a region during the glacial maxima (**A**) the and subsequent morphology (**B**), with an example of direct observation, photo of the Gleen Tilt tourgh (**C**) and trough multibeam imagery (**D**). Sources: http://brian-mountainman.blogspot.pt/2014/07/glen-tilt-classic-glacial-trough.html; http://jupiter.plymouth.edu/~sci_ed/Turski/Courses/Earth_Science/Images/10.3glacial.JPG; http://mareano.no/en/news/nyheter_2010/mapping_seabe d_soroya.

2.3.2. Middle continental shelf

The middle continental shelf marks the transition between the rocky inner shelf and sedimentary bed of the outer shelf, exposing slightly more elongated glacial features than the inner region (Graham et al., 2009; Shaw et al., 2008). In the mid shelf it is more frequent to find drumlins, with more elongation ratio; basins, (ix) mega scale glacial lineations (MSGLs) and (x) iceberg plougmarks.

ix) Mega scale glacial lineations (MSGLs)

On the middle shelf, MSGLs replace attenuated drumlins and can persist until the shelf edge (Shaw et al., 2008). They are elongated ridges of sediment produced subglacially and indicative of streaming activity (Fig. 2.36). They are similar to other bedforms parallel to the ice flow, such as drumlins or flutes, but are typically much longer (~10-100 km). MSGLs are the largest flow parallel bedform (Clark, 1993; Stokes et al., 2013).

Like drumlins, the MSGLs are enigmatic bedforms. Several hypotheses/theories were proposed to explain their formation. Among them it can be highlighted the subglacial deformation of till and the attenuation downstream hypothesis (Clark, 1993), and the catastrophic meltwater floods hypothesis (Shaw et al., 2008).

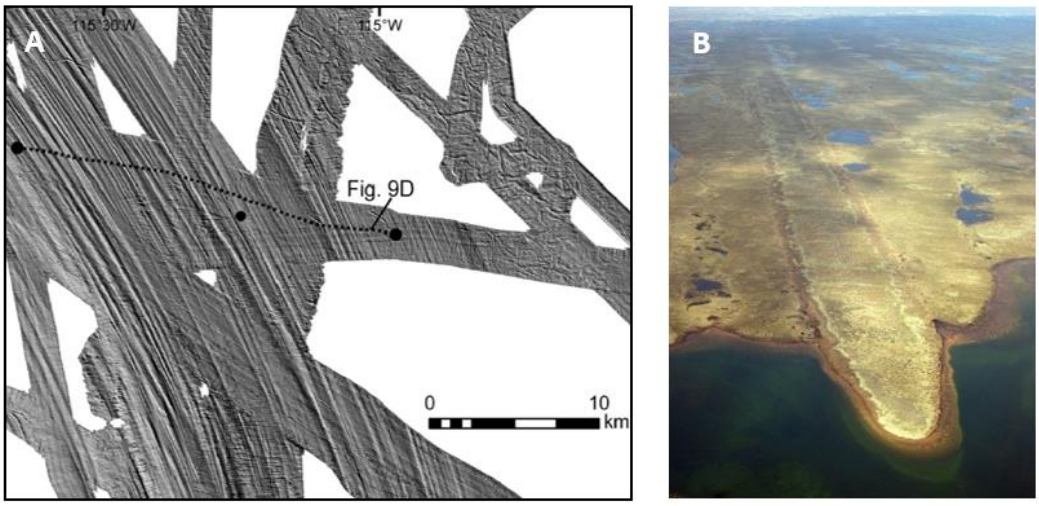

Figure 2.36. Mega scale glacial lineations on the seafloor (**A**, from Graham et al., 2009) and on land (**B**, Source: https://www.sheffield.ac.uk/drumlins/msgl).

x) Iceberg ploughmarks

The iceberg ploughmarks or Iceberg furrows are linear to curvilinear depressions characterised by casual orientations. Ploughmarks are produced by iceberg drifts while their keel came in contact with non-cohesive deposits at the seabed (Graham et al., 2009) (Fig. 2.37). Their morphology depends upon sedimentological characteristics of the seafloor, iceberg keel geometry, and motion (Bennett and Glasser, 2009). Iceberg ploughmarks on the Antarctic shelf are commonly found at depths between 140 and 500m (until the outer shelf) and become rarer at greater depths. The authors also refer that the finding depths that exceed the value of 500 m are probably indicative of either:

(a) the presence of fast-flowing ice-sheet outlet glaciers; (b) ice shelves fed from major interior basins where lateral spreading is constrained topographically; or (c) a pulse of large icebergs released during major deglaciation or ice-sheet/ice shelf collapse. The ploughmarks give a good approximation of ice thickness at the calving margin, as their formation is clearly dependent of the iceberg size (Benn and Evans, 2010).

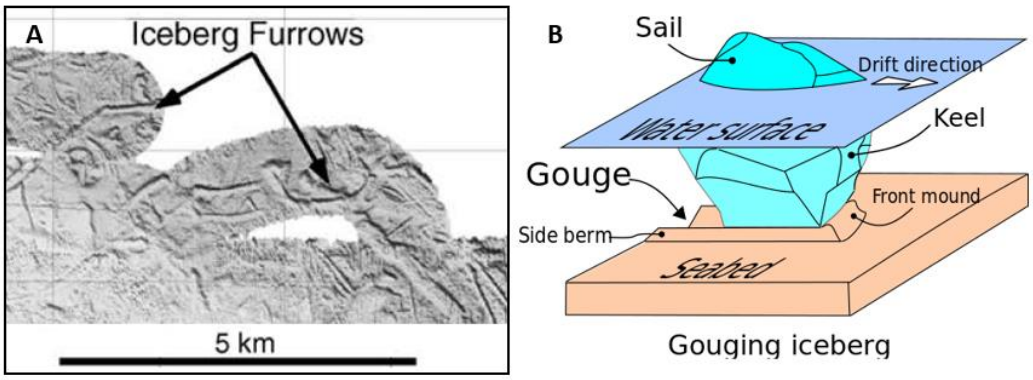

Figure 2.37. Example of Iceberg furrows (gouge) on the seafloor (**A**, from Wellner et al., 2006) and their formation (**B**, from: https://en.wikipedia.org /wiki/Seabed_gouging_ by_ice).

2.3.3. Outer continental shelf

The outer shelf area has widespread, highly elongated features in great part of cases associated deposition and/or molding of sediments (Wellner et al., 2006). The predominant features are mainly: MSGLs, iceberg furrows and (xi) submarine gullies.

xi) Submarine gullies

The gullies are incisions, in order of tens of meters depth, formed on the continental edge/slope generally related to the erosion of non-cohesive deposits by subglacial meltwater from ice margin grounded at the shelf break (Fig. 2.38) (e.g. Noormets et al, 2009; Wellner et al., 2006; Gales et al., 2013a). On the Antarctic continental shelf edge, gullies are the most common morphological features (Gales et al., 2013a). The gullies morphology are mainly influenced by environmental controls such as the local slope character (i.e., slope gradient and geometry), large-scale parameters (i.e., ice drainage basin size, location of cross-shelf troughs, regional heat flow), ice sheet history and sediment yield (Gales et al., 2013b).

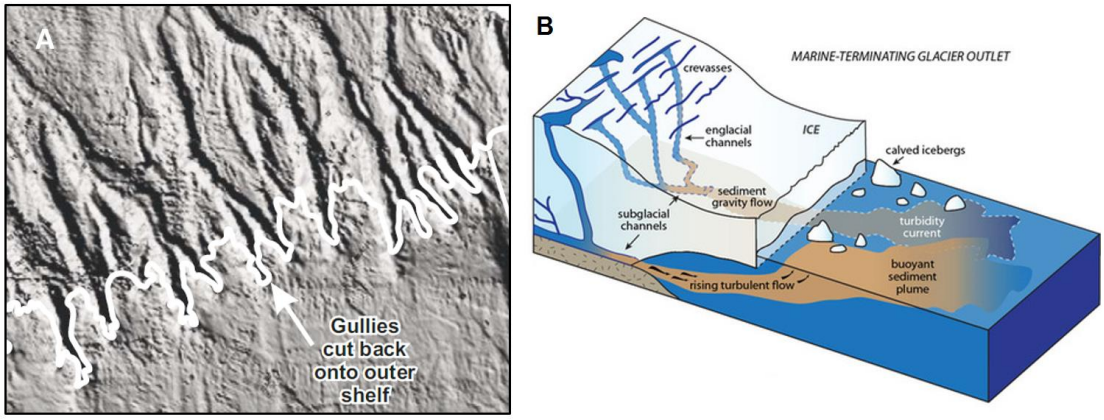

Figure 2.38. Gullies on the seafloor (**A**, from Dowdeswell et al., 2006) and diagram of marine-terminating glacier showing gullies formation (**B**, adapted from: *https://notendur.hi.is/oi/glacial_geology_photos.htm*).

2.3.4. Ice-marginal depocentres and other landforms

The terminating zones of ice sheets or glaciers are considered a location where sediment is transferred from the ice to an external environment forming a sedimentary depocentre.

The grounding zones are a typical terminating zone associated to marine environments where grounded ice ceases to be in contact with the underlying substrate. According to Batchelor and Dowdeswell (2015), a grounding zone is the limit between the grounded ice and the floating ice of marine-terminating glaciers (Fig. 2.39).

At the grounding zone during still-stands of the ice margin, different features can be generated including (xii) grounding-zone wedges (GZWs), (xiii) moraine ridges and (xiv) ice-proximal fans. Bedforms that present several morphological and stratigraphical similarities, especially between GZWs and submarine moraines (Batchelor and Dowdeswell, 2015).

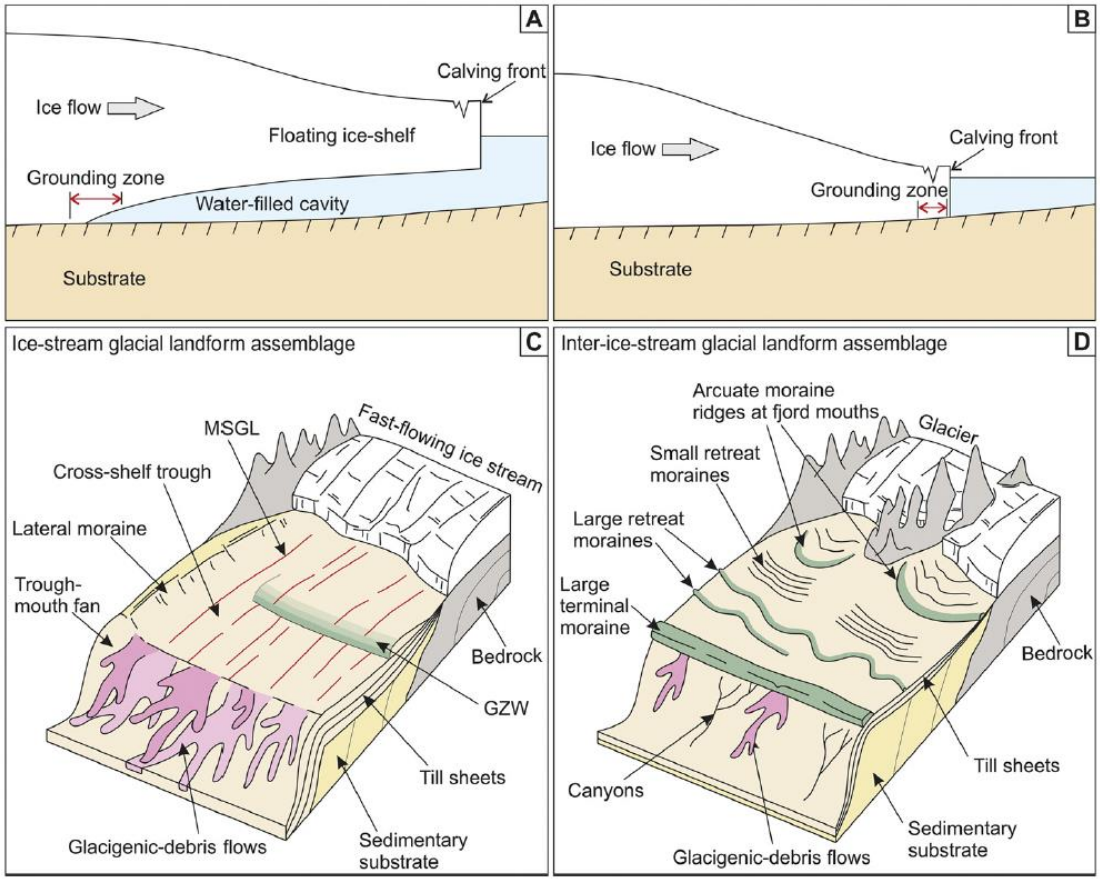

Figure 2.39. Schematic diagram with the position of the grounding zone at the margin of an ice sheet/glacier with a floating ice shelf (**A**) and at a tidewater ice-sheet margin (**B**). Typical ice-stream landforms assemblage produced by fast (**C**) and slow (**D**) ice-stream flow on a continental shelf. Image from Batchelor and Dowdeswell (2015).

xii) Grounding zone wedges (GZWs)

GZWs are asymmetric sedimentary depocentres formed by the rapid accumulation of glacigenic debris, subglacial sediments together with sediment remobilization from gravity flows, along a line source at a grounding zone. The size of the GZWs is controlled by the flux of sediment to the grounding zone, the shape of the sub-ice cavity (Fig. 2.40), the width of the palaeo-ice stream, and the duration of the still-stand. Typical high-latitude GZWs are less than 15 km in along-flow direction and 15 to 100 m thick (Batchelor and Dowdeswell, 2015).

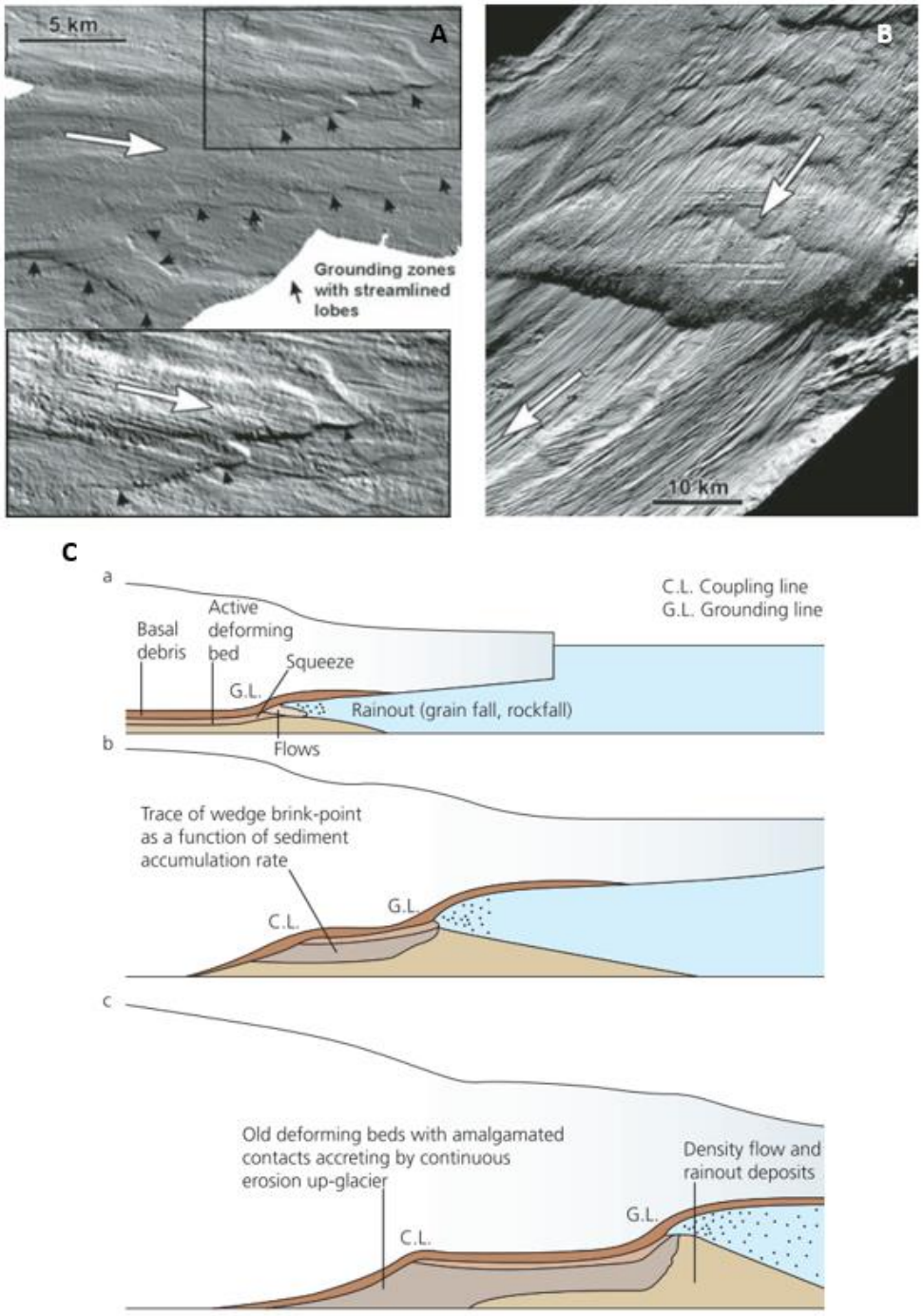

Figure 2.40. Grounding zone wedges (GZWs) from Larsen A Ice Shelf, AP (**A**) and GZWs from Vestfjorden, north Norway (**B**). The white arrows show the direction of the former ice flow. (Adapted from Dowdeswell et al., 2008). **C** - Depositional model explaining the formation of the grounding-line wedges (from Benn and Evans, 2010).

xiii) Moraines

The moraines are sedimentary ridges with a great variation in sizes and shapes, occurring with linear or sinuous crest lines (Anderson, 1999; Benn and Evans, 2010). The transverse moraines are associated to grounding zones (Fig. 2.41) and are

categorized into large terminal and recessional moraine ridges, hummocky-terrain belts and small retreat moraines (Batchelor and Dowdeswell, 2015). They are formed by a combination of processes, including meltwater deposition, melt-out of basal and glacial debris, squeeze-push processes from under the ice, lodgement and sediment deformation.

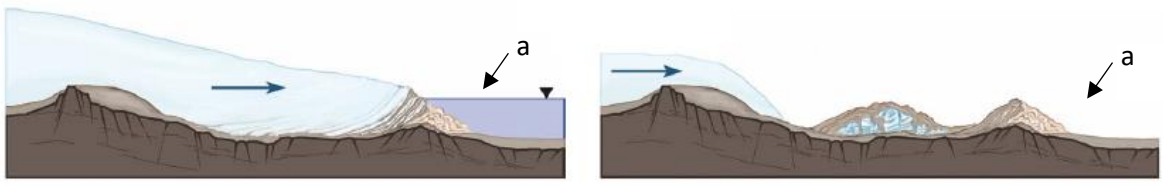

Figure 2.41. Schematic diagram showing a case of a transverse moraine formation (a). Image adapted from: https://www.geocaching .com/geocache/GC5MWT9_mor-y03-005-utterinvuori-hauho.

- The large terminal and recessional moraine ridges are typically several tens of meters thick and less than 2 km. These moraines have similar thicknesses than GZWs: they have clear positive relief and lower length-to-height ratios (typically less than 10:1). Unlike GZWs, moraine ridges are not constrained by the roof of a sub-ice shelf cavity and are probably formed mainly at tidewater ice cliffs (Fig. 2.42) (Batchelor and Dowdeswell, 2015).

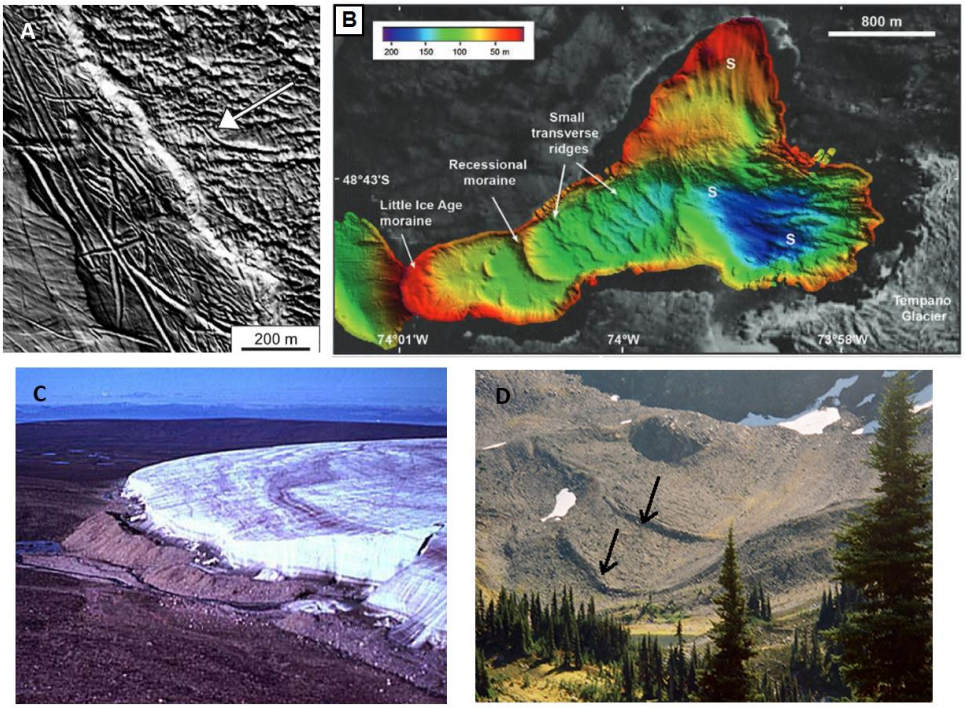

Figure 2.42. Case of large terminal and recessional moraine ridges found trough multibeam images (A and B respectively) and through direct observations (C and D). Sources: Batchelor and Dowdeswell, 2015; Dowdeswell et al., 2014 and http://www.mleziva.info/unit5/U05L01.htm.

- The submarine hummocky-terrain belts are characterised by irregular assortments of ridges and depressions (Fig. 2.43), and are formed by uneven sediment deposition and redistribution close to the ice margin. Hummocky moraine can be formed by a variety of processes, including sediment lodgement and deformation (Batchelor and Dowdeswell, 2015).

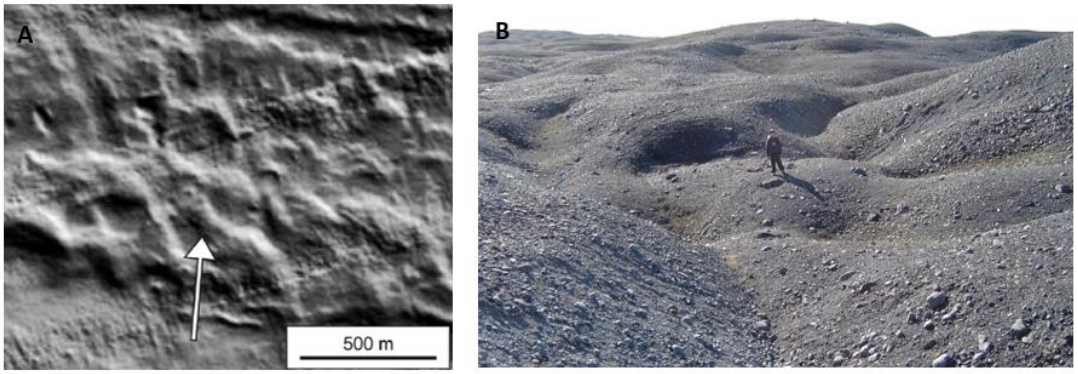

Figure 2.43. Hummocky moraines observed on the seafloor (**A**) (from Batchelor and Dowdeswell, 2015) and on land (**B**) (Photo: Ó. Ingólfsson, 2004. in https://notendur.hi.is/oi/bruarjokull_project.htm).

- The small retreat moraines generally have few meters of height (Fig. 2.44). They are referred frequently as the De Geer moraines and occur often as closely spaced ridges, formed by the delivery of sediment to the grounding zone during minor ice-margin still-stands or oscillations during an overall retreat of a grounded ice. These sedimentary ridges are typically less than 15 m thick and less than 300 m wide (Benn and Evans, 2010; Batchelor and Dowdeswell, 2015).

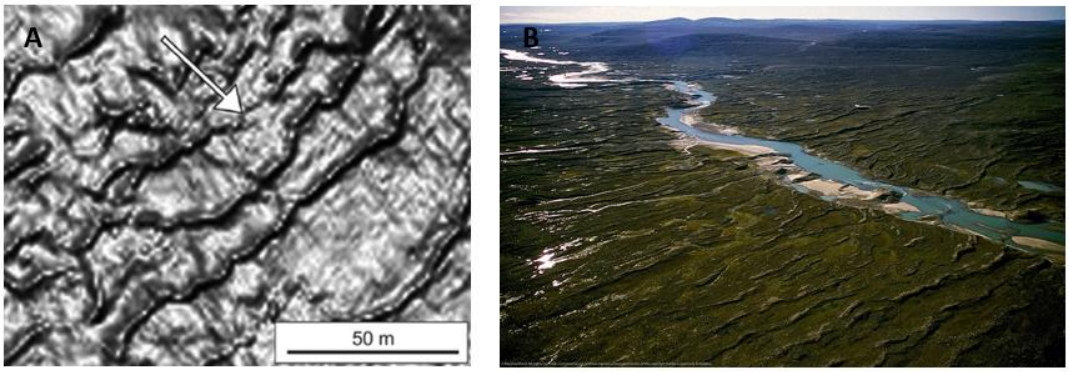

Figure 2.44. Small retreat moraines (or De Geer moraines) on the seafloor (**A**) and on land, Baffin Island (Canada) (**B**). Sources: Batchelor and Dowdeswell, 2015; http://brian-mountainman.blogspot.pt/2015_04_01_archive.html.

From successive moraines (such GZWs and recessional moraines), it is possible to infer the rate of the ice-sheet retreat across the polar continental shelves and possible ice-stream collapse. Their presence gives important information either on the maximum extent of the grounded ice or on the recessional positions during deglaciation. The different response on ice-sheets and grounding line retreat can be triggered by external (atmospheric and oceanic) forcing events and associated to ice recession rates (Dowdeswell et al., 2008; Livingstone et al., 2012) In general, the deglaciation of the marine-based ice sheets at the end of the last glacial period occurred in three main ways: (1) rapidly, by flotation and break-up, (2) episodically, by stillstands and/or grounding events punctuating rapid retreat, and (3) slow retreat of grounded ice (Dowdeswell et al., 2008; Benn and Evans, 2010; Livingstone et al., 2012) (Fig.2.45).

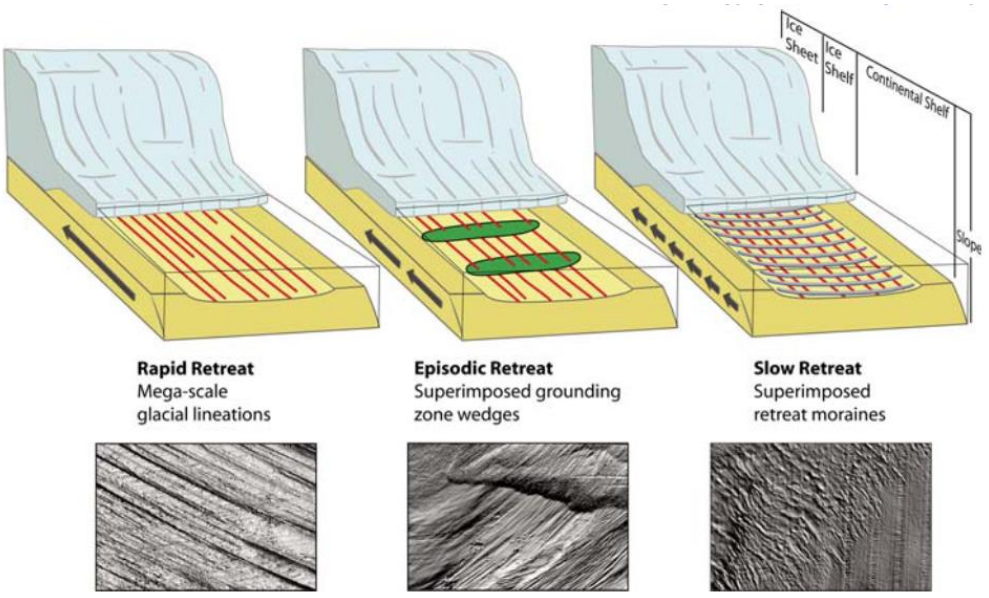

Figure 2.45. Different landsystem models with examples of swath-bathymetric data, showing different recession rates (from Dowdeswell et al., 2008).

xiv) Ice-proximal fans

The ice-proximal fans (or ice-contact fans) are sedimentary deposits build up at efflux points of subglacial meltwater conduits located at the grounding zone of a marine-terminating ice mass (Benn and Evans, 2010; Batchelor and Dowdeswell, 2015). These landforms are composed of a variety of sediments, including subaquatic outwash, gravity flow sediments and suspension settling deposits (Fig. 2.46). The ice-proximal fan-shaped geometry is indicative of the point-source deposition (Batchelor and Dowdeswell, 2015).

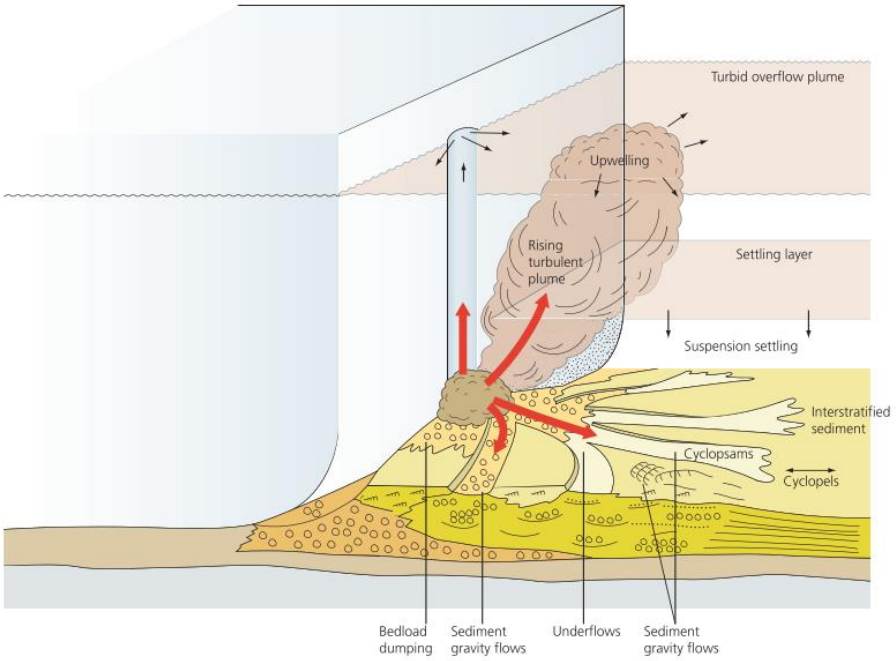

Figure 2.46. Processes of sediment transport and deposition that constitute a marine grounding-line fan (from Benn and Evans, 2010).

2.4. Continental slope and rise bedforms and processes

Continental slopes around Antarctica are constructed largely of prograded sedimentary sequences, deposited during a series of glacial cycles (Fig. 2.47) (e.g. Anderson, 1999; Barker et al., 1999; Gales, 2013). Slope gradient and morphology vary along the continental margin, but has a steep character that can reach 17º (Gales, 2013).

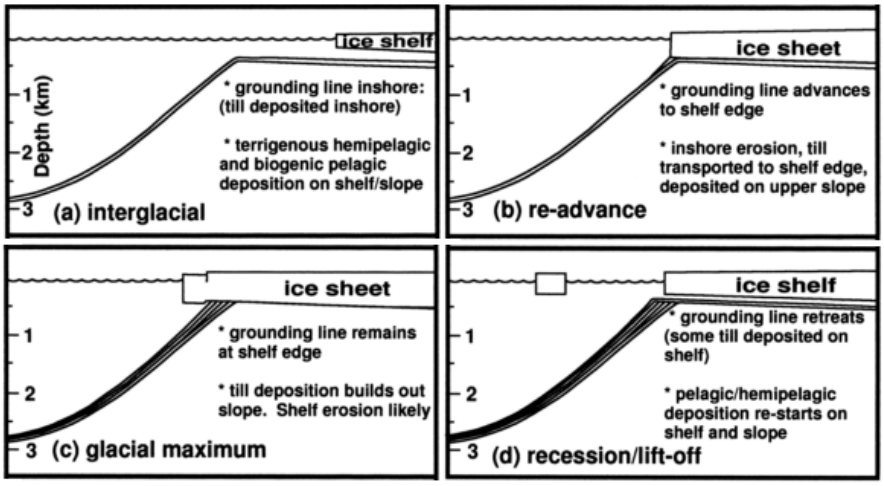

Figure 2.47. Sequence model of deposition on shelf and slope through a glacial cycle (from Barker et al., 1999).

The Antarctic continental margin contains features, such as iceberg scours or keel marks, gullies, (xv) mass-wasting bedforms (slides, slumps), (xvi) canyon-channel systems, and (xvii) sediment mounds (e.g. Cofaigh et al., 2003; Gales, 2013).

xv) Mass-wasting bedforms

Mass-wasting or mass movement is a geomorphic process in which unconsolidated materials (sediments) move downslope, typically such a mass, mainly under the influence of gravity (e.g. Fig. 2.48). On continental slopes, mass-wasting bedforms include sediment slides, slumps, debris flows and turbidity currents (Monroe and Wicander, 2006; Gales, 2013; Gales et al., 2013b).

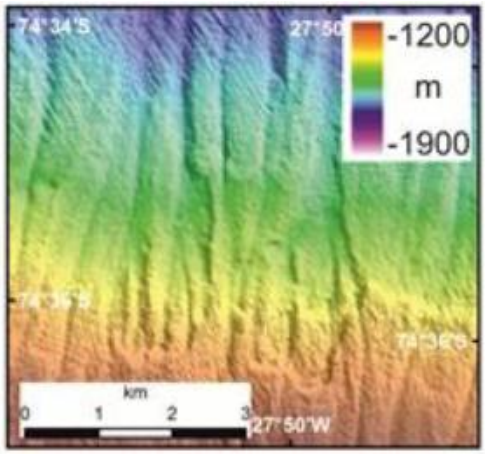

Figure 2.48. Multibeam image showing evidences of small-scale mass wasting, where it is possible to recognize several characteristics such steep headwalls, and absence of well-defined gullies (from Gales, 2013).

There is a great variety of mechanisms that can trigger the development of such features, as the presence of gas hydrate dissociation, sediments in resuspension by shelf and contour currents, subglacial meltwater discharge, tectonic disturbances, iceberg scouring or rapid accumulations of glacigenic debris at the shelf edge during glacial maxima (Fig. 2.49) (Gales, 2013; Gales et al., 2013b).

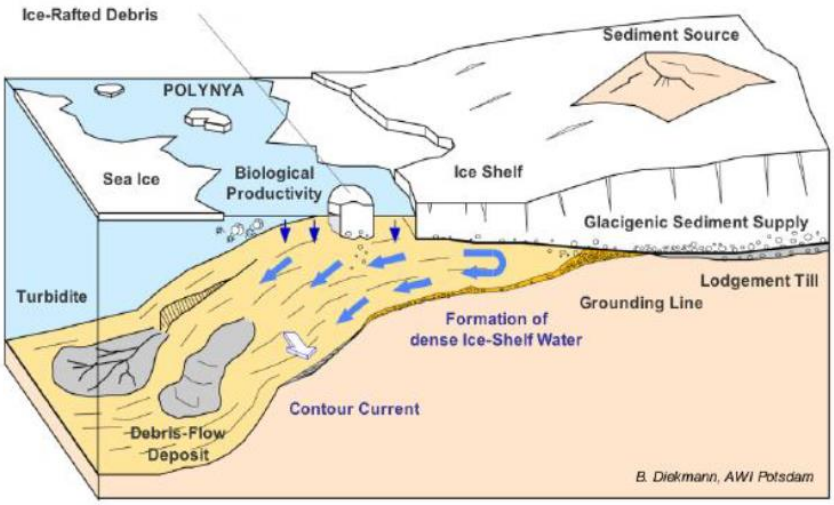

Figure 2.49. Schematic diagram with main processes which control morphology in Antarctic submarine slopes. Image taken from Gales, 2013.

xvi) Canyon-Channel systems

Canyon-channels are steep-sided valley and important conduits for the sediment transport to deep marine (abyssal plain) environments. They have dendritic or sinuous morphology, and can show a high number of tributaries (Fig. 2.50). In some cases, levees may be present (Gales, 2013). According to Gales (2013), canyon-channels have been measured on the Antarctic margins with widths of >1 km, depths of tens of metres and lengths of tens of km.

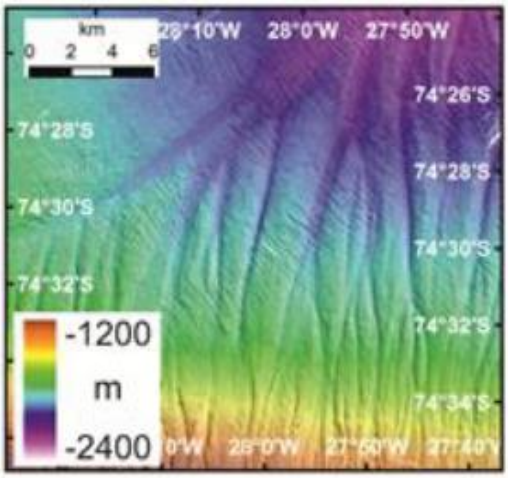

Figure 2.50. Channels observed in a multibeam image (from Gales, 2013).

xvii) Sediment mounds

Several sediment mounds have been founded along Antarctic continental rise. These features are defined by large sediment sequences delivered to the continental rise during glacial cycles (McGinnis et al., 1997). Several of the sediment mounds found have been interpreted as sediment drifts, produced by bottom currents that rework the hemipelagic sediments at the lower regions of the slope (Amblas et al., 2006; Barker et al., 1999) (Fig. 2.51). This body sediments have been found in Antarctica with lengths of 150 km, widths of >50 km and a relief of 1 km in most of the cases (Gales, 2013).

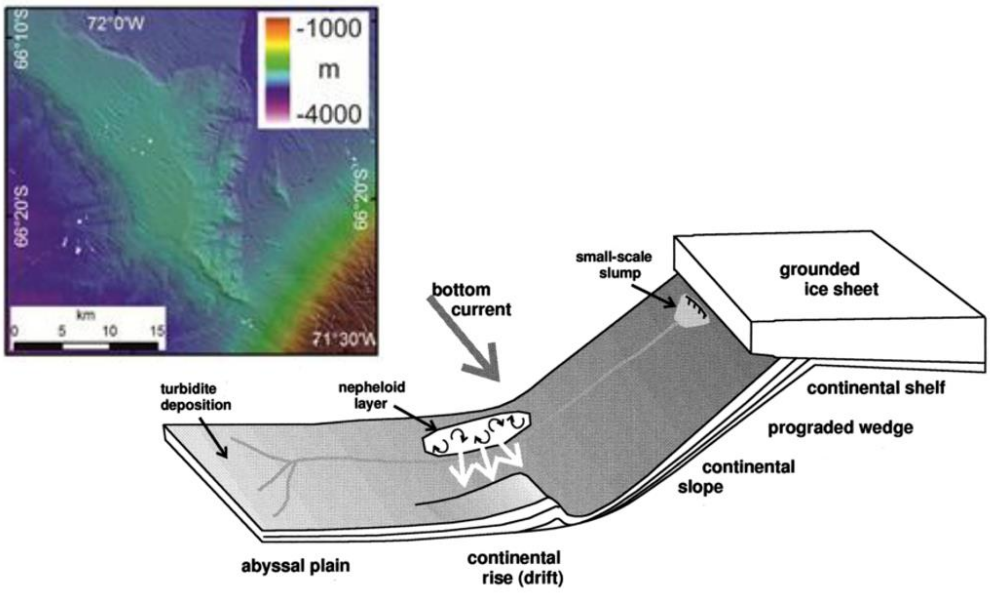

Figure 2.51. A sediment mound/drift observed trough multibeam image (from Gales, 2013) and schematic diagram showing the formation of the sediment drifts (from Barker et al., 1999).

References

Amblas, D., Urgeles, R., Canals, M., Calafat, A. M., Rebesco, M., Camerlenghi, A., ... and Hughes-Clarke, J. E., **2006**. Relationship between continental rise development and palaeo-ice sheet dynamics, Northern Antarctic Peninsula Pacific margin. *Quaternary Science Reviews*, 25(9), 933-944.

Anderson, B. A., Shipp, S. S., Lowe, A. L., Wellner, J. S., Amanda, B. M., **2002**. The Antarctic Ice Sheet during the Last Glacial Maximum and its subsequent retreat history: a review. *Quaternary Science Reviews*, 21, pp 49-70.

Anderson, J.B., **1999**. *Antarctic Marine Geology*, New York: Cambridge University Press.

Bamber, J. L., Riva, R. E. M., Vermeersen, B. L. A. and LeBrocq, A. M., **2009**. Reassessment of the potential sea-level rise from a collapse of the west antarctic ice sheet. *Science* 324 (5929), pp. 901-903.

Barker, P. and Thomas, E., **2006**. Potential of the Scotia Sea Region for determining the onset and development of the Antarctic Circumpolar Current, in Futterer, D.K., D. Damaske, G. Kleinschmidt, H. Miller, D. Tessensohn (eds.), Antarctica: Contributions to Global Earth Sciences, pp. 433–440.

Barker, P. F., Barrett, P. J., Cooper, A. K., Huybrechts, P., **1999**. Antarctic glacial history from numerical models and continental margin sediments. *Palaeogeography Palaeoclimatology Palaeoecology*, 150(3-4), pp.247–267.

Batchelor, C. L., and Dowdeswell, J. A., **2015**. Ice-sheet grounding-zone wedges (GZWs) on high-latitude continental margins. *Marine Geology*, 363, 65-92.

Benn, D.I. and Evans, D.J.A., **2010**. *Glaciers and Glaciations*. London: Hodder Education.

Bennett, R.W. and Glasser, N. F., **2009**. *Glacial Geology*. 2nd Ed. UK: John Wiley and Sons Ltd.

Bentley, M. and Hodgson, D., **2009**. Antarctic Ice Sheet and climate history since the last Glacial Maximum. *Pages News*, 17(1), pp.28–29.

Bindschadler, R., **2006**. The environment and evolution of the West Antarctic ice sheet: setting the stage. Philosophical transactions. *Series A, Mathematical, physical, and engineering sciences*, 364(1844), pp.1583–1605.

Boyce, J.I. and Eyles, N., **1991**. Drumlins carved by deforming till streams below the Laurentide ice sheet. *Geology*, 19, pp. 787–90.

Bradwell, T., Stoker, M. S., Golledge, N. R., Wilson, C. K., Merritt, J. W., Long, D., ... and Mathers, H. E., **2008**. The northern sector of the last British Ice Sheet: maximum extent and demise. *Earth-Science Reviews*, 88(3), pp. 207-226.

Clark, C. D., **1993**. Mega-scale glacial lineations and cross-cutting ice-flow landforms. *Earth Surface Processes and Landforms*, 18(1), pp. 1-29.

Clark, C. D., Hughes, A. L., Greenwood, S. L., Spagnolo, M., and Ng, F. S., **2009**. Size and shape characteristics of drumlins, derived from a large sample, and associated scaling laws. *Quaternary Science Reviews*, 28(7), 677-692.

Cofaigh, C. Ó., Taylor, J., Dowdeswell, J. A., and Pudsey, C. J., **2003**. Palaeo-ice streams, trough mouth fans and high-latitude continental slope sedimentation. *Boreas*, 32(1), 37-55.

Cogley, J.G., R. Hock, L.A. Rasmussen, A.A. Arendt, A. Bauder, R.J. Braithwaite, P. Jansson, G. Kaser, M. Möller, L. Nicholson and M. Zemp, **2011**. *Glossary of Glacier Mass Balance and Related Terms*, IHP-VII Technical Documents in Hydrology No. 86, IACS Contribution No. 2, UNESCO-IHP, Paris. pp.114.

Comiso, J.C., Kwok, R., Martin, S. and Gordon, A. L., **2011**. Variability and trends in sea ice extent and ice production in the Ross Sea. *Journal of Geophysical Research: Oceans*, 116(4), pp.1–19.

Convey, P., Bindschadler, R., Di Prisco, G., Fahrbach, E., Gutt, J., Hodgson, D. A., Mayewski, Paul Andrew, Summerhayes, C. P., Turner, J., and ACCE Consortium, **2009**. Antarctic climate change and the environment. *Antarctic Science*, 21(06), pp.541.

Cook, A. J., Fox, A. J., Vaughan, D.G. and Ferrigno, J.G., **2005**. Retreating glacier fronts on the Antarctic Peninsula over the past half-century. *Science* (New York, N.Y.), 308(5721), pp.541–544.

Cuffey, K.M., Paterson, W.S.B., **2010**. *The Physics of Glaciers* (4thed.). Burlington, USA: Elsevier.

Dalziel, I.W.D., **1992**. Antarctica; a tale of two supercontinents?. *Annu. Rev. Earth Planet, Sci.*, 20, pp. 501-26.

Davis, C. H., Li, Y., McConnell, J. R., Frey, M. M., and Hanna, E., **2005**. Snowfall-driven growth in East Antarctic ice sheet mitigates recent sea-level rise. *Science*, 308(5730), pp. 1898-1901.

Dinniman, M.S., J.M. Klinck, and E.E. Hofmann, **2012.** Sensitivity of Circumpolar Deep Water Transport and Ice Shelf Basal Melt along the West Antarctic Peninsula to Changes in the Winds*. Journal of Climate*, 25(14), pp. 4799-4816.

Doake, C.S.M., **2001**. Ice-Shelf Stability. *British Antartic Survey*, 1282-1290.

Dowdeswell, J. A., and **Bamber**, J. L., **2007**. Keel depths of modern Antarctic icebergs and implications for sea-floor scouring in the geological record. *Marine Geology*, 243(1), pp. 120-131.

Dowdeswell, J. A., Ottesen, D., Evans, J., Cofaigh, C. Ó., and Anderson, J. B., **2008**. Submarine glacial landforms and rates of ice-stream collapse. *Geology*, 36(10), 819-822.

Dowdeswell, J., Dowdeswell, E., Rodrigo, C., Diaz, J., and Araya, C. Z, **2014**. Assemblage of glacial and related landforms in the fjords of southern Chile.

Eyles, N., **2006**. The role of meltwater in glacial processes. *Sedimentary Geology*, 190(1), pp. 257-268.

Fox, A.J. and **Cooper**, A.P.R., **1994**. Measured properties of the Antarctic Ice Sheet derived from the SCAR Antarctic Digital Database, Pol. Rec., 30(174), 201-206.

Fretwell, P., Pritchard, H. D., Vaughan, D. G., Bamber, J. L., Barrand, N. E., Bell, R., Bianchi, C., …, Zirizzotti, A., **2013**. Bedmap2: Improved ice bed, surface and thickness datasets for Antarctica. *Cryosphere*, 7(1), pp.375–393.

Gales, J. A., **2013**. The geomorphology of Antarctic submarine slopes. (Doctor of Philosophy Thesis), University of Manchester.

Gales, J. A., Forwick, M., Laberg, J. S., Vorren, T. O., Larter, R. D., Graham, A. G. C., Baeten, N.J., Amundsen, H. B., **2013(a)**. Arctic and Antarctic submarine gullies—A comparison of high latitude continental margins. *Geomorphology*, 201, pp. 449-461.

Gales, J. A., Larter, R. D., Mitchell, N. C., and Dowdeswell, J. A., **2013(b)**. Geomorphic signature of Antarctic submarine gullies: implications for continental slope processes. *Marine Geology*, 337, pp. 112-124.

Goodge, J. W., **2007**. Metamorphism in the Ross orogen and its bearing on Gondwana margin tectonics. *Geological Society of America Special Papers*, 419, 185-203.

Graham, A. G., Larter, R. D., Gohl, K., Hillenbrand, C. D., Smith, J. A., and Kuhn, G., **2009**. Bedform signature of a West Antarctic palaeo-ice stream reveals a multi-temporal record of flow and substrate control. *Quaternary Science Reviews*, 28(25), pp. 2774-2793.

Hanna, E., Navarro, F. J., Pattyn, F., Domingues, C. M., Fettweis, X., Ivins, E. R., Nicholls, R. J., Ritz, C., Smith, B., Tulaczyk, S., Whitehouse, P. L. and Zwally, H. J., **2013**. Ice-sheet mass balance and climate change. *Nature*, 498(7452), pp.51–9.

Hart, J. K., **1997**. The relationship between drumlins and other forms of subglacial glaciotectonic deformation. *Quaternary Science Reviews,* 16(1), pp. 93-107.

Hughes, T., **1973**. Is the West Antarctic ice sheet disintegrating?. *Journal of Geophysical Research*, 78(33), 7884-7910.

Ingólfsson, Ó., **2004**. Quaternary glacial and climate history of Antarctica. *Developments in Quaternary Science*, 2(PART C), pp.3–43.

Ingólfsson, O., Hjort, C., Berkham, P.A., Björck, S., Colhoun, E., Goodwin, I.D., Hall, B., Hirakawa, K., Melles, M., Möller, P. and Prentice, M.L., **1998**. Antarctic glacial history since the Last Glacial Maximum: an overview of the record on land. *Antarctic Science* 10, pp. 326-344.

IPCC, **2013**: Annex III: Glossary [Planton, S. (ed.)]. In: Climate Change 2013: The Physical Science Basis. Contribution of Working Group I to the Fifth Assessment Report of the Intergovernmental Panel on Climate Change [Stocker, T.F., D. Qin, G.-K. Plattner, M. Tignor, S.K. Allen, J. Boschung, A. Nauels, Y. Xia, V. Bex and P.M. Midgley (eds.)]. Cambridge University Press, Cambridge, United Kingdom and New York, NY, USA.

Jacobs, S.S., Jenkins, A., Giulivi, C. F. and Dutrieux, P., **2011**. Stronger ocean circulation and increased melting under Pine Island Glacier ice shelf. *Nature Geoscience*, 4(8), pp. 519-523.

Katz, R. F., and **Worster**, M. G., **2010**. Stability of ice-sheet grounding lines. *Proceedings of the Royal Society A: Mathematical, Physical and Engineering Science* 466 (2118):1597-1620.

King, J. C., and Turner, J., **2007**. Antarctic meteorology and climatology. Cambridge University Press.

Lawrence, J.F., Driscoll, N. W., Raymond, C. and van Wijk, J. W., **2007**. Tectonic implications for uplift of the Transantarctic Mountains. *Open-File Report - U. S. Geological Survey*, (1986), p. 1-4, Extended Abstract 016.

Livingstone, S. J., Cofaigh, C. Ó., Stokes, C. R., Hillenbrand, C. D., Vieli, A., and Jamieson, S. S., **2012**. Antarctic palaeo-ice streams. *Earth-Science Reviews*, 111(1), 90-128.

Lowe, A. L., and **Anderson**, J. B., **2003**. Evidence for abundant subglacial meltwater beneath the paleo-ice sheet in Pine Island Bay, Antarctica. **Journal of Glaciology**, 49(164), pp. 125-138.

Lowe, A. L., and **Anderson**, J. B., **2002**. Reconstruction of the West Antarctic ice sheet in Pine Island Bay during the Last Glacial Maximum and its subsequent retreat history. *Quaternary Science Reviews*, 21(16), pp. 1879-1897.

Lythe, M.B., Vaughan, D.G., the, B.C., **2001**. BEDMAP: a new ice thickness and sub- glacial topographic model of Antarctica. *J. Geophys. Res*., 106, pp. 11335-11351.

Manson, R., Richard, C., Morgan, P. and King, M., **2000**. Ice velocities of the Lambert Glacier from static GPS observations. *Earth Planets Space*, 52, pp.1031–1036.

McGinnis, J. P., Hayes, D. E., and Driscoll, N. W., **1997**. Sedimentary processes across the continental rise of the southern Antarctic Peninsula. Marine Geology, 141(1), 91-109.

Meert, J. G., and Van Der Voo, R., **1997**. The assembly of Gondwana 800-550 Ma. *Journal of Geodynamics*, 23(3), 223-235.

Mengel, M. and **Levermann**, A., **2014**. Ice plug prevents irreversible discharge from East Antarctica. *Nature Climate Change*, pp.451–455.

Miles, B. W. J., Stokes, C. R., Vieli, A., and Cox, N. J., **2013**. Rapid, climate-driven changes in outlet glaciers on the Pacific coast of East Antarctica. *Nature*, 500(7464), pp. 563-566.

Monroe, J. S., and **Wicander**, R., **2006**. *The changing earth: Exploring geology and evolution*. 4nd Ed. Pacific Grove, CA: Brooks/Cole.

Moore, J. K., Abbott, M. R., Richman, J. G., **1999**. Location and dynamics of the Antarctic Polar Front from satellite sea surface temperature data. *Journal of Geophysical Research*, 104 (C2), pp. 3059-3073.

National Research Council (of National Academies), **2011**. Future Science Opportunities in Antarctica and the Southern Ocean, Washington, D.C.: The national Academies Press.

Nitsche, F. O., Gohl, K., Larter, R. D., Hillenbrand, C. D., Kuhn, G., Smith, J. A., Jacobs, S., Anderson, J. B., and Jakobsson, M., **2013**. Paleo ice flow and subglacial meltwater dynamics in Pine Island Bay, West Antarctica. *The Cryosphere*, 7(1), pp. 249-262.

Noormets, R., Dowdeswell, J. A., Larter, R. D., Cofaigh, C. Ó., and Evans, J., **2009**. Morphology of the upper continental slope in the Bellingshausen and Amundsen Seas–Implications for sedimentary processes at the shelf edge of West Antarctica. Marine Geology, 258(1), pp. 100-114.

Ó Cofaigh, C., **1996**. Tunnel valley genesis. Progress in Physical Geography 20, 1–19.

Ó Cofaigh, C., **2012**. Ice sheets viewed from the ocean: the contribution of marine science to understanding modern and past ice sheets. *The Royal Society*, 370, pp. 5512–5539.

Petit, J. R., Jouzel, J., Raynaud, D., Barkov, N. I., Barnola, J.-M., Basile, I., Bender, M., Chappellaz, J., Davisk, M., Delaygue G., Delmotte, M., Kotlyakov, V.M., Legrand, M., Lipenkov, V. Y., Lorius, C., Pe´ pin, L., Ritz, C., Saltzmank, E. and Stievenard, M., **1999**. Climate and atmospheric history of the past 420,000 years from the Vostok ice core, Antarctica. *Nature*, 399, pp.429–413.

Pickard, G.L., and **Emery**, W.J., **1982**. *Descriptive Physical Oceanography: An Introduction.* Fourth Enlarged ed. Oxford: Pergamon Press.

Pisarevsky, S. A., Wingate, M. T., Powell, C. M., Johnson, S., and Evans, D. A. **2003**. Models of Rodinia assembly and fragmentation. *Geological Society, London, Special Publications*, *206*(1), 35-55.

Pollard, D., and **DeConto**, R. M., **2009**. Modelling West Antarctic ice sheet growth and collapse through the past five million years. *Nature*, 458(7236), 329-332.

Pritchard, H. D., Ligtenberg, S. R. M., Fricker, H. A., Vaughan, D. G., Van den Broeke, M. R., and Padman, L., **2012**. Antarctic ice-sheet loss driven by basal melting of ice shelves. *Nature*, 484(7395), pp. 502-505.

Rignot, E., **2006**. Changes in ice dynamics and mass balance of the Antarctic ice sheet. *Philosophical Transactions of the Royal Society of London A: Mathematical, Physical and Engineering Sciences*, 364(1844), pp. 1637-1655.

Rignot, E., Bamber, J. L., Van Den Broeke, M. R., Davis, C., Li, Y., Van De Berg, W. J., and Van Meijgaard, E., **2008**. Recent Antarctic ice mass loss from radar interferometry and regional climate modelling. *Nature Geoscience*, 1(2), pp. 106-110.

Rignot, E., Jacobs, S., Mouginot, J. and Scheuchl, B., **2013**. Ice-shelf melting around Antarctica. Science, 341(6143), pp.266–70.

Rignot, E., Mouginot, J., and Scheuchl, B., **2011**. Ice flow of the Antarctic ice sheet. *Science*, 333(6048), pp. 1427-1430.

Rintoul, S.R., Hughes, C., Olbers, D., **2001**. The Antarctic circumpolar system. In: Siedler G, Church J, Gould J, eds. Ocean circulation and climate. London: Academic Press, pp. 271–302.

Satish-Kumar, M., Motoyoshi, Y., Osanai, Y., Hiroi, Y., and Shiraishi K., **2008**. Geodynamic Evolution of East Antarctica: A Key to the East-West Gondwana Connection. **Geological Society of London**.

Scher, H. D., and Martin, E. E., **2006**. Timing and climatic consequences of the opening of Drake Passage. *Science*, 312(5772), 428-430**.**

Shaw, J., **2002**. The meltwater hypothesis for subglacial bedforms. *Quaternary International*, 90(1), pp. 5-22.

Shaw, J., and **Sharpe**, D. R., **1987**. Drumlin formation by subglacial meltwater erosion. *Canadian Journal of Earth Sciences*, 24(11), pp. 2316-2322.

Shaw, J., Pugin, A. and Young, R.R., **2008**. A meltwater origin for Antarctic shelf bedforms with special attention to megalineations. *Geomorphology*, 102(3-4), pp.364–375.

Shepherd, A., Ivins, E. R., Geruo, A., Barletta, V. R., Bentley, M. J., Bettadpur, S., ... and Zwally, H. J., **2012**. A reconciled estimate of ice-sheet mass balance. *Science*, 338(6111), pp. 1183-1189.

Siegert, M. J., Carter, S., Tabacco, I., Popov, S., and Blankenship, D. D., **2005**. A revised inventory of Antarctic subglacial lakes. Antarctic Science, 17(03), 453-460.

Smellie, J. L., **1981**. A complete arc-trench system recognized in Gondwana sequences of the Antarctic Peninsula region. *Geological Magazine*, *118*(02), 139-159.

Stampfli, G. M., Hochard, C., Vérard, C., and Wilhem, C., **2013**. The formation of Pangea. *Tectonophysics*, 593, 1-19.

Stokes, C. R., Spagnolo, M., Clark, C. D., Cofaigh, C. Ó., Lian, O. B., and Dunstone, R. B., **2013**. Formation of mega-scale glacial lineations on the Dubawnt Lake Ice Stream bed: 1. size, shape and spacing from a large remote sensing dataset. *Quaternary Science Reviews*, 77, pp. 190-209.

Stokes, C.R., Spagnolo, M. and Clark, C.D., **2011**. The composition and internal structure of drumlins: Complexity, commonality, and implications for a unifying theory of their formation. *Earth science reviews*, 107 (3-4). pp. 398-422.

ten Brink, U. S., Hackney, R. I., Bannister, S., Stern, T. A., and Makovsky, Y., **1997**. Uplift of the Transantarctic Mountains and the bedrock beneath the East Antarctic ice sheet. *Journal of Geophysical Research: Solid Earth*, 102(B12), pp. 27603-27621.

Torsvik, T.H., Gaina, C. and Redfield, T.F., **2008**. Antarctica and global Paleogeography: From Rodinia, through Gondwanaland and Pangea, to the Birth of the Southern Ocean and the Opening of gateways. *Antarctica: A keystone in a changing world. Proceedings of the 10th International Symposium on Antarctic Earth Sciences*, pp.125–140.

Turner, J., and **Overland**, J., **2009**. Contrasting climate change in the two Polar Regions. *Polar Research*, 28(2), 146-164.

Turner, J., Bindschadler, R., Convey, P., Prisco, G., Fahrbach, E., Gutt, J., Hodgson, D., Mayewski, P., Summerhayes, C., eds., **2009**. *Antarctic Climate Change and the Enviroment*, Cambridge: Victorie Press.

Turner, J., Colwell, S.R., Marshall, Gareth J., Lachlan-Cope, T. a., Carleton, A. M., Jones, P. D., Lagun, V., Reid, P. a. and Iagovkina, S., **2005**. Antarctic climate change during the last 50 years. *International Journal of Climatology*, 25(3), pp.279–294.

Van der Vegt, P., Janszen, A., and Moscariello, A., **2012**. Tunnel valleys: current knowledge and future perspectives. *Geological Society, London, Special Publications*, 368(1), pp. 75-97.

Vaughan, D.G., J.C. Comiso, I. Allison, J. Carrasco, G. Kaser, R. Kwok, P. Mote, T. Murray, F. Paul, J. Ren, E. Rignot, O. Solomina, K. Steffen and T. Zhang, **2013**. Observations: Cryosphere. In: Climate Change 2013: The Physical Science Basis. Contribution of Working Group I to the Fifth Assessment Report of the Intergovernmental Panel on Climate Change [Stocker, T.F., D. Qin, G.-K. Plattner, M. Tignor, S.K. Allen, J. Boschung, A. Nauels, Y. Xia, V. Bex and P.M. Midgley (eds.)]. Cambridge University Press, Cambridge, United Kingdom and New York, NY, USA.

Vorren, T. O., and **Laberg**, J. S., **1997**. Trough mouth fans—palaeoclimate and ice-sheet monitors. Quaternary *Science Reviews*, 16(8), 865-881.

Walton, D. ed., **2013**. *Antarctica: global science from a frozen continent*, New York: Cambridge University press.

Wellner, J. S., Lowe, A. L., Shipp, S. S., and Anderson, J. B., **2001**. Distribution of glacial geomorphic features on the Antarctic continental shelf and correlation with substrate: implications for ice behaviour. Journal of Glaciology, 47(158), pp. 397-411.

Wellner, J.S, Heroy, D.C. and Anderson, J.B., **2006**. The death mask of the Antarctic Ice Sheet: Comparison of glacial geomorphic features across the continental shelf. *Geomorphology* 75, pp. 157-171.

Yang, H., Kulesa, C.A., Walker, C.K., Tothill, N.F.H., Yang, J., Ashley, M.C.B., Cui, X., Feng, L., Lawrence, J.S., Luong-Van, D.M., Storey, J.W.V., Wang, L., Zhou, X., Zhu, Z., **2010**. Exceptional terahertz transparency and stability above Dome A, Antarctica. *PASP,* 122, pp. 490–494.

Zachos, J. C., Breza, J. R. and Wise, S. W., **1992**. Early Oligocene ice-sheet expansion on Antartica: Stable isotope and sedimentological evidence from Kerguelen Plateau, Southern Indian Ocean. Geology, 20, pp. 569-573.

Internet References

Australian Antarctic Division, **2004**. *About Antarctica* [Online]. Available: http://www.antarctica.gov.au/about-antarctica. [Accessed 18 July 2015]

British Antarctic Survey, **2015**. *About Antarctica* [Online]. Available: http://www.antarctica.ac.uk/about_antarctica/index.php. [Accessed 18 July 2015]

Harley, S. L., **2011**. *The Geology of Antarctica.* In S.L. Harley, *Geology* (Vol. IV, Chap. 1&2) [Online]. Available: http://www.eolss.net/sample-chapters/c01/e6-15-07-07.pdf. [Accessed 24 July 2015]

NASA-LIMA (Landsat Image Mosaic Of Antartica)**, 2015.** Fact Sheets [Online]. Available: http://lima.nasa.gov/pdf/A4_context.pdf. [Accessed 13 August 2015]

National Geographic, **2015**. *Education - Antarctica* [Online]. Available: http://education.nationalgeographic.com/encyclopedia/antarctica/. [Accessed 18 July 2015]

Polar History, **2013**. *Antarctica Map Geographic* [Online]. Available: http://www.polarhistory.net/antarctica-map-geographic/. [Accessed 24 July 2015]

CHAPTER 3:
Methods

3.1 Swath bathymetry

Swath sounding is a technique used for measuring water depths, mainly based on the time intervals between transmitted acoustic pulses from the source and their reflection (or echo) from the seafloor. In this project the multibeam echo sounders (MBES) technology was used to collect swath soundings resulting in a bathymetric map from the East Antarctic continental shelf. The acquired data of the seafloor relief allowed to identify important morphological aspects of the studied area. In that way, the MBES was used to accomplish the main objectives of the project: (1) *Detail the seafloor morphology of the East Antarctic continental shelf* and (2) *reconstruct the past ice flow drainages.*

3.1.1 System description and operations

Swath bathymetry data were obtained during the NBP1503 cruise in 2015 on board the U.S. Antarctic Programs' RVIB Nathaniel B. Palmer (NBP) using the Simrad multibeam echosounder EM122, which replaced the EM120 in 2014 (Fig. 3.1). The system works at a main frequency of 12 kHz with the capacity to receive up to 432 individual return (soundings) per swath or 864 soundings per ping (2 swaths per ping) with pointing angles automatically adjusted. It is designed to perform seabed mapping to full ocean depth (range between 20 to 11,000 m) and cover approximately 6 times the water depth. During the expedition, the useable angular coverage was reduced to less than 60° to each side of the ship, due to the ice protector of the transducers, and the system was operated in equidistant mode (beam spacing). This configuration of the system allowed to have a swath covering 1 to 3 times the water depth. Furthermore, a real time compensation for the vessel motions, roll, pitch and heave have been applied to the collected data using the Seatex Seapath 200 motion sensor.

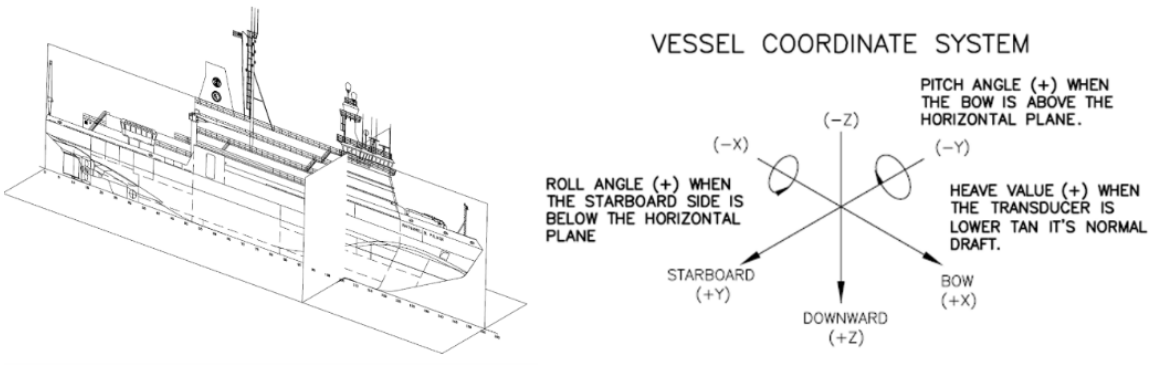

Figure 3.1. NBP primary reference frame established during MBES array installation in 2002. The origin was at the center of the RX array face using axis orientations and sign conventions in agreement with Kongsberg conventions. Image from Johnson and Jerram (2015).

Strong variations of physical parameters (temperature, salinity and density) in the water column influence the acoustic waves propagation (velocity) that may lead to depth errors (observed as 'smiling' or 'frowning' lines when processing the data). In order to get accurate water depths, CTD (conductivity, temperature and depth) and XBT (eXpendable Bathy Thermograph) data were collected and used to originate sound velocity profiles for sound velocity corrections. Throughout the campaign data from15 CTD stations and one XBT station was used to adjust for changes in sound velocity. The conditions directly near the transducers under ship were continuously monitored using a thermosalinograph connected to seawater intake under the ship and directly integrated into the system.

The raw data were recorded digitally and displayed in real-time using the Kongsberg's Seafloor Information System (SIS). During the cruise the acquisition of the data has been continuous, except when scientific stations were performed and during the transits from and to Hobart, Tasmania. Considering the sudy area of this work about 1650 km of multibeam transects have been recorded, corresponding to a total coverage of 33.9 x 10^{09} m^2 and files storage size of ~36 Gigabytes.

3.1.2 Data processing and visualisation

On board additional processing was applied to the raw data using the software package Caris HIPS and SIPS version 8. Figure 3.2 shows the main workflow used to

create the final grid. The processing of the data aims to remove possible outliers and false bottom returns on the recorded pings, in order to get realistic soundings to reproduce the seafloor relief properly. In this project, the ping editing to remove false soundings was done manually and no additional water level correction (both astronomical tide and residual effects, for example local meteorological conditions) was applied.

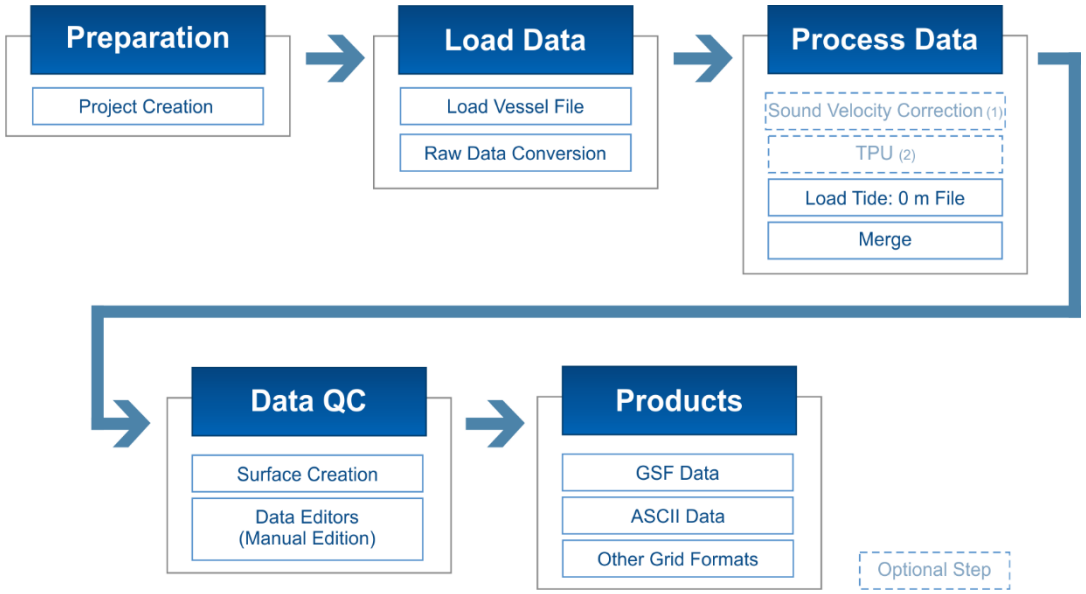

Figure 3.2. Overview of workflow states. Adapted from Caris Training Module (for HIPS and SIPS 9.0).

The processed data was gridded at cell sizes of 25 and 40 m, and exported in several formats such as GSF and ASCII files for further analysis into a Geographic Information System (GIS) environment, in this case, Esri ArcGis Software. Based on different tools available in the software, Digital Elevation Models (DEMs) were represented as a raster (a grid of pixels or cells) from ASCII files and used to generate relief-shaded maps from different azimuth and elevation values to identify the morphological features and determine different quantitative parameters (Fig. 3.3).

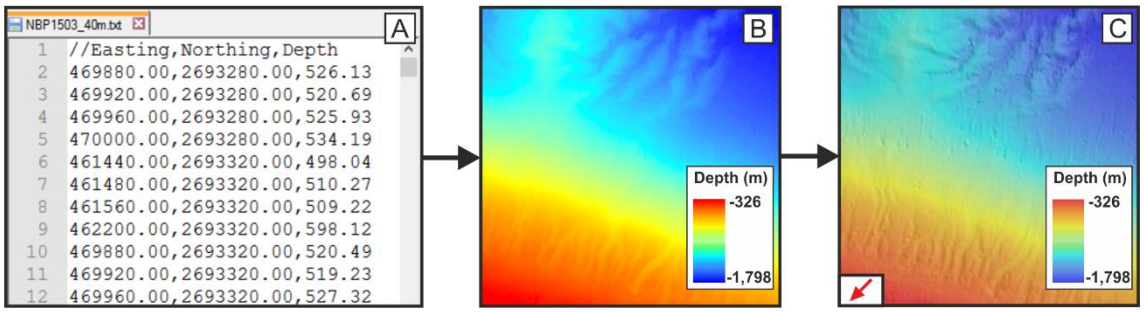

Figure 3.3. ASCII file (**A**) used to generate a DEM with 40 m resolution (**B**). From the DEM was generated a relief-shaded map (**C**) with idealised light source was defined with 45° azimuth (red arrow) and 45° elevation.

The identified bedforms were mapped by visual identification using Caris HIPS and SIPS and Esri ArcGIS software and some features such meltwater channels, drumlin-like features and gullies were individually digitalised within the GIS environment in order to get quantitative parameters.

Each recognisable meltwater channels and drumlin-like features were mapped using complementary shaded-relief maps. Those shaded surfaces were defined with attention to avoid perception biases that can derive from the established illumination (e.g. Smith and Clark, 2005; Saha, 2010). Therefore, two shaded surfaces were created, with illumination sub-perpendicular to the main lineament, in both directions, and another one sub-parallel to the alignment (Fig. 3.4). In addition, the information from the slope component from the DEM were used to support the mapping and get more criteria to delimit the features individually (Fig. 3.4D), an useful criteria which is not dependent on the illumination (Smith and Clark, 2005).

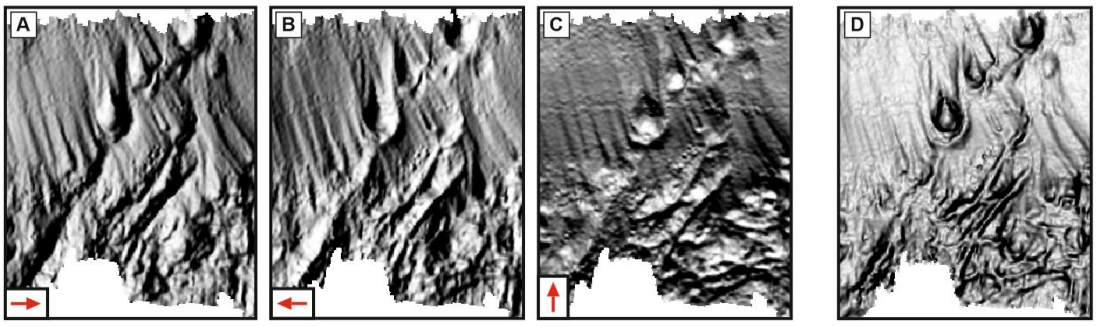

Figure 3.3.4. Relief-shaded maps with three azimuth illumination (red arrows) and an elevation of 30° to support the drumlin-like mapping (**A**, **B** and **C**), presented with a vertical exaggeration of 3. **D** Slope component map from the DEM: dark colours for steep regions and lighter colours for flat regions.

Similar procedures were conducted on gullies visualization and mapping. In this case, two shaded reliefs and slope component were generated (Fig. 3.5). The illumination from the two shaded surfaces were oriented perpendicular to the general lineament of the features.

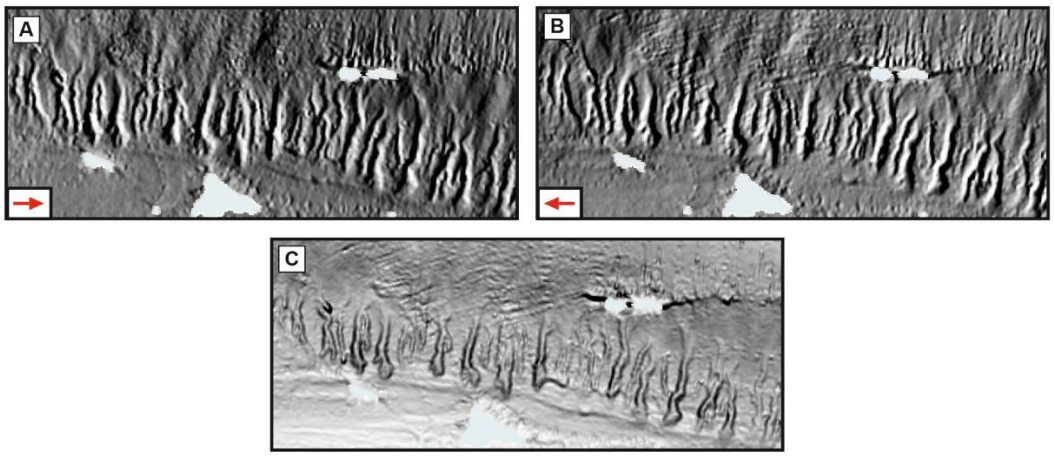

Figure 3.5. Gullies visualization using relief-shaded maps with different azimuth illumination (red arrows) and an elevation of 30º to support gullies mapping (**A** and **B**, vertical exaggeration of 3). **C** Slope map from the DEM: dark colours for steep regions and lighter colours for flat regions.

3.2 Geomorphometry

To provide further morphological description and more comparable results from the studied areas, a quantitative surface analysis was done. The quantitative parameters (or measurements) can be defined for general (surface) and specific (identified bedforms) geomorphometry (Mark, 1975).

For general characterisation of the seabed surface, basic DEM components such slope, curvature and ruggedness were extracted from the multibeam data using Esri ArcGIS-based tools. The slope component corresponds to the change of elevation or the measurement of the steepness (generally expressed in degrees). It constitutes an important terrain variable for seabed analysis, especially for the characterisation of the continental slope. The curvature parameter allows to highlight the convex and concave features on the bed surface, a valuable tool to identify the channelised or ridged bedforms. Finally, the ruggedness characterises the surface irregularity by combining the variability on slope and aspect into a single measure. The ruggedness values in the output raster can range from 0 (no terrain variation) to 1 (complete terrain variation) (Wright et al., 2012). The extracted geomorphometric surface information were expressed as grid formats and presented as maps (Fig. 3.6).

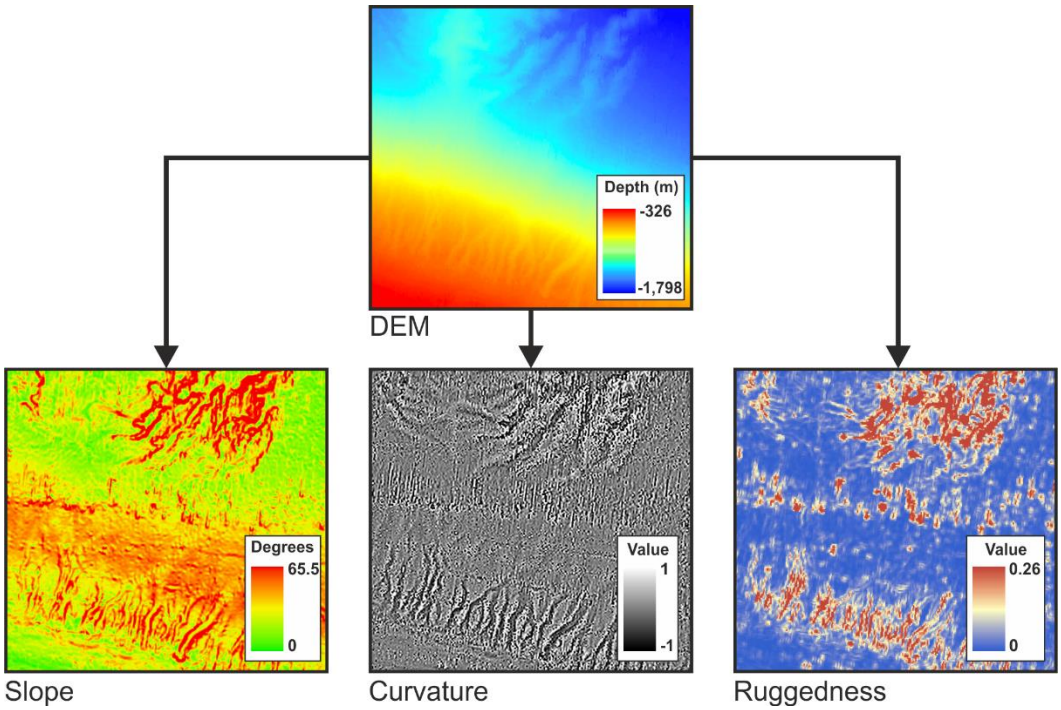

Figure 3.6. Quantitative parameters derived from the DEM (general morphometry): slope, curvature and ruggedness.

3.2.1 Drumlin-like parameters

Different shape parameters were measured during the characterisation of the mapped drumlin-like features, including length (L), width (W), relief (h) (see Fig. 3.7 and Table 3-I), elongation ratio (E=L/W), area, and perimeter.

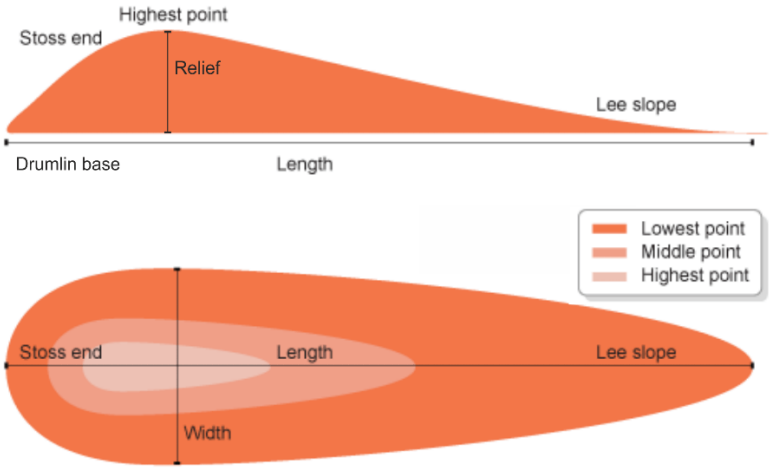

Figure 3.7. Morphological parameters of a classical drumlin (smooth hill) (Adapted from: https://www.geocaching.com/geocache/GC3WT7R_ulsters-only-fjord?guid=54c443fa-0a70-4b fb-956c-f80d71ec0298).

Table 3-I. Description of measured drumlin parameters.

Parameter	Description
Length	Greatest distance on drumlin base parallel to main alignment (Fig. 3.7).
Width	Greatest distance on drumlin base perpendicular to main alignment (Fig. 3.7).
Relief	Distance from the top of the landform and its base, measured perpendicularly to the base (Spagnolo et al., 2012) (Fig. 3.7 and 3.8).
Elongation Ratio	Dimensionless value which results from the division of maximum drumlin length by maximum width (e.g. Clark et al., 2009).

The morphological parameters L and W were measured manually, directly on the shape file composed by different polygons that delimit each recognisable drumlin-like feature. From longitudinal profiles (coincident to L line) taken from each feature was determined the h. The real values of L and h were obtained after the correction of the base surface according to the slope of the terrain. For instance, the relief of each drumlin-like has been, in many cases, measured as the difference between the highest and the lowest point elevation. If a drumlin-like is present on a flat horizontal landscape, the measurement does in fact correspond to the truth elevation. However, on inclined terrains the drumlin-like base is not necessarily horizontal, as considered by Spagnolo et al. (2012) (Fig. 3.8).

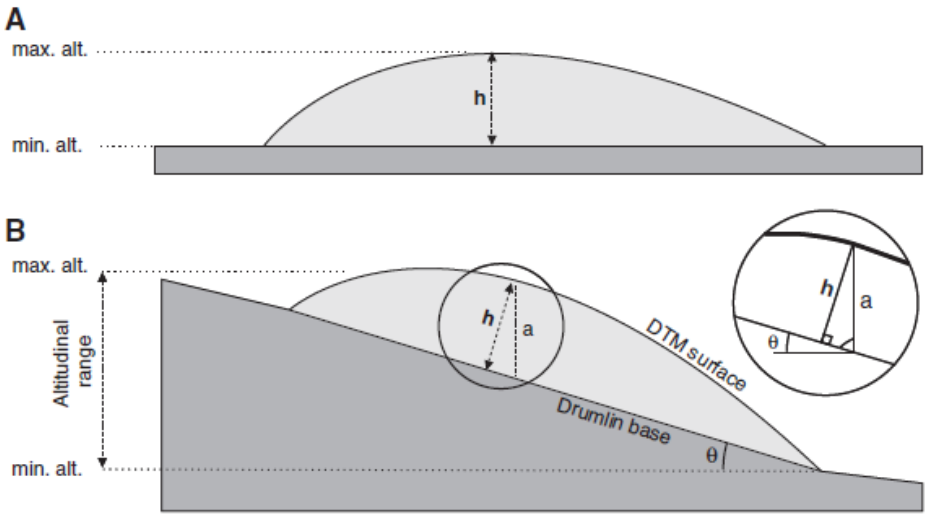

Figure 3.8. Definition of drumlin-like relief for (A) flat and (B) hillslope contexts. This figure show clearly the difference between altitudinal range and the real relief when drumlins are found on hillslopes. From a drumlin-like profile is possible to determine the vertical offset (a), which is then converted to drumlin relief based on the equation: h= a x cos(θ), where θ is the slope angle of the apparent drumlin-like base. Image from Spagnolo et al., 2012.

Based on this approach, each longitudinal profile taken from Esri ArcGIS software was exported into Excel software for posterior corrections of L and h (Fig. 3.9).

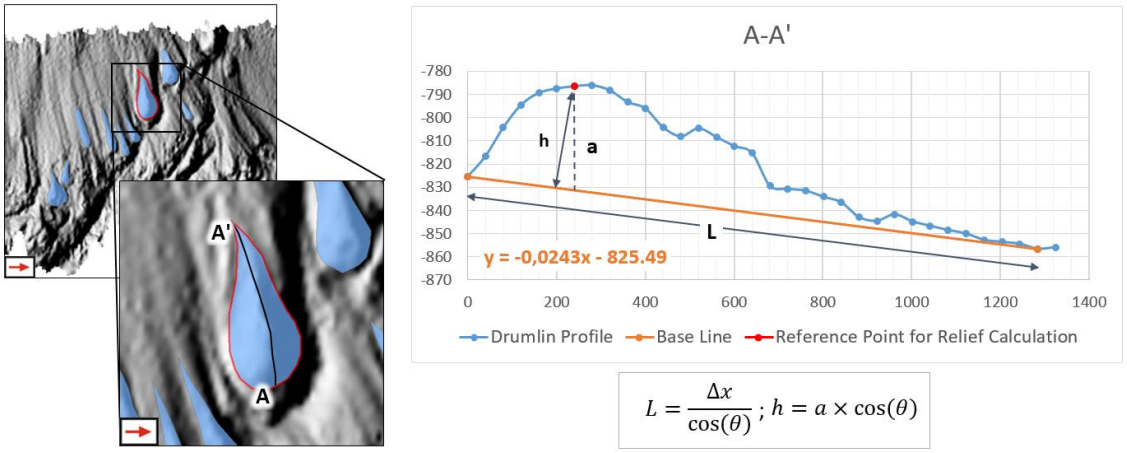

Figure 3.9. An example of drumlin profile extracted from ArcGIS for length (L) and relief (h) calculation. Once defined the drumlin base equation, is possible to determine the slope angle (θ) and that value to find the real length and relief values of a drumlin. The vertical offset (a) correspond to the difference between the reference point on the profile and its projection on the drumlin base equation.

Additional parameters such elongation ratio, area and perimeter were determined. The last two parameters were calculated from the Esri ArcGIS geometric calculator, available on the attribute table options. All the information have been incorporated into a single Excel table for further analysis.

3.2.2 Gully parameters

Based on Gales (2013) work, morphological parameters from the identified gullies on the continental slope were gathered along cross profiles starting at 50 or 100 m below the shelf edge, depending on the starting point of the gullies. Gully parameters, such as width, length and depth incision (Fig. 3.10), sectional shape (U/V, Fig. 3.11), spatial distribution and patterns of the gully were extracted and analysed using Esri ArcGIS software. The extracted gully parameters are synthesised in Table 3-II.

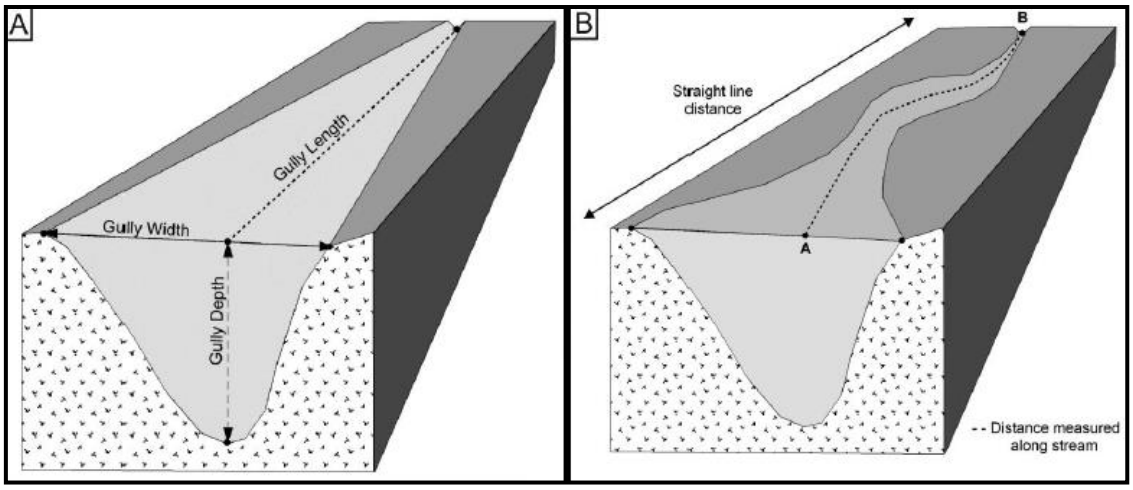

Figure 3.10. Morphometric parameters of a gully: **A**- width, length and incision depth, **B**- sinuosity. From Gales (2013).

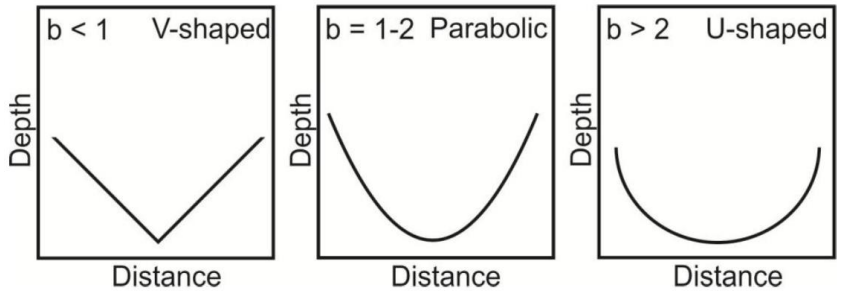

Figure 3.11. Schematic of cross-sectional shape (U/V) and associated 'b' values derived from the General Power Law programme (from Gales, 2013).

Table 3-II. Description of measured gully parameters based on Gales, 2013.

Parameter	Description
Length	Distance a gully can be traced down-slope from the gully head, this is limited by down-slope data extent (Fig. 3.10).
Width	Distance between points of maximum curvature of gully flanks (Fig. 3.10).
Incision depth	Vertical distance from the gully base to the line defining gully width (Fig. 3.10).
Width/depth ratio (W/D)	Dimensionless ratio giving an indication of the gully shape.
Slope gradient	General gradient angle measured from the continental slope.

Sinuosity (S)	Dimensionless ratio of length along gully thalweg divided by the linear distance where*:* Sinuosity index (*S*) = distance measured along gully / straight line distance. (Fig. 3.10B) A gully with sinuosity index greater than 1.04 is considered sinuous and, by definition, a straight gully would have *S* = 1.
Cross-sectional shape (U/V)	The shape of a profile taken parallel to the shelf edge, which is characterised using the General Power Law (GPL) programme (Pattyn and Van Huele, 1998). GPL approximates the cross-sectional shape of a gully based on the equation: $y - y0 = a \mid x - x0 \mid^b$ (Eq. 3.1). The programme calculates a measure of cross-sectional shape (*b* value) based on general least-squares method, thereby minimises the error between cross-section and a large set of defined symmetrical shapes by the equation (Eq. 3.1, see Fig. 3.12). In equation (1), *a* and *b* are constants and *x* and *y* are the horizontal and vertical coordinates taken from a cross-sectional profile of a gully. The programme automatically determines x_0 and y_0 as the coordinates of the minimum elevation of the gully profile (which correspond to the origin). The *b* value gives a measure of the cross-sectional shape of the gully and ranges from 1 (V-shape) to 2 (parabolic, commonly referred to as U-shape) on the U/V index (Fig. 3.11)

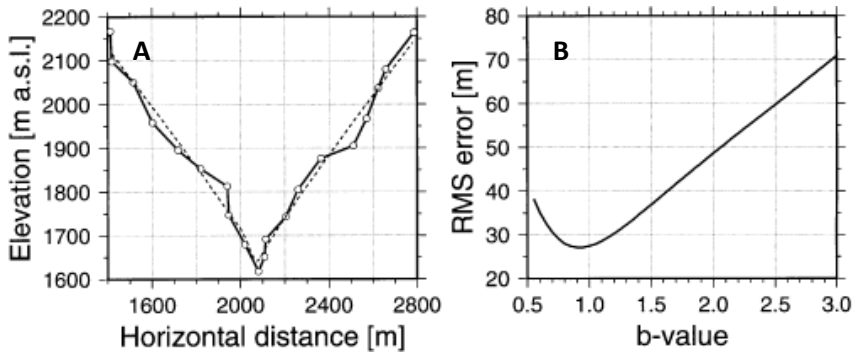

Figure 3.12. A representation of curve fitting with GPL (dotted line) of a cross-profile (**A**) and the respective RMS error calculation in function of b value (**B**). For this case the optimal b value is 0.92 and the origin has the following coordinates: xo=2081 m, yo=1642 m (from Pattyn and Van Huele, 1998).

The measured parameters were compiled into a general table, where all the information was submitted into a classification process based on a diagnostic diagram proposed by Gales et al.(2013). From this diagram 5 types of gully are categorised based on the presence or absence of branching gullies (connected gullies), depth, cross-sectional shape, sinuosity and length (Fig. 3.13).

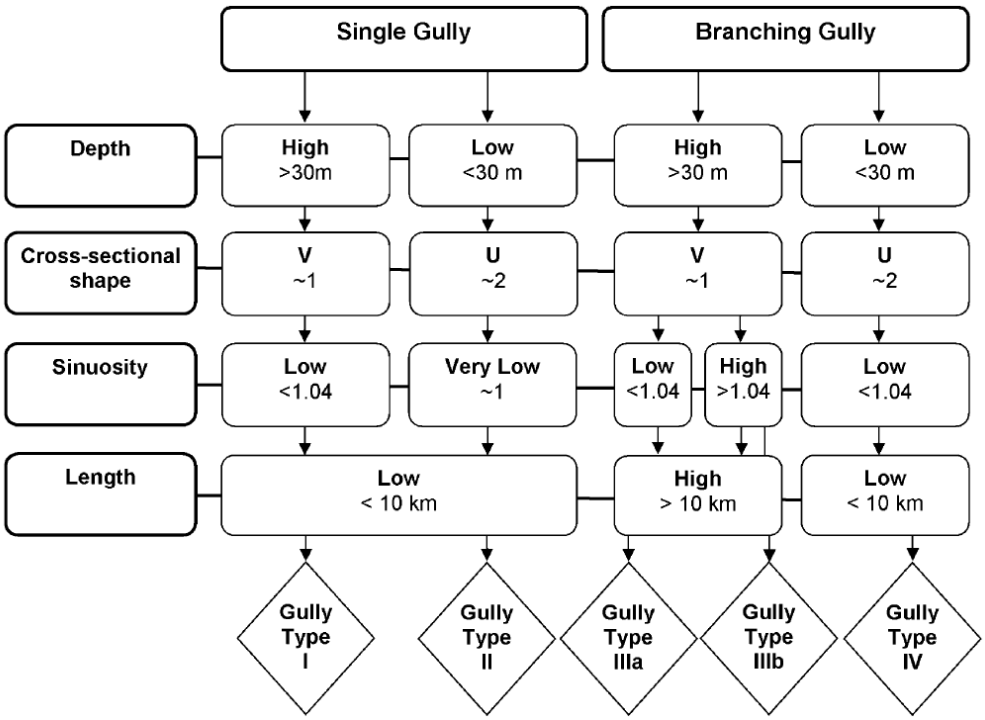

Figure 3.13. Diagnostic diagram to identify Antarctic gullies based on the quantitative parameters measured at 50 m below the shelf edge including: gully branching order, depth, cross-sectional shape, sinuosity and length (from Gales et al., 2013).

3.3 Statistical Analysis

Descriptive statistics were calculated from the morphological parameters of the mapped drumlins-like and gullies features. Univariate statistics, where only one outcome variable is involved, were performed to analyse each parameter separately. On the other hand, multivariate statistics were also determined to obtain a simultaneous observation and analysis of more than one variable, in order to understand the relationships between the different morphological parameters.

The univariate statistics performed are (1) central tendency (mean and median) for a probability distribution, (2) statistical dispersion, in this case variance and standard deviation, and (3) shape measurements that describe the distribution using skewness and kurtosis. The multivariate analysis carried out are agglomerative hierarchical clustering (AHC) to build a hierarchy of clusters and principal component analysis (PCA) to correlate parameters.

The AHC was applied on drumlin-like parameters in order to find potential similarities/correlation among then, as Clark et al. (2009) and Spagnolo et al. (2012) investigated. The results were presented graphically by a two-dimensional diagram,

known as dendrogram, which was used as posteriorly for further correlation analysis and formulation of hypotheses.

On the other hand the PCA was conducted on gully parameters (length, width, incision depth, W/D, sinuosity and U/V index) similar to Gales (2013). The purpose is to find which morphological parameters (variables) are most important in distinguishing encountered gullies groups in the study area and eventually compare them.

The statistical measurements and methods mentioned were conducted through Excel and the analysis software STATISTICA, from Stat Soft Inc.

3.4 Sub-Bottom profiler

In addition to the MBES system, a sub-bottom profiling system was used throughout the cruise. It is an important tool during navigation for the identification, characterization and quantification of the layers of sediment or rock under seafloor. With those capabilities, the system is generally used as a guidance to identify potential locations for sediment sampling, and to describe and interpret the nature of the seafloor features, including the distinction between facies as well as erosional or depositional environments. The signal penetration and resulting images depends on acquisition frequencies and on the type of substrate which affects the acoustic impedance contrasts.

3.4.1 System description and operations

The Knudson Chirp 3260 system was used on board the RVIB Nathaniel B. Palmer to collect high-resolution seismic reflection data. The system allows operations with central frequencies of 3.5 and 12 kHz within a user-specified band of frequencies, known as sweep, to better adjust the signal penetration under seafloor.

The 3.5 kHz mode with sweep length between 1 ms (shallow) and 32 ms (>4000 m depth) was used to collect the data during the cruise, with different amplitude correction settings (TVG mode between 5logR-30logR). The outer limits for the start and stop frequencies of the sweep were 2.3 kHz and 5.3 kHz providing a maximum vertical resolution of approximately 0.5 meters (Table 3-III).

Table 3-III. Most frequent settings/acquisition parameters used during the sub-bottom imaging on board the *RVIB* Nathaniel B. Palmer (NBP15-03).

Signal Setting	
Start frequency	2.3 kHz
Stop frequency	5.3 kHz
Bandwidth	3 kHz
Recording window range	200 m, 500 m, 1000 m
Sample rate	60 µs
Gain Mode	Auto
TVG Mode	5logR-30logR
Channel Setting	
Eco strength	-125 dB
Pulse length	8-15ms

The system was controlled by the terminal software which contained all the necessary tools for standard operation of the echo sounder, data acquisition and archiving. The application gives access to the operational controls to define the acquisition parameters and displays a graphical representation of real-time received data (Fig. 3.14).

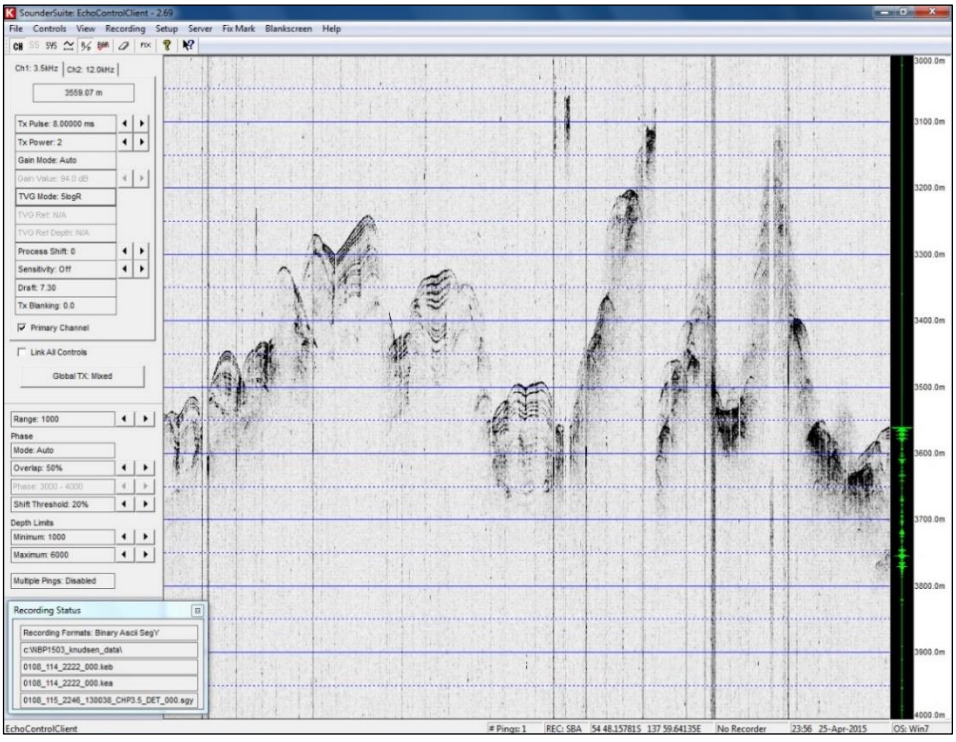

Figure 3.14. Knudsen sub-bottom control interface.

Data were stored in Knudson *.keb and SEGY formats. The profiles were named by default through the acquisition software, starting with a consecutive line number, followed by Julian day and time of the start of the line. While there is only one file for the *.keb format for the same line, there are several files associated to SEGY format. SEGY files were automatically truncated over 25 Mbytes in size or when the length, i.e. the number of samples, was changed.

The acquisition of sub-bottom data started after crossing the Australian's Exclusive Economic Zone (EEZ) and the archiving was stopped during science stations.

3.4.2 Data processing

The sub-bottom Chirp data profiler processing consists in application of routines on the raw data in order to get representative subsurface profiles. The workflow to apply depends on the objectives and pretended results. In general the purpose of the seismic processing is to improve the signal-to-noise ratio of the data, increase seismic resolution and to display the seismic events in their correct spatial position.

The processing work flows concerning the Chirp sonar are slightly different from the conventional seismic. The processing applied to Chirp data was developed within a working flow according to the particularities of the data. Since the acquired signal has been defined for a range of frequencies and had real-time gain compensation (see table 3-III) the workflow was essentially defined to: (1) apply static corrections, (2) remove or reduce additional noise effect at the frequency and (3) apply early mute to clear the noise from water column.

The processing was conducted similarly to all lines to ensure consistent interpretation from line to line using the SPW (Seismic Processing Workshop) software. For example, Figure 3.15 shows the work flow and the processing results obtained for a Chirp profile (line: 0030_095_1333_130038 CHP3.5_FLT_000). To execute the static shift correction the seismic traces were resampled to generate a new unprocessed profile with greater time length. In that way, it was possible to fit the delay record times for each trace and correct their vertical position to restore the image coherence (Fig. 3.15A and B). In order to obtain a cleaner profile, with informative data preserved, a low-pass filter and early mute were used in most of the cases (Fig. 3.15C). To remove potential noise on the frequency domain the filter was defined with cutting frequencies between 3000-3500 kHz. The cutting frequencies were established based on spectral frequency

analysis and conducting tests to find the best possible result. The early mute was applied based on sea bottom pick to cancel any amplitude value on the water column.

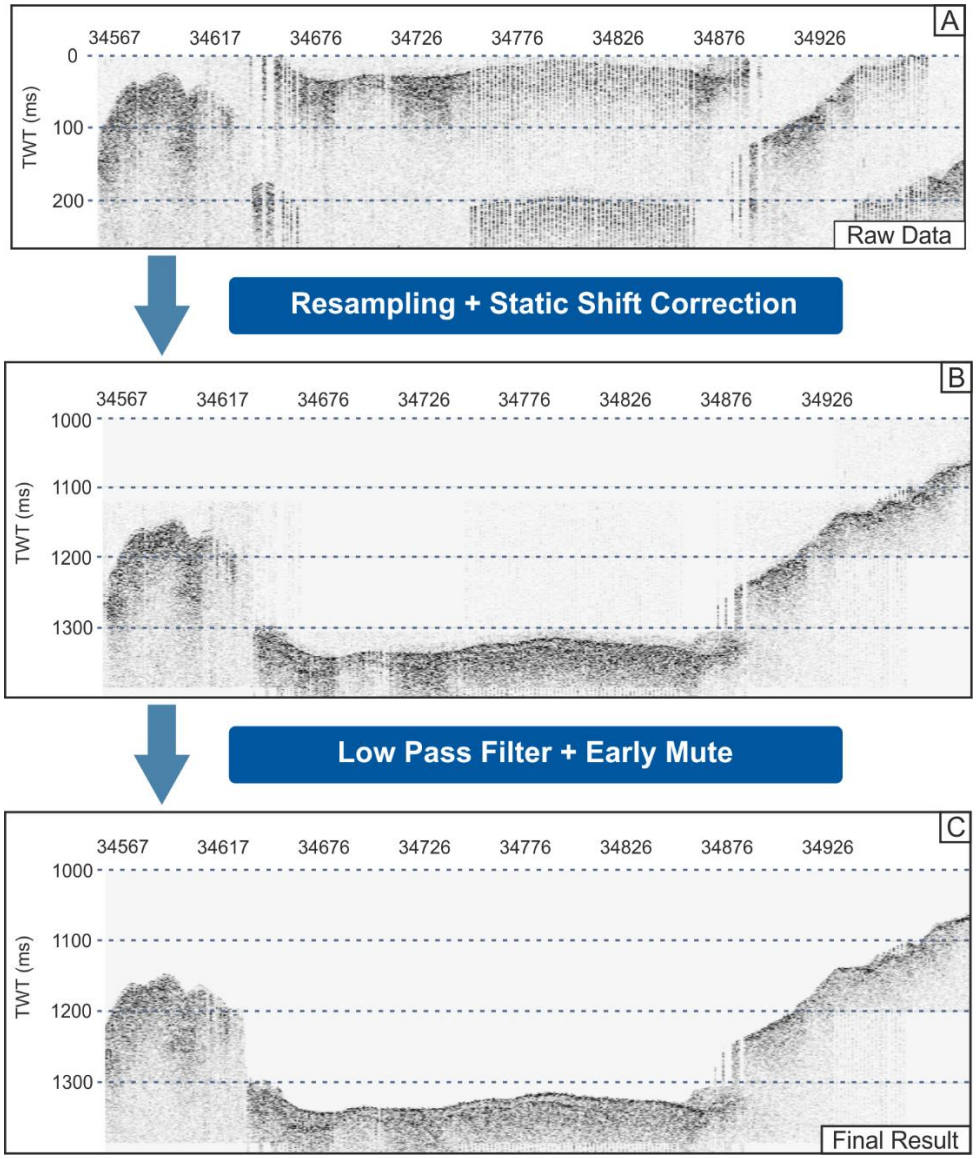

Figure 3.15. Main processing work flow applied on Chirp data with respective results from each step. Example from line 0030_095_1333_130038 CHP3.5_FLT_000.

3.5 Considerations and limitations

For swath bathymetry studies the major conditioning factors are data availability (coverage) and resolution (Gales, 2013). In this project, the interpretation of the features was difficult to perform in some parts of the data set, and in certain cases a complete morphometrical analysis of the bedforms was not possible to implement due to limited

data coverage. Heavy sea ice cover and storms during the expedition made navigation and acquisition of MBES data very difficult.

Beside the acquisition frequency, the resolution of multibeam data is strongly influenced by water depths. The depth increment leads to a reduced density of the depth measurements (soundings) due to expansion of footprint. Due to this effect it is important to find the best cell size of the gridded surface that will represent the seafloor. Two DEMs from the swath bathymetry data defined with different resolution (cell size), 25 m (more detailed data) and 40 m (more continuous data), were created for this project (Fig. 3.16). Most of the interpretation of the sea bottom morphology was applied from the 40 m resolution DEM, although such resolution limit the interpretation of small-scale features. When possible, the analysis and interpretation were done at 25 m resolution.

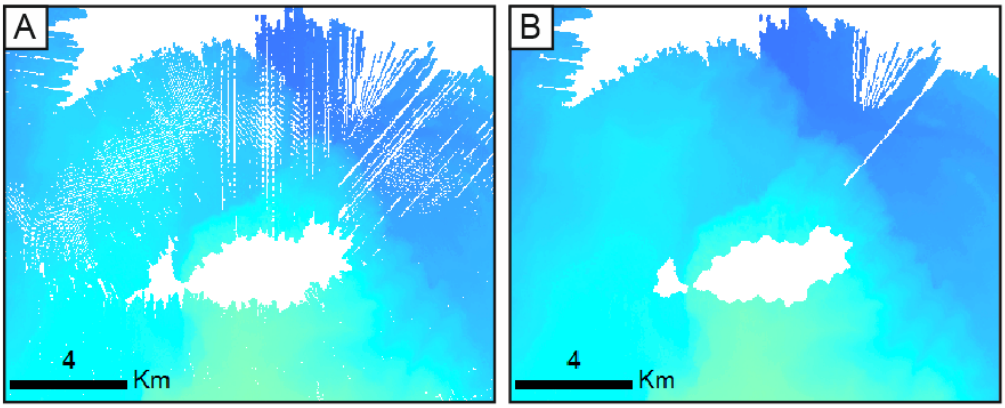

Figure 3.16. Comparison between DEMs with different resolution, 25 m (**A**) and 40 m (**B**).

The presence of artefacts and anomalies in MBES data are another characteristic which can limit or hinder interpretation by masking the good data beneath noisy data (Fig. 3.17). During the cruise, artefacts were mainly originated by variations in the water column (e.g. during a storm), winds and heavy sea-ice conditions that created turbulence/bubbles in the water column reducing the efficacy of the MBES transmitter and receiver. Their associated disturbance also affected the translational ship motions (heave, pitch, roll and yaw) leading to outliers or spikes data. Even the survey speed, mainly during ship turns and windy conditions influenced data quality along track direction.

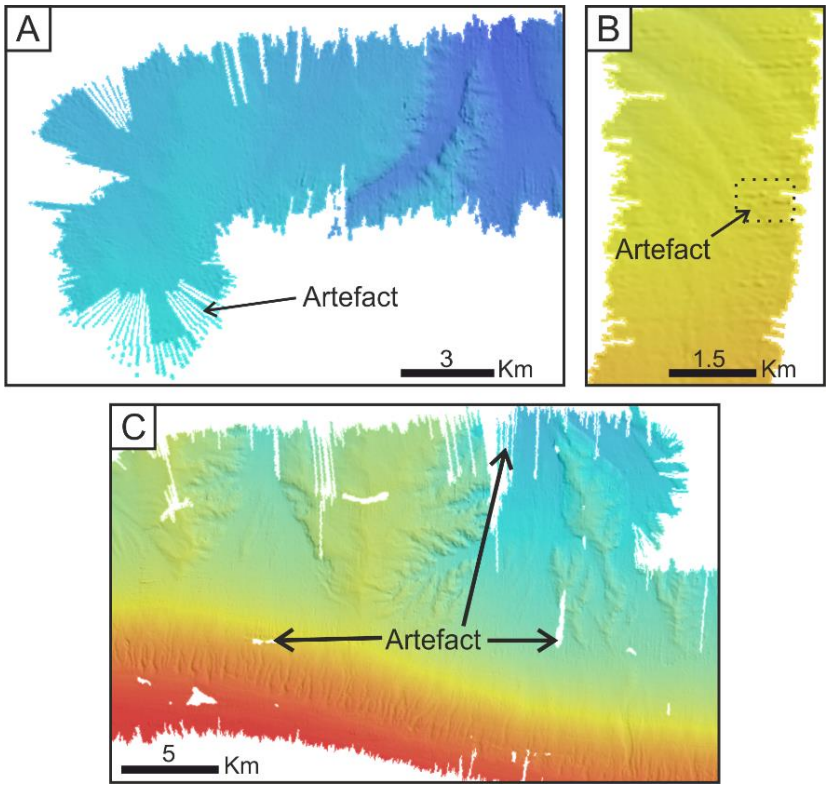

Figure 3.17. Example of artefacts found on the swath bathymetric data (DEM with 40 m resolution). A - Artefacts caused by changes in vessel speed. B - False depth soundings. C – Lines-drop out.

Concerning the Chirp data acquisition, the main limitation was the acoustic penetration due to the navigation conditions (heavy sea-ice cover, storms and vessel speed). This factor limited the substrate analysis and interpretation of the evolution of the bedforms trough time.

References

Clark, C. D., Hughes, A. L., Greenwood, S. L., Spagnolo, M., and Ng, F. S. **2009**. Size and shape characteristics of drumlins, derived from a large sample, and associated scaling laws. Quaternary Science Reviews, 28(7), 677-692.

Gales, J. A., **2013**. The geomorphology of Antarctic submarine slopes. (Doctor of Philosophy Thesis), University of Manchester.

Gales, J. A., Larter, R. D., Mitchell, N. C., and Dowdeswell, J. A. **2013**. Geomorphic signature of Antarctic submarine gullies: implications for continental slope processes. *Marine Geology*, 337, 112-124.

Johnson, P., and Jerram, K. **2015**. RVIB Nathaniel B. Palmer EM122 Multibeam Echosounder Sea Acceptance Trial for TX/RX Arrays NBP1505 June 10-15, 2015.

Mark, D. M. **1975**. Geomorphometric parameters: a review and evaluation. Geografiska Annaler. Series A. *Physical Geography*, 165-177.

Pattyn, F. and **Van Huele**, W. 1998. Power Law or Power Flaw. Earth Surface Processes and Landforms 23, 761-767.

Saha, K. **2010**. Object-oriented classification of drumlins from digital elevation models (Doctoral dissertation, Kent State University).

Smith, M. J., and **Clark**, C. D. **2005**. Methods for the visualization of digital elevation models for landform mapping. *Earth Surface Processes and Landforms*, 30(7), 885-900.

Spagnolo, M., Clark, C. D., and Hughes, A. L. **2012**. *Drumlin relief. Geomorphology*, 153, 179-191.

Wright, D. J., Pendleton, M., Boulware, J., Walbridge, S., Gerlt, B., Eslinger, D., ... and Huntley, E., **2012**. ArcGIS Benthic Terrain Modeler (BTM), v. 3.0, Environmental Systems Research Institute, NOAA Coastal Services Center, Massachusetts Office of Coastal Zone Management. *esriurl. com/5754*.

CHAPTER 4:
Results and interpretations

The swath bathymetric imagery and the sub-bottom profiling revealed for the first time the detailed seafloor character of the west region of the Dibble Ice Tongue, East Antarctic, between 185 and 2,670 m of water depth.

Geomorphological features observed on the records are described and morphological parameters of drumlins-like features and gullies (the most abundant seabed bedforms) are analysed statistically in order to get representative and summarised information. The study area was divided in three main physiographic segments, distinguished on the basis of the seabed topography: (I) inner to outer continental shelf, (II) continental edge and slope, and (III) continental rise (Fig. 4.1).

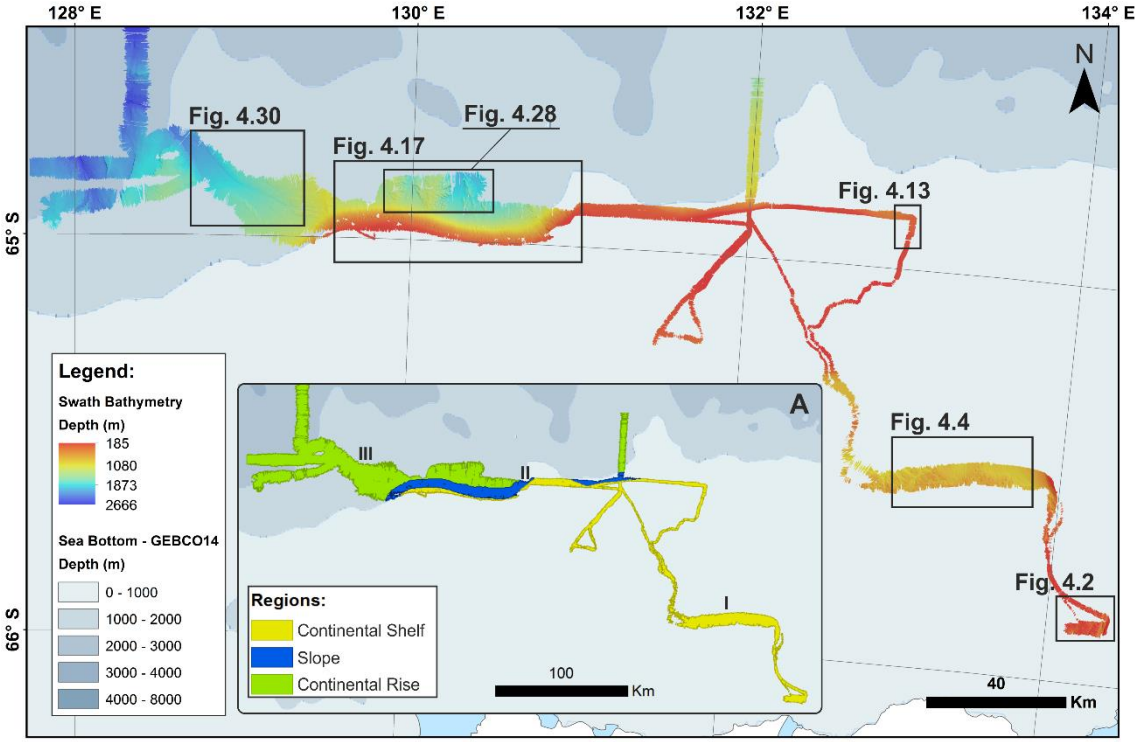

Figure 4.1. General swath bathymetric image of the study area. The black rectangles show the location of the main glacial geomorphic features presented in this chapter. (**A**) Regions map identifying the inner continental shelf (**I**), slope (**II**) and continental rise (**III**).

4.1 Inner to outer continental shelf

The seafloor morphology of the inner to outer continental shelf is mainly characterised by irregular crudely streamlined bedforms with heights up to 70 m and subglacial meltwater channels, drumlin-like bedforms, mega scale glacial lineations (MSGLs) and iceberg scours.

4.1.1 Subglacial meltwater channels

The inner shelf exhibits a range of streamlined features including elongated channelised features, interpreted has subglacial meltwater channels (Fig. 4.2). A subglacial meltwater channel is a waterway carved to great depths by the power of the hydrostatic pressure beneath ice grounded sheets (or mass of ice), roughly parallel to the main ice flow direction (e.g. Bennett and Glasser, 2009). In general, the channels found are 80-190 m deep, 300-900 m wide, and run mainly SSW-NNE. The orientation is more variable on the smaller channels, where merging cases are also observed. The channels exhibit steep walls and have relatively smooth thalwegs, U-shaped flat bottom and low sinuosity.

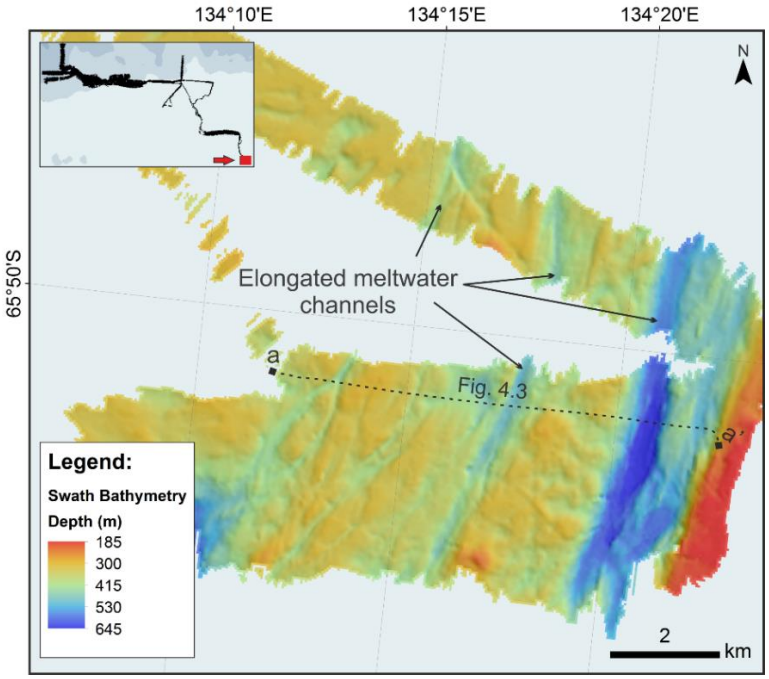

Figure 4.2. Swath-bathymetric record showing irregular crudely streamlined bedforms and elongated meltwater channels on inner continental shelf.

The sub-bottom acoustic data over the crudely streamlined area show a general top reflector with little or no acoustic penetration (Fig. 4.3).The acoustic stratigraphy profiles across the elongated subglacial meltwater channels indicate a poor or absent sedimentary cover, suggesting that the seafloor is probably carved into the bedrock or underlain by cobbles and gravelly sediments.

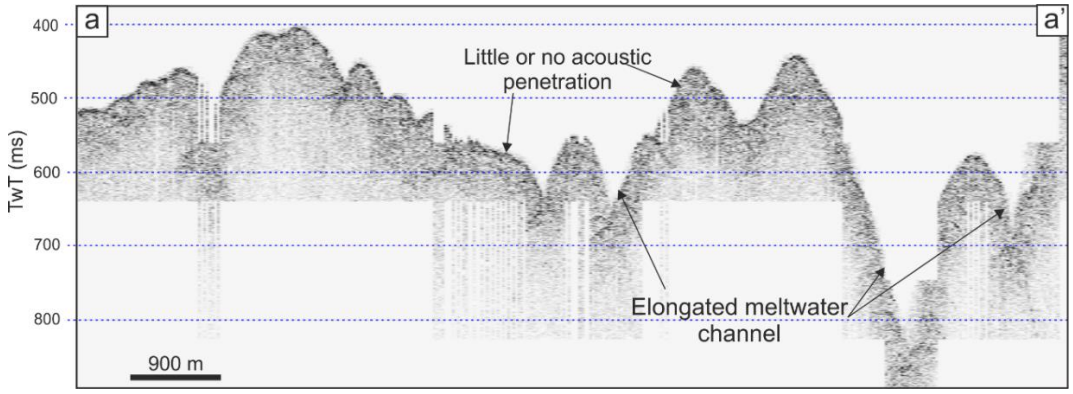

Figure 4.3. Sub-bottom profile showing an acoustically impenetrable substrate, without any distinct sub-bottom information. This record suggests the presence of a hard subtract such bedrock. For location see figure 4.2.

Although mapping of the pattern of the channel network is limited by the acquired data, a more extend of the network is expected on this part of the continental shelf. Northward, on the mid shelf, channelised features are still visible. The subglacial meltwater channels have the same characteristics described previously and some of them are observed around the base of, the drumlin-like bedforms.

The meltwater channels observed suggest an erosion of the seafloor by subglacial water flow, similar to the features reported in the Amundsen Sea embayment (Larter et al., 2009), Pine Island Bay (Wellner et al., 2001; Lowe and Anderson, 2002; 2003), Palmer Deep (Domack et al., 2006) and Kvitøya Trough, north-western Barents Sea (Hogan et al., 2010). In Antarctica, the bedforms are described to be 500-1,000 m width and 200-400 m deep on the West Antarctica continental shelf and about 200 m width and 50-100 m deep on the pacific margin of the AP (e.g.Domack et al., 2006).

4.1.2. Drumlin-like bedforms

On the mid shelf, a field of drumlin-like bedforms is observed seaward a crudely streamlined landscape. The drumlin bedforms are characterised by low, smoothly rounded and elongated oval hills, mounds, or ridges built under the margin of the ice

(Bates and Jackson, 1980). Their longer axis are generally parallel to the direction of the ice movement.

The observed drumlin-like field covers an area of 22 km long and seems to extend northward, beyond the range of the data (Fig. 4.4). A total of 30 recognised individual drumlin-like bedforms were mapped (Fig. 4.4D), and 29 of them were used for descriptive statistical analysis. Their validation has been conditioned by the measurement of the morphometric parameters (length, width, relief and eventually elongation ratio), not constrained by the coverage of the geophysical data (see Appendix I).

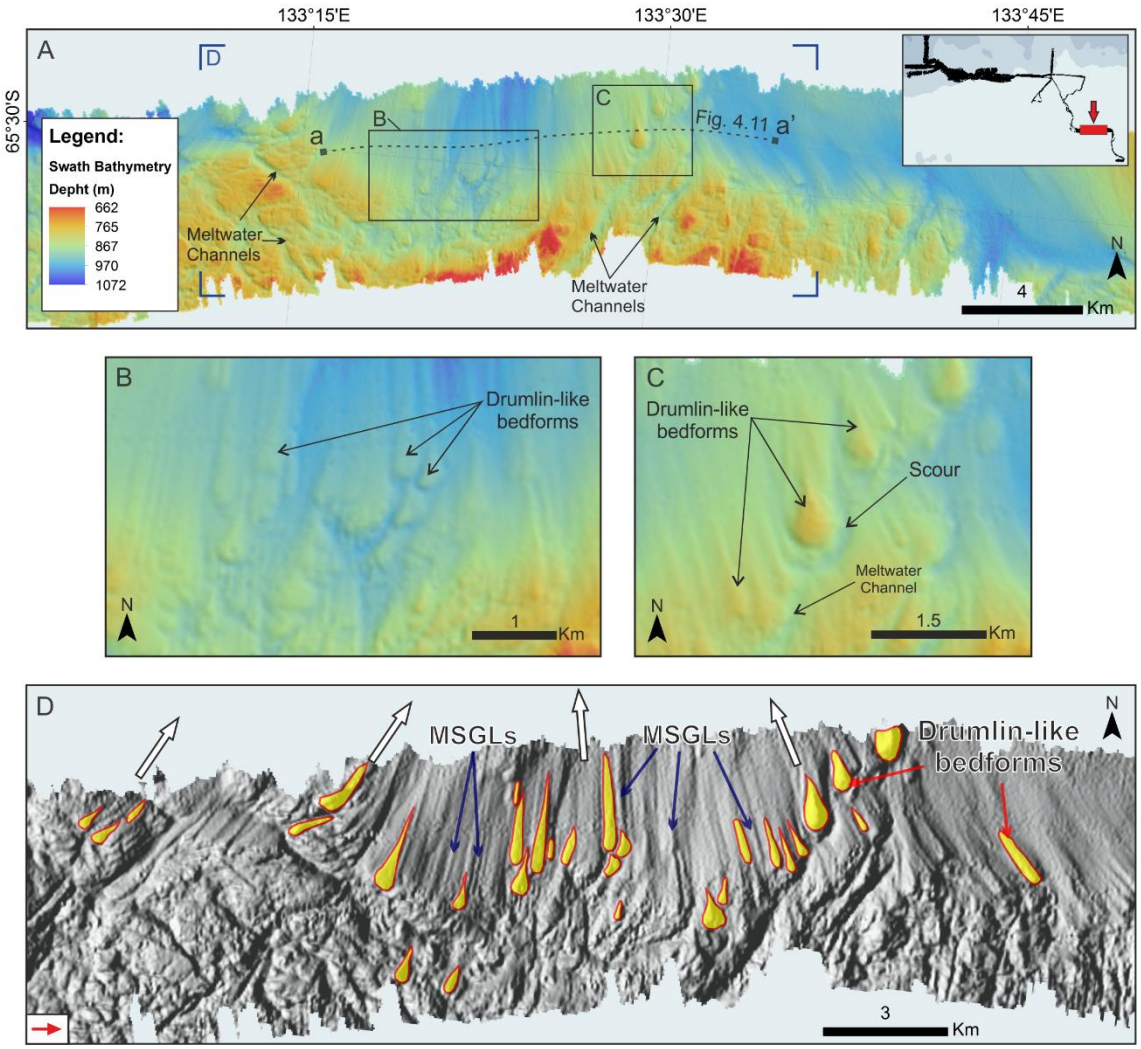

Figure 4.4. Swath bathymetric imagery of the mid continental shelf showing drumlin-like bedforms field (**A**) and close-up to the features (**B**, **C** and **D**). The inset image D corresponds to a shaded relief image with an illumination from west and 30º elevation were the former ice flow direction is represented by withe arrows.

The drumlin-like bedforms are 450 to 2,111 m long and 109-568 m wide. Both parameters, length and width showing a unimodal class distribution (Fig. 4.5). The elongation ratio distribution shows a wide range of values, varying from 1 (practically

circular shape) to 5.75 (elongated shapes), with a major concentration between 2.90 and 3.85. The drumlin-like bedforms show a convergent alignment toward the north region and a more elongated pattern in the central region, where they are linked with elongate and sub-parallel mega scale glacial lineations (MSGLs) (Fig. 4.4D). The drumlin-like bedforms are 2.5-58.3 m high, but mostly between 2.5 and 13.6 m.

The measured parameters show a single-peaked distribution, meaning that the drumlin-like bedforms are mainly spread around an unimodal distribution (Fig. 4.5). In detail, the distribution shape measurements are defined by an heavy-tailed kurtosis and asymmetric skewness indicating that the measured parameters do not follow the perfect normal distributions. The negative excess kurtosis values of the width, elongation ratio and relief parameters are associated to a platykurtic distribution, i.e. the distributions have more data in their tails and less data in their peak (less extreme outliers). In other words, the parameters are, generally, not concentrated around the modal class, meaning higher variability and amplitude for the measured parameters. In opposition, the length parameter has a positive excess kurtosis value associated to more data in its peak and less variability and amplitude. In addition, the asymmetry of the probability distribution for all the measured parameters is defined by a positive skew (right-skewed), indicating that the distribution tail on the right side is longer or fatter than the left side. The positive skew values indicate that the mean and the median of the parameters are both greater than the mode, and the mean is greater than the median.

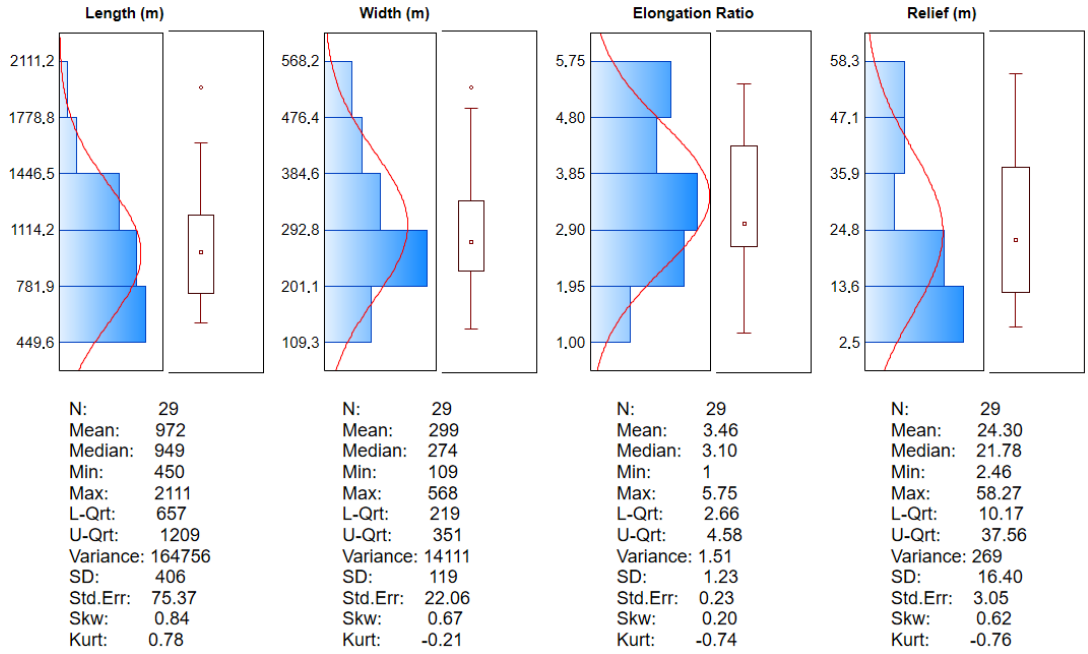

Figure 4.5. Graphical summary and descriptive statistics of drumlin-like parameters: length, width, elongation ration and relief. The class number was defined though empirical rule of: $2^K > N$, where k is the number of classes and N the number of samples. Superimposed on the histograms is represented the best fit Gaussian curve (in red).

The relatively high standard deviation (SD) values indicate that the data points are spread out over around the mean, reflecting significant dispersion and a large amount of variation in the data set (Table 4-I). Based on the distance from the mean, the SD values of the morphological parameters are strongly affected by the outliers. The coefficient of variation (CV) ratios, that represent the ratios or percentage of the SD to the mean, are also high and show great dispersion in the parameters. Additionally, the compared CV values show that the parameter elongation ratio is the less dispersed and the parameter relief has the greatest dispersion (Table 4-I).

Table 4-I. Coefficient variation (Coef. Var.) determined for all drumlin-like parameters, based on their respective mean and standard deviation (Std. Dev.).

	Mean (m)	Std. Dev. (m)	Coef. Var. (%)
Length (m)	972	405.90	41.76
Width (m)	299	118.79	39.68
Elongation Ratio	3.46	1.23	35.56
Relief (m)	24.30	16.40	67.49

In addition, a hierarchical agglomerative clustering (HAC) was performed in order to find potential relationships between the morphological parameters (called morphometric variables). The bottom-up clustering method started with every single variables, as individual points in a single cluster, and successively merged (agglomerated) the closest pair of clusters by satisfying some similarity criteria into sub-clusters, until all of the morphometric variables is in one cluster. The merging was executed based on Ward's Method and on the correlation coefficient Pearson r, which considers the similarity between cluster centroids (gravity centres). The clustering analysis shows two strong correlations defined by the variable pairs relief-width and elongation ratio-length (Fig. 4.6). Moreover, the cluster relief-width generated in earlier stage of the HAC shows more nested relation than the morphometric variable pair elongation ratio-length generated in later stage. The closest relation of the cluster relief-width is characterised by a positive correlation (r) of 0.66 (Fig. 4.7). Through a linear regression this relation is defined by the following equation: $R = -3.155 + 0.091 \times W$ (E.q. 4.1), where R and W correspond to the relief and width, respectively. The correlation of the cluster elongation ratio-length is defined by a value of r=0.54 (Fig. 4.8). This correlation is expected since the elongation ratio values are dependent of the length, but shows how more important is the length parameter versus the width.

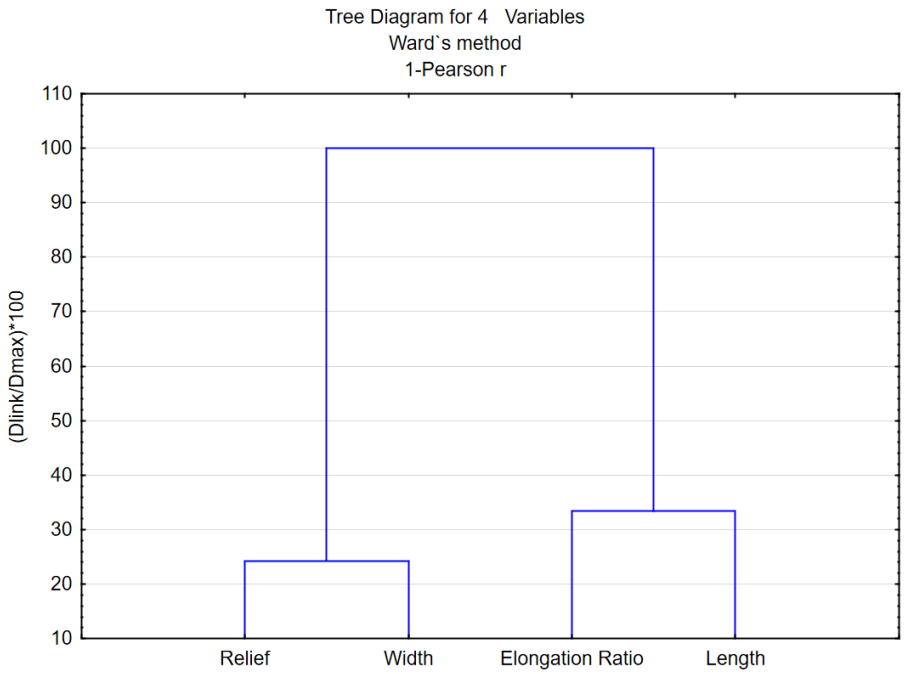

Figure 4.6. Dendrogram showing relationships between the four measured morphological parameters: relief, width, elongation ratio and length. The diagram was generated based on Ward's method and the similarity factor considered was the correlation coefficient Pearson r.

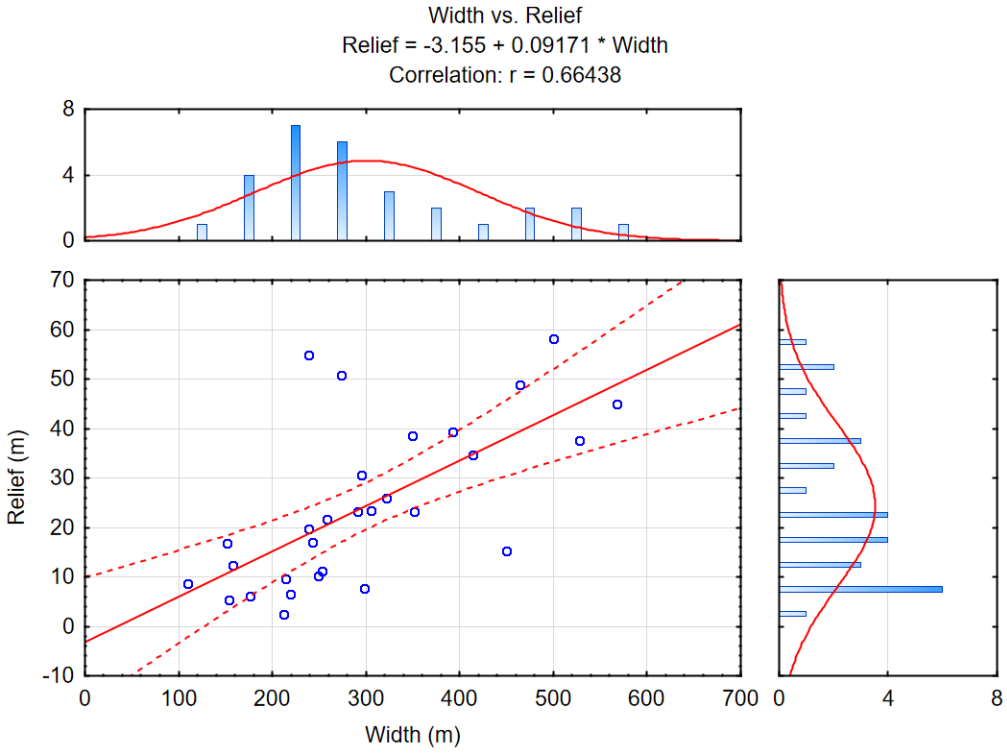

Figure 4.7. Scatterplot of the cluster relief-width, with the respective correlation (r) and 95 % confidence intervals (red dashed curves). The adjacent histograms show the defined classes according to the main grid of the scatter plot.

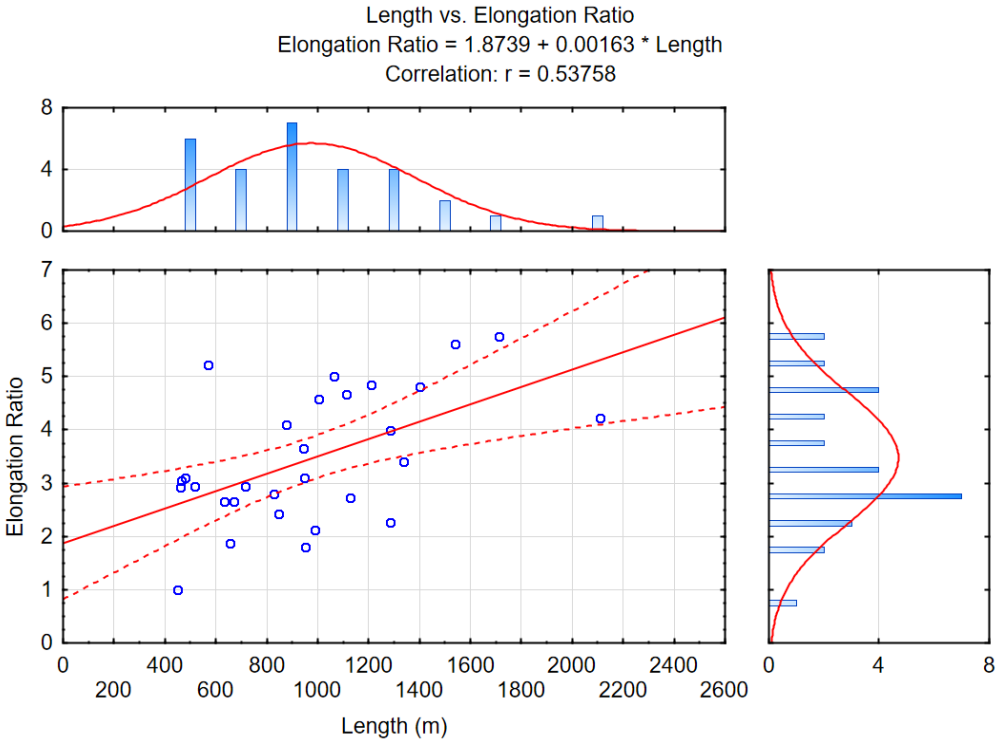

Figure 4.8. Scatterplot of the cluster elongation ratio-length, with the respective correlation (r) and 95 % confidence intervals (red dashed curves). The adjacent histograms show the defined classes according to the main grid of the scatter plot.

Beyond the relatively strong correlations identified through clustering analysis, it was found another correlation with similar value (r=0.53) between the morphometric variables length and relief (to see all correlation values between drumlin-like parameters see Appendix II). This correlation is meaningful for drumlin modelling as examined by Spagnolo et al., 2012. The linear regression which models the relationship between the two variables is represented by the following equation: $R = 3.52 + 0.02 \times L$ (E.q. 4.2), where R corresponds to the relief and L to the length (Fig. 4.9).

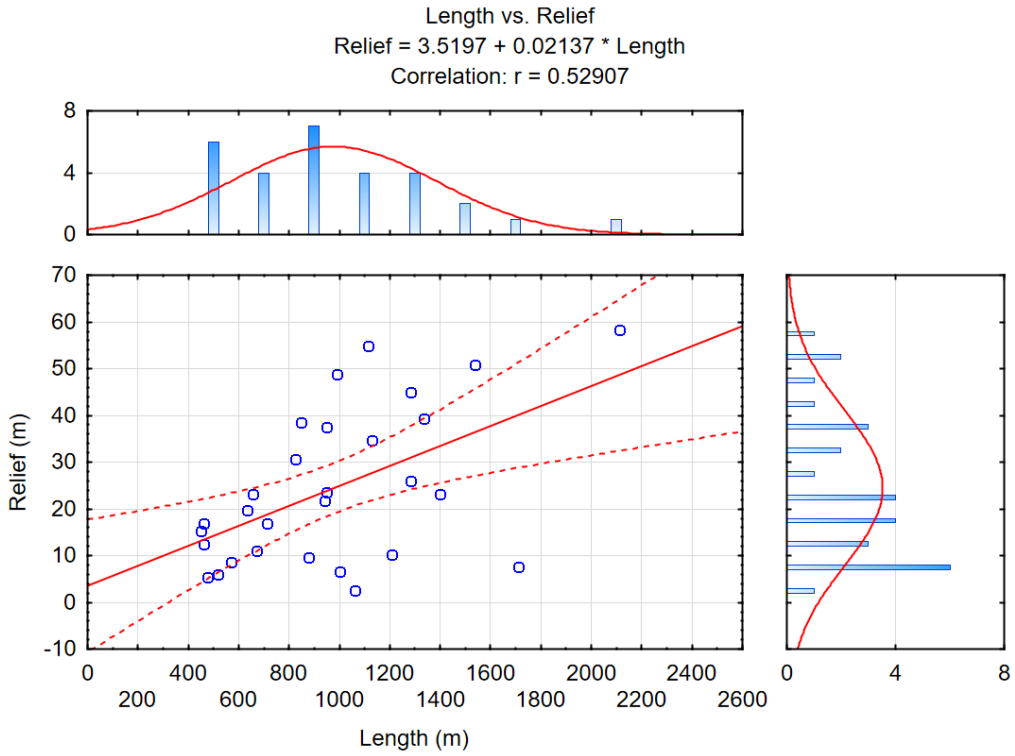

Figure 4.9. Scatter plot showing the correlation (r) between morphometric variables length and relief, and the 95 % confidence intervals (red dashed curves). The adjacent histograms show the classes defined according to the main grid of the scatter plot.

The heads of the drumlin-like bedforms are often characterised by surrounding channel-like depressions (scours), highlighted trough standard curvature analysis (Figs. 4.4C and 4.10). According to Wellner et al. (2006) and Cofaigh et al. (2010), the channel-like depressions are associated to the interaction of subglacial meltwaters during or after the formation of the drumlin-like bedforms.

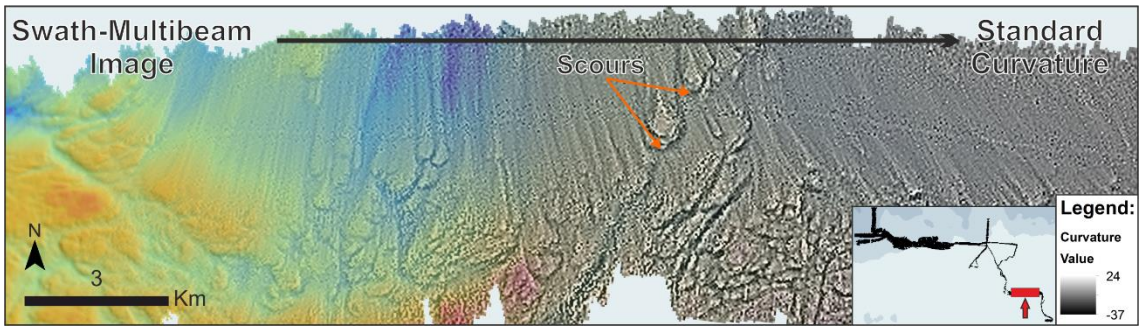

Figure 4.10. Superposition of standard curvature raster on top of the swath bathymetry imagery, with gradual transition. This figure demonstrates how convex forms (as drumlins-like bedforms) and concave forms (as channel-like depressions) can be highlighted.

The sub-bottom CHIRP profile along the drumlin-like field shows a high reflective surface with low acoustical penetration (Fig. 4.11). However, near the surface, a thin transparent acoustic unit is observed, which can probably correspond to a thin sediment layer. Longitudinal profiles from the drumlin-like bedforms exhibit irregular lee sides (Fig. 4.12), suggesting that those bedforms were formed in hard substrate (e.g. Evans et al., 2004).

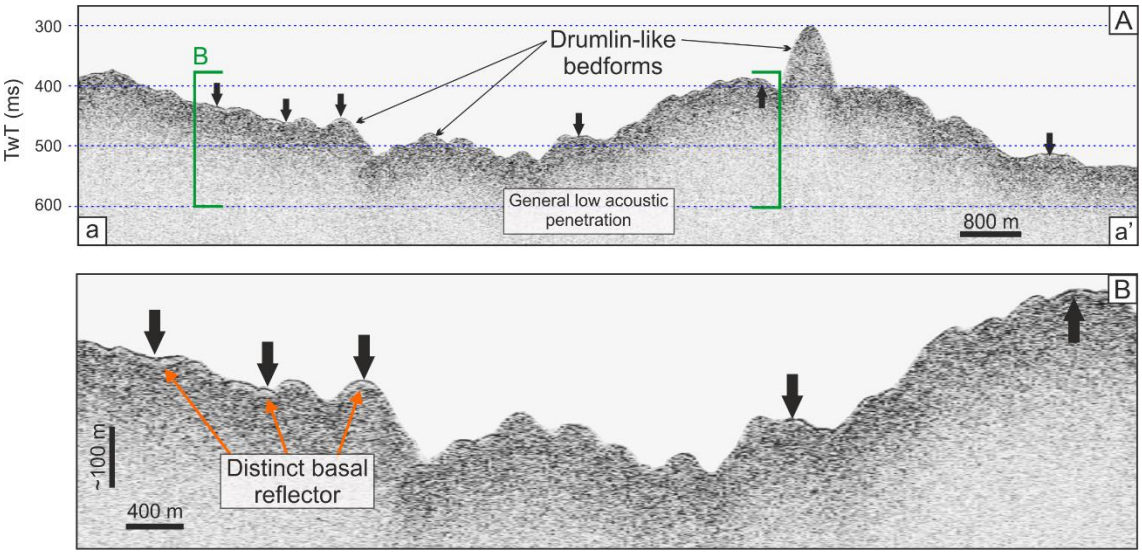

Figure 4.11. A- Sub-bottom Chirp profile along the drumlin-like field (for location see Fig. 4.4). The profile show general low acoustic penetration, and (**B**) a thin potential sediment layer (black arrow) covering some drumlin-like bedforms.

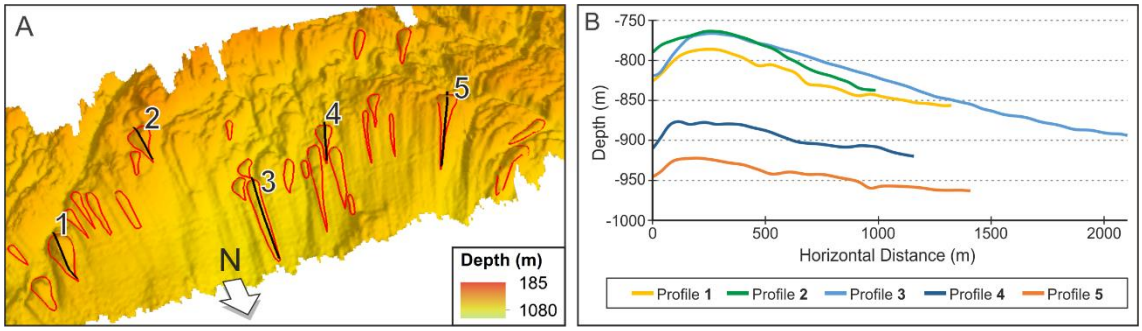

Figure 4.12. Longitudinal profiles taken from five identified drumlin-like bedforms: **A**- Three dimensional view of the drumlin-like filed; **B**- Graphical representation of profiles taken.

Analogous bedforms have been documented on the continental shelf of Antarctica and from other areas in the Arctic. The drumlin-like bedforms on the West Antarctica shelf are described as individual features of 5-10 km long and up to 100 m high (Wellner et al., 2006). The bedforms observed on the AP continental shelf are, generally, shorter (0.5 to 1.5 km long) and lower (tens of meters height) with 100-200 m wide (Anderson and Fretwell, 2008). Their elongation ratios show values (between 1 and 6), which are in

accord to typical drumlinised bedforms documented in literature, usually situated among the values 2-7 (see Clark et al., 2009).

4.1.3 Iceberg scours

Sporadic cases of furrows over the seafloor are identified on the outer continental shelf, generally around 450 m of depth. They are up to 1,000 m long and 10 m deep, irregular, and they have linear to curvilinear crosscutting pattern. The crosscutting and seemingly random orientation of these bedforms lead to interpret them as iceberg scours (or ploughmarks, see section 2.3.2) (Fig. 4.13). The iceberg scours are difficult to see on the bathymetric data, possibly due to insufficient data resolution or reduced deepness variation. However with curvature calculation (in profile view) their presence become more evident (Fig. 4.13B). The iceberg scours are generally confined to regions of 'softer' substrate and hardly manifested on the 'tougher' seafloor substrate (Graham et al., 2009). The sub-bottom chirp data show low acoustical penetration, suggesting that those features probably rest on relatively compacted sediments (Fig. 4.14). Occurrences of Iceberg scours have been imaged in West Antarctica in water depths < 570 m and in some cases down to 700 m on middle-outer trough regions (Evans et al., 2006; Lowe and Anderson, 2002). On the AP region, iceberg scours were documented in water depths lower than 450 m (Evans et al., 2005).

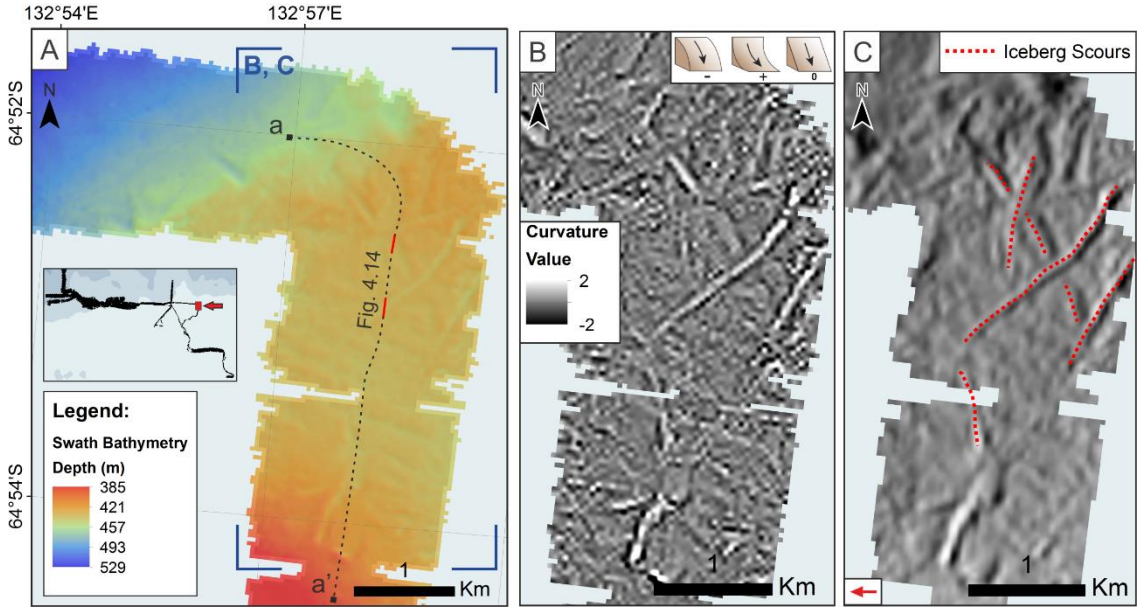

Figure 4.13. Iceberg scours observed on the outer continental shelf: **A**- shaded-relief swath bathymetric image; **B** - curvature index showing convex (dark colour) and concave (bright colour) forms; **C** - close up showing a more detailed representation (with a vertical exaggeration of 3).

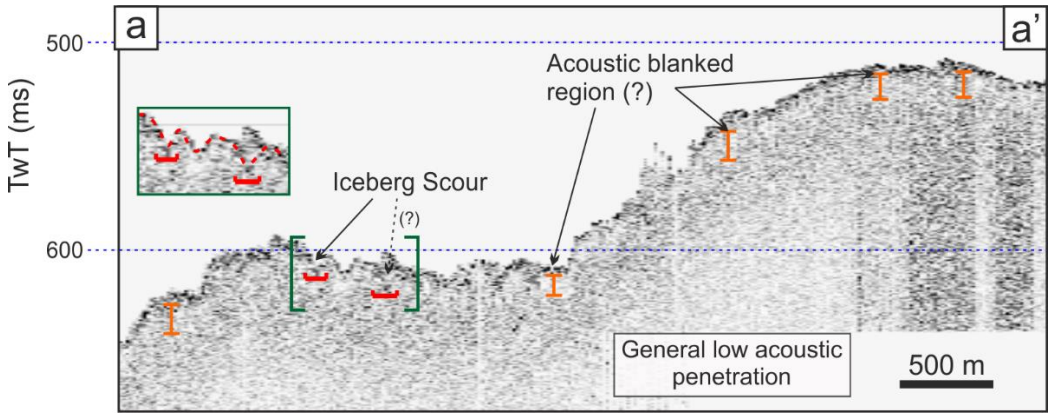

Figure 4.14. Sub-bottom chirp profile along the iceberg scours region. For location of the profile see Fig. 4.13A, where iceberg scours are identified by red segments.

Finally, from inner to outer continental shelf seafloor roughness was also characterised. A roughness analysis captures the variability on slope and aspect into a single measure. According to Wright et al. (2012), typical values for natural terrains range between 0 and about 0.4. The result shows a general relatively smooth surface, values are between 0 and 0.16 (Fig. 4.15). In the inner-middle shelf, generally high roughness values are caused by the presence of subglacial meltwater channels and drumlin-like bedforms. In the middle to outer continental shelf, the data show relatively low roughness values, in contrast with the previous region. It is important to keep in mind that the presence of certain multibeam artefact can also affect this type of data models.

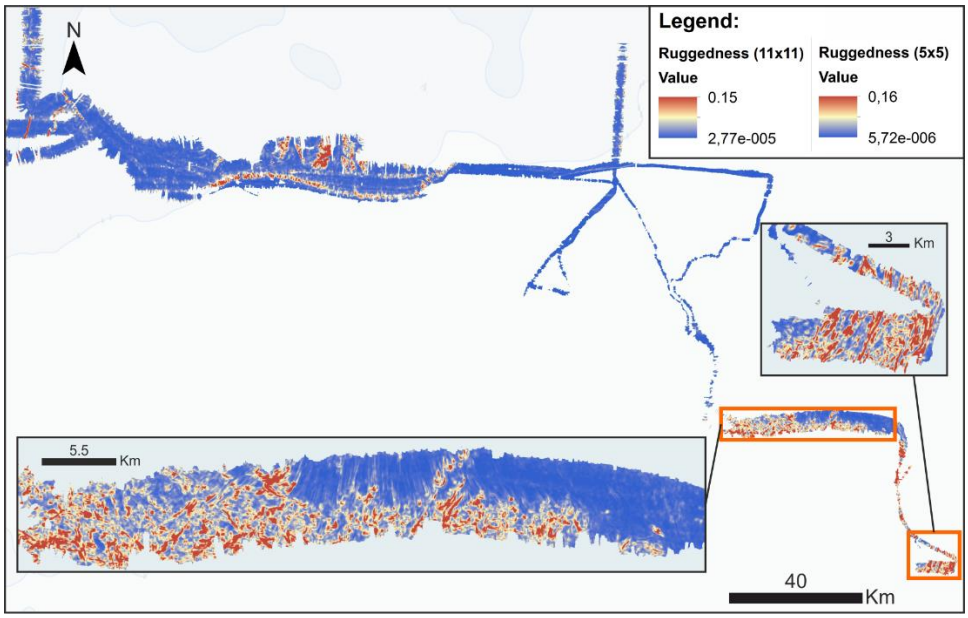

Figure 4.15. Roughness index over the swath bathymetry grid. On this image are displayed two roughness surfaces with neighbourhood size of 11x11 cells for the general multibeam data, and 5x5 for detailed inset figures.

4.2 Continental shelf edge and slope

The continental shelf edge in our study area is defined generally at 440 m water depth, reaching a minimum depth of 360 m in some parts. Seaward, the continental slope extends more than 5,000 m, from the continental edge to 1,400 m water depth, and dipping at an average of 9º.

The continental shelf edge and the uppermost part of the slope are predominantly dissected by numerous incisions, interpreted as submarine gullies. Those incisions become less expressive eastwards and give place to dispersed ridges and slide scars, indicative of significant mass wasting processes (Fig. 4.16).

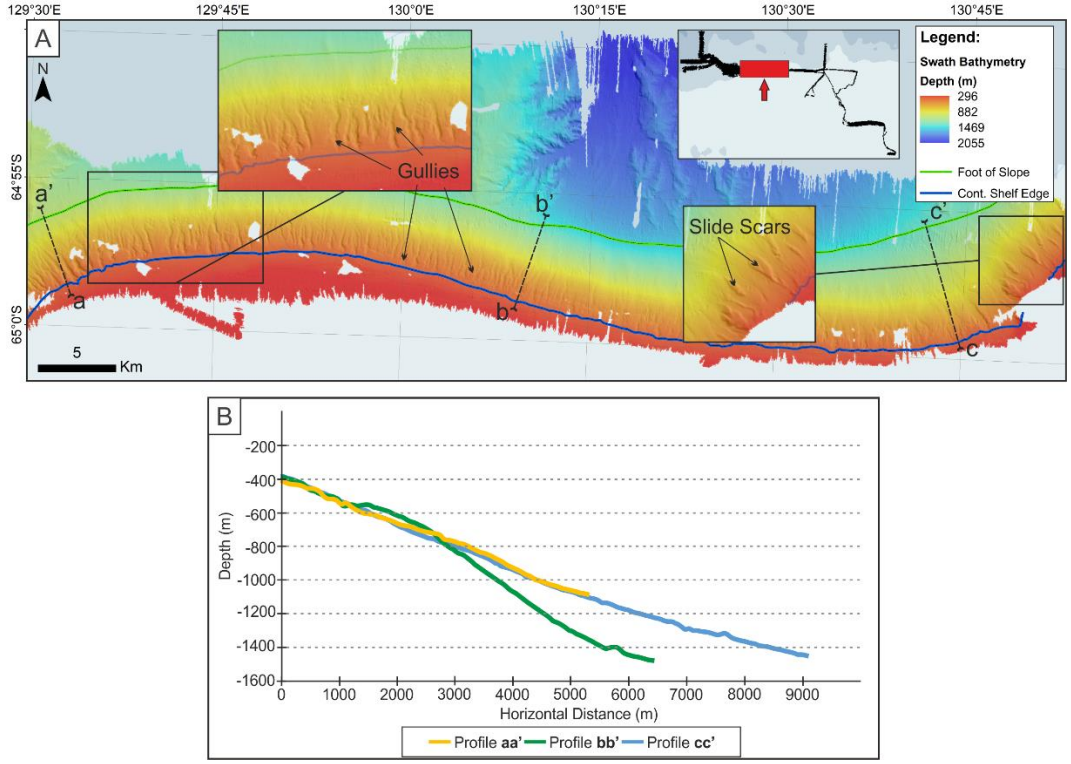

Figure 4.16. Swath bathymetry showing general morphology of the continental shelf margin (**A**).The general character of the slope is plotted on topographic profiles (**B**).

4.2.1 Submarine gullies

A concentration of closely spaced submarine gullies, eroded ravines, are visible in the uppermost continental slope regions regularly distributed between 129º30'E and 130º45'E (Fig. 4.17). In general, their starting points are found very close to shelf break, however in some cases, their incisions start (or become visible) downward.

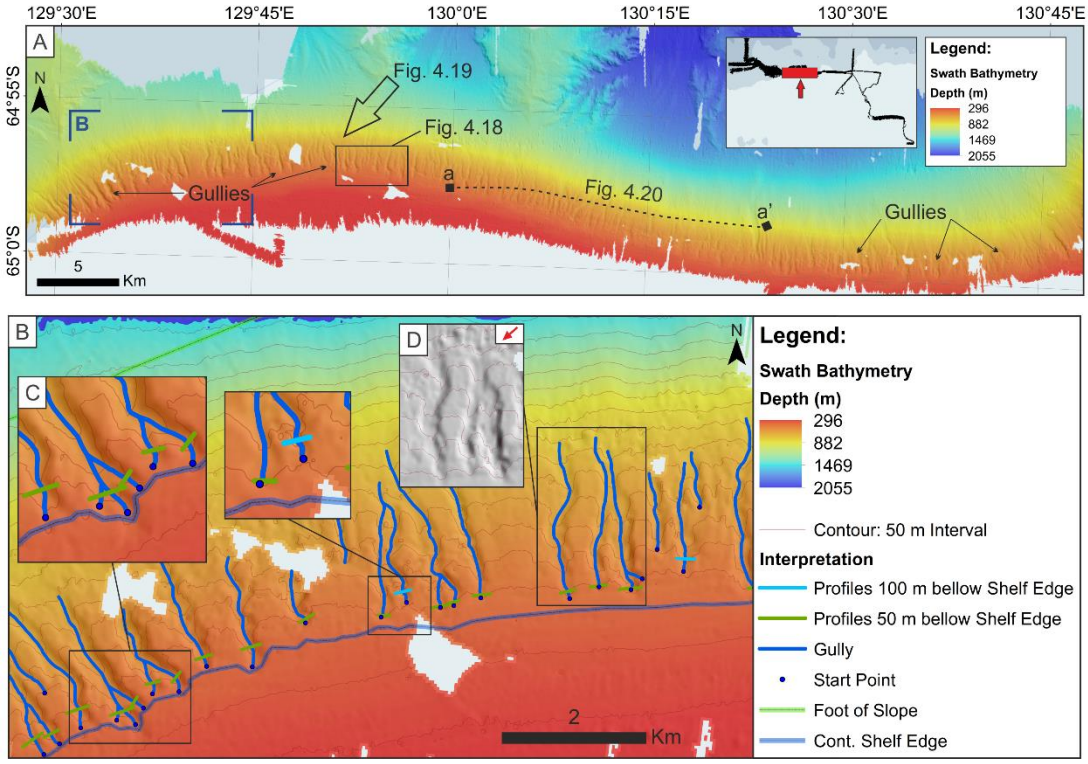

Figure 4.17. A- General swath bathymetry imagery along the continental slope showing **B**- analysed gullies for morphometric parameters, **C**- Close up on converging gullies and **D**- Shaded relief image showing the morphological aspect of the gullies.

The gully heads, generally found at the shelf edge in water depth between 510 and 550 m, are characterised by elongated and amphitheatre-like shaped depressions of 35-45 m depth and about 350 m wide (plan view). In some cases, second and third incisions are observed, converging into the main downslope incision (Fig. 4.18).

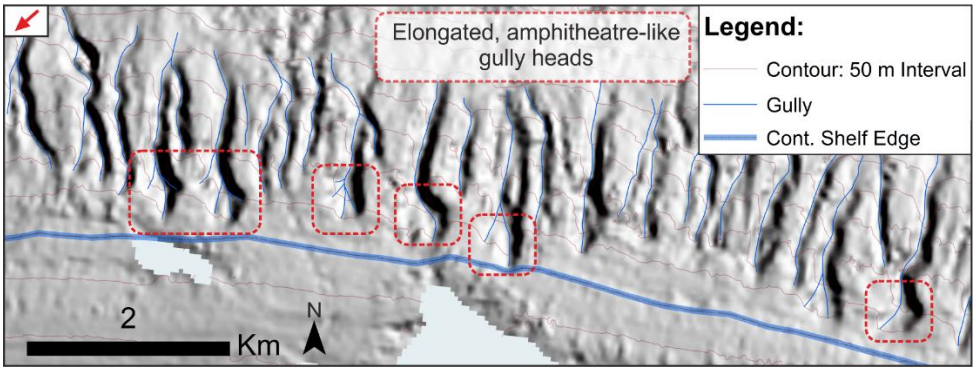

Figure 4.18. Shaded-relief image showing elongated and amphitheatre-like depressions formed at the upper stream area of the gullies (gully heads). Illumination with 45° azimuth and vertical exaggeration of 3.

In general, the course of the gullies is slightly sinuous and are developed downslope, with some cases of coalescence (branching gullies). The gullies are 790 to 3,880 m long,

averaging 1,900 m, 110 to 370 m wide, and from 5 to 45 m deep. In most of the cases, cross-section profiles show a V-shaped upstream part that changes gradually to a U-shape downslope (Fig. 4.19). In cases where the gullies have a U-shape upstream, the course of the gullies remains with this configuration until downslope (see Fig. 4.19 gully c). Most of the gullies show smoother relief around 900 m deep giving place to continental rise sediment mounds. The acoustical returns of the seismic records show low penetration of the signal into the gullies floor (Fig. 4.20).

From a total of 73 individual gullies mapped, 46 were analysed using cross-section depth profiles taken at 50 m below the shelf edge (gullies with starting point nearby the continental shelf limit) and 27 gullies with cross-section profiles taken at 100 m (when the starting point of the gullies was found down slope, see Fig. 4.17B). Due the fact that the profiles were taken at different relative positions (50 and 100 m) the 46 and 27 gullies were posteriorly categorised in two designated groups: Group A and B, respectively (see Appendix III). Both groups were submitted to a diagnostic diagram by Gales et al. (2013) for classification (see Fig. 3.13, Chapter 3). This classification is based on quantitative parameters such as gully branching order, depth, cross-sectional shape, sinuosity and length. According to this classification, three geomorphically distinct gully types (Type I, II, and IV) were identified for the Group A and Group B (Table 4-II and 4-III). However, a very low percentage of gullies fit the Gales' Antarctic classification and fulfil all imposed conditions.

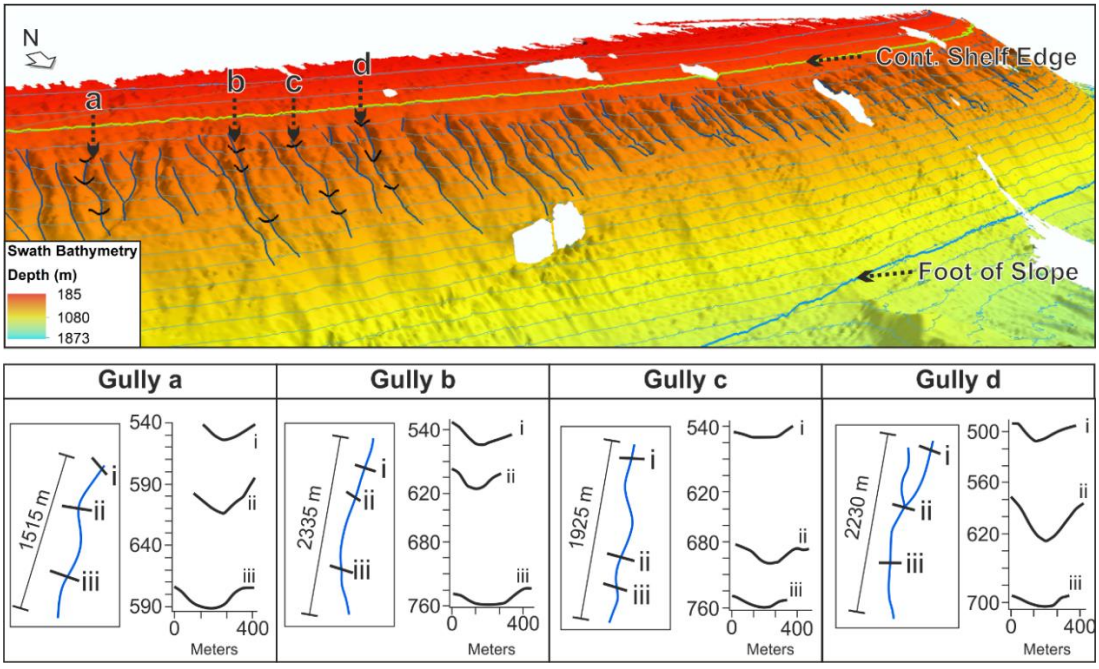

Figure 4.19. 3D perspective view of the shelf break and the continental slope showing morphological aspects of four sampled gullies (a, b, c and d). For each example, three cross-sections taken along the slope exhibit variation between U and V shapes.

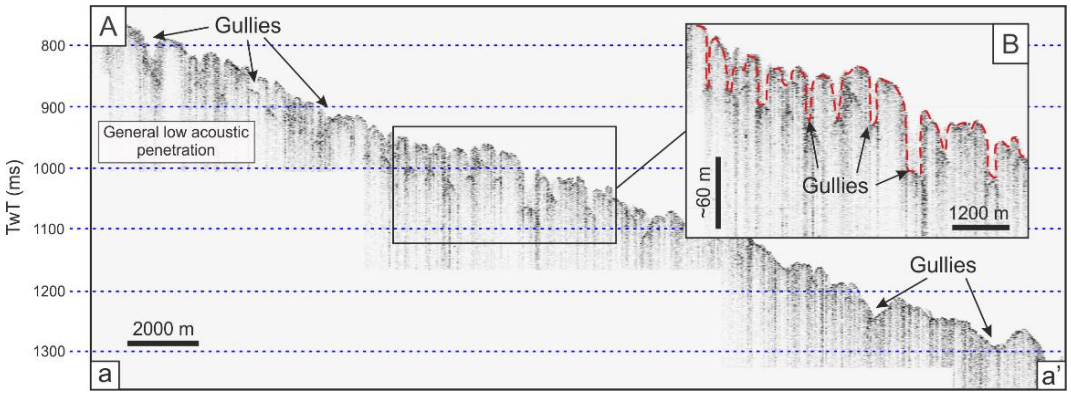

Figure 4.20. Sub-bottom profile taken from the continental shelf edge to lower slope regions showing the presence of gullies. On the inset figure **B** the seafloor is marked with a red dashed line to make gully incision more evident. For location see Fig. 4.17.

Table 4-II. Geomorphical Gully types found in Group A (gully set with cross section profiles taken 50 m bellow continental shelf edge).

	Group A - Observed Gully type					
Nº of Obs	**Type I**	**Type II**	**Type IIIa**	**Type IIIb**	**Type IV**	**No Class**
46	6	9	0	0	5	26
100%	13.00%	19.60%	0	0	10.70%	56.50%

Table 4-III. Geomorphical Gully types found in Group B (gully set with cross section profiles taken 100 m bellow continental shelf edge).

	Group B - Observed Gully type					
Nº of Obs	**Type I**	**Type II**	**Type IIIa**	**Type IIIb**	**Type IV**	**No Class**
27	1	2	0	0	1	23
100%	3.70%	7.40%	0	0	3.70%	85.20%

The morphological parameters used for the statistical analysis of the gullies are: cross-sectional shape index (b value), total length, sinuosity, width, incision depth and width/depth (W/D) ratio. However, it was not possible to determine the cross sectional shape index (b value, see table 3-II, Chapter 3) for all gullies. The General Power Law (GPL) algorithm could not obtain the index value to characterise the cross-sectional shape (U or V), possibly due to the topographic complexity of the taken profiles. Consequently, two gullies from Group A and seven gullies from Group B were left without classification and discarded from further statistical analysis. In that way the groups A and B are now defined by 44 and 20 elements, respectively.

The morphological parameters of the 44 gullies from the Group A present an unimodal distribution tendency (Fig. 4.21). The distribution character from all morphological parameters slightly differ from a normal distribution, as reported by the shape measurements of the kurtosis and the skewness. The frequency distributions show a positive excess kurtosis, a leptokurtic shape tendency, for the variables U/V index, length, incision depth and W/D. Their distributions have more data in their peak, meaning they are more clustered around the mean and has a relatively smaller standard deviation. With different behaviour the variable width is relative close to a mesokurtic shape, closely resembling to a normal frequency distribution. The morphological parameter sinuosity shows negative excess kurtosis and has a platykurtic distribution, i.e. the distribution has more data in its tails and less data in the peak. The asymmetry of the probability distribution for all the measured parameters is defined by a positive skew (right-skewed), with the exception of the length. The right-skewed distribution indicates that the distribution tail on the right side is longer or fatter than the left side. The positive skew values indicate that the mean and the median of the parameters are both greater than the mode, and the mean is greater than the median. In contrast, the distribution of the morphological parameter length shows a negative skew, meaning that the distribution tail is longer or fatter on the left side.

The Group B, with 26 samples, presents similar tendencies (Fig.4.22). This similarity extends also through other statistical measures, such mean and median. The most significant differences reside on the distribution shape between variables width and length. In this group differently from the results obtained in Group A, width presents a small negative kurtosis excess and length shows an accentuated positive kurtosis excess and positive skew.

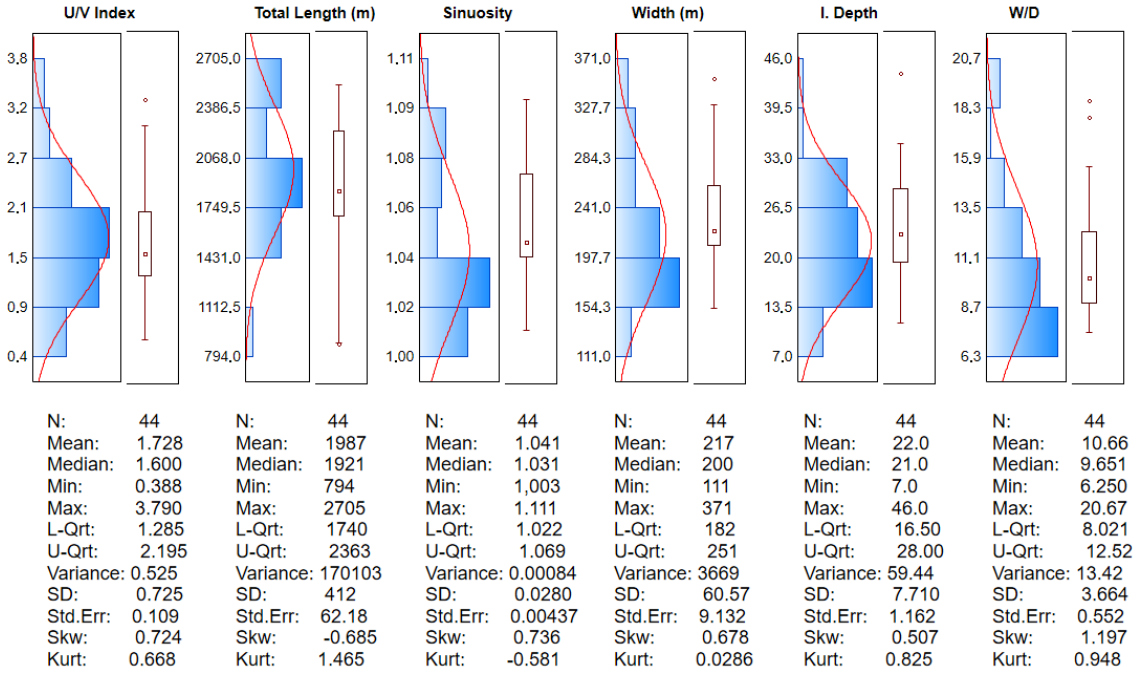

Figure 4.21. Graphical summary and descriptive statistics of gully parameters at 50 m below shelf break: U/V index, length, sinuosity width, depth and W/D. The modal classes for each parameter are respectively: 1.5-2.1; 2068-1750 m; 1.02-1.04; 154-198 m; 14-20 m and 6.3-8.7. The class number was defined though empirical rule of: $2^K > N$, where k is the number of classes and N the number of samples. Superimposed on the histograms is represented the best fit Gaussian curve (in red).

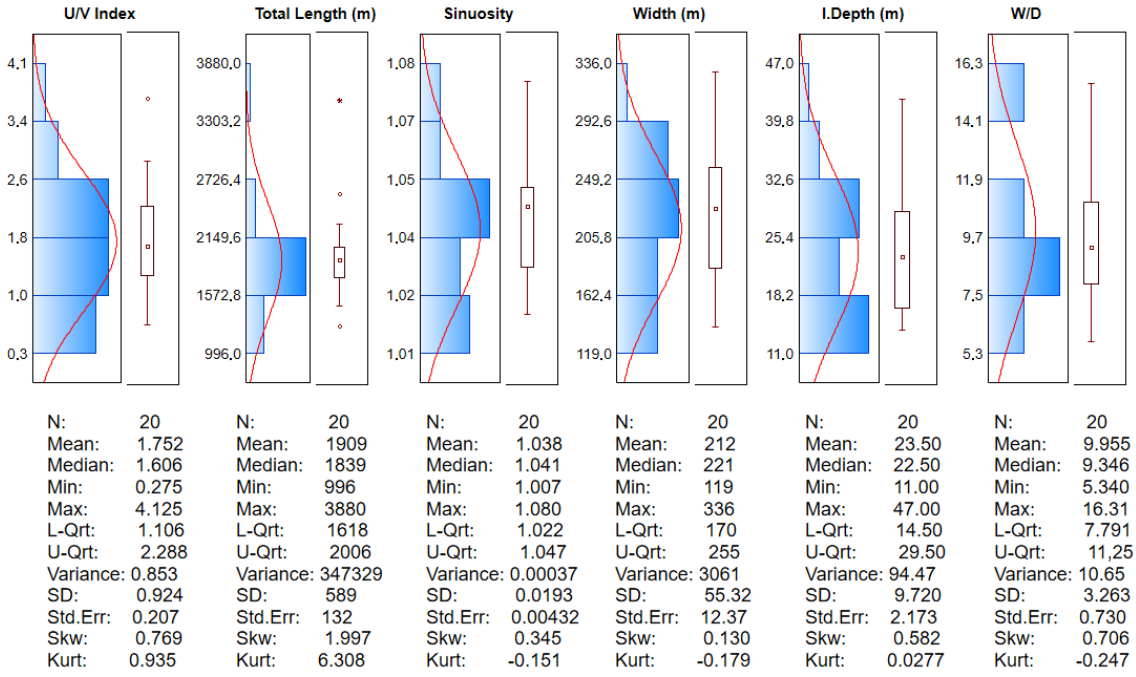

Figure 4.22. Graphical summary and descriptive statistics of gully parameters at 100 m below shelf break: U/V index, Length, Sinuosity width, depth and W/D. The modal classes for each parameter are respectively: 1-2.6; 1572-2150 m; 1.04-1.05; 206-249 m; 11-18 m and 7.5-9.7. The class number was defined though empirical rule of: $2^K > N$, where k is the number of classes and N the number of samples. Superimposed on the histograms is represented the best fit Gaussian curve (in red).

Because of the potential similarity, both groups were submitted to a multivariate analysis based on the Principal Component Analysis (PCA) to emphasise variation and bring out strong patterns in the morphological parameters. The purpose to run a PCA is to provide a statistically privileged view of the data set and to find which parameters are the most important to characterize the two gullies groups and to test their similarity level. A PCA allows to interpret the data in a more meaningful form, reducing the number of variables (the morphological parameters) in interpretable linear combinations of the data. Each linear combination will correspond to a principal component (PC). For this case, the number of the PC (six) is equal to the number of the morphological parameters (original variables).

Figure 4.23 shows the plot of the eigenvalues of the variance-covariance matrix and the proportion of variation (%) explained by the PCs. The results show that about 32% of the variation is explained by the first eigenvalue (largest possible variance), and 75% of the variance by the first three components. Usually, components which represent 70-80% of the cumulative variance in the data set are considered sufficient for the interpretation (e.g. Suhr, 2005).

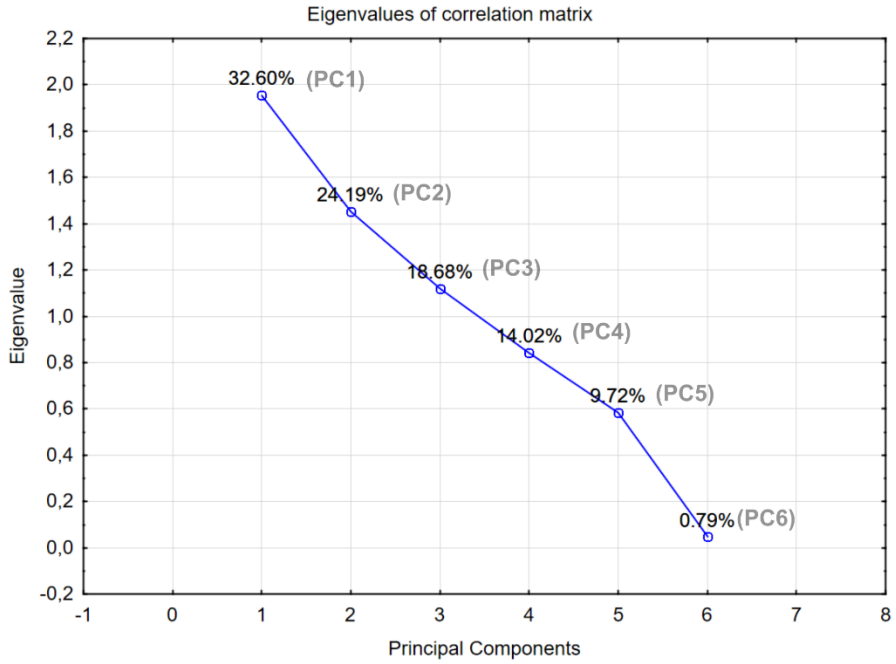

Figure 4.23. Screen plot showing the six PCs and the proportion of variation (%) explained by the PCs.

The interpretation of the PCs is based on finding which variables (morphological parameters) are most strongly correlated with each component. In this study, a correlation value above 0.5, in either positive or negative direction, is deemed important. Considering the variables relation to the first three components (Table 4-IV), the first PC

is strongly correlated with three of the original variables, the incision depth, width and W/D ratio (score values of 0.91, 0.69 and 0.50, respectively). This suggests that these three criteria vary together, and the PC1 correlates most strongly with the incision depth of the gullies. The second PC is correlated also with three of the morphological parameters, increasing W/D ratio, decreasing width and length (score values of 0.81, 0.56 and 0.51, respectively). The third PC variability is mostly resented by increasing length and U/V index (with score values of 0.71 and 0.61, respectively) suggesting that long gullies also tend to have high U/V index. Considering those components and scores we have reasons to infer that most representative parameters for both populations of gullies involve aspects of cross-sectional profile (mainly incision depth and width) and then the longitudinal parameter length.

Table 4-IV. Variable correlations for the first three principal components of the PCA. The larger considered correlations are in boldface.

	PC 1	PC 2	PC 3
U/V Index	-0.46	-0.31	**0.61**
Length (m)	-0.08	**-0.51**	**-0.71**
Sinuosity	0.44	0.20	-0.38
Width (m)	**-0.69**	**-0.56**	-0.15
Depth (m)	**-0.91**	0.28	-0.23
W/D	**0.50**	**-0.81**	0.15

Combining different components we can obtain the most representative variance plans of the data set. Considering the gullies on the components space, it is possible to understand their relations and consequently detect any case of similarity between gullies that belong to the Groups A and B. PCA score plots from the combinations: PC1-PC2 and PC1-PC3 do not reveal different or individualised clusters, meaning that all gullies have close similarity as was inferred before in the univariate statistics (Fig. 4.24). In that way the morphological parameters in the two main groups, A and B, can be studied together, as a single population.

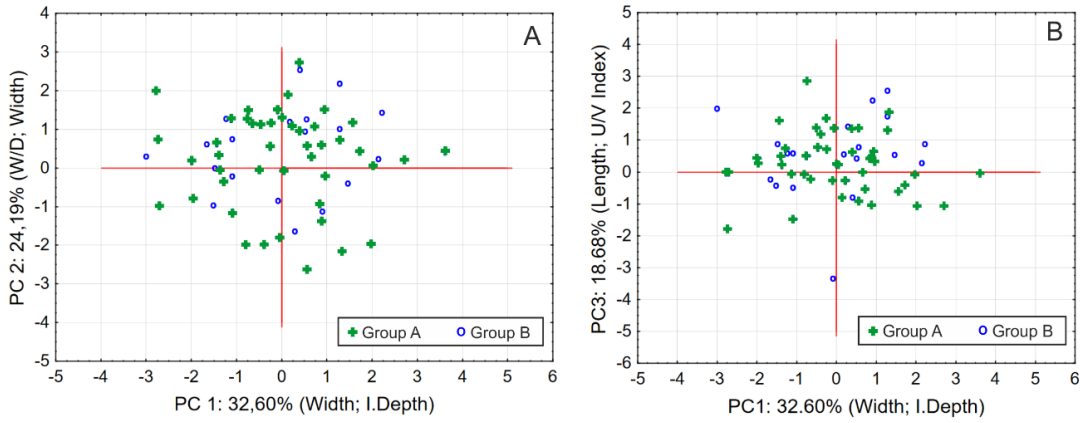

Figure 4.24. Score plot from the combinations of PC1-PC2 (**A**) and PC1-PC3 (**B**) for Groups A (green cross) and B (blue circle). The most representative variables (parameters) for each PC are also indicated on the plots.

According to the distributions of the morphological parameters from the unified groups, A and B, most of the gullies have U/V index between 1,3 and 1,9, which means that the cross-section profiles are closer to U-shaped profiles (b>2). The gullies length distribution shows a modal class of 1,675-2,116 m, representing 38% of the total samples, and mean value of 1,962 m. Most of the gullies have width values concentrated between 150 and 200 m and the sinuosity tendency varies from 1.01 to 1.03 (straight features). Finally, looking at the W/D ratio, most of gullies are between 7.5 and 9.7. All the distributions from this data set reveals asymmetrical tendencies (Fig. 4.25).

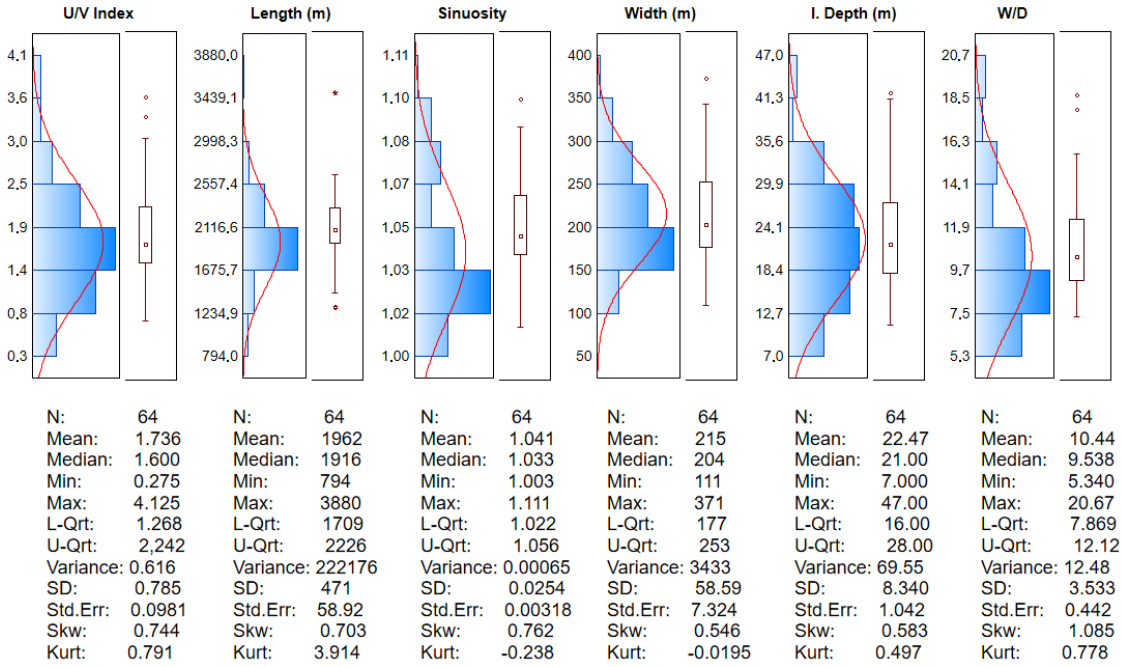

Figure 4.25. Graphical summary and descriptive statistics of gully parameters of joined Groups A and B: U/V index, length, sinuosity width, depth and W/D. The modal classes for each parameter are respectively: 1.4-1.9; 1676-2117 m; 1.02-1.03; 150-200 m; 18-24 m and 7.5-9.7. The class number was defined though empirical rule of: $2^K > N$, where k is the number of classes and N the number of samples. Superimposed on the histograms is represented the best fit Gaussian curve (in red).

In a more general aspect, the continental slope shows inclinations mostly between 3-8º on the upper parts, increasing the steepness on mid slope (8-14º), and decreasing gradually reaching the continental rise (Fig. 4.26). The seafloor roughness of the shelf edge and slope regions is characterised by relatively high roughness values, where gullies are observed (Fig. 4.27). Gullies found along the continental shelf edge are relatively well documented specially on the West Antarctic region (e.g. Gales, 2013; Noormets et al., 2009; Evans et al., 2006). The studied gullies system shows cross-section profiles between 419-891 m width and incision depths between 12-53 m. The bedforms are also observed on the AP shelf (e.g. Amblas et al. 2006; Canals et al. 2016).

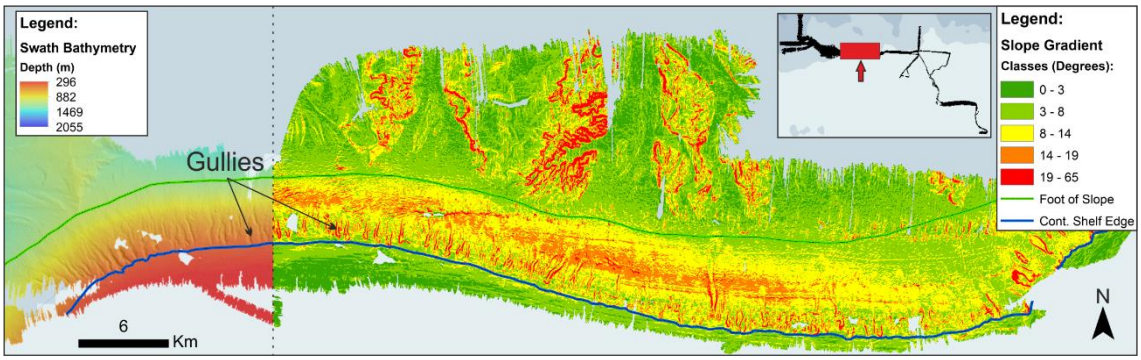

Figure 4.26. Slope grid surface represented by a colour scale between green (low steepness values) and red (high steepness values).

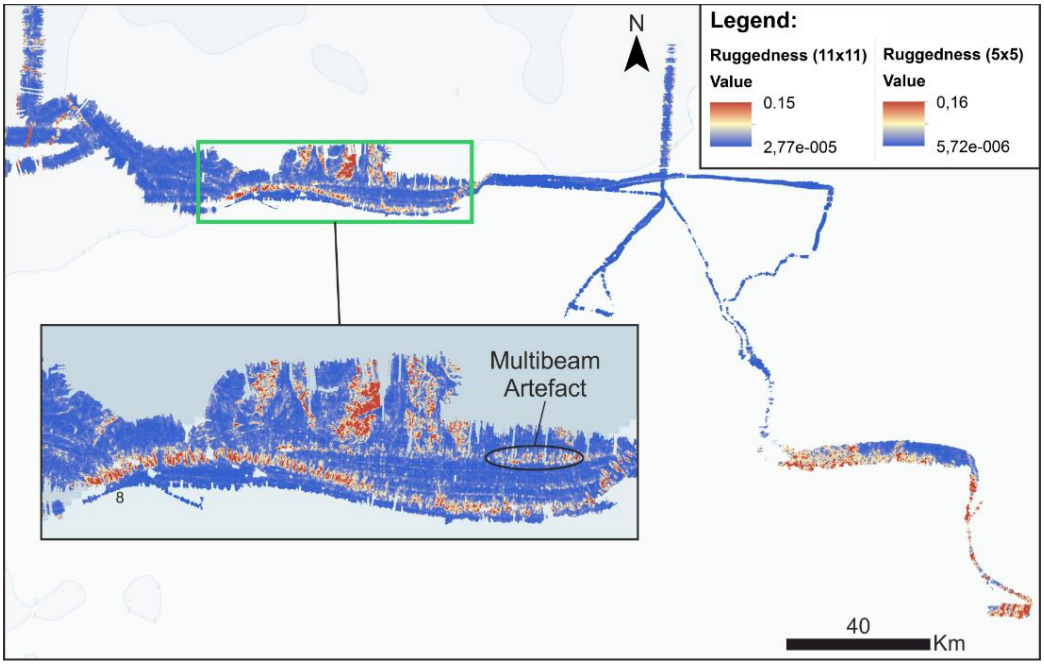

Figure 4.27. Roughness index over the swath bathymetry grid. On this image are displayed two roughness surfaces with neighbourhood size of 11x11 cells for the general multibeam data, and 5x5 for detailed inset figure.

4.3 Continental rise

The continental rise represents the transition between the continental slope and the deep ocean floor (abyssal plain). In the study area, large elongate mounds oriented perpendicular to the shelf edge and a large channel are the main features observed.

The sediment mounds are defined by a narrow and long crest, and dendritic v-shaped eroded ravines along their walls down to a flat seafloor, probably the seafloor of large channels In general, the mound tops lay at about 175-350 m above the flat seafloor and are roughly asymmetrical (with steeper side on west side). The two shallowest mounds are nearly attached to the continental slope (Fig. 4.28). The sub-bottom CHIRP records over the sediment mounds show basal reflector (Fig.4.29) that, probably, indicate the presence of sediments. The sediment mounds are well documented on the AP continental rise by Rebesco et al. (2007) and Amblas et al. (2006). The imaged sediment mounds by Amblas et al. (2006) lay at about 500–1,000 m above the canyon-channel system axes.

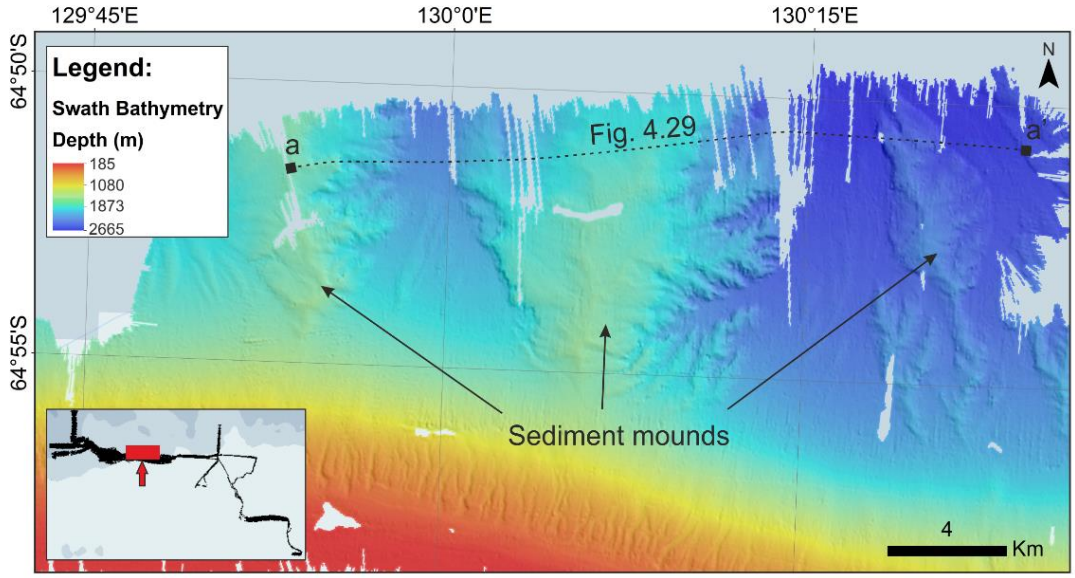

Figure 4.28. Swath bathymetry image showing three sediment mounds with their crest, sub-perpendicular to the continental shelf edge, and the pervasive dendritic v-shaped eroded ravines

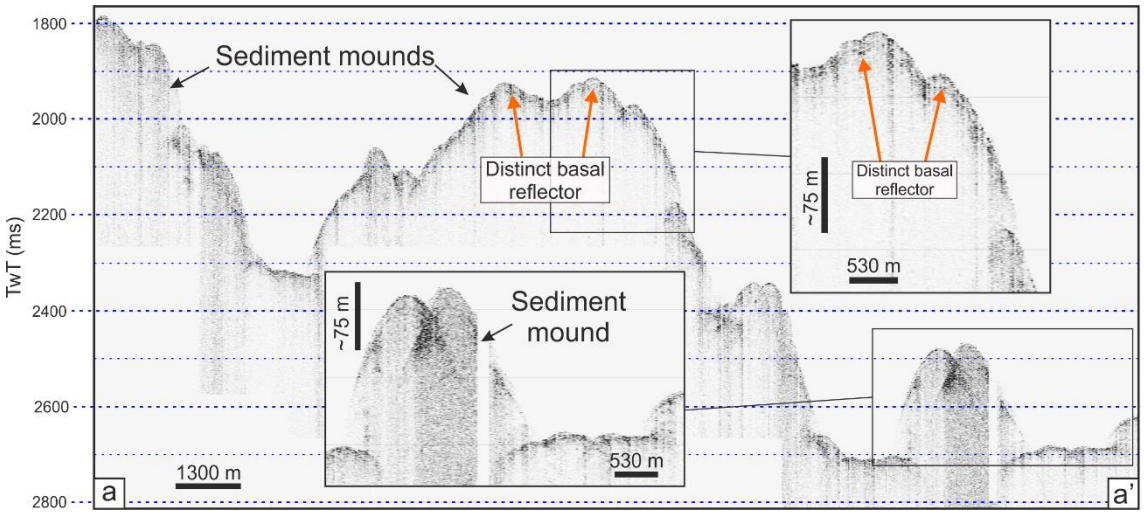

Figure 4.29. Sub-bottom profile which intercepts the tree sediment mounds. For location see Fig. 4.28.

With a great extension but not a very expressive depth, a channelized form is found along the continental rise (Fig. 4.30). The channel start down cutting at 1,600 m water depth. It averages 4,000 m wide and, considering the limits of the swath bathymetry data, is more than 30 km long. The wide channel is around 100 m deep and its course shows a linear shape. According to the location of the channel, we suppose that the channel ends on the abyssal plain.

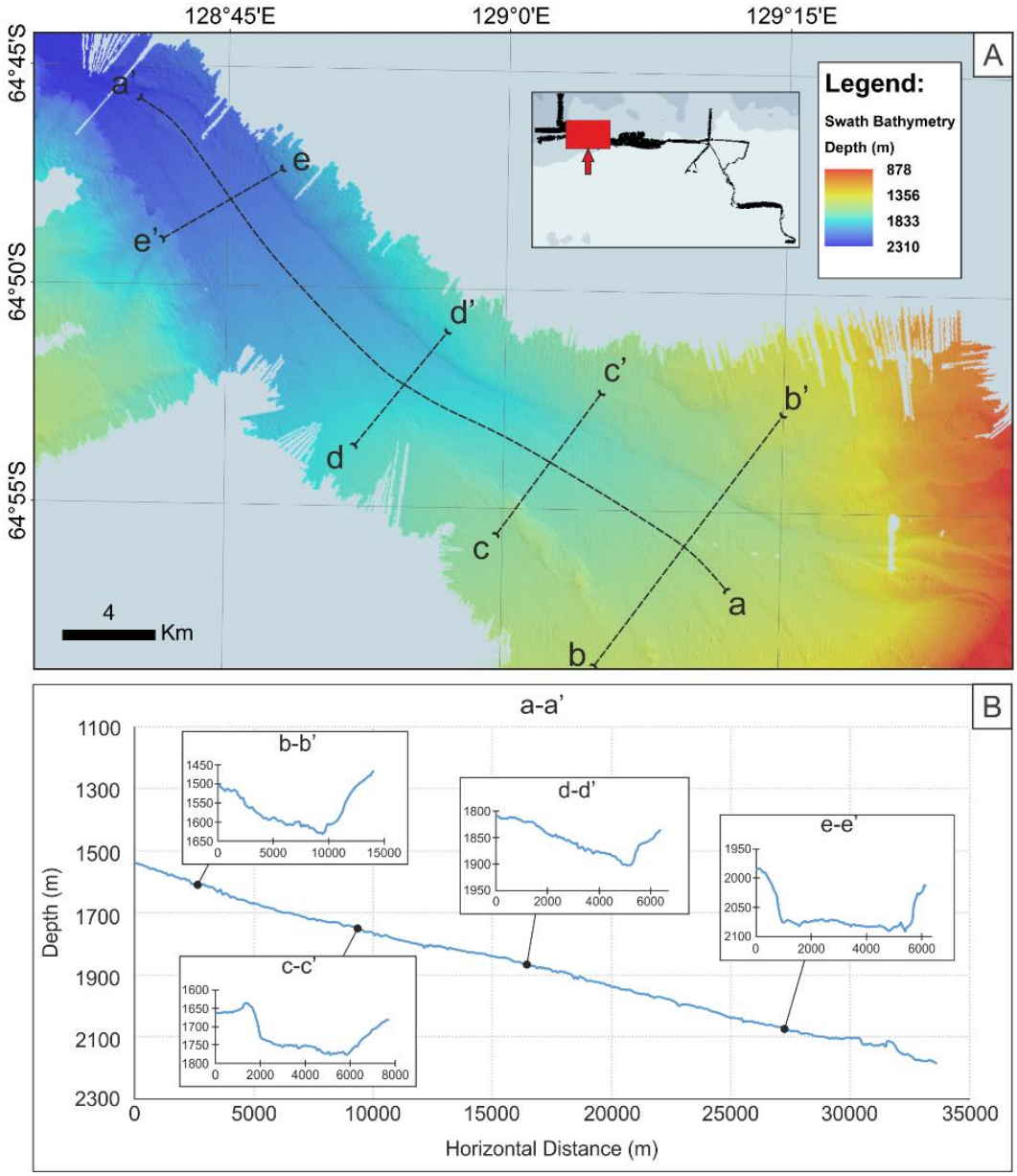

Figure 4.30. Swath bathymetry image showing the wide channelised bedform which extends more than 30 km long (A). Several profiles where taken to demonstrate the general character of the channel (B).

References

Amblas, D., Urgeles, R., Canals, M., Calafat, A. M., Rebesco, M., Camerlenghi, A., ... and Hughes-Clarke, J. E., **2006**. Relationship between continental rise development and palaeo-ice sheet dynamics, Northern Antarctic Peninsula Pacific margin. *Quaternary Science Reviews*, 25(9), 933-944.

Anderson, J. B., and **Fretwell**, L. O., **2008**. Geomorphology of the onset area of a paleo-ice stream, Marguerite Bay, Antarctic Peninsula. *Earth Surface Processes and Landforms*, 33(4), 503-512.

Bates, R.L. and **Jackson**, J.A. (Editors), **1980**. *Glossary of Geology*. Am. Geol. Inst., Falls Church, Va., 2nd ed., 749 pp.

Bennett, R.W. and **Glasser**, N. F., **2009**. *Glacial Geology*. 2nd Ed. UK: John Wiley and Sons Ltd.

Canals, M., Amblas, D., Domack, E. W., Lastras, G., Lavoie, C., Casamor, J. L., and Smith, C, **2016**. The seafloor imprint of the Gerlache–Boyd ice stream (65–62 S), northern Antarctic Peninsula. Geological Society, London, Memoirs, 46(1), 477-484.

Clark, C. D., Hughes, A. L., Greenwood, S. L., Spagnolo, M., and Ng, F. S. **2009**. Size and shape characteristics of drumlins, derived from a large sample, and associated scaling laws. Quaternary Science Reviews, 28(7), 677-692.

Cofaigh, C. Ó., Dowdeswell, J. A., King, E. C., Anderson, J. B., Clark, C. D., Evans, D. J., ... and Stokes, C. R., **2010**. Comment on Shaw J., Pugin, A. and Young, R.(2008):"A meltwater origin for Antarctic shelf bedforms with special attention to megalineations", Geomorphology 102, 364–375. *Geomorphology*, 117(1), 195-198.

Domack, E., Amblas, D., Gilbert, R., Brachfeld, S., Camerlenghi, A., Rebesco, M., ... and Urgeles, R., **2006**. Subglacial morphology and glacial evolution of the Palmer deep outlet system, Antarctic Peninsula. *Geomorphology*, 75(1), 125-142.

Evans, J., Dowdeswell, J. A., and Cofaigh, C. Ó., **2004**. Late Quaternary submarine bedforms and ice-sheet flow in Gerlache Strait and on the adjacent continental shelf, Antarctic Peninsula. *Journal of Quaternary Science*, 19(4), 397-407.

Evans, J., Dowdeswell, J. A., Cofaigh, C. Ó., Benham, T. J., and Anderson, J. B., **2006**. Extent and dynamics of the West Antarctic Ice Sheet on the outer continental shelf of Pine Island Bay during the last glaciation. *Marine Geology*, 230(1), 53-72.

Evans, J., Pudsey, C. J., ÓCofaigh, C., Morris, P., and Domack, E., **2005**. Late Quaternary glacial history, flow dynamics and sedimentation along the eastern margin of the Antarctic Peninsula Ice Sheet. *Quaternary Science Reviews*, 24(5), 741-774.

Gales, J. A., **2013**. The geomorphology of Antarctic submarine slopes. (Doctor of Philosophy Thesis), University of Manchester.

Gales, J. A., Larter, R. D., Mitchell, N. C., and Dowdeswell, J. A. **2013**. Geomorphic signature of Antarctic submarine gullies: implications for continental slope processes. *Marine Geology*, 337, 112-124.

Graham, A. G., Larter, R. D., Gohl, K., Hillenbrand, C. D., Smith, J. A., and Kuhn, G., **2009**. Bedform signature of a West Antarctic palaeo-ice stream reveals a multi-temporal record of flow and substrate control. *Quaternary Science Reviews*, 28(25), 2774-2793.

Hogan, K.A., Dowdeswell, J.A., Noormets, R., Evans, J., Ó Cofaigh, C. and Jakobsson, M., **2010**. Submarine landforms and ice-sheet flow in the Kvitoya Trough, northwestern Barents Sea. *Quaternary Science Reviews* 29, 3545-3562.

Larter, R.B., Graham, A.G.C., Gohl, K., Kuhn, G., Hillenbrand, C.D., Smith, J.A., Deen, T.J., Livermore, R.A., Schenke, H.W., **2009**. Subglacial bedforms reveal complex basal regime in a zone of paleo-ice stream convergence, Amundsen Sea Embayment, West Antarctica. *Geology* 37, 411-414.

Lowe, A. L., and **Anderson**, J. B., **2002**. Reconstruction of the West Antarctic ice sheet in Pine Island Bay during the Last Glacial Maximum and its subsequent retreat history. *Quaternary Science Reviews*, 21(16), 1879-1897.

Lowe, A. L., and **Anderson**, J. B., **2003**. Evidence for abundant subglacial meltwater beneath the paleo-ice sheet in Pine Island Bay, Antarctica. *Journal of Glaciology*, 49(164), 125-138.

Noormets, R., Dowdeswell, J. A., Larter, R. D., Cofaigh, C. Ó., and Evans, J., **2009**. Morphology of the upper continental slope in the Bellingshausen and Amundsen Seas–Implications for sedimentary processes at the shelf edge of West Antarctica. *Marine Geology*, 258(1), 100-114.

Rebesco, M., Camerlenghi, A., Volpi, V., Neagu, C., Accettella, D., Lindberg, B., ... and Party, M., **2007**. Interaction of processes and importance of contourites: insights from the detailed morphology of sediment Drift 7, Antarctica. *Geological Society, London, Special Publications*, 276(1), 95-110.

Spagnolo, M., Clark, C. D., and Hughes, A. L. **2012**. *Drumlin relief. Geomorphology*, 153, 179-191.

Suhr, D. D., **2005**. *Principal component analysis vs. exploratory factor analysis*. SUGI 30 proceedings, 203, 230.

Wellner, J. S., Heroy, D. C., and Anderson, J. B., **2006**. The death mask of the Antarctic ice sheet: comparison of glacial geomorphic features across the continental shelf. *Geomorphology*, 75(1), 157-171.

Wellner, J. S., Lowe, A. L., Shipp, S. S., and Anderson, J. B., **2001**. Distribution of glacial geomorphic features on the Antarctic continental shelf and correlation with substrate: implications for ice behavior. *Journal of Glaciology*, 47(158), 397-411.

Wright, D. J., Pendleton, M., Boulware, J., Walbridge, S., Gerlt, B., Eslinger, D., ... and Huntley, E., **2012**. ArcGIS Benthic Terrain Modeler (BTM), v. 3.0, Environmental Systems Research Institute, NOAA Coastal Services Center, Massachusetts Office of Coastal Zone Management. *esriurl. com/5754*.

CHAPTER 5:
Discussion

5.1 Glacial bedforms context and control factors

The different seabed features described in this study (Table 5-I) are not unique, but they are described in detail for the first time on the East Antarctic continental shelf. Similar bedforms have been found on West Antarctic, AP and Arctic continental shelves, slopes and rises.

Part of the inner shelf between Frost and Dibble Glaciers (between 128º E and 134º E) is defined by the presence of irregular crudely streamlined bedforms and subglacial meltwater channels. Moreover, it is expected that the channel network extends beyond the acquired data for this part of the continental shelf. The subglacial meltwater channels are the result of the seabed erosion by meltwater circulation beneath a paleo grounded ice sheet (Wellnner et al., 2001; Bennett and Glasser, 2009). The meltwater sources can be related to surface melting processes where water flowed down the base of the ice sheet through moulins (glacier mills) and crevasses, and to the most common source: basal melting processes. The subglacial melting is possibly caused by the combination of the ice thickness, geothermal heat and frictional heating during ice flow events (Eyles, 2006; Llubes et al., 2006; Bennett and Glasser, 2009; Nitsche et al., 2013). Indeed, according to Llubes et al. (2006), the EAIS is allied to important geothermal fluxes, which contribute to increased the melting rates (Fig. 5.1).The presence of elongated meltwater channels with considerable dimensions indicates that water drainage/erosion occurred at high hydrostatic pressures and for long periods of time on impermeable subtract (e.g. Sugden et al., 1991), such as crystalline bedrock as our sub-bottom profiles suggested. The predominant direction of the water flows in the study area is difficult to infer due to the limited bathymetry coverage, and because the subglacial water circulations are mainly controlled by the hydraulic potential gradient, which in this case depend of ice sheet (glacier) surface slope, the topography beneath and its geological characters (Bennett and Glasser, 2009). One question regarding the subglacial meltwater channels observed on the Antarctic continental shelf remains barely tested: what is the age of those erosional features. Are they originated from the last glaciation, i.e. during the LGM, or they are much older?

Northward, on the mid shelf, subglacial meltwater channels are still visible along an irregular topography also defined by the presence of irregular crudely streamlined bedforms. The meltwater features have smaller scale when compared with previous region, but still represent significant volumes of water flow from the continent and perhaps at catastrophically times (Wellner et al., 2006).

Table 5-I. Summarized morphology of the bedforms observed in the continental shelf, slope and rise, and their comparison (West Antarctica and AP).

Interpreted Bedforms	Geometry Description (Min-Max)	Potential Substrate Type	Figure	Example (Citation)
Meltwater Channels	Deep: 80-119 m; Width: 300-900 m.	Crystalline Bedrock	Fig. 4.2	Lowe and Anderson, 2003; Domack et al., 2006
Drumlin-like bedforms	Length: 450-2111 m; Width: 104-568 m; Elongation ratios 1-6; Relief: 3-58 m.	Hard till or even bedrock	Fig. 4.4.	Anderson and Fretwell (2008); Wellner et al., 2006
Iceberg Scours	Water depths: 380-490 m	Soft till	Fig. 4.13	Evans et al., 2006; Lowe and Anderson, 2002; Evans et al., 2005
Submarine Gullies	U/V index: 0.2-4.1; Width: 11-371 m, Incision depth: 7-47; W/D ratio: 5-21; Length: 794-3880, Sinuosity: 1-1.1	Glaciamarine deposits	Fig. 4.17	Gales, 2013; Noormets et al., 2009; Evans et al., 2006
Sediment Mounds	Elevation (from the general flat seafloor) : 175-350 m	Sediment	Fig. 4.28	Rebesco et al., 2007; Amblas et al., 2006

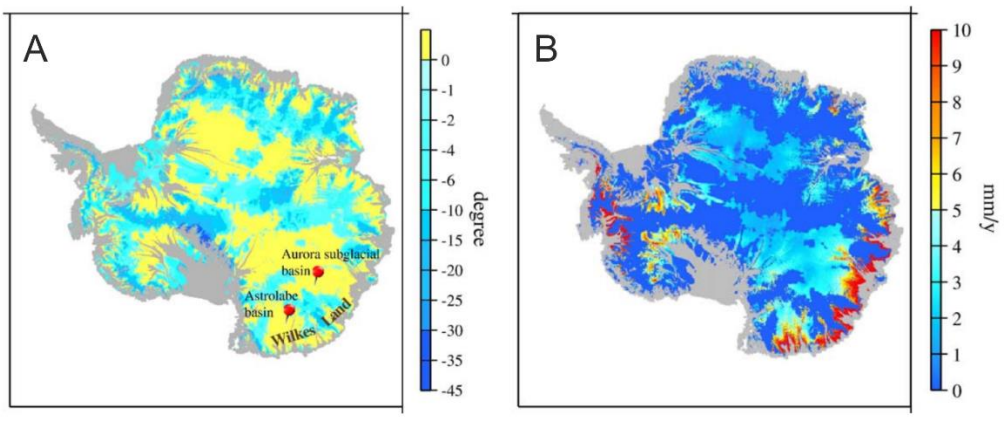

Figure 5.1. A- Modelled basal temperatures based on geothermal flux values (inferred trough crustal age and identified geological units). The yellow areas correspond to melted ice at the base of Antarctic ice sheet; B- Ice melting rate estimate for the Antarctic ice sheet from the geothermal flux influence. Image adapted from Llubes et al. (2006).

A set of bedforms, including drumlin-like bedforms and MSGLs (mega scale glacial lineations), characterises the seafloor of the mid continental shelf, in front of the irregular crudely streamlined and subglacial meltwater channels topography. Those streamlined bedforms are genetically related and often thought to be indicative of ice streaming (e.g. Graham et al., 2009; Stokes et al., 2013). The transition to this lineated topography (drumlin-like bedforms and MSGLs) occurs abruptly, pointing a transition to a paleo-ice flow acceleration and confluence (Anderson et al., 2001; Wellner et al., 2006). The spatial variations in bedforms size and shape suggest that the seabed has been moulded by non-uniform factors (Fig. 5.2). The factors can be small-scale variations on basal conditions such as meltwater circulation, local topography and outcrops, as well as changing in ice flow conditions over time (Graham et al., 2009). The complex basal conditions can explain simultaneous presence and distribution of the drumlin-like bedforms and MGSLs. Considering that those bedforms were generated along unconsolidated substrates, the paleo grounded ice could flowed over a mixture of stiffer and weak till (subglacial sediment) where the drumlins-like bedforms should be associated to the stiffer glacial till (e.g. Stokes et al., 2011). The crescentic overdeepenings observed around the stoss side of some drumlin-like bedforms indicate warmed-based ice and free water beneath parts of the former ice sheet (Downdeswell et al., 2010). Moreover, the visible connections between the drumlin-like bedforms and an upstream meltwater channels system also shows the important role of the subglacial meltwater on their formation. This observation clearly supports the theory that drumlins characterised with crescentic scours are associated to subglacial meltwater erosion, an hypothesis defended by Cofaigh et al. (2010). With higher elongations, the MSGLs are typically associated to soft sediments (e.g. Graham et al., 2009; Stokes et al., 2013), which offer less resistance to the ice flow and, consequently, will generate more attenuated and elongated shapes.

As shown before the measurement of morphological parameters (morphometry) on the drumlin-like bedforms revealed important clues to infer with more details the ice dynamics involved to their formation, as Clark et al. (2009) and Spagnolo et al. (2012) tried to demonstrate. Statistical analyses from measured parameters (length, width, elongation ratio and relief) show single peaked distributions, meaning that all considered drumlin-like bedforms belong to a single population. This result allow us to propose that their formation are probably related to a single glacial event during a same period of time, and not to successive glaciations over time. Analysing the frequency distributions, was verified a positive skewness for all parameters. According to Clark et al. (2009), the distribution shapes of the drumlins are associated to the physical conditions during their

formation, suggesting that a left side tail is associated to a physical threshold which means the drumlins do not form below certain parameter values. On the other hand, the right side tail suggests that there is not a defined physical threshold in this direction.

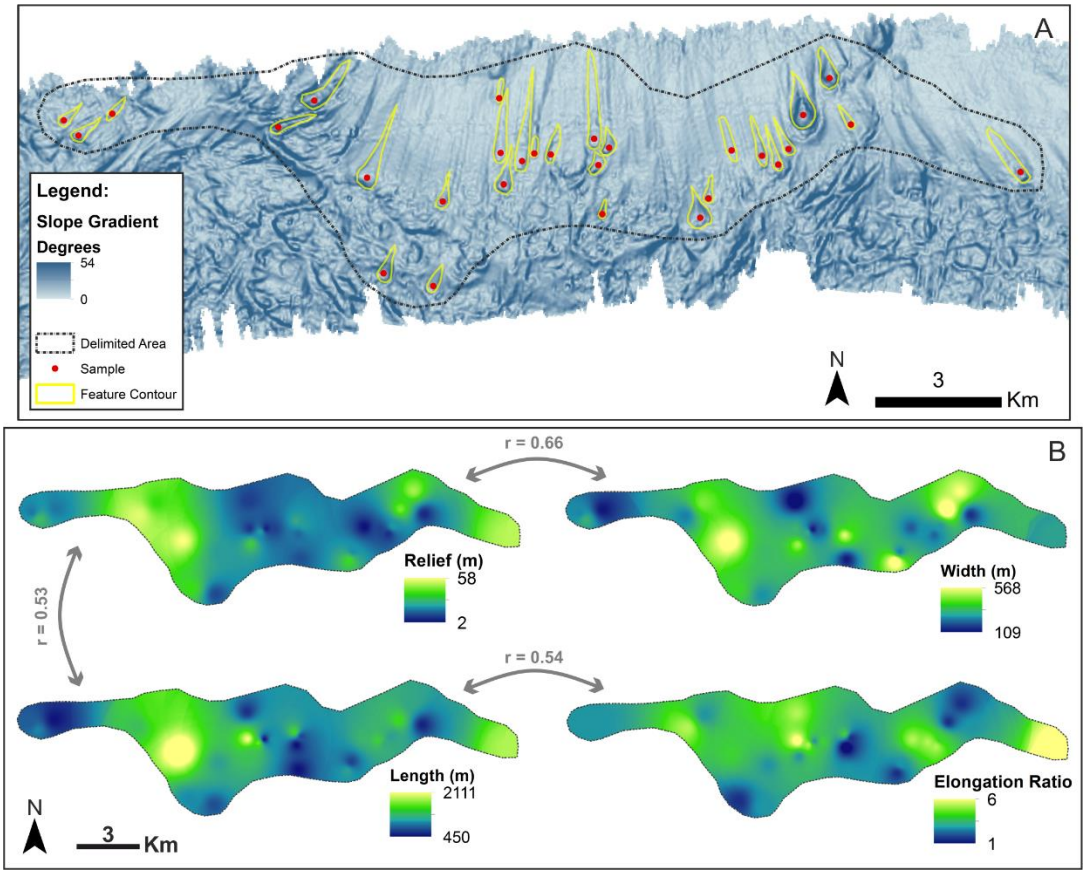

Figure 5.2. Slope gradient map (A) and spatial interpolation of drumlin parameters (relief, length, width and elongation ratio) based on 29 validated samples through the regression method IDW (Inverse Distance Weighting) (B).

Looking at the potential relationships between morphologic parameters, it was found in this study the strongest correlations between the variable pairs: relief-width and elongation ratio-length. The strong and positive correlation (r=0.66) of the pair relief-width possibly indicates that the drumlins-like needed a large base to stand against the ice flow during their formation (Spagnolo et al., 2012). Besides, the significant correlation observed between the cluster elongation ratio-length does not represent a surprising relationship, since the elongation ratio values are dependent of the length. However, it is possible to verify that drumlin-like bedforms are not created with fixed proportions of the elongation ratios, as Clark et al. (2009) suggested. For instance, if the drumlin features had tendency to form with fixed proportions, the behaviour of the length in the elongation ratio (length/width) would be constant, which is not the case. This observation

can be illustrated through the drumlin formation model presented by Menzies et al. (2016) (Fig. 5.3).

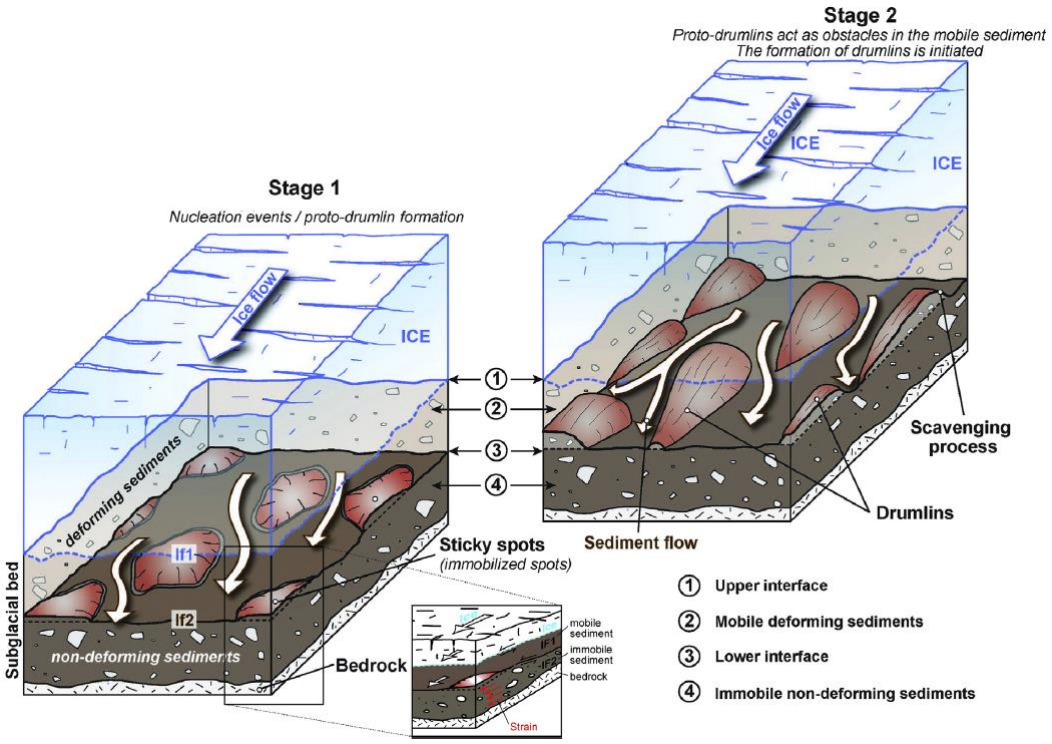

Figure 5.3. Drumlin formation considering sediment deformation/sediment flux rate fluctuation between the different interfaces. Image adapted from Menzies et al. (2016).

This positive correlation of elongation ratio-length also indirectly leads to interpret that the length has to grow faster than the width. Considering the relation between the morphometric variables length-width, despite the weak correlation coefficient (r=0.47) the best tendency line found (with r^2=0.29) makes evident that the length of the drumlin-like bedforms grown faster than their width (Fig. 5.4), although this tendency only explains 29% of the total variation in width.

Figure 5.4. Scatterplot showing the correlation between the morphometric variables length and width trough tendency lines.

The positive correlation of the pair of variables length-relief shows also a significant relationship, where the greater reliefs are associated to greater lengths. According to Spagnolo et al. (2012) this relation suggests that drumlins do not grow in length by redistributing sediments from their summits to their lee sides, differently from what it was hypothesised in other studies (e.g. Piotrowski, 1989). The relationships and behaviour among the drumlin-like parameters in this study are in agreement with the studies of Spagnolo et al. (2012) and Clark et al. (2009). However, it is important to reinforce the idea that this analysis is not as much robust and precise when compared with those two studies.

Abundant incisions, identified as gullies, are observed along the shelf break and the upper continental slope. Those bedforms have been associated to erosion processes of non-cohesive deposits by subglacial meltwaters from beneath a paleo-ice margin grounded at the shelf break (Noormets et al., 2009; Wellner et al., 2006; Gales et al., 2013). With sediment load due the meltwater discharge the erosional processes can be triggered by turbidity current flows, being in that way an important mechanism for the formation of a gully system (Gales, 2013). Considering the presence of subglacial meltwaters, it should be expected the presence of subglacial meltwater flow features across the outer shelf, which are not observed in this study area. The absence of those features can be explained by the fact that the meltwater reached the shelf edge mainly either through the topmost soft sediment layers or in the form of dispersed flow beneath the ice cover (Noormets et al., 2009).

The numerous incisions observed along the shelf break and the upper most slope region, become less expressive eastwards and give place to dispersed ridges and slide scars. The concentration of more expressive gullies westwards is indicative of higher energy gully-eroding processes, possible related to additional meltwater flow in this area. Some of those gullies present elongated and amphitheatre-like shaped depressions found close to the shelf edge, which are associated to multi-stage sliding factor on gullies formation (Noormets et al., 2009). On the other hand, the lower expression of gullies on the east can be associated to relatively reduced energy gully-eroding processes. The occurrence of slide scars are associated to unstable and failure-prone uppermost slope, mostly associated with rapid sediment loading during glacial periods (Noormets et al., 2009). Therefore, the reduced expression of gullies on the eastern region could be attenuated or even erased by sediment loading and slope instability, which did not let a continuous development of well-expressed gullies as on the west region. This observation may lead to variable sedimentary conditions along the shelf break and the upper continental slope.

The measured gully parameters (branching order, incision depth, cross-sectional shape, sinuosity and length) were submitted into a classification process based on a diagnostic diagram proposed by Gales et al. (2013). However, only a reduced percentage of gullies could fit in Gales' classification. The resolution of the bathymetric image, can be a possible explanation, or the gullies parameters in this study area are distinct from the ones considered by Gales (2013) and point out that this classification cannot be used as a general model for Antarctica. Therefore, the statistical and spatial analysis was considered into a single gully population without any defined classes.

Analysing the measured morphometric parameters in relation with the slope map, it was observed that the continental slope geometry presents an important role on the gullies morphology, particularly on the length and sinuosity (Fig. 5.5). The higher sinuosity and the greater lengths of the gullies to the west and the central steeper regions, show that the morphological parameters present visible variations that follow the character of the continental slope. The higher steepness of the slope will enhance the dense water down-flow creating in this way sinuous and longer incisions on the continental slope (e.g. Noormets et al., 2009). The sediment load, heterogeneity and local roughness may also be an important factor for greater sinuosity values (e.g. Gales, 2013; Aswathy and Satheesh, 2008). According to Gales (2013), the gullies with high W/D ratios and U-shaped cross sections (e.g. central region) are generally associated to great bedload (reduced flow intensity), in opposition to the deeply incised and v-shaped gullies with low W/D ratios (e.g. west region) that are related to greater suspended

sediment load (higher flow intensity) (Fig. 5.6A). The central region, defined by relative high steepness and the presence of wider gullies with high sinuosity, high W/D ratios and U-shape cross sections, represented likely an intermediate state characterised by dense water down-flow and an important bedload transport linked to a reduced flow intensity. This observation could be explained by differences on the sedimentary structure associated with glacial-interglacial sedimentation, which can create plan of weakness and lead to small-scale slides creating wider shapes (Fig. 5.6B).

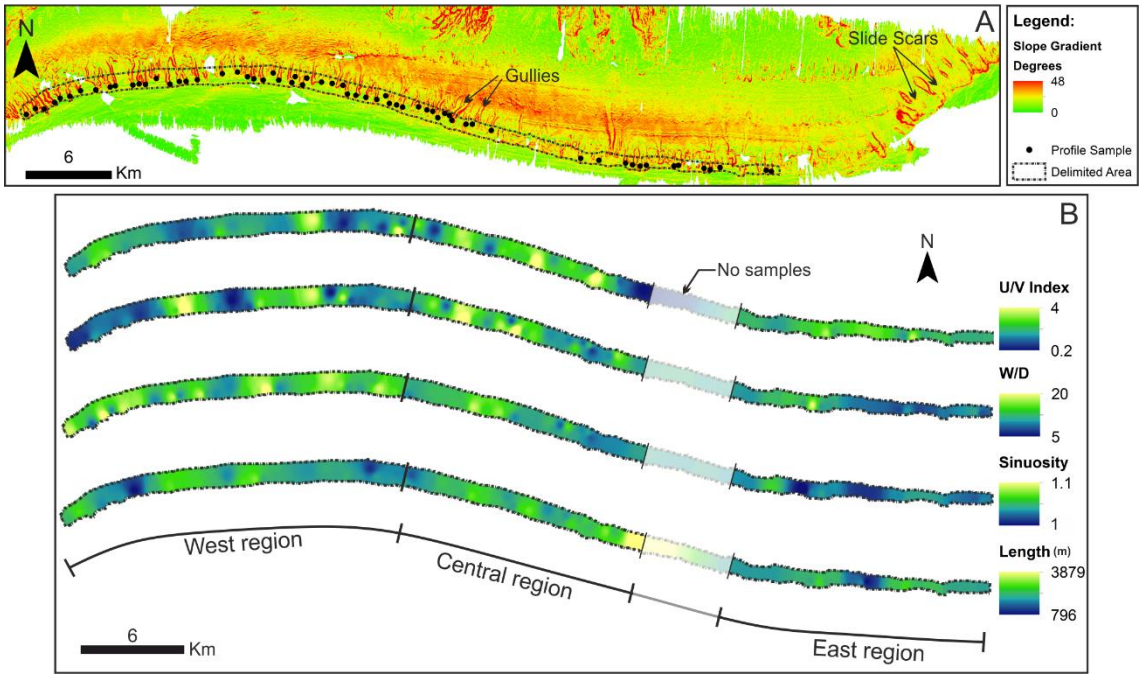

Figure 5.5. Slope gradient map (A) and spatial interpolation of gully parameters (U/V index, W/D, Sinuosity and Length) based on 64 validated samples trough the regression method IDW (Inverse Distance Weighting) (B).

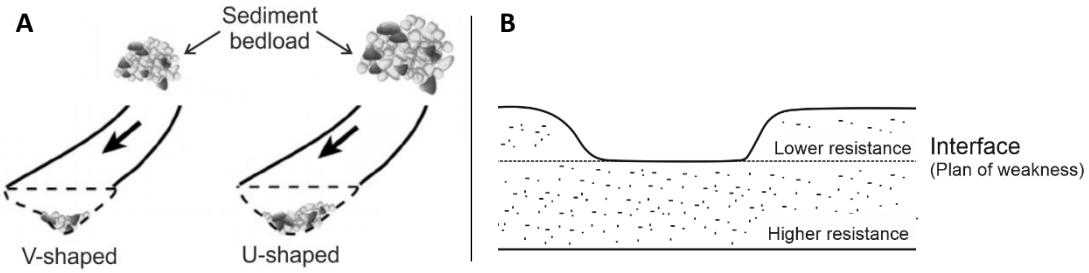

Figure 5.6. A - Schematic diagram showing the influence of sediment bedload on cross-sectional shape of a gully (adapted from Vietz et al., 2016). **B** - Potential influence sedimentary structure on gully cross sectional shape (adapted from: http://www.fao.org/docrep/006/ad082e/AD082e01.htm).

The smother character of lower slope regions suggest that the erosive processes were less effective there, and the sediment transport of the finer particles continues further to the base of the continental slope and the continental rise. The decreasing energy downwards lead to great sediment accumulations identified as sediment mounds on the continental rise. Those large volumes of sediment provided through erosion and transport of sediments by downslope processes from the outer continental shelf, together with an efficient system distribution of sediments along the continental rise created the conditions to form the mounds (e.g. Amblas et al., 2006; Rebesco et al., 2007). The most significant developments of this kind of features have been attributed to glacial periods (Amblas et al., 2006).

5.2 Extent and dynamics of the EAIS since LGM

The seafloor morphology found in the study area constitutes a strong evidence of past EAIS extension, probably from the last glacial maximum event (LGM) that occurred about 20,000-18,000 years ago (Ingólfsson et al., 1998). The spatial distribution of the identified glacial bedforms (Fig. 5.7) is coherent with other studies and models from Antarctica (e.g. Wellner et al., 2001, 2006; Graham et al., 2009), and appears to be conditioned by a number of factors such as the type of substrate, the topography, the amount of subglacial meltwater, the availability of sediments, and the internal behaviour and dynamics of the ice sheet.

The presence of the gully-channel system found along the continental shelf edge leads to interpret that the EAIS reached the shelf break during the past glaciation event. Unfortunately, we were unable to define a clear cross-shelf bathymetric trough associated to a fast-streaming ice path links to the shelf edge. The terrible sea ice conditions limited the acquirement of the data. However, we found evidences of streamlined subglacial features, such as drumlin-like bedforms and MSGLs, that are usually observed at the seafloor of a cross-shelf trough. The identified streamlined subglacial bedforms indicate a paleo-ice flow direction. However, because of the limited data coverage, it is not possible to predict the paleo-ice flow behaviour (i.e. changes of direction) from the inner to the outer continental shelf regions.

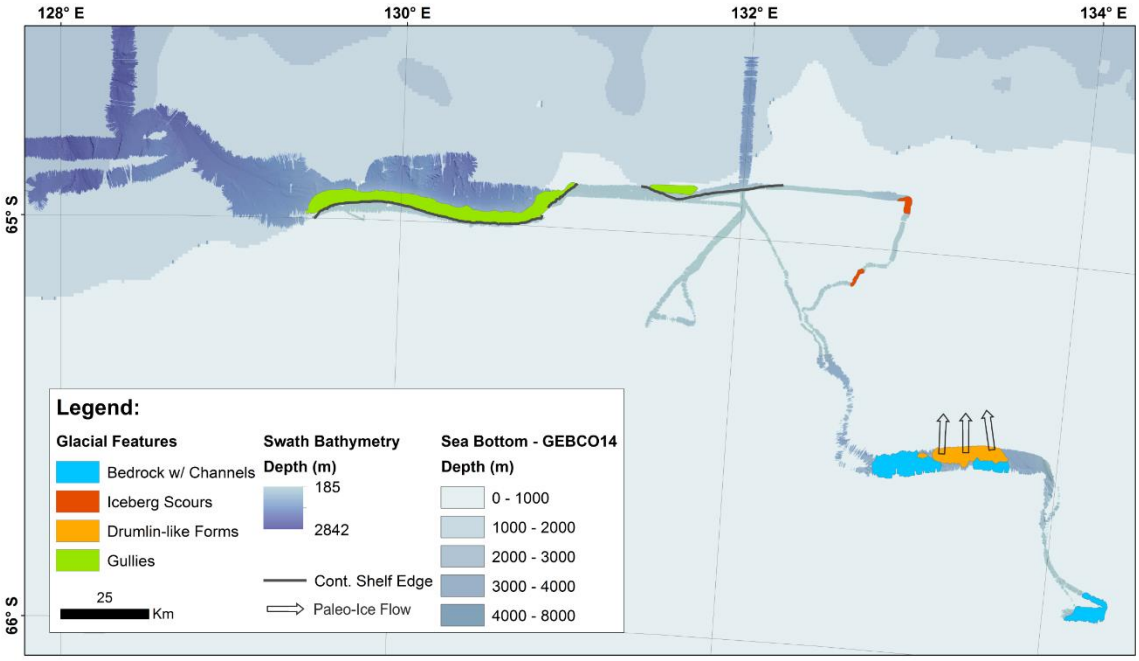

Figure 5.7. Distribution of geomorphic features identified in the study area and used to reconstruct the glacial history since LGM**.**

The deglaciation of the EAIS mostly began between ~14 kyr and 12 kyr before present (BP) (Mackintosh et al., 2011). From the available geophysical data, retreating events in the study area are documented by few calved icebergs from the margins, which scoured the seafloor in water depths between 380-490 m. The apparent absence of grounding line features suggest that the deglaciation would occur rapidly (e.g. Dowdeswell et al., 2008), however there is not enough data coverage to support this hypothesis.

References

Amblas, D., Urgeles, R., Canals, M., Calafat, A. M., Rebesco, M., Camerlenghi, A., ... and Hughes-Clarke, J. E., **2006**. Relationship between continental rise development and palaeo-ice sheet dynamics, Northern Antarctic Peninsula Pacific margin. *Quaternary Science Reviews*, 25(9), 933-944.

Anderson, J. B., and **Fretwell**, L. O., **2008**. Geomorphology of the onset area of a paleo-ice stream, Marguerite Bay, Antarctic Peninsula. *Earth Surface Processes and Landforms*, 33(4), 503-512.

Anderson, J. B., Wellner, J. S., Lowe, A. L., Mosola, A. B., and Shipp, S. S., **2001**. Footprint of the expanded West Antarctic Ice Sheet: ice stream history and behavior. *GSA today*, 11(10), 4-9.

Aswathy, M. V., Vijith, H., and Satheesh, R., **2008**. Factors influencing the sinuosity of Pannagon River, Kottayam, Kerala, India: An assessment using remote sensing and GIS. Environmental Monitoring and Assessment, 138(1-3), 173-180.

Bennett, R.W. and **Glasser**, N. F., **2009**. *Glacial Geology*. 2nd Ed. UK: John Wiley and Sons Ltd.

Clark, C. D., Hughes, A. L., Greenwood, S. L., Spagnolo, M., and Ng, F. S., **2009**. Size and shape characteristics of drumlins, derived from a large sample, and associated scaling laws. *Quaternary Science Reviews*, 28(7), 677-692.

Cofaigh, C. Ó., Dowdeswell, J. A., King, E. C., Anderson, J. B., Clark, C. D., Evans, D. J., ... and Stokes, C. R., **2010**. Comment on Shaw J., Pugin, A. and Young, R.(2008):"A meltwater origin for Antarctic shelf bedforms with special attention to megalineations", Geomorphology 102, 364–375. *Geomorphology*, 117(1), 195-198.

Domack, E., Amblas, D., Gilbert, R., Brachfeld, S., Camerlenghi, A., Rebesco, M., ... and Urgeles, R., **2006**. Subglacial morphology and glacial evolution of the Palmer deep outlet system, Antarctic Peninsula. *Geomorphology*, 75(1), 125-142.

Dowdeswell, J. A., Ottesen, D., Evans, J., Cofaigh, C. Ó., and Anderson, J. B., **2008**. Submarine glacial landforms and rates of ice-stream collapse. *Geology*, 36(10), 819-822.

Dowdeswell, J. A., Evans, J., and Cofaigh, C. Ó., **2010**. Submarine landforms and shallow acoustic stratigraphy of a 400 km-long fjord-shelf-slope transect, Kangerlussuaq margin, East Greenland. *Quaternary Science Reviews*, 29(25), 3359-3369.

Evans, J., Dowdeswell, J. A., Cofaigh, C. Ó., Benham, T. J., and Anderson, J. B., **2006**. Extent and dynamics of the West Antarctic Ice Sheet on the outer continental shelf of Pine Island Bay during the last glaciation. *Marine Geology*, 230(1), 53-72.

Evans, J., Pudsey, C. J., ÓCofaigh, C., Morris, P., and Domack, E., **2005**. Late Quaternary glacial history, flow dynamics and sedimentation along the eastern margin of the Antarctic Peninsula Ice Sheet. *Quaternary Science Reviews*, 24(5), 741-774.

Eyles, N., **2006**. The role of meltwater in glacial processes. *Sedimentary Geology*, 190(1), 257-268.

Gales, J. A., **2013**. The geomorphology of Antarctic submarine slopes. (Doctor of Philosophy Thesis), University of Manchester.

Gales, J. A., Larter, R. D., Mitchell, N. C., and Dowdeswell, J. A., **2013**. Geomorphic signature of Antarctic submarine gullies: implications for continental slope processes. *Marine Geology*, 337, 112-124.

Graham, A. G., Larter, R. D., Gohl, K., Hillenbrand, C. D., Smith, J. A., and Kuhn, G., **2009**. Bedform signature of a West Antarctic palaeo-ice stream reveals a multi-temporal record of flow and substrate control. *Quaternary Science Reviews*, 28(25), 2774-2793.

Ingólfsson, O., Hjort, C., Berkham, P.A., Björck, S., Colhoun, E., Goodwin, I.D., Hall, B., Hirakawa, K., Melles, M., Möller, P. and Prentice, M.L., **1998**. Antarctic glacial history since the Last Glacial Maximum: an overview of the record on land. *Antarctic Science* 10, pp. 326-344.

Llubes, M., Lanseau, C., and Rémy, F., **2006**. Relations between basal condition, subglacial hydrological networks and geothermal flux in Antarctica. *Earth and Planetary Science Letters*, 241(3), 655-662.

Lowe, A. L., and **Anderson**, J. B., **2002**. Reconstruction of the West Antarctic ice sheet in Pine Island Bay during the Last Glacial Maximum and its subsequent retreat history. *Quaternary Science Reviews*, 21(16), 1879-1897.

Lowe, A. L., and **Anderson**, J. B., **2003**. Evidence for abundant subglacial meltwater beneath the paleo-ice sheet in Pine Island Bay, Antarctica. *Journal of Glaciology*, 49(164), 125-138.

Mackintosh, A., Golledge, N., Domack, E., Dunbar, R., Leventer, A., White, D., ... and Gore, D., **2011**. Retreat of the East Antarctic ice sheet during the last glacial termination. Nature Geoscience, 4(3), 195-202.

Menzies, J., Hess, D. P., Rice, J. M., Wagner, K. G., and Ravier, E., **2016**. A case study in the New York Drumlin Field, an investigation using microsedimentology, resulting in the refinement of a theory of drumlin formation. *Sedimentary Geology*, 338, 84-96.

Nitsche, F. O., Gohl, K., Larter, R. D., Hillenbrand, C. D., Kuhn, G., Smith, J. A., ... and Jakobsson, M., **2013**. Paleo ice flow and subglacial meltwater dynamics in Pine Island Bay, West Antarctica. *The Cryosphere*, 7(1), 249-262.

Noormets, R., Dowdeswell, J. A., Larter, R. D., Cofaigh, C. Ó., and Evans, J., **2009**. Morphology of the upper continental slope in the Bellingshausen and Amundsen Seas–Implications for sedimentary processes at the shelf edge of West Antarctica. *Marine Geology*, 258(1), 100-114.

Piotrowski, J.A., **1989**. Relationship between drumlin length and width as a manifestation of the subglacial processes. *Zeitschrift für Geomorphologie* 33 (4), 429–441.

Rebesco, M., Camerlenghi, A., Volpi, V., Neagu, C., Accettella, D., Lindberg, B., ... and Party, M., **2007**. Interaction of processes and importance of contourites: insights from the detailed morphology of sediment Drift 7, Antarctica. *Geological Society, London, Special Publications*, 276(1), 95-110.

Spagnolo, M., Clark, C. D., and Hughes, A. L., **2012**. Drumlin relief. *Geomorphology*, 153, 179-191.

Stokes, C. R., Spagnolo, M., Clark, C. D., Cofaigh, C. Ó., Lian, O. B., and Dunstone, R. B., **2013**. Formation of mega-scale glacial lineations on the Dubawnt Lake Ice Stream bed: 1. size, shape and spacing from a large remote sensing dataset. *Quaternary Science Reviews*, 77, 190-209.

Stokes, C.R., Spagnolo, M. and Clark, C.D., **2011**. The composition and internal structure of drumlins: Complexity, commonality, and implications for a unifying theory of their formation. *Earth science reviews*, 107 (3-4). pp. 398-422.

Sugden, D. E., Denton, G. H., and Marchant, D. R., **1991**. Subglacial meltwater channel systems and ice sheet overriding, Asgard Range, Antarctica. *Geografiska Annaler. Series A. Physical Geography*, 109-121.

Vietz, G. J., Rutherfurd, I. D., Fletcher, T. D., and Walsh, C. J., **2016**. Thinking outside the channel: Challenges and opportunities for protection and restoration of stream morphology in urbanizing catchments. *Landscape and Urban Planning*, 145, 34-44.

Wellner, J. S., Heroy, D. C., and Anderson, J. B., **2006**. The death mask of the Antarctic ice sheet: comparison of glacial geomorphic features across the continental shelf. *Geomorphology*, 75(1), 157-171.

Wellner, J. S., Lowe, A. L., Shipp, S. S., and Anderson, J. B., **2001**. Distribution of glacial geomorphic features on the Antarctic continental shelf and correlation with substrate: implications for ice behavior. *Journal of Glaciology*, 47(158), 397-411.

CHAPTER 6:
Conclusions and recommendations

6.1. Conclusions

The configuration and distribution of glacial bedforms observed along the different continental shelf segments between Frost and Dibble Glaciers provide direct evidence of a past grounded EAIS extended until the shelf break, and the presence of a fast-flowing paleo-ice stream during the last glaciation. The detailed analyses of the interpreted glacial features in this study reveal important indications to understand the past ice behaviour, subglacial processes and spatial variability. The analyses suggest that:

- The arrangement and the morphology of the glacial bedforms mapped present similarities with the West Antarctic and AP continental shelf segments;
- The expressive meltwater channels system observed on the inner continental shelf and carved into crystalline bedrock suggests the paleo presence of significant amounts of meltwater flow, probably sourced mostly by subglacial melting processes that could be derived from important geothermal fluxes in the Wilkes Land and/or the catastrophically drainage of subglacial lakes;
- The streamlined bedforms, such as drumlin-like bedforms and MSGLs, record the pattern and flow dynamics of a paleo-ice stream towards the north on the mid continental shelf;
- The morphometric analysis of the drumlin-like bedforms shows that their imprint was strongly conditioned by non-uniforms factors such as local basal conditions, topography, presence of outcrops, and ice flow conditions through time;
- The correlations found between some morphological parameters on drumlin-like bedforms are in agreement with the studies of Clark et al. (2009) and Spagnolo et al. (2012). However, the classification model proposed by Gales et al. (2013) do not match the gullies of this study;
- The spatial analysis of the gully parameters, such as sinuosity and length allow to recognise the continental slope geometry as an important factor during the formation of the gullies;

- The gullies system found on the shelf break constitute a strong evidence that the grounded paleo-ice reached the shelf edge in the past;
- The sediment mounds present on the continental rise represent large volumes of sediment provided through erosion and transport of sediments, by downslope processes from the outer continental shelf.

6.2. Recommendations for further study

The morphometric data together with spatial interpolation seems to be a promising tool to characterise environment controls and to constrain the forming mechanisms of the glacial features. This study can be used to provide improved information about glacial dynamics. For instance, the elongation ratio of drumlinised forms can be correlated to ice velocity (e.g. Stokes et al., 2013) allowing to produce enhanced paleo-flow dynamic models. Those models can be applied all around the Antarctic continental shelf (were those features can be identified) in order to obtain a better assessment of glacial dynamics among the different Antarctic ice sheets (EAIS, WAIS and AP) during the past, and compare them to the current observations.

References

Clark, C. D., Hughes, A. L., Greenwood, S. L., Spagnolo, M., and Ng, F. S., **2009**. Size and shape characteristics of drumlins, derived from a large sample, and associated scaling laws. *Quaternary Science Reviews*, 28(7), 677-692.

Spagnolo, M., Clark, C. D., and Hughes, A. L., **2012**. Drumlin relief. *Geomorphology*, 153, 179-191.

Stokes, C. R., Spagnolo, M., Clark, C. D., Cofaigh, C. Ó., Lian, O. B., and Dunstone, R. B., **2013**. Formation of mega-scale glacial lineations on the Dubawnt Lake Ice Stream bed: 1. size, shape and spacing from a large remote sensing dataset. *Quaternary Science Reviews*, 77, pp. 190-209.

Appendix I – Drumlin-like measurements

No.	Arcgis Ref	Real Length (m)	Width (m)	Elongation Ratio	Real Heigth (m)	Area (m2)
1	1	1,712	298	6	8	354,430
2	2	1,128	414	3	35	234,218
3	3	2,111	500	4	58	423,900
4	4	450	450	1	15	121,238
5	5	657	351	2	23	136,751
6	6	989	465	2	49	286,960
7	7	517	176	3	6	76,983
8	8	1,209	249	5	10	186,324
9	9	848	349	2	39	170,330
10	10	949	306	3	23	122,480
11	11	478	154	3	5	64,429
12	12	1,004	219	5	7	130,111
13	13	942	258	4	22	122,775
14	14	-	-	-	-	-
15	15	571	109	5	9	59,520
16	16	633	238	3	20	94,534
17	17	462	158	3	12	49,353
18	18	1,337	393	3	39	403,507
19	19	1,284	321	4	26	536,669
20	20	671	253	3	11	125,204
21	21	1,063	212	5	2	203,954
22	22	1,114	238	5	55	182,817
23	23	951	528	2	38	296,890
24	24	1,540	274	6	51	402,321
25	25	1,285	568	2	45	476,513
26	26	1,401	291	5	23	424,075
27	27	878	214	4	10	164,401
28	30	714	243	3	17	99,093
29	31	827	295	3	31	136,936
30	32	464	152	3	17	86,916

No. Insufficient bathymetry coverage

Appendix II – Correlation matrix of drumlin-like morphological parameters

	Length (m)	Width (m)	E. Ratio	Relief (m)
Length (m)	1	0,47	**0,54**	**0,53**
Width (m)	0,47	1	-0,44	**0,66**
E. Ratio	**0,54**	-0,44	1	-0,12
Relief (m)	**0,53**	**0,66**	-0,12	1

Appendix III – Gully measurements

Group A - Profiles taken 50 m bellow continetal shelf edge											
No.	**ArcGis Ref**	**Studied Gully**	**U/V index (b Value)**	**Profile Shape**	**Total Length (m)**	**Straith Lengh (m)**	**Sinuosity**	**Width (m)**	**Depth (m)**	**W/D**	**Gully Type**
1	1	Branching Gully	1.3	V	1,983	1,832	1.08	175	28	6.3	x
2	2	Single Gully	1.4	V	2,494	2,381	1.05	295	46	6.4	x
3	3	Branching Gully	2.4	U	2,117	2,086	1.01	254	26	9.8	Type IV
4	4	Branching Gully	2.5	U	1,536	1,382	1.11	169	20	8.5	x
5	5	Single Gully	1.7	U	1,715	1,679	1.02	195	25	7.8	Type II
6	6	Single Gully	1.4	V	1,694	1,567	1.08	228	25	9.1	x
7	7	Single Gully	1.6	U	805	752	1.07	166	25	6.6	x
8	8	Branching Gully	1.5	V	1,915	1,877	1.02	162	19	8.5	x
9	9	Branching Gully	1.0	V	2,556	2,356	1.08	126	10	12.6	x
10	10	Single Gully	0.7	V	2,362	2,309	1.02	216	11	19.6	Type I
11	11	Single Gully	0.9	V	2,363	2,179	1.08	179	14	12.8	x
12	12	Single Gully	1.3	V	2,156	2,084	1.03	188	18	10.4	Type I
13	13	Branching Gully	2.3	U	2,000	1,961	1.02	273	33	8.3	x
14	14	Single Gully	1.7	U	2,497	2,369	1.05	135	19	7.1	x
15	15	Single Gully	1.6	U	2,705	2,532	1.07	247	17	14.5	x
16	16	Single Gully	1.2	V	1,875	1,712	1.10	199	16	12.4	x
17	17	Branching Gully	1.2	V	1,900	1,857	1.02	243	21	11.6	x
18	18	Single Gully	-	-	1,805	1,681	1.07	111	7	15.9	x
19	19	Branching Gully	0.9	V	1,917	1,854	1.03	185	26	7.1	x
20	20	Branching Gully	1.8	U	1,736	1,683	1.03	188	24	7.8	Type IV
21	21	Branching Gully	0.6	V	1,763	1,632	1.08	187	18	10.4	x
22	22	Single Gully	3.4	U	1,726	1,631	1.06	185	21	8.8	x
23	23	Branching Gully	1.2	V	1,784	1,741	1.02	231	32	7.2	x
24	24	Single Gully	-	-	1,731	1,715	1.01	138	20	6.9	x
25	25	Branching Gully	2.8	U	1,920	1,851	1.04	216	11	19.6	Type IV
26	26	Single Gully	1.7	U	2,574	2,393	1.08	342	29	11.8	x
27	27	Branching Gully	0.8	V	2,315	2,215	1.05	199	21	9.5	x
28	28	Branching Gully	2.3	U	2,068	1,930	1.07	371	24	15.5	x
29	29	Single Gully	1.9	U	1,740	1,704	1.02	310	15	20.7	Type II
30	30	Single Gully	1.9	U	2,434	2,364	1.03	157	14	11.2	Type II
31	31	Branching Gully	3.8	U	2,605	2,525	1.03	206	15	13.7	Type IV

32	32	Branching Gully	2.0	U	2,448	2,388	1.03	187	14	13.4	Type IV
33	33	Single Gully	1.7	U	1,702	1,664	1.02	279	30	9.3	Type II
34	34	Single Gully	1.3	V	1,687	1,604	1.05	200	18	11.1	x
35	35	Single Gully	1.9	U	1,922	1,895	1.01	204	20	10.2	Type II
36	36	Single Gully	2.1	U	1,856	1,826	1.02	315	19	16.6	Type II
37	37	Single Gully	2.8	U	2,394	2,330	1.03	333	35	9.5	Type II
38	38	Single Gully	1.6	V	1,922	1,893	1.02	285	29	9.8	Type I
39	39	Single Gully	-	-	1,201	1,197	1.00	133	7	19.0	x
40	40	Single Gully	2.4	U	1,549	1,542	1.00	231	28	8.3	Type II
41	41	Single Gully	2.4	U	794	791	1.00	197	24	8.2	Type II
42	42	Single Gully	1.3	V	2,101	2,055	1.02	196	28	7.0	Type I
43	43	Single Gully	2.9	U	2,417	2,351	1.03	286	30	9.5	x
44	44	Branching Gully	1.5	V	2,000	1,944	1.03	163	23	7.1	x
45	45	Single Gully	1.5	V	1,818	1,803	1.01	124	12	10.3	Type I
46	46	Single Gully	1.6	U	1,739	1,698	1.02	203	28	7.3	Type I

No. Was not possible to determine the U/V index due to complex form of the taken profile or lack of points.

x The parameters do not fit on the gullies classification.

Group B - Profiles taken 100 m bellow continetal shelf edge											
No.	**ArcGis Ref**	**Studied Gully**	**U/V index (b Value)**	**Profile Shape**	**Total Length (m)**	**Straith Lengh (m)**	**Sinuosity**	**Width (m)**	**Depth (m)**	**W/D**	**Gully Type**
1	47	Single Gully	1.31	V	1,543	1,517	1.02	251	47	5.3	Type I
2	48	Single Gully	1.66	U	1,692	1,585	1.07	206	21	9.8	x
3	49	Branching Gully	3.06	U	1,652	1,579	1.05	212	13	16.3	x
4	50	Branching Gully	0.94	V	1,894	1,754	1.08	152	28	5.4	x
5	51	Branching Gully	-	-	1,449	1,355	1.07	136	17	8.0	x
6	52	Single Gully	-	-	1,175	1,121	1.05	107	5	21.4	x
7	53	Single Gully	1.28	V	996	957	1.04	137	16	8.6	x
8	54	Single Gully	0.90	V	1,536	1,467	1.05	119	11	10.8	x
9	55	Single Gully	2.46	U	1,254	1,212	1.03	131	12	10.9	Type II
10	56	Single Gully	-	-	1,399	1,368	1.02	169	20	8.5	x
11	57	Branching Gully	0.53	V	1,783	1,708	1.04	173	12	14.4	x
12	58	Single Gully	-	-	1,786	1,687	1.06	111	12	9.3	x
13	59	Single Gully	1.91	U	2,145	2,061	1.04	261	34	7.7	x
14	60	Single Gully	-	-	1,822	1,760	1.04	178	13	13.7	x
15	61	Single Gully	2.82	U	2,000	1,917	1.04	259	16	16.2	x
16	62	Single Gully	2.23	U	1,703	1,619	1.05	230	32	7.2	x

17	63	Branching Gully	-	-	1,588	1,544	1.03	309	42	7.4	**x**
18	64	Single Gully	1.39	V	1,583	1,518	1.04	183	20	9.2	**x**
19	65	Single Gully	2.04	U	1,907	1,894	1.01	268	28	9.6	Type II
20	66	Single Gully	2.35	U	1,677	1,577	1.06	260	30	8.7	**x**
21	67	Single Gully	1.50	V	1,940	1,894	1.02	166	21	7.9	**x**
22	68	Single Gully	1.55	V	2,295	2,232	1.03	336	29	11.6	**x**
23	69	Single Gully	4.12	U	2,011	1,994	1.01	235	36	6.5	**x**
24	70	Branching Gully	1.85	U	2,694	2,643	1.02	238	27	8.8	Type IV
25	71	Single Gully	0.88	V	1,989	1,954	1.02	191	13	14.7	**x**
26	72	Branching Gully	0.28	V	3,880	3,769	1.03	229	24	9.5	**x**
27	73	Single Gully	-	-	1,815	1,795	1.01	120	16	7.5	**x**

No. Was not possible to determine the U/V index due to complex form of the taken profile or lack of points.

x The parameters do not fit on the gullies classification.